REPORT DOCUMENTATION PAGE

DTIC FILE COPY

1a. REPORT SECURITY CLASSIFICATION
Unclassified

1b. RESTRICTIVE MARKINGS
None

2a. SECURITY CLASSIFICATION AUTHORITY

3. DISTRIBUTION / AVAILABILITY OF REPORT
Approved for public release, distribution unlimited

2b. DECLASSIFICATION / DOWNGRADING SCHEDULE

AD-A218 370

5. MONITORING ORGANIZATION REPORT NUMBER(S)
AFOSR·TR· 90 0217

6a. NAME OF PERFORMING ORGANIZATION
Department of Aeronautics and Astronautics, M.I.T.

6b. OFFICE SYMBOL *(If applicable)*
31-264

7a. NAME OF MONITORING ORGANIZATION
See #8

6c. ADDRESS *(City, State, and ZIP Code)*
77 Massachusetts Avenue
Cambridge, MA 02139

7b. ADDRESS *(City, State, and ZIP Code)*
See #8

8a. NAME OF FUNDING / SPONSORING ORGANIZATION
AFOSR

8b. OFFICE SYMBOL *(If applicable)*
NA

9. PROCUREMENT INSTRUMENT IDENTIFICATION NUMBER
Contract F49620-85-C-0018

8c. ADDRESS *(City, State, and ZIP Code)*
AFOSR
Bolling AFB, DC 20332

10. SOURCE OF FUNDING NUMBERS

PROGRAM ELEMENT NO.	PROJECT NO.	TASK NO.	WORK UNIT ACCESSION NO.
61102F	2307	A4	

11. TITLE *(Include Security Classification)*
Unsteady Flow Phenomena in Turbomachines

12. PERSONAL AUTHOR(S)
E.M. Greitzer, A.H. Epstein, M.B. Giles, J.E. McCune, C.S. Tan

13a. TYPE OF REPORT
FINAL

13b. TIME COVERED
FROM 10/19/87 TO 10/18/89

14. DATE OF REPORT *(Year, Month, Day)*
January 24, 1990

15. PAGE COUNT
193

16. SUPPLEMENTARY NOTATION

17. COSATI CODES

FIELD	GROUP	SUB-GROUP

18. SUBJECT TERMS *(Continue on reverse if necessary and identify by block number)*
Computational Fluid Mechanics, Unsteady Flows in Turbomachines, Vortex Wakes, Compressor Stability, Transonic Compressors.

19. ABSTRACT *(Continue on reverse if necessary and identify by block number)*

This report describes work carried out at the Gas Turbine Laboratory at M.I.T. during the period 10/19/87 - 10/18/89, as part of our multi-investigator effort on basic unsteady flow phenomena. Within the overall project, four separate tasks are specified. These are, in brief: I. Unsteady Flow in Compressors; II. Computational Techniques for Unsteady Flows; III. Unsteady Phenomena, Inlet Distortion, and Flow Instabilities in Multistage Compressors; IV. Unsteady Vortical Wakes Behind Blade Rows- Prediction of Relationships with Blade Properties.

20. DISTRIBUTION / AVAILABILITY OF ABSTRACT
☒ UNCLASSIFIED/UNLIMITED ☐ SAME AS RPT. ☐ DTIC USERS

21. ABSTRACT SECURITY CLASSIFICATION

22a. NAME OF RESPONSIBLE INDIVIDUAL
HENRY E HELIN

22b. TELEPHONE *(Include Area Code)*
202-767-0471

22c. OFFICE SYMBOL
AFOSR/NA

DD FORM 1473, 84 MAR   83 APR edition may be used until exhausted.
All other editions are obsolete.

Gas Turbine Laboratory
Department of Aeronautics and Astronautics
Massachusetts Institute of Technology
Cambridge, MA 02139

Final Technical Report

on

Contract No. F49620-85-C-0018

entitled

UNSTEADY FLOW PHENOMENA IN TURBOMACHINES

for the period

October 19, 1987 to October 18, 1989

submitted to

AIR FORCE OFFICE OF SCIENTIFIC RESEARCH
Building 410
Bolling Air Force Base, DC 20332

Attention: Captain H. Helin

PRINCIPAL
INVESTIGATOR: Edward M. Greitzer
                    H.N. Slater Professor and Director,
                    Gas Turbine Laboratory

CO-INVESTIGATORS: Professor Alan H. Epstein
                    Professor Michael B. Giles
                    Professor James E. McCune
                    Dr. Choon S. Tan

January 1990

90 02 23 050

1

TABLE OF CONTENTS

1. INTRODUCTION AND RESEARCH OBJECTIVES

This is a final report on work carried out at the Gas Turbine Laboratory at MIT, as part of a multi-investigator effort on unsteady flow phenomena in turbomachines. Support for this program was provided by the Air Force Office of Scientific Research under Contract Number F49620-85-C-0018, Captain H. Helin, Program Manager.

The present report gives a summary of the work for the period 10/19/87 - 10/18/89. As such, it is not intended to be the primary source and the referenced reports and publications, as well as the previous progress report [1], should be consulted for details and background. These address the work in considerable depth.

Within the general area of turbomachinery fluid dynamics, four separate tasks are specified under this contract. These are, in brief:

I. Unsteady flow effects in compressors including the three-dimensional nature of, and radial transport in, the unsteady flow field due to the vortical wake structure.

II. Development and application of computational techniques for unsteady flows, including investigation of unsteady flows in transonic diffusers and assessment of losses due to unsteady rotor/stator interaction.

III. Unsteady phenomena, inlet distortion and flow instabilities in multistage compressors, including experimental and analytical investigations of the structure of instability modes in advanced blading geometries.

IV. Unsteady blade-vortex street interaction in transonic cascades including models to describe the unsteady development of vortex streets in and around blades.

In addition to these tasks, the multi-investigator contract encompassed the Air Force Research in Aero Propulsion Technology (AFRAPT) Program. The work carried out in each of

the tasks will be described in the next section. Publications generated are given in the individual task descriptions, and an overall list appears in Section 4.

Reference

1. Greitzer, E.M., Epstein, A.H., Giles, M.B., McCune, J.E., Tan, C.S., Annual Technical Report on Contract F49620-85-C-0018, "Unsteady Flow Phenomena in Turbomachines," December 1988.

TASK I: UNSTEADY FLOW IN COMPRESSORS

(Investigators: A.H. Epstein, T. Barber)

Objectives

Compressors have very heavily loaded boundary layers and, as in any high Reynolds number device, the boundary layer behavior controls the performance of the machine. This is especially true for modern current transonic, low choke margin designs. Understanding and (hopefully) prediction of the three-dimensional boundary layer behavior -- especially transition and separation -- are a key to improved design tools and design realization. Unfortunately, the prediction of transonic three-dimensional, unsteady boundary layer on airfoils with strong rotation in turbulent flow is among the most difficult of fluid mechanics problems from theoretical, numerical, and experimental points of view.

The focus of the research described herein is to make first-of-a-kind measurements of the three-dimensional, unsteady boundary layer behavior on full-scale compressors under typical operation, and to understand the influence of this behavior on compressor design and operation.

Progress During This Reporting Period

Progress during this reporting period can be divided into two : the analysis of radial transport caused by separated blade boundary layers and other mechanics, and the design of thin film boundary layer sensors. The radial transport analysis of work (supported under previous AFOSR sponsorship) is detailed in the attached paper which will be presented at the ASME Gas Turbine Conference in June 1990.

The thin film gauge development work has concentrated on the construction of analytical models to aid in the design of sensors capable of yielding quantitative measurements of wall shear on operating high speed compressors. There are two goals that these sensors are being designed to meet. The first is that they have sufficient spatial extent so they can yield accurate information on boundary layer separation and shock wave-boundary layer interaction without requiring precise

foreknowledge of the location of these interactions. This problem is being addressed by using spatially dispersed sensors.

The use of ladder-type gauges increases the spatial extent of the measurements while conserving gauge number and thus wire number (an important factor governing the cost and complexity of an experiment in a rotating environment). The concept, illustrated in Fig. 1, is to use multiple, closely spaced, sensing elements which are electrically in parallel. This would generate a staircase-like waveform as a separation or shock wave passed over the sensor, permitting the unambiguous determination of the flow structure position. Flow reversals can be handled by an analysis technique recently developed at NASA.

The second goal is the quantitative measurement of wall shear in a compressor, where the wall and freestream boundary conditions are not well known. The solution here is multilayer thin film geometries (see Fig. 2) in which the bottom sensor serves to monitor the heat flow into the substrate, thus allowing calibration and operation from dc through tens of kilohertz. One problem that has come up is that the magnitude of the steady state conduction heat loss to a metal substrate (a blade, in this case) is much larger than the unsteady fluid mechanic signal of interest. To avoid having to measure the small difference between two large signals (the heat flow with and without flow), we have been analyzing the use of a constant temperature gas heater under the temperature sensor to reduce or eliminate the heat flow to the blade.

Work Planned for Next Reporting Period

During the next reporting period, we intend to finish the analytical modelling of sensor behavior, construct sample gauges, and test their behavior in a shock tube and free jet.
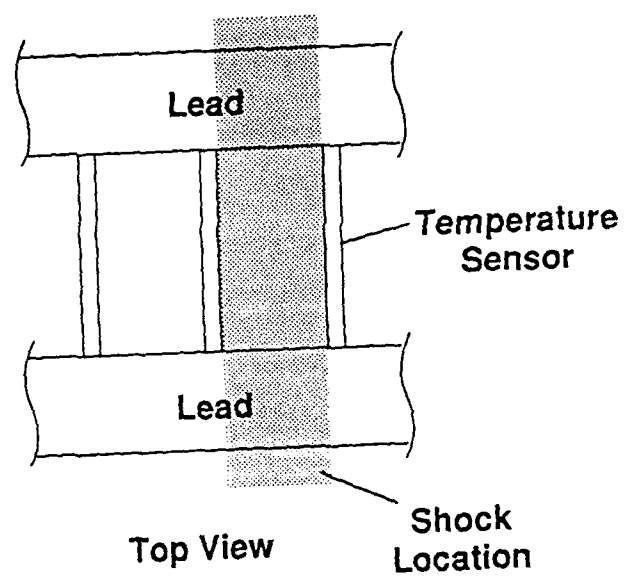
Fig. 1: Ladder-type gauge geometries are being explained to extend spatial coverage while reducing complexity
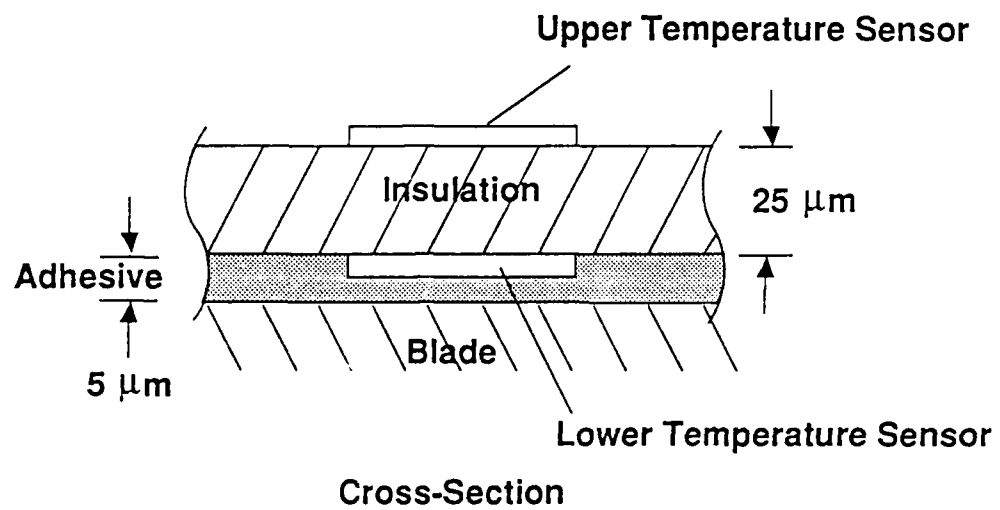
Fig. 2: Multilayer gauge decouples sensor response from substrate heat flow

UNSTEADY RADIAL TRANSPORT IN A TRANSONIC COMPRESSOR STAGE

by
P.A. Kotidis[*] and A.H. Epstein
Gas Turbine Laboratory
Massachusetts Institute of Technology
Cambridge, MA 02139

ABSTRACT

Time-resolved radial transport has been measured in a transonic compressor rotor by injecting a thin sheet of tracer gas upstream of the rotor and then surveying the tracer concentration at the rotor exit. The simultaneous, co-located, high frequency response measurements of local tracer gas concentration, total temperature, and total pressure made downstream of the rotor showed that most of the fluid transported radially appears in the blade wakes and that this fluid has considerably higher entropy than the circumferential mean. Both inward and outward fluid transport along the span was observed (3.5% of the total throughflow moved toward the tip while 1.6% moved toward the hub). Tracer concentration and fluid total temperature and pressure varied considerably from wake to wake, even on multiple samplings of the same blade. The time mean spreading rate inferred from these measurements is in general agreement with previously reported studies on multi-stage low speed compressors and is well predicted by the method of Gallimore and Cumpsty. It is suggested that a vortex street in the blade wakes could be responsible for both the observed radial transport and the large wake to wake variability. A quasi-three-dimensional model of a vortex street wake was developed and shown to be consistent with the data. The model predicts all of the inward transport but only 20% of the outward transport. It is hypothesized that outflow in separated regions on the blade suction surface is responsible for the remainder of the transport toward the rotor tip. Since the entropy, as well as the mass of the fluid transported radially, was measured, an estimate of the redistribution of loss in rotor due to radial fluid transport could be made. This showed that the effect of radial transport in this rotor was to move substantial loss from the rotor hub to tip, implying that a conventionally measured spanwise efficiency survey may not accurately represent the performance of individual blade sections.

NOMENCLATURE

a	longitudinal spacing between vortices
c_p	constant pressure specific heat
C_{max}	maximum tracer gas concentration (mass fraction)
C_p	static pressure coefficient
C_{rel}	$C(X,Y)/C_{max}$

$C(X,Y)$	tracer gas concentration (mass fraction) at point X,Y
d	maximum blade thickness
F	strength of line source of tracer gas injection per unit length
h	lateral spacing at the two rows of vortices in the vortex street
k	vortex circulation outside the vortex
K_0	modified Bessel function of the second kind, zero order
L	axial chord
M	Mach number
p	static pressure
P_T	total (stagnation) pressure
r	radial distance from vortex center
r_0	radius of vortex core edge
$\mathcal{R}$	gas constant
R	radial (spanwise) distance, measured from the rotor centerline
Re	vortex Reynolds number = k/ν
R_t	tip radius of the rotor
Δs	specific entropy change
t	time
T_T	total (stagnation) temperature
U	free stream velocity
$\underline{w}(R,\theta,z)$	velocity in vortex core in the blade relative frame
$W(R,\theta,z)$	freestream velocity in blade relative frame
W_i	velocity induced by vortex street
W_p	peripheral velocity at vortex core edge
α	empirical eddy viscosity constant
ε	mixing coefficient
γ	ratio of specific heats
ρ	static density
ν	kinematic viscosity
ν_t	eddy kinematic viscosity
ϕ	flow coefficient
ω	relative total pressure loss coefficient
Ω	rotor angular velocity
$< >$	averaged over vortex core circumference

Subscripts

c	within vortex core
core	isolated vortex core
pot	isolated potential vortex
row	single row of potential vortices
R	spanwise direction

[*] Current address: Avco Research Laboratory-Textron, Everett, MA 02149

x	vortex streamwise direction
y	direction orthogonal to vortex streamwise
z	rotor axial direction
θ	rotor tangential direction
∞	freestream, outside vortex core

Superscripts

⁻	non-dimensional
'	frame moving with vortices with origin along vortex street centerline
"	frame moving with vortices with origin at vortex center

INTRODUCTION

Traditionally, axial compressors have been designed on a primarily two-dimensional basis, using streamline curvature techniques to ensure radial equilibrium. The mean streamsurfaces were designed, the blade-to-blade flows calculated, and then the spanwise variations taken into account. The advent of three-dimensional Euler calculational procedures have permitted more detailed looks at the 3-D inviscid flow structure. Stages are designed for the most part to minimize radial flows. It has long been known, however, that some spanwise transport does occur across the nominal steady state 2-D streamsurfaces. This three-dimensional mixing is clearly important in multistage compressors and has been accounted for in the design process by empirically based models of spanwise mixing such as that proposed by Adkins and Smith (1981).

Radial transport may also be of concern in single-stage compressors as well. Kerrebrock (1980) noted that although the total loss in transonic rotors may be well predicted, the spanwise loss distribution often is not. It is puzzling in that the rotor efficiency is much lower near the tip and higher near the hub than could be explained by strictly 2-D shock and viscous loss models, including tip clearance losses. Accounting for the 3-D shock structures as proposed by Prince (1980) does not help here since the shock leaning predicts reduced rather than increased loss in the supersonic tip region and has no direct influence in the subsonic region near the hub. Kerrebrock speculated that the high tip and low hub efficiencies might be caused by radial flows which would serve to redistribute losses radially without necessarily generating much loss themselves. Thompkins and Usab (1981) examined the radial flow on a transonic fan rotor blade using a quasi-three-dimensional boundary layer code and concluded that centrifuging of the attached boundary layer would not transport much loss radially. Given a sufficiently large separated region, however, a considerable amount of lossy fluid could be moved radially.

What was clearly needed at this point was some additional data which could clearly delineate the physical processes at work in these machines. Gallimore and Cumpsty (1986) and Wisler et al. (1987) have measured radial mixing in multistage low speed compressors.

Their data, however, were measured in the time average only so that the mechanisms and structure of the radial mixing remained in some debate. Furthermore, although many flow phenomena are well modelled in low speed machines, some are not. Given the degree of uncertainty in the detailed fluid mechanics of compressor radial flows and the lack of data on loss redistribution (if any), measurements on high speed compressors seemed in order.

The objective of the research described herein was to make quantitative measurements of the radial transport in a modern transonic rotor with sufficient spatial and temporal resolution so as to establish the magnitude of the radial flows and to elucidate mechanisms responsible. In the next sections, we describe the experimental apparatus, present the data, develop an analytical model of the flow field to explain the observations, and finally comment on the importance of radial flows in transonic fans and compressors.

EXPERIMENTAL APPARATUS

The conceptual basis of the experiment was to inject a thin sheet of tracer gas upstream of the rotor (the sheet is oriented normal to the radial direction) and then map the tracer gas distribution downstream of the rotor with instrumentation whose frequency response is large compared to blade passing (Fig. 1). The frequency response of the laboratory frame instrument translates into spatial resolution in the rotor relative frame and also yields information on the rotor relative unsteadiness of the flow. The instrument chosen also measures time resolved total temperature and pressure and thus entropy so that the instantaneous loss distribution can be determined simultaneously with the tracer distribution.

The test compressor selected was a low aspect ratio, high throughflow, transonic machine designed by Wennerstrom (1984). With a design stage pressure ratio of 2.1 and peak efficiency of 90%, this 0.43m diameter, 427 m/s tip speed machine is the prototype for a current generation of military compressors now under development. The compressor was operated in the MIT Blowdown Compressor Facility (Kerrebrock et al., 1974) which provides steady state running conditions for approximately 50 ms in an argon-Freon 12 atmosphere. Previous measurements on this high throughflow stage in the blowdown facility were reported by Ng and Epstein (1985).

The tracer gas was injected through the hollow trailing edge of a NACA 65-021 airfoil located approximately 0.2 chords upstream of the rotor. (This section was chosen because it remained subcritical at the rotor inlet Mach number, while having sufficient cross-sectional area to pass the tracer mass flow at low loss.) The airfoil was hollow with a thin (0.75 mm) slot along the trailing edge and oriented so as to inject the thin sheet of tracer tangent to the circumference at one radial location spanning approximately two rotor blade pitches (Fig. 2). The airfoil was supported on two radial struts (also NACA 65-021) such that its spanwise position could be varied between tests. The struts were hollow and supplied the gas to the injector. In order that the sheet of injectant gas suffer the minimum dispersion, it is
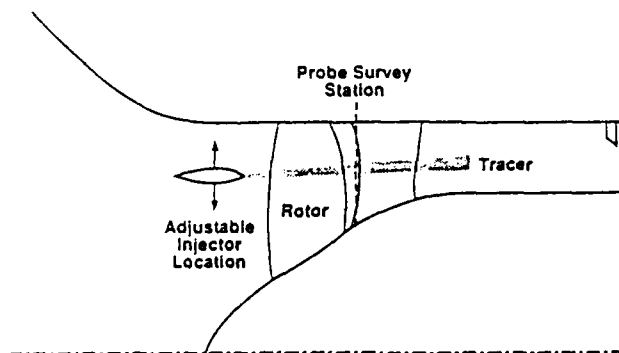

Fig. 1: Experimental arrangement in high throughflow compressor showing upstream tracer gas injector and probe survey station
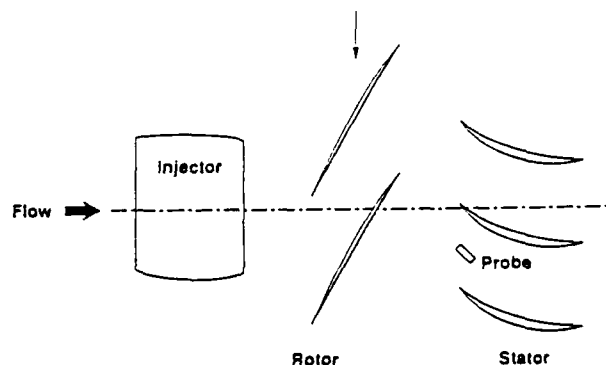

Fig. 2: Scale drawing of compressor near tip section showing relative scale of injector and concentration probe

important that the velocity at the injection slot exit match that of the freestream. In a blowdown tunnel the Mach numbers are constant, however, the freestream temperature and thus velocity decays with time. Therefore, the injectant was also blown down from its own supply tank whose volume was adjusted so that its decay rate matched that of the main flow. A miniature, high frequency response pressure transducer was mounted within the injector to monitor the pressure during the blowdown test.

INSTRUMENTATION

The principal instrumentation for this experiment was a dual hot wire aspirating probe first reported by Ng and Epstein (1983). This probe (Fig. 3) consists of two co-planar, 6.25 μm diameter hot wires at different temperatures, mounted in a constant area channel with a choked exit. When operated in constant temperature anemometer loops, the hot wires respond to the total temperature (T_T) of the gas and the mass flux (ρU) by the wires. The mass flux through the choked channel of fixed geometry is a function of the freestream total pressure (P_T) and total temperature (T_T). Thus, there are only two unknowns (P_T and T_T) and two measurements (the voltage from each hot wire). Nonuniform gas composition influences both the mass flux by the wires and the heat transfer from the wires and thus introduces a third variable which requires a third measurement. This was provided by "piggybacking" a high frequency response pressure transducer (Kulite XCQ-093) on the aspirating probe to measure pressure directly. The two signals from the hot wires are then used to determine temperature and gas composition. The spatial resolution of the measurement is limited by the size of the probe (3 mm circumferentially and 6 mm radially). The frequency response was established through shocktube testing and calculation to be approximately 20 kHz (4-5 times blade passing frequency). More details on the probe are given by Kotidis and Epstein (1990) , and Kotidis (1989).

The probe sensitivity is dependent on the chemical composition of fluid. The criteria for tracer selection were that it match the density of the main flow in order to properly follow flow accelerations within the rotor and that it give maximum sensitivity and thus signal output from the probe. After considering many tracers, including CO_2 and a He-Xe mix, a mixture of helium and Freon-12 was selected. This 57% weight fraction He mixture matched the 54.5 molecular weight of the main flow argon-Freon 12 mixture in the blowdown facility, while having the high thermal conductivity necessary for good probe sensitivity. Since we were unable to accurately calculate the properties of a quaternary gas mixture, the probe response was established by steady state parametric testing at various temperatures, pressures, and concentrations to establish calibration curves. These curves were then dynamically checked at a few points in a shocktube. Kotidis gives details of the data reduction procedure.
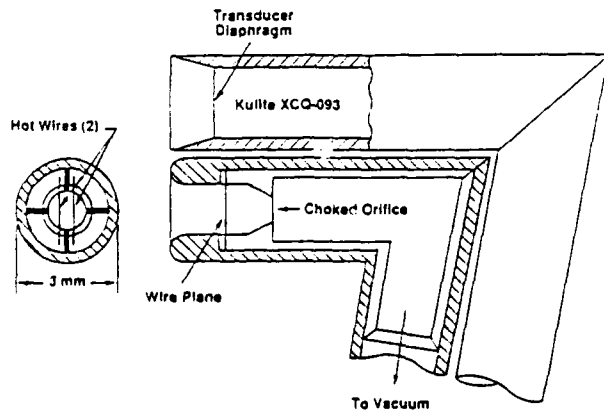
Fig. 3: High frequency response concentration, temperature, and pressure probe
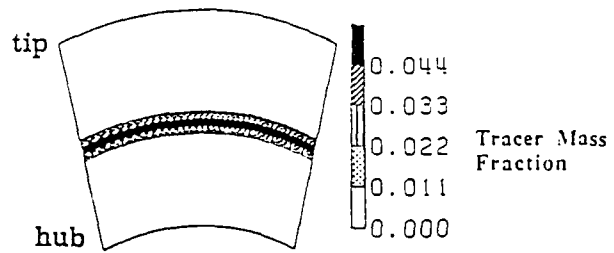
Fig. 4: Time-averaged survey of tracer distribution with blading removed

The principal sources of measurement error were noise in the anemometers and drift between calibrations. The exact magnitude was a nonlinear function of the instantaneous concentration, temperature, and pressure, and this error was calculated for each time point for each test. The average total uncertainty was 0.08% in total pressure and 0.21% in total temperature as a percentage of instantaneous value; and 0.33% of full scale in mass fraction of the tracer gas.

The rotor and stator are closely coupled in this stage and the stator sweeps forward from midspan to both the hub and tip. Thus, the probe was traversed at constant velocity from tip to hub during each test at a station located just ahead of the midspan stator leading edge at mid stator pitch. (The traverse velocity is less than 1% of that of the freestream.)

PROOF OF CONCEPT TESTS

There were two criteria which were critical for the success of these measurements. The first was that the presence of the upstream injector and injectant not influence the operation or performance of the compressor stage. The second was that the sheet of tracer gas not mix excessively due to factors other than the influence of the rotor flowfield during the transit from the injector to the survey station at the stator leading edge.

The influence of the injector on the rotor performance was assessed by examining radial traverses of the time averaged rotor outflow. Since the distribution of rotor exit total pressure, temperature, and flow angle were the same with and without the injector present, we concluded that the influence of the injector on the rotor flow was not a concern.

The degree of radial spreading of the jet which is independent of the rotor flowfield was assessed by blowdown tests with the rotor and stators replaced by casing fairings. Figure 4 shows a measurement of the time averaged tracer distribution measured at the same axial station as it would be with the stage in place. The measured jet thickness (0.9 cm) is small compared with the passage height at this station (10 cm) and is consistent with estimates of spreading from turbulent jets. (The inflow turbulence intensity level was measured as 0.6%.) This amount of spreading is sufficiently small for our purposes.

Another concern was to insure that the total amount of tracer gas detected by the probe was consistent with the amount injected. This checked both that the probe d.c. calibration was valid and that the injector flow was mainly two-dimensional. The total mass of gas measured by the probe was 80% of that injected, based upon the assumption that the flow from the injector is only two-dimensional. Again, this agreement was sufficient for our purposes. Thus, we conclude from these consistency and proof of concept checks that we understand the nature of the experiment and that the artifacts introduced in the data by nonideal behavior were small.

DATA PRESENTATION

The data reported herein were all obtained at design point operation of the compressor. The experiments were performed with the injector positioned at three spanwise locations which we will refer

to is tip (R/R_t = 0.95), midspan (R/R_t = 0.86), and hub (R/R_t = 0.81). All data were taken as instantaneous values of concentration, pressure, and temperature as the probe was slowly traversed from tip to hub. The entropy change of the fluid was calculated from the temperature, pressure, and concentration. The instantaneous data were then ensemble averaged or time averaged in post-test processing, depending on the use.

We present the ensemble averaged data first in Fig. 5, which shows 10 blade ensemble averages of the concentration, temperature, pressure, and entropy assembled into contour plots as viewed looking upstream over two blade pitches. The blade wake positions as indicated on the figures are judged from the location of the total pressure defects (or excesses depending on the local velocity triangles). Comparing the total pressure and temperature plots, we see some variation with injector location of these flow quantities whose spanwise time-averaged distributions are unaffected by the presence of the injector (see Proof of Concept Tests, above). This variation is not due to the injector presence but rather is a result of the relatively small number of blade passages averaged to make the contour plots in this highly unsteady flowfield (dictated by the short running time of the facility). Here, we are concerned mainly with the average flow features which are reproduced from test to test.

In the case of near tip injection in Fig. 5, while most of the tracer remains near the tip, some does travel inward all the way to the hub. The fluid which migrates inward does so in the blade wakes. When the tracer is injected near midspan, the tracer actually moves both radially inward and outward. The inward transport is again confined to the wake region. When the injection is done closer to the hub, the

tracer moves outward toward the tip, mostly in the wake region. By comparing the contours of the three tests, we note that there is relatively less radial transport with tip injection than with midspan or hub injection. Note that these contours do not extend all the way to the tip and hub surfaces so that details of the endwall flows are not seen. In particular, the edge of the tip vortex may just be at the top of the contours.

While the contour plots are effective in conveying large amounts of data quickly, the ensemble averaging process can filter information from the data. Figure 6 shows a short segment of time resolved data taken with midspan (r/r_t = 0.86) tracer injection for measurements made at three spanwise positions. (Note that the tip, midspan, and hub measurements are not taken simultaneously since the probe is traversed from tip to hub during a test.) In the hub region, the downspikes in total pressure are the blade wakes. In the tip region, the velocity triangles are such that the wakes have a total pressure excess. Note that all quantities show the flow to be highly unsteady and aperiodic. There are very significant blade to blade differences. These are much larger than can be explained by minor geometry differences between blades or turbulent fluctuation, Epstein et al., 1988. (It is this high level of fluctuation which causes the variation in the contour plots of Fig. 5.) The tracer concentration at each spanwise position is not uniform across the blade pitch but rather all of the tracer gas is concentrated in a relatively few "spikes" which appear only in the blade wakes. Not all wakes contain tracer, however. It is important to note that those wakes with tracer concentration spikes also contain high entropy. A more complete presentation of these time resolved measurements can be found in
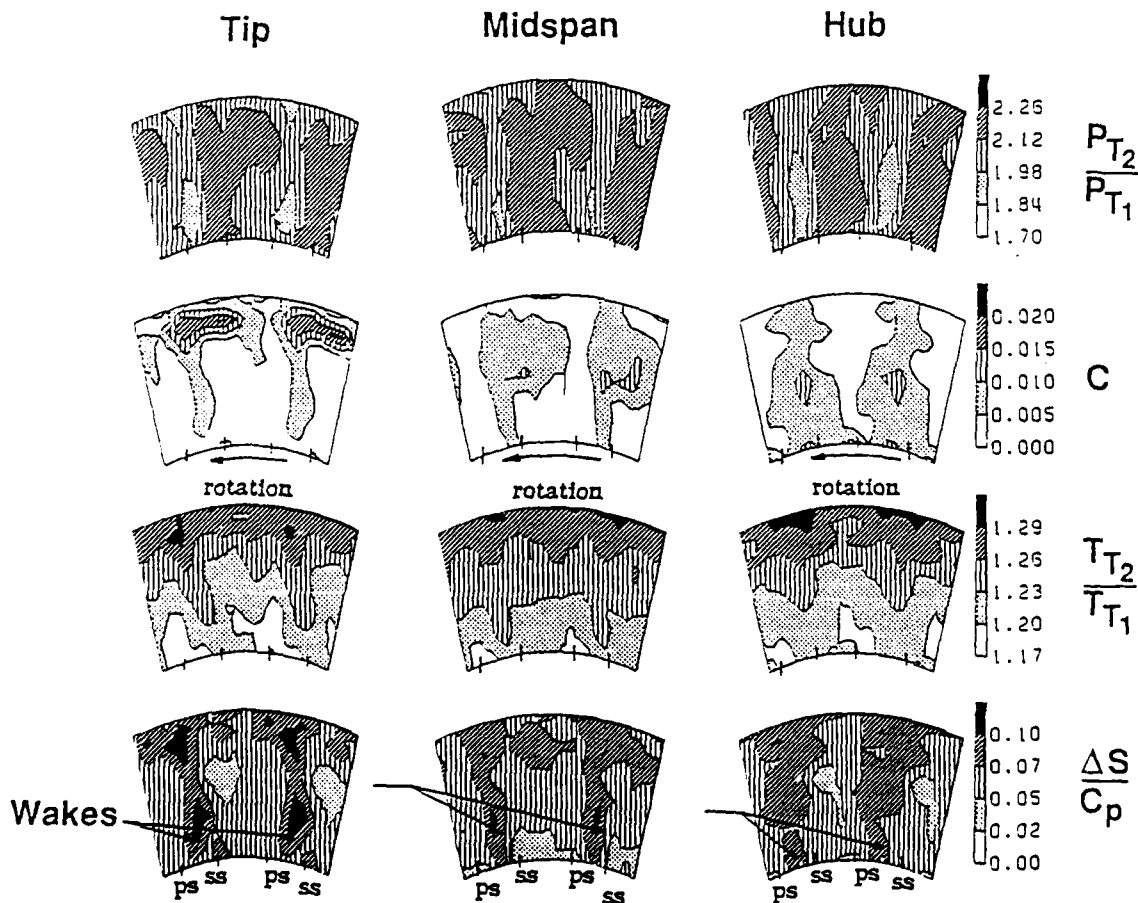

Fig. 5: Ten blade ensemble averaged contour plots of total pressure ratio, tracer concentration (C), total temperature ratio, and entropy measured near the stator leading edge for various injector locations; two blade pitches of data are shown

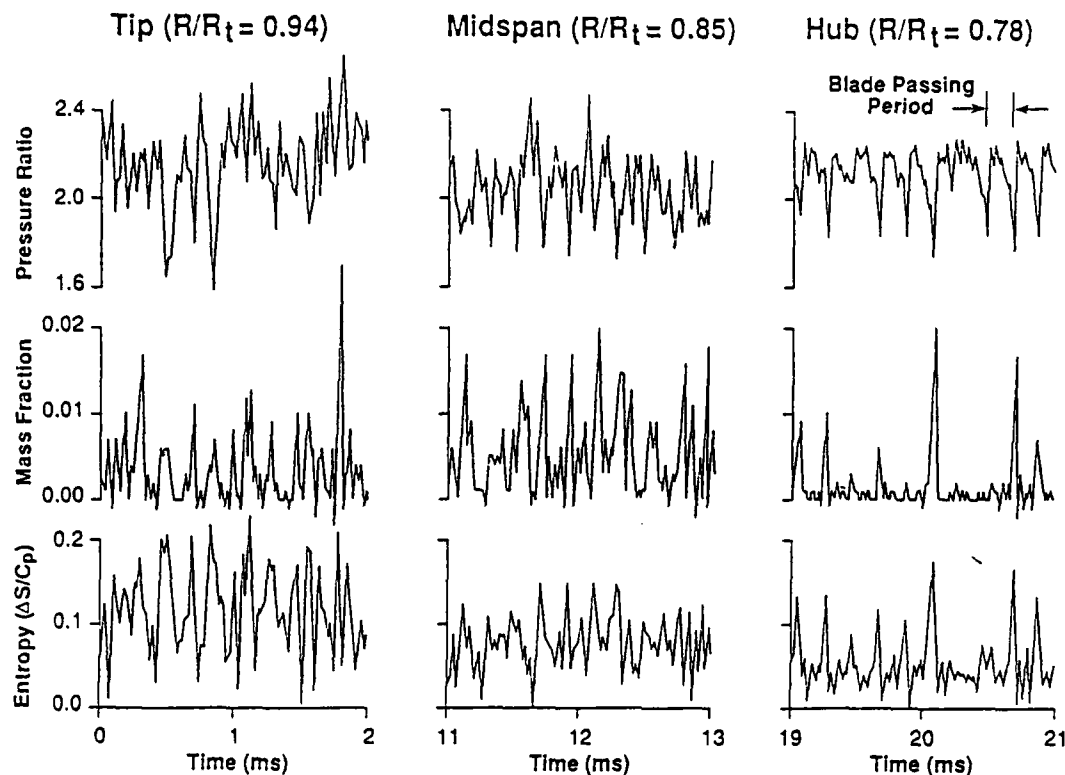Tip (R/R$_t$ = 0.94) Midspan (R/R$_t$ = 0.85) Hub (R/R$_t$ = 0.78)

Fig. 6: Instantaneous measurements of total pressure, tracer concentration, and entropy measured at different radii with the injector located near midspan

Kotidis.

The measurements thus show that most of the fluid transported along the span in this transonic compressor rotor appears in the blade wakes but does not appear in every wake sampled. Furthermore, the fluid that is transported radially has high entropy relative to the mean. The implication is thus that the radial transport may modify the spanwise efficiency distribution of the rotor.

COMPARISON OF TIME AVERAGED MIXING RATES

While our interest here is more toward elucidating the details of the radial flow in a transonic compressor rather than deducing empirical spanwise mixing rates for a designer, it is useful as a first step to compare our time averaged results with published data such as Gallimore and Cumpsty, and Adkins and Smith, if for no other reason than as an additional validity check on our measurements and data reduction procedure.

The goal here is to derive a diffusion constant, ε, from the experimental data in a manner consistent with previous work. The only difference is that, in this case, the tracer is introduced as a line source rather than the point source as used by Gallimore and Cumpsty. The solution of the diffusion equation for a line source of strength F per unit length is given by Hinze (1959) as

$$C(X,Y) = \frac{F}{2\pi\epsilon} K_o \left[\frac{U(X^2 + Y^2)^{1/2}}{2\epsilon} \right] \exp\left(\frac{UX}{2\epsilon}\right) \quad (1)$$

where C is the concentration at X and Y, X is the flow direction, Y the radial (spanwise) direction, U the free stream velocity, and K_o the modified Bessel function of the second kind, zero order. This can be simplified for small values of ε/UX and small values of Y/X as

$$C(X,Y) = \frac{F}{2(\pi\epsilon U|X|)^{1/2}} \exp\left[-\frac{UY^2}{4\epsilon|X|}\right] \quad (2)$$

Following the procedure of Gallimore and Cumpsty, we then derive an expression for spanwise spreading rate, Y/L (where L is chosen as the rotor axial chord), as a function of normalized mixing coefficient ε/UL, and $C_{rel} = C(X,Y)/C_{max}$,

$$\frac{Y}{L} = \left[-4 \frac{\epsilon}{UL} \frac{|X|}{L} \ln C_{rel} \right] \quad (3)$$

C_{max} is assumed to occur along the X axis.

Given the measured concentration distributions (Fig. 5), the mixing coefficient can now be estimated with Eq. (3). The crossflow dimension, Y, was derived from the contour plots in a manner consistent with that of Wisler et al., which was concerned with only the turbulent diffusion contribution to the mixing; specifically, the cross-stream dimension, Y, is taken as the point at which the concentration is 20% of the maximum value. This is illustrated in Fig. 7. Note that the tracer in the wakes has been ignored in this analysis.

The results of this fit to the data are shown in Fig. 8, along with some data reported in the literature for multistage compressors. The values from this work fall within the range of values expected from the literature. Single-stage low speed compressors with high inflow turbulence exhibit comparable mixing rates, but those with low inflow turbulence levels (the case here) show considerably reduced mixing (Cumpsty). The high level observed in this compressor could be due either to a higher level of inherent flow unsteadiness within the transonic machine due to such phenomena as shock oscillations (Ng and Epstein, 1985), or to some interaction between
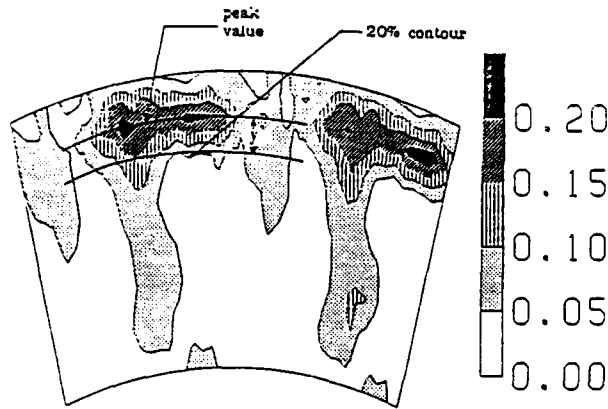
Fig. 7: The 20% concentration contours were used to derive an average mixing coefficient for Eq. (3)

the injection process and rotor flowfield that doesn't appear in the time averaged rotor performance. (Note though that the no-rotor data point in Fig. 8 is a factor of 5 below the with-rotor mixing coefficient, implying that most of the mixing is due to the rotor.)

Gallimore and Cumpsty proposed that the turbulent mixing coefficient can be estimated as

$$\frac{\varepsilon}{UL} = A \frac{d}{L} \left[\frac{2\overline{\omega}(d/L)}{3\phi^2} \right]^{1/3}$$

(4)

where d is the blade thickness, L the compressor length, ϕ the flow coefficient, ω the loss coefficient, and A a property of turbulent flow with a proposed value of about 0.4. Applying Eq. (4) to this compressor yields the dashed straight line on Fig. 8, which is in quite good agreement with the data. Note that the measured relative total pressure loss coefficient (about one half of which is shock loss in this transonic compressor) was used here.

From these comparisons we concluded two things. First, that the data reported herein is in fact consistent with previously reported multistage measurements. The second is that the techniques of Gallimore and Cumpsty, derived from low speed multistage data, do a quite reasonable job in predicting the time averaged mixing in a transonic compressor rotor.

RADIAL TRANSPORT BY SPANWISE WAKE VORTICES

The measurements show that the fluid in the wakes at the measurement station has undergone considerable radial transport, both radially in and out. Wake outward centrifuging has long been observed on low speed compressors and, although some experimenters have reported measurements of inward flows, they have not been explained. An order of magnitude analysis of such classical mechanisms as secondary flow and tip leakage vortices does not account for this degree of transport (Kotidis). Radial flow in the rotor blade boundary layers can account for much of the radial outflow if the boundary layers are separated (Thompkins and Usab), but does not explain the inward radial migration of the tracer. One physical phenomenon which may account for much of this transport is the spanwise vortex street structure within the blade wakes. In the following sections, we shall present some background on this phenomena, develop a very simple 3-D vortex street model, and compare the radial fluid transport predicted by the model with the measurement.

The presence of vortex streets has long been recognized in the wakes of high Reynolds number, transonic flat plates and turbine airfoils in steady flow (Paterson and Weingold, 1984; Heinemann et

al., 1976; Greenway and Wood, 1973). More recently, Gertz (1986) identified vortex streets in the wakes of highly loaded transonic compressor rotor blades. The flow in these vortex street wakes can explain several of the more puzzling aspects of the high frequency response measurements, including the large wake-to-wake variability (Epstein et al., 1988) and also, as we shall see, some of the spanwise fluid transport. The large blade-to-blade variation in wake total temperature, pressure, and concentration (Fig. 6, for example) can be seen as an artifact of the pseudo-random sampling of the vortex street (which is periodic in the blade relative frame) by instrumentation fixed in the laboratory frame. Thus, the wake total temperature (for example) may appear to vary by ±20°C, depending upon whether a vortex core happens to be sampled by the probe.

Gertz constructed a simple, two-dimensional model of the vortex street wake, details of which are given in the Appendix. The wake is modelled as two staggered rectilinear rows of Rankine vortices of opposite sign in a uniform freestream. The vortices consist of an inner region with a forced-vortex core and an outer region following the irrotational flowfield of the classic von Karman vortex street. The wake is characterized by the vortex size (r_o) and strength and the ratio of streamwise vortex spacing (a) to the distance between vortex rows (h) (Fig. 9). This is sufficient to completely describe the vortex street with such parameters as vortex convection velocity, shedding frequency and wake average temperature and pressure defect yielded directly by the model. These parameters were derived by Gertz from fitting the model to experimental data as measured at one spanwise and axial station. As such, the model describes the wake only at that position and offers information neither on the temporal evolution of the wake nor on its three-dimensional structure. We have extended this model in a simple fashion to provide this information. The approach taken is to fit a 2-D vortex street model at several radial positions, establish consistency between the 2-D layers, and then to stack the 2-D models to yield the spanwise static pressure gradient from which the radial transport can be calculated. We realize that this approach is neither rigorous nor complete but rather is presented as a first estimate of the role that wake vortices may play in spanwise fluid transport in a high speed compressor.

The first step in constructing this quasi-3-D model is to fit the 2-D model at various spanwise locations; $R/R_{tip} = 0.95, 0.88, 0.81$, and 0.75 were chosen. Gertz fit his model to laser anemometer data, inferring the vortex strength from the wake velocity defect and the vortex spacing ratio (h/a) from the statistical distribution of velocities. Since we did not have laser anemometry data available for this stage, we developed a procedure based on the wave forms of the high frequency response probe data. Basically, the vortex street model was fit to the data by guessing the values for the vortex strength and spacing ratio, predicting the time resolved total pressure in the laboratory frame, and comparing the model prediction with the measurement. (Other information was needed to establish the flow
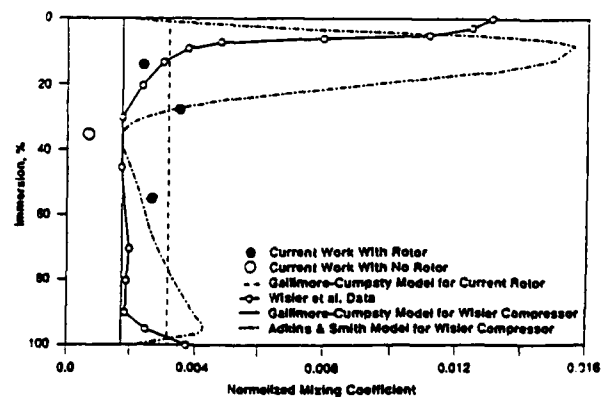

Fig. 8: Normalized spanwise mixing coefficients for this single stage transonic compressor compared to low speed multistage data from the literature
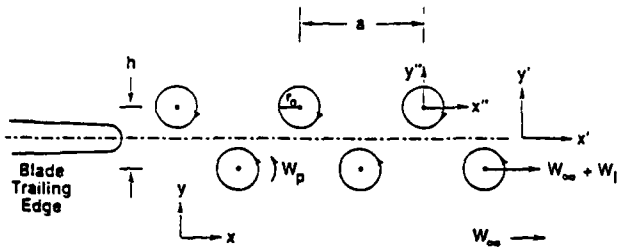
Fig. 9: Schematic of 2-D vortex street wake behind rotor blade

geometries, namely wheel speed, flow angle, Mach No., and wake-to-pitch ratio which came from time resolved measurements on this stage reported by Ng and Epstein.) In particular, the maximum peak-to-peak pressure excursion (related to vortex strength, k) and the relative number of up spikes and down spikes about the mean (related to the vortex spacing) were compared, Fig. 10. The guess of vortex strength and spacing ratio was then modified and the procedure repeated until the model prediction and data agreed. This procedure was less tedious than it might appear, quickly converging to seemingly unique values of vortex strength and spacing. An uncertainty analysis was performed in which the uncertainties of the individual measurement quantities input to the model were assessed (total pressure, wheel speed, flow angle, Mach No., and wake-to-pitch ratio), and then fed in the worst case through the procedure. The net result was an uncertainty of approximately 5% in vortex strength and spacing. More detail on this procedure may be found in Kotidis.

The vortex model was then used to predict the shedding frequency of the vortex street at the specified radii. This is shown in Table 1 along with a Strouhal number based on wake momentum thickness at the blade trailing edge (estimated by the method of Koch and Smith, 1976). The frequencies are about the same at each radius within the experimental error (as discussed above). This condition is *absolutely necessary* for the vortices to be coherent along the blade span. The relative phase coherence of the shedding among the radii (the other necessary condition) could not be assessed from this data. It seems likely to us, however, that natural processes evident, for example, in cylinders in shear flow (Gaster, 1969; Gerrard, 1966) tend to enforce coherence over at least part of the span. We predicate the remainder of the analysis, then, on the assumption that the shed vortices in the wake are coherent over much of the blade span.

TABLE 1
VORTEX SHEDDING FREQUENCY FROM 2-D VORTEX MODEL FIT

Radius Ratio (R/R_t)	Frequency (kHz)	Strouhal Number
0.95	16.9 ±1.5	0.155
0.88	16.7 ±1.5	0.151
0.81	17.3 ±1.5	0.164
0.75	16.4 ±1.5	0.180

Also of interest are the numerical values of the shedding frequency (about three times blade passing) and the Strouhal number. These are consistent with the findings of Gertz on a different transonic rotor. The Strouhal numbers are within the general range of universal wake Strouhal numbers, St*, based on wake width that would be expected for a cylinder or bluff body at this Reynolds number (Griffin, 1980).

FLOW ALONG THE VORTEX CORES

The 2-D vortex models (Eqs. (A.10) and (A.12)) show a strong spanwise gradient of static pressure (Fig. 11) and we will use this information to calculate the resultant fluid transport along the core.

To simplify the process, we will neglect: (a) any tilting or distorting of the vortex, and (b) any influence the endwalls may have on the vortex formation and development, since the radial pressure gradient should be a predominant influence. We justify these assumptions on the basis that this vortex model is basically empirical and descriptive rather than predictive.

We write the equation of motion for the vortex core region in rotor relative frame (neglecting viscous stresses) as

$$\frac{D\vec{w}}{Dt} + 2\vec{\Omega} \times \vec{w} = \Omega^2 \vec{R} - \frac{\nabla p_c}{\rho_c} \tag{5}$$

where D/Dt denotes the substantial derivative, Ω is the angular velocity of the rotor, $\vec{w}$ the velocity in the core, R the radial (spanwise) location, and p_c and ρ_c the vortex core fluid static pressure and density. Similarly, in the free stream,

$$\frac{D\vec{W}}{Dt} + 2\vec{\Omega} \times \vec{W} = \Omega^2 \vec{R} - \frac{\nabla p_\infty}{\rho_\infty} \tag{6}$$

where p_∞ and ρ_∞ are the freestream static pressure and density, and $\vec{W}$ is the freestream velocity. When the vortex core and the freestream are at the same spanwise location, we can subtract Eq. (6) from Eq. (5) yielding

$$\frac{D\vec{w}}{Dt} = \frac{D\vec{W}}{Dt} + 2\vec{\Omega} \times \left(\vec{W} - \vec{w}\right) + \frac{\nabla p_\infty}{\rho_\infty} - \frac{\nabla p_c}{\rho_c} \tag{7}$$

The radial (spanwise) velocity in the vortex, Δw_R, can be derived from Eq. (7) by vector manipulation (the radial velocity in the freestream is assumed to be small compared to that in the vortex cores):

$$\Delta w_R = -\Delta t \left[(W_\theta - w_\theta)\left(\frac{W_\theta + w_\theta}{R} + 2\Omega\right) - \frac{1}{\rho_\infty}\frac{\partial p_\infty}{\partial R} + \frac{1}{\rho_c}\frac{\partial p_c}{\partial R} \right] \tag{8}$$

This can then be translated into the laboratory frame, since the wheel speed and vortex geometry are known. We estimate the quantities in Eq. (8) in the following manner. The time interval, Δt, is calculated as the particle convection time from the blade trailing edge to the probe survey location using the calculated distribution of axial velocity in the vortex cores. The vortex model fit to the data at each spanwise station yields w_θ (the θ component of Eq. (A.9)), while W_θ is taken from the direct measurement on this rotor by Ng and Epstein. The density is calculated with the state equation

$$\rho_\infty = \frac{p_\infty}{\mathcal{R} T_\infty} = \frac{\gamma p_\infty}{W_\infty^2} M_\infty^2 \tag{9}$$
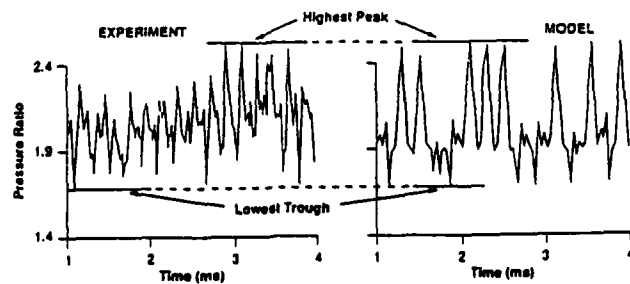

Fig. 10: Comparison of experimental data and model prediction; the peak-to-peak amplitude and relative number of up and down spikes are matched to derive vortex strength and spacing ratio
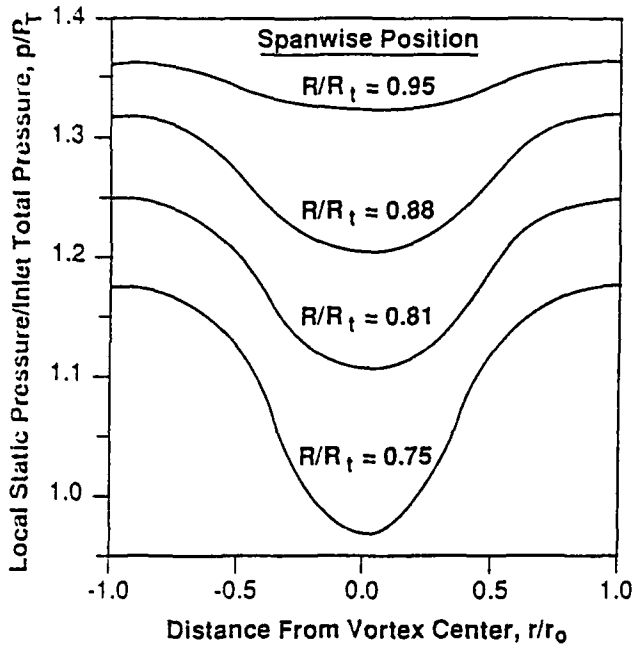
Fig. 11: Static pressure distribution through the vortex cores as predicted by the 2-D model at four spanwise locations

and, assuming the static temperature is uniform

$$p_c = \frac{\gamma p_c}{W_\infty} M_\infty^2 \qquad (10)$$

where M_∞ is the blade relative free stream Mach number. M_∞ and p_∞ were measured by Ng and Epstein. The spanwise static pressure gradients ($\partial p_\infty/\partial R$ and $\partial p_c/\partial R$) are estimated from the vortex model results in Fig. 11. Note that p_c and p_c are functions of r/r_0.

We now have a snapshot of the three-dimensional vortex structure at the probe survey location. The radial velocity distribution calculated with Eq. (8) is shown in Fig. 12. The spanwise vortex core shape resulting from the model tapers by 80% from tip to hub (the diameter varies from 2.9% to 1.6% of the rotor tip chord) and contains both inward and outward flow along the blade at each spanwise location. The substantial outward flow in the core is a result of the rotor tangential velocity component introduced by the non-inertial frame of vortices. (If the vortex were in the laboratory frame, the flow would be entirely inward along the span, given the same static pressure gradients.) The net fluid motion is essentially zero at the three outer spanwise locations indicated on the figure, and about 40% of the freestream velocity toward the hub at $R/R_t = 0.75$. The ratio of peak spanwise to freestream total velocity, 0.6-0.7, is similar to that observed by Koochesfahani (1989) in vortices in the wake of a pitching airfoil (a somewhat different flow), implying that this model and data fitting procedure give physically realizable values.

ESTIMATING VORTEX EVOLUTION

In order to estimate the total spanwise transport of fluid in the compressor, we must establish the time history of the shed vortices in the wake. We would, in general, expect both their size and strength to change with time as they are convected from the blade trailing edge to the probe measurement station. Unfortunately, we do not have measurements of this process but here must rely on modelling. We will make an analogy between the wake vortex evolution and that of wing trailing edge vortices (of which much

more is known), noting differences between the two such as the non-inertial frame of the wake and the streamwise orientation of the trailing edge vortices.

Lamb (1945) estimated the growth of a vortex in laminar flow, giving the circumferential velocity, |w"|, as

$$|w"| = \frac{k}{2\pi r}\left(1 - e^{(-r^2/4\nu t)}\right) \qquad (11)$$

where r is the radius of the vortex core, ν the kinematic viscosity, and k the circulation outside the vortex. Squire (1965) extended this to turbulent flow by simply replacing ν with an eddy viscosity, ν_t,

$$\nu_t = \alpha K \qquad (12)$$

where α is an empirical constant. Govindaraju and Saffman (1971) reported values for α ranging from 5×10^{-5} to 7.6×10^{-3}, depending on vortex Reynolds number. For our vortices $Re = 10^5$, so that $\alpha = 4\times10^{-4}$. Following Squire's suggestion of defining the radius of the edge of the vortex core, r_0, as the distance at which the vorticity is 5% of that at the center, we can write the vortex edge radius at any time (t) as

$$r_0(t) = (12\,\nu_t\,t)^{1/2} \qquad (13)$$

We must include the effects of the initial vortex size when it is formed, so Eq. (13) can be rewritten as

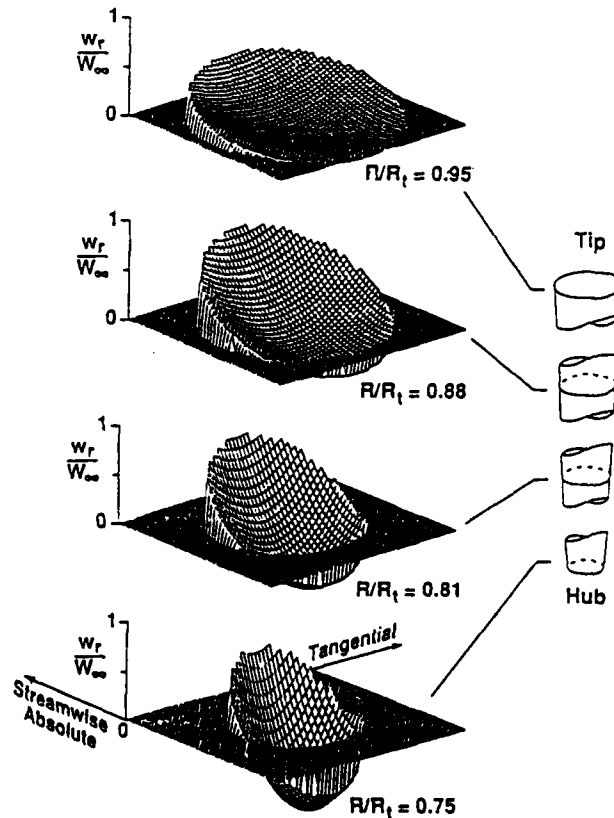$$r_0(t) = (r_0(t=0)^2 + 12\,\nu_t\,\Delta t)^{1/2} \qquad (14)$$

Fig. 12: Perspective of radial velocity distribution within the vortex cores as predicted by the model at the probe survey station

8

where $r_0(t=0)$ is the core size near the blade trailing edge where the vortex can first be considered fully formed. The location of this vortex origin point has not been rigorously determined. For simplicity, we will adopt the findings of Cantwell and Coles (1983) who found the vortex to be fully formed approximately three diameters downstream of right circular cylinders. Since the characteristic of length scale for the compressor blade shedding is the boundary layer momentum thicknesses, we will assume that the vortices are fully formed three momentum thicknesses downstream of the blade trailing edge. For the vortex convection velocities derived from the data fit, this formation period (the end of which is now defined as $t=0$) is 20% of the total flow time from the trailing edge to the probe sampling location. Thus, the Δt in Eq. (14) is 80% of the flow time. The vortex evolution can now be estimated by marching downstream in small time steps, starting at the vortex formation location. At each time step, the vortex core radius, r_0, is calculated with Eq. (14). Gertz's 2-D vortex model is then fit to the new r_0 at each spanwise station, assuming the vortex strength is constant. (The only role that viscosity plays in this modelling is to diffuse the vortex.) Numerical values are presented in Table 2. Overall, the vortex size does not change greatly, implying that the accuracy of the growth rate estimate may not be critical. Figure 13 illustrates the vortex evolution as it is convected downstream.

TABLE 2
WAKE VORTEX GROWTH ESTIMATE

Spanwise Location, R/R_{tip}	$r_0(0)$* Near Trailing Edge	$r_0(t)$* at Probe Location
0.95	2.7%	2.9%
0.88	2.1%	2.4%
0.81	1.5%	1.9%
0.75	1.1%	1.6%

* As percent of rotor tangential tip chord.

Using this description of vortex growth, we can then calculate the total spanwise transport numerically. At each streamwise station, he Gertz model is refit to yield the velocity and density distributions within the core, from which the instantaneous radial velocity distribution is calculated with Eq. (8). This procedure is repeated for each time step as we march downstream to the probe survey station. Integration of the spatial distribution of the radial velocities then directly yields the total spanwise transport.
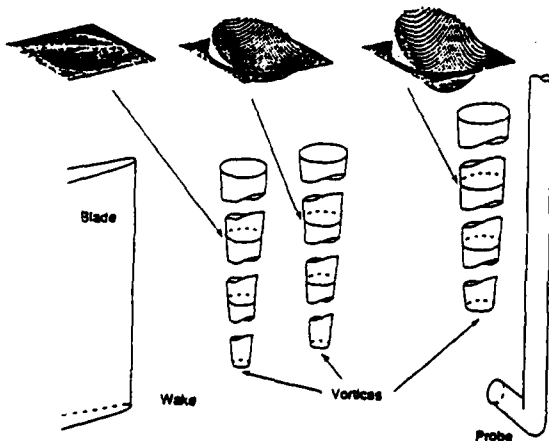

Fig. 13: An example of the streamwise evolution of the radial velocity distribution within the vortex cores

COMPARISON OF VORTEX MODEL AND DATA

A comparison between the vortex model estimate above and the measured spanwise transport is summarized in Table 3. The model predicts about 85% of the total mass transport from tip to hub but only 15% of that from hub to tip. The spanwise extent of the motion is in reasonable agreement.

TABLE 3
SPANWISE TRANSPORT BEHIND ROTOR

	Vortex Model	Measurement
% of Compressor Mass Flow Moving From:		
Hub to Tip	0.6%	3.5%
Tip to Hub	1.3%	1.6%
Extent of Spanwise Fluid Motion as Fraction of Span:		
Hub to Tip	0.58	0.40
Tip to Hub	0.44	0.40

We infer from this comparison that a spanwise coherent vortex street in the wake is the principal physical mechanism for inward radial transport in the transonic compressor rotor studied, but that a different mechanism may account for the major portion of the outward transport. A likely candidate for the outward transport is motion within separated regions of the blade boundary layers. A previous 2-D numerical study (Epstein et al.) showed that vortex shedding was itself tied to boundary layer separation in that the larger the region of separation on the blade, the stronger (and larger) the vortices in the wakes (since the vorticity in the boundary layer can end up as vorticity in the wake vortices). When there was little separation, the vortex shedding was very weak. An unpublished experimental investigation of two transonic fans with similar relative Mach numbers and pressure ratios, but different blading, showed that the blades with suction surface separation (as inferred from deviation measurements) shed strong vortices (as inferred from laser anemometer statistics), while the unseparated (or at least less separated) blades did not. Thus, some separation would seem to be necessary for strong vortex shedding in the blade wake. It is quite likely that very highly loaded blading such as the rotor studied here have some regions of boundary layer separation, even though the overall rotor performance is very good. Thus, we believe that the vortex transport described in this paper is not necessarily present in all rotors but is a function of individual blade design. Furthermore, this phenomena should be of more importance for transonic and supersonic blading since the shock wave boundary layer interaction often results in regions of separated flow, especially at higher Mach numbers. To the degree to which such 2-D thinking can be extended to 3-D, we believe that the less the separation, the less the radial transport. Verification of this hypothesis will require further experimental evidence and would greatly benefit from more sophisticated modelling of the 3-D separation and vortex structure.

INFLUENCE OF SPANWISE FLUID TRANSPORT
ON APPARENT ROTOR SPANWISE PERFORMANCE

We have presented measurements of spanwise fluid transport in a transonic compressor rotor. A key feature of this data is that most of the transport is within the blade wakes and the measured entropy of this fluid is quite high compared to the mean. Thus, the transport serves to redistribute entropy as well as fluid along the span. We wish here to assess the impact of this fluid motion on the apparent spanwise distribution of rotor efficiency. The question we ask is whether the efficiency as measured at (for example) the stator leading edge plane represents the true loss incurred along the nominal 2-D design streamsurfaces through the rotor, or does the spanwise entropy transport significantly alter the apparent loss of each blade element? We will base this calculation on the information from the experimental measurements rather than the analytical model.

The distribution of rotor adiabatic efficiency in the absence of radial flow was estimated in the following manner. The rotor flowfield was divided into four streamtubes centered at the spanwise locations of Fig. 12 with the quantitative mass exchange among the streamtubes inferred from the measured tracer concentration and the fluid state from the temperature and pressure measurements. The results of the vortex model were then used to establish the fraction of the mass exchange occurring downstream of the blade trailing edge (85% of the inward flow and 15% of the outward). The remaining mass exchange was assumed to occur within the blade passage (presumably in the blade boundary layers or separated regions). The total temperature change due to the work done on the fluid displaced radially within the rotor passage was calculated with Euler's turbine equation. This fluid was then mixed out assuming a constant area mixing process, thus incurring a total pressure loss. Because the transit time from the blade trailing edge to the probe survey station is so short compared to turbulent mixing times, the fluid transported radially downstream of the rotor trailing edge was assumed not be be mixed at the measurement station and thus was not debited with a mixing loss. We now have a quantitative measure of the change in total temperature and pressure in each streamtube due to the spanwise fluid transport. Subtracting this change from the measurements along the span then yields an estimate of what the efficiency distribution would be were there no spanwise fluid exchange. (The turbulent mixing, as in Figs. 7 and 8, has a significantly lesser spanwise extent than the processes of importance here). The exact magnitude of the entropy change proved sensitive to the fraction of the mass transport assumed to occur within the blade passage, since only this mass was debited with mixing losses. (Other than in providing this information by way of the model, wake vortices do not enter into this calculation. The results would be the same should some other physical mechanism be responsible for the measured spanwise transport.)

The results of this calculation are presented in Fig. 14, which shows the rotor adiabatic efficiency distribution (1) as measured, (2) as it would be without spanwise entropy transport (the above calculation), and (3) as estimated by Kerrebrock as the sum of 2-D viscous plus normal shock losses. In the first and second cases, the efficiency integrated over the span is similar. We wish to emphasize the general trend of these calculations (which are based on several layers of approximate models) rather than make a strictly quantitative comparison. It is clear that a principal effect of this spanwise transport is to move a substantial amount of loss from the rotor hub to tip, making the hub performance appear quite good and the tip

quite bad. This quantitatively bears out Kerrebrock's original conjecture on the loss distribution in transonic rotors.

To generalize, we would infer from these measurements and calculations that the performance of the hub sections of high pressure ratio transonic rotors can be much worse than generally realized, with much of their loss mistakenly attributed to the tip sections. (This should not be surprising since these hub sections have quite large turning and diffusion while tending to exhibit (apparently) extremely low loss.) It may make sense, therefore, to revisit the design of the hub region in transonic rotors in an attempt to improve overall efficiency. There may be more loss there than meets the eye.

SUMMARY AND CONCLUSIONS

This paper describes a set of time resolved measurements of spanwise fluid transport in a high pressure ratio transonic compressor stage. The measurements show spanwise transport of several percent of the total mass flow. This transport is both radially inward and outward and is concentrated mainly in the blade wakes. The fluid which moves along the span has considerably higher entropy than the mean and this can redistribute the loss without necessarily altering the overall efficiency of the machine.

A quasi-three-dimensional vortex street wake model is presented. When fit to the data to derive the vortex characteristics, the model predicts most of the inward fluid transport along the span and about 15% of the outward motion. It is hypothesized that most of the outward transport is in separated regions within the blade boundary layers. The net effect of the spanwise fluid transport is to move some of the loss incurred in the blade passage near the hub toward the rotor tip, making the hub section performance appear better than it actually is and the tip section performance concomitantly worse.

Future work in this area could include more sophisticated 3-D modelling of the boundary layer separation, vortex formation, and vortex evolution processes. Experimental information on the steady and unsteady boundary layer behavior of full scale compressors is required here. (Flow visualization would be very helpful.) Also the question of loss generation (rather than just loss migration) in these processes should be studied.

ACKNOWLEDGEMENTS

REFERENCES

Adkins, G.G., Jr., Smith, L.H., Jr., 1981, "Spanwise Mixing in Axial-Flow Turbomachines," ASME Paper No. 81-GT-57.

Batchelor, G.K., 1964, "Axial Flow in Trailing Line Vortices," *Journal of Fluid Mechanics*, Vol. 20, Part 4, pp. 645-658.

Cantwell, B., Coles, D., 1983, "An Experimental Study of Entrainment and Transport in the Turbulent Near Wake of a Circular Cylinder," *Journal of Fluid Mechanics*, Vol. 136, pp. 321-374.

Cumpsty, N.A., Private Communication, October 1989.

Epstein, A.H., Gertz, J.B., Owen, P.R., Giles, M.B., 1988, "Vortex Shedding in High Speed Compressor Blade Wakes," *Journal of Propulsion and Power*, Vol. 4, No. 3.

Gallimore, S.J., Cumpsty, N.A., 1986, "Spanwise Mixing in Multistage Axial Flow Compressors: Part I - Experimental Investigation," *ASME Journal of Turbomachinery*, Vol. 108, pp. 2-9.

Gallimore, S.J., Cumpsty, N.A., 1986, "Spanwise Mixing in Multistage Axial Flow Compressors: Part II - Throughflow Calculations Including Mixing," *ASME Journal of Turbomachinery*, Vol. 108, pp. 10-16.

Gaster, M., 1969, "Vortex Shedding from Slender Cones at Low Reynolds Numbers," *Journal of Fluid Mechanics*, Vol. 38, Part 3, pp. 565-576.

Gerrard, J.H., 1966, "The Three-Dimensional Structure of the Wake of a Circular Cylinder," *Journal of Fluid Mechanics*, Vol. 25, Part 1, pp. 143-164.
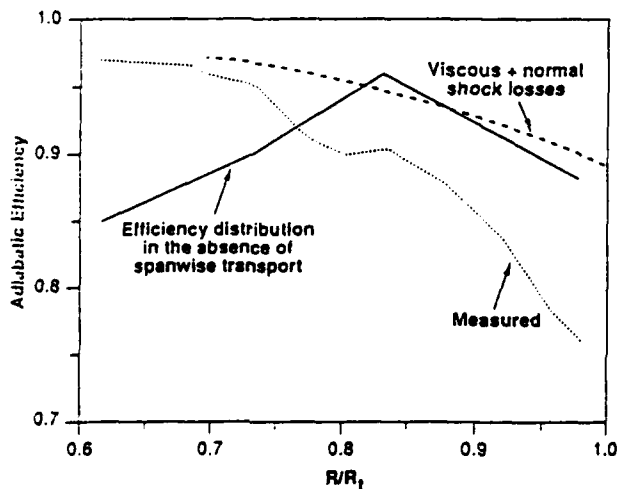

Fig. 14: Comparison of the measured spanwise efficiency distribution as it would be without spanwise entropy transport, and as the sum of 2-D shock and viscous losses as estimated by Kerrebrock

Gertz, J.B., 1986, "Unsteady Design Point Flow Phenomena in Transonic Compressors," Ph.D. Thesis, Dept. of Aeronautics and Astronautics, MIT; also MIT GTL Report No. 188.

Govindaraju, S.P., Saffman, P.G., 1971, "Flow in a Turbulent Trailing Vortex, *The Physics of Fluids*, Vol. 14, No. 10, pp. 2074-2080.

Greenway, M.E., Wood, C.J., 1973, "The Effect of a Bevelled Trailing Edge on Vortex Shedding and Vibration," *Journal of Fluid Mechanics*, Vol. 61, Part 2.

Griffin, O.M., "Universal Similarity in the Wakes of Stationary and Vibrating Bluff Structures," ASME Paper 80-WA/FE-4, 1980.

Heinemann, H.J., Lawaczeck, O., Butefisch, K.A., 1976, "Von Karman Vortices and Their Frequency Determination in the Wakes of Profiles in the Sub- and Transonic Regimes," IUTAM Symposium, pp. 75-82.

Hinze, J.O., 1959, *Turbulence*, McGraw-Hill, New York.

Kerrebrock, J.L. et al., 1974, "The MIT Blowdown Compressor Facility," *Journal of Engineering for Power*, Vol. 46, No. 4.

Kerrebrock, J.L., 1980, "Flow in Transonic Compressors," AIAA-80-0124, Dryden Lectureship in Research, Pasadena, CA.

Koch, C.C., Smith, L.H., 1976, "Loss Sources and Magnitudes in Axial Flow Compressors," *ASME Journal of Engineering for Power*, Vol. 98, No. 3.

Koochesfahani, M.M., 1989, "Vortical Patterns in the Wake of An Oscillating Airfoil," *AIAA Journal*, Vol. 27, No. 9, pp. 1200-1205.

Kotidis, P.A., Epstein, A.H., "High Frequency Response Concentration, Temperature, and Pressure Probe for Compressible Flows," submitted to *Rev. of Sci. Inst.*

Kotidis, P.A., 1989, "Unsteady Radial Transport in a Transonic Compressor Stage," Ph.D. Thesis, Department of Aeronautics and Astronautics, MIT.

Lamb, H.L., 1945, *Hydrodynamics*, Dover Publications, New York.

Ng, W.G., Epstein, A.H., 1983, "High Frequency Temperature and Pressure Probe for Unsteady Compressible Flows," *Review of Scientific Instruments*, Vol. 54, No. 12.

Ng, W.G., Epstein, A.H., 1985, "Unsteady Losses in Transonic Compressors," *Journal of Engineering for Gas Turbines and Power*, Vol. 107, No. 2.

Owen, P.R., 1986, "Computational Simulation of Unsteady Flow in a Transonic Compressor Rotor," MIT GTL Report No. 189.

Paterson, R.W., Weingold, H.P., 1984, "Experimental Investigation of a Simulated Compressor Airfoil Trailing Edge Flowfield," AIAA-84-0101.

Prince, D.C., Jr., 1980, "Three-Dimensional Shock Structures for Transonic/Supersonic Compressor Rotors," *Journal of Aircraft*, Vol. 17, No. 1.

Squire, H.B., 1965, "The Growth of a Vortex in Turbulent Flow," *The Aeronautical Quarterly*, Vol. XVI, pp. 302-306.

Thompkins, W.T., Jr., Usab, W.J., Jr., 1981, "A Quasi-Three-Dimensional Blade Surface Boundary Layer Analysis for Rotating Blade Rows," ASME Paper No. 81-GT-126.

Wennerstrom, A.J., 1984, "Experimental Study of a High-Throughflow Transonic Axial Compressor Stage," *Journal of Engineering for Gas Turbines and Power, Trans. ASME*, Vol. 106, pp. 553-560.

Wisler, D.C., Bauer, R.C., Okiishi, T.H., 1987, "Secondary Flow, Turbulent Diffusion, and Mixing in Axial-Flow Compressors," *Journal of Turbomachinery*, Vol. 109, pp. 455-482.

APPENDIX A: TWO-DIMENSIONAL VORTEX WAKE MODEL

The rotor blade wakes have been modeled as modified ideal Karman vortex streets consisting of two staggered rectilinear rows of Rankine vortices of opposite sign in a uniform freestream. The analysis is performed in the reference frame moving with the vortex cores, and a coordinate transformation is used to compute the flowfield, as would appear to a stationary probe.

The vortex street is modeled by summing the contributions of the two staggered rows of Rankine vortices. Each vortex consists of

an inner and an outer region, the boundary of which is denoted as the core radius, r_0. The inner region consists of forced-vortex flow, while the outer region follows the irrotational flowfield of a classical Karman vortex street of point vortices. The addition of finite vortex cores is considered a more realistic assumption, since it avoids infinite velocities at the vortex centers and also allows for smoothly varying averaged wake profiles, as seen in the experimental data. Following Lamb, the complex velocity of a single infinite row of equally spaced vortices of strength k and spaced a distance a can be written as

$$w(\zeta)'' = w_x^* - iw_y^* = \frac{-ik}{2a}\cot\frac{\pi z}{a} \qquad (A.1)$$

where $\zeta = x'' + iy''$. Here the (x'',y'') frame moves with the vortex cores and is fixed to the center of a vortex in either the upper or lower row. In this frame, the velocity components parallel and perpendicular to the direction of motion of the vortices are w''_x and w''_y, respectively. The (x',y') frame also moves with the vortex cores, but is positioned at the centerline between the two rows of vortices. A third reference frame, (x,y), is fixed to the rotor blade trailing edge. The velocity components in the (x',y') and (x,y) frames are (w'_x, w'_y) and (w_x, w_y), respectively.

These components will be non-dimensionalized with respect to the pressure-defect velocity W_p, which represents the velocity at the edge of an isolated vortex core and is related to the pressure drop from the freestream to the edge of an isolated core.

$$W_p = k/2\pi r_0 \qquad (A.2)$$

All lengths will be expressed with respect to the vortex spacing a, and the equations describing the velocity components of a single isolated row in the (x'',y'') frame are then

$$\overline{w}_{x_{row}}^* = -\overline{k}\frac{\sinh 2\pi\overline{y}''}{\cosh 2\pi\overline{y}'' - \cos 2\pi\overline{x}''} \qquad (A.3a)$$

$$\overline{w}_{y_{row}}^* = \overline{k}\frac{\sin 2\pi\overline{y}''}{\cosh 2\pi\overline{y}'' - \cos 2\pi\overline{x}''} \qquad (A.3b)$$

where we non-dimensionalize as

$$\overline{w}_x^* = \frac{w_x^*}{W_p}, \quad \overline{w}_y^* = \frac{w_y^*}{W_p}, \quad \overline{x}'' = \frac{x''}{a}, \quad \overline{y}'' = \frac{y''}{a},$$

$$\overline{k} = \frac{k}{2aW_p}, \quad \overline{W}_i = \frac{W_i}{W_p}, \quad \overline{r} = \frac{r}{a}, \quad \overline{r}_0 = \frac{r_0}{a}, \quad \overline{W}_\infty = \frac{W_\infty}{W_p}$$

To ensure that the velocity decays smoothly from the edge to the center of the vortex core, the velocity in the vortex core is obtained by subtracting the contributions of an isolated potential vortex from the velocity field of the row of vortices and adding the contributions of an isolated viscous core. The velocity components in a vortex core of positive circulation (lower row) are then

$$\overline{w}_x^* = \left[\overline{w}_{x_{row}}^* - \overline{w}_{x_{pot}}^*\right] + \overline{w}_{x_{core}}^* \qquad (A.4a)$$

$$\overline{w}_y^* = \left[\overline{w}_{y_{row}}^* - \overline{w}_{y_{pot}}^*\right] + \overline{w}_{y_{core}}^* \qquad (A.4b)$$

where

$$\overline{w}_{x_{pot}}^* = -\left(\frac{\overline{r}_0}{\overline{r}}\right)\left(\frac{\overline{y}''}{\overline{r}}\right), \quad \overline{w}_{x_{core}}^* = -\left(\frac{\overline{y}''}{\overline{r}_0}\right)$$

$$\overline{w}_{y_{pot}}^* = -\left(\frac{\overline{r}_0}{\overline{r}}\right)\left(\frac{(\overline{x}'')_{min}}{\overline{r}}\right), \quad \overline{w}_{y_{core}}^* = \left(\frac{(\overline{x}'')_{min}}{\overline{r}_0}\right)$$

Here $(\overline{x}'')_{min}$ is the axial distance to the center of the nearest vortex core. For a vortex core of negative circulation (upper row), the

direction of the contributions due to the isolated vortex must be reversed.

The flowfield of the complete vortex street is now found by summing the velocity components of two isolated rows spaced h apart and staggered by a/2. Each row induces a motion in the opposite row, which results in motion of the entire vortex street. This motion, the induced velocity W_i, is found by solving for the velocity induced at the center of a vortex by the opposing row

$$\overline{W}_i = -\overline{k} \tanh\left(\pi \frac{h}{a}\right)$$
(A.5)

if the vortex street is formed in a freestream of velocity, W_∞, then in the frame of reference fixed to the blades (x,y) the vortex street moves with velocity equal to $W_\infty + W_i$. In the (x',y') frames, the freestream velocity is simply $(-W_i)$. The velocity components in the primed frame are then

$$\overline{w}_x' = \overline{w}_{x\,\text{upper row}}' + \overline{w}_{x\,\text{lower row}}' - \overline{W}_i$$
(A.6a)

$$\overline{w}_y' = \overline{w}_{y\,\text{upper row}}' + \overline{w}_{y\,\text{lower row}}'$$
(A.6b)

The velocity $|\overline{w}'|$ is then

$$|\overline{w}'| = \sqrt{(\overline{w}_x')^2 + (\overline{w}_y')^2}$$
(A.7)

Given a location in the (x',y') frame, the upper and lower velocity components can be calculated from Eqs. (A.3) by a simple coordinate transformation and by noting that the sign of k changes. For the upper row,

$$\overline{x}'' = \overline{x}' - \frac{1}{2} , \quad \overline{y}'' = \overline{y}' - \frac{h}{2a}$$

and, for the lower row,

$$\overline{x}'' = \overline{x}' , \quad \overline{y}'' = \overline{y}' + \frac{h}{2a}$$

Since the vortex cores move at a velocity of $(W_\infty + W_i)$, the parallel and perpendicular velocity components in the frame relative to the rotor blades (x,y) are then

$$\overline{w}_x = \overline{w}_x' + \left(\overline{W}_\infty + \overline{W}_i\right)$$
(A.8a)

$$\overline{w}_y = \overline{w}_y'$$
(A.8b)

The blade relative velocity is then

$$|\overline{w}| = \sqrt{(\overline{w}_x)^2 + (\overline{w}_y)^2}$$
(A.9)

In the frame of reference moving with the vortices (x',y') the flow is steady and the freestream velocity is equal to $(-W_i)$. For the cases considered herein, it is sufficient to assume constant density since the maximum Mach number in this frame of reference is approximately 0.10. The pressure is expressed in terms of a pressure coefficient based on the pressure-defect velocity W_p.

$$\overline{C}_p = \frac{(p - p_\infty)}{\rho_\infty W_p^2}$$
(A.10)

Thus, in the irrotational, inviscid regions outside of a vortex core, $r > r_o$, the pressure is found from Bernouilli's equation

$$\overline{C}_p = -\frac{1}{2}\left[(|\overline{w}'|)^2 - \overline{W}_i^2\right]$$
(A.11)

Within a vortex core, the radial momentum equation is integrated across the core. The inner- and outer-pressure solutions are matched at r_o with the variation in velocity accounted for by the average of the velocity squared around the circumference. The pressure at the center of the vortex is then expressed in terms of this average velocity, $|\overline{w}_o|$, and the pressure coefficient inside the vortex cores, $r < r_o$.

$$\overline{C}_p = -\frac{1}{2}\left(|\overline{w}_o^2|\right)\left[2 - \left(\frac{r}{r_o}\right)^2\left(2 - \frac{|\overline{w}_o^2|}{\langle|\overline{w}_o^2|\rangle}\right)\right] + \frac{\overline{W}_p^2}{2}$$
(A.12)

The average of the velocity squared at the vortex core, $r = r_o$, can be found numerically given the vortex street geometry. For a typical von Karman-like street (h/a = 0.28), $\langle|\overline{w}_o^2|\rangle$ is nearly equal to unity (1.002). For values of $r < r_o$, $|\overline{w}_o|$ is evaluated at a point on the circumference ($r = r_o$) where a ray from the center of the vortex through the point in question intersects the edge of the core at $r = r_o$.

Using the Model

The 2-D vortex model was utilized in the following manner. To begin with, h/a and W_p/W_∞ were guessed (classic von Karman vortex street values could be used to start). The ratio r_o/h was set constant and equal to 0.5 following the arguments of Gertz.

Now, the non-dimensional vortex strength, $\overline{k}$, can be calculated using the non-dimensional version of Eq. (A.2). The induced velocity of the vortex street, W_i, is then calculated with Eq. (A.5). Equations (A.3) now give the velocity components, $(\overline{w}''_x)_{\text{row}}$ and $(\overline{w}''_y)_{\text{row}}$, of an isolated row of vortices which are then used in Eqs. (A.4) to calculate the velocity distribution in the vortex core frame, w''_x and w''_y. This is then transformed into the frame of the vortex street with Eq. (A.6), which is in turn transformed into the blade relative frame using Eq. (A.8). We now have the velocity field everywhere in the blade relative frame. $|\overline{w}_o|$ can be calculated with Eq. (A.9) at $r = r_o$, the square of which can then be averaged about the circumference of the vortex to yield $\langle|\overline{w}_o^2|\rangle$. The pressure coefficient, C_p, is now calculated with Eq. (A.12).

W_∞ can be calculated from the measured M_∞ and T_∞ so therefore, since W_p/W_∞ is known (it was guessed), the static pressure, p, is given by Eq. (A.9) (p_∞ was measured). Alternately, W_∞ can be calculated from a standard data match (streamline curvature fit) to the time averaged measurements. (These two approaches yielded similar answers.)

We now have a complete description of the flowfield and can calculate the laboratory frame total pressure history. This is then compared to the measurement (Fig. 10) and the guesses for h/a and W_p/W_∞ revised until the model prediction and measurements agree. The values which best fit the data are presented in Table A.1.

TABLE A.1
2-D VORTEX MODEL PARAMETERS WHICH FIT DATA

Spanwise Position, R/R_t	0.95	0.88	0.81	0.75
h/a (±0.03)	0.66	0.57	0.48	0.40
W_p/W_∞ (±0.02)	0.15	0.30	0.38	0.52

In the body of the paper, w(x,y) -- the 2-D model blade relative velocity derived in this appendix -- is referred to as $\overline{w}(R,\theta,z)$ inside the vortex cores ($r < r_o$) and as $W(R,\theta,z)$ outside the cores ($r > r_o$).

TASK II: COMPUTATIONAL TECHNIQUES FOR UNSTEADY FLOWS
(Investigators: M.B. Giles, S. Allmaras, G. Fritsch)

A. Non-Reflecting Boundary Conditions for the Euler Equations

The work on this topic was completed over a year ago, but in the last year a paper was presented at the AIAA CFD Conference in Buffalo [1]. A copy of this paper is attached to this report. Also, extensions to the theory for isolated airfoils, with applications to aeroacoustics and radar scattering, are being pursued under a separate research grant from the Northrop Corporation.

B. Numerical Method for Unsteady Diffuser Flows

This project was to develop a novel method for the calculation of unsteady diffuser flows. It involved a coupled inviscid/viscous analysis with a flux-vector-splitting Euler method in the inviscid region and a box-method Navier-Stokes method in the viscous region. The components of the method have been described in previous years' progress reports, and are contained in a report that appears as Appendix A [2].

The primary work in the early part of this last year was to solve problems in the unsteady coupling of the inviscid and viscous solutions. These problems were overcome and self-excited unsteady solutions were indeed obtained for the transonic diffuser problem, matching, at least qualitatively, experimental results. Quantitative agreement was not as good as hoped for, partially because of problems in properly modelling the experimental setup in which there was significant boundary layer suction near the outflow of the experiment, and partially because of lack of sufficient numerical grid resolution to accurately resolved the unsteady shock motion.

This work was written up by Steven Allmaras in his Ph.D. thesis which was completed in January 1989 [3]. A research paper was presented at the AIAA Aerospace Sciences Meeting in Reno in January 1989 [4], and is attached to this report. Dr. Allmaras is now working at Boeing Commercial Airplane Company, adapting his work for use in coupled viscous/inviscid analyses of aircraft configurations, with the inviscid analysis being performed by full potential or panel methods.

C. Assessment of Unsteady Losses in Stator/Rotor Interactions

The objective in this area is to assess the importance of different unsteady effects in turbomachinery. The first component of this research, which was completed in the last year, was to investigate the unsteady losses associated with the vortex sheet shed by an airfoil that is experiencing an unsteady circulation due to an unsteady stator/rotor interaction. This research together with preliminary results was discussed in last year's annual report.

The second component of this research has been to examine the consequences of the highly unsteady pressure field on the boundary layer. Using a high frequency asymptotic analysis, following ideas due to Lighthill, it can be shown that in the high frequency limit, the boundary layer can be split into two layers. In an outer layer, which comprises almost all of the boundary layer, the vorticity is essentially steady since the diffusion time scale is large compared with the frequency of oscillation. This means that the velocity profile is essentially invariant and a change in the freestream velocity causes the entire outer layer to vary by the same amount. The inner layer is a very thin Stokes layer in which the unsteady vorticity is generated so that the no-slip velocity boundary condition is maintained. This unsteady vorticity in the Stokes layer contributes to the mean dissipation rate, producing a source of loss due to unsteadiness which is the main objective of interest. A full analysis including arbitrary spatial and temporal pressure fluctuations has recently been completed and is currently being written up. Applying the theory to an unsteady stator/rotor interaction for which the unsteady surface pressures are known, shows that the unsteady losses are of the order of 0.4% on the rotor, with the major contribution being on the suction surface in the region where the mean flow is almost sonic. Like the losses due to the unsteady circulation, this is a small but significant effect.

References

1. Giles, M.B., "Non-Reflecting Boundary Conditions for Euler Equation Calculations," AIAA Paper 89-1942, 1989.

2. Giles, M.B., "Numerical Methods for Unsteady Turbomachinery Flow" (VKI Lecture Series Notes), Technical Report TR-89-3, MIT Computational Fluid Dynamics Laboratory, 1989.

3. Allmaras, S.R., "A Coupled Euler/Navier-Stokes Algorithm for 2-D Unsteady Transonic Shock/Boundary Layer Interaction," Ph.D. Thesis, MIT, January 1989.

4. Allmaras, S.R., Giles, M.B., "A Coupled Euler/Navier-Stokes Algorithm for Unsteady 2-D Transonic Flows," AIAA Paper 89-0556, 1989.

AIAA-89-1942-CP

Non-Reflecting Boundary Conditions For Euler Equation Calculations

Michael B. Giles

Department of Aeronautics and Astronautics
Massachusetts Institute of Technology
Cambridge, MA

Non-Reflecting Boundary Conditions
For Euler Equation Calculations

Michael B. Giles[*]

Department of Aeronautics and Astronautics
Massachusetts Institute of Technology
Cambridge, MA 02139

Abstract

This paper presents a unified theory for the construction of steady-state and unsteady non-reflecting boundary conditions for the Euler equations. These allow calculations to be performed on truncated domains without the generation of spurious non-physical reflections at the far-field boundaries. The general theory, developed previously by mathematicians, is presented in a more easily understood form based upon fundamental ideas of Fourier analysis and eigenvectors. The application to the Euler equations is given, and the relation to standard "quasi-one-dimensional" boundary conditions is explained. Results for turbomachinery problems show the effectiveness of the new boundary conditions, particularly the steady-state non-reflecting boundary conditions.

1 Introduction

The objective in formulating non-reflecting boundary conditions is to prevent spurious, non-physical reflections at inflow and outflow boundaries, so that the calculated flow field is independent of the position of the far-field boundary condition. This leads to greater accuracy and greater computational efficiency since the computational domain can be made much smaller.

The theoretical basis of non-reflecting boundary conditions stems from a paper by Engquist and Majda [1], which discusses both ideal non-reflecting boundary conditions and a method for constructing approximate forms, and a paper by Kreiss [2], which analyses the wellposedness of initial boundary value problems for hyperbolic systems. Many workers have been active in this area in the last ten years, but their work has been mainly concerned with scalar p.d.e.'s, with only a couple of recent applications to the Euler equations in specific circumstances [3,4]. Also, almost all of the literature has been written by mathematicians, and in their desire to be absolutely rigorous in their analysis,

they use a formalism and assume a background foundation in advanced differential theory which makes it difficult for the papers to be appreciated by others with an engineering background.

The author has recently completed a lengthy report on the formulation of non-reflecting boundary conditions and the application to the Euler equations [5]. This report presents a unified view of the theory, with some extensions required for the Euler equations, and does so using the simplest approach possible based upon Fourier analysis and eigenvectors. In taking this approach some rigor is sacrificed, and the conditions for wellposedness become necessary, but possibly not sufficient. The report also shows in full detail the application of the theory to the Euler equations. Another report describes the details of the implementation of the numerical boundary conditions [6] for two-dimensional turbomachinery applications.

The purpose of this paper is to summarize the principal parts of these two reports, and present results which demonstrate the effectiveness of the new boundary conditions in turbomachinery applications. Because of space limitations, all of the wellposedness analysis, a large amount of algebraic detail, some interesting additional applications, and a variety of helpful comments and insights have been omitted from this paper; the interested reader is urged to refer to the original two reports to obtain these.

2 General analysis

2.1 Fourier analysis

In two dimensions, the analysis is concerned with the following unsteady, hyperbolic partial differential equation.

$$\frac{\partial U}{\partial t} + A\frac{\partial U}{\partial x} + B\frac{\partial U}{\partial y} = 0 \tag{1}$$

U is a N-component vector and A and B are constant $N \times N$ matrices. Fourier analysis considers wave-like solutions which are equal to a scalar wave function multiplying

---

[*]Harold E. Edgerton Assistant Professor

a constant column vector.

$$U(x,y,t) = e^{i(kx+ly-\omega t)}u^R. \tag{2}$$

Substituting this into the differential equation gives

$$(-\omega I + kA + lB)u^R = 0. \tag{3}$$

which has non-trivial solutions provided that

$$\det(-\omega I + kA + lB) = 0 \tag{4}$$

This equation is called the dispersion relation, and is a polynomial equation of degree N in each of ω, k, and l. We will be concerned with the roots k_n of this equation for given values of ω and l. By dividing the dispersion relation by ω we obtain

$$\det(-I + \frac{k_n}{\omega}A + \frac{l}{\omega}B) = 0 \tag{5}$$

and so it is clear that k_n/ω is a function of l/ω. Thus the variable $\lambda = l/\omega$ will play a key role in constructing all of the boundary conditions.

A critical step in the construction and analysis of boundary conditions is to separate the waves into incoming and outgoing modes. If ω is complex with $Im(\omega) > 0$ (giving an exponential growth in time) then the right-propagating waves are those for which $Im(k) > 0$. This is because the amplitude of the waves is proportional to $e^{Im(\omega)(t-x/c)}$ where $c = Im(\omega)/Im(k)$ is the apparent velocity of propagation of the amplitude.

If ω and k are real then a standard result in the analysis of dispersive wave propagation [7] is that the velocity of energy propagation is the group velocity defined by

$$\vec{c}_g = \begin{pmatrix} \frac{\partial \omega}{\partial k} \\ \frac{\partial \omega}{\partial l} \end{pmatrix} \tag{6}$$

Hence for real ω the incoming waves are those which either have $Im(k) > 0$, or have real k and $\frac{\partial \omega}{\partial k} > 0$.

The column vector u^R is the right null-vector of the singular matrix $(-\omega I + kA + lB)$. The construction of the non-reflecting boundary conditions requires the row vector v^L which is the left null-vector of the singular matrix $A^{-1}(-\omega I + kA + lB)$.

$$v^L A^{-1}(-\omega I + kA + lB) = 0. \tag{7}$$

One of the important features of this left null-vector is its orthogonality to u^R. If k_m and k_n are two different solutions of the dispersion relation for the same values of ω and l, and if u_m^R and v_n^L are the corresponding right and left eigenvectors, then

$$v_n^L A^{-1}(-\omega I + k_m A + lB)u_m^R = 0, \tag{8}$$

and

$$v_n^L A^{-1}(-\omega I + k_n A + lB)u_m^R = 0. \tag{9}$$

Subtracting one from the other gives

$$(k_m - k_n)v_n^L u_m^R = 0 \Rightarrow v_n^L u_m^R = 0 \tag{10}$$

2.2 Ideal non-reflecting b.c.'s

Suppose that the differential equation is to be solved in the domain $x > 0$, and one wants to construct non-reflecting boundary conditions at $x = 0$ to minimize or ideally prevent the reflection of outgoing waves. At the boundary at $x = 0$, U can be decomposed into a sum of Fourier modes with different values of ω and l, so the analysis begins by considering just one particular choice of ω and l. In this case this most general form for U is

$$U(x,y,t) = \left[\sum_{n=1}^{N} a_n u_n^R e^{ik_n x}\right] e^{i(ly-\omega t)}. \tag{11}$$

k_n is the nth root of the dispersion relation for the given values of ω and l, and u_n^R is the corresponding right eigenvector.

The ideal non-reflecting boundary conditions would be to specify that $a_n = 0$ for each n that corresponds to an incoming wave. Because of orthogonality,

$$v_n^L U = v_n^L \left[\sum_{m=1}^{N} a_m u_m^R e^{ik_m x}\right] e^{i(ly-\omega t)}$$
$$= a_n(v_n^L u_n^R)e^{ik_n x}e^{i(ly-\omega t)} \tag{12}$$

and so an equivalent specification of non-reflecting boundary conditions is

$$v_n^L U = 0 \tag{13}$$

for each n corresponding to an incoming mode.

In principle these exact boundary conditions can be implemented in a numerical method. The problem is that in general v_n^L depends on λ and so the implementation would involve a Fourier transform in y and a Laplace transform in t. Computationally this is both difficult and expensive to implement. In situations in which there is only one known frequency, it is possible to use the ideal boundary conditions, and this has been done for linearized, unsteady potential and Euler equations. The remainder of this paper is concerned with three types of approximation which can be used in the more general situation, without requiring the Laplace transform.

2.3 One-dimensional, unsteady b.c.'s

The one-dimensional, non-reflecting boundary conditions are obtained by ignoring all variations in the y-direction and setting $\lambda = 0$. The corresponding right and left eigenvectors are important in defining and implementing the other boundary conditions, and so we label them w.

$$w_n^R = u_n^R\big|_{\lambda=0} \tag{14}$$

$$w_n^L = v_n^L\big|_{\lambda=0} \tag{15}$$

The one-dimensional boundary condition, expressed in terms of the primitive variables, is

$$w_n^L U = 0 \qquad (16)$$

for all n corresponding to incoming waves. If the right and left eigenvectors are normalized so that

$$w_m^L w_n^R = \delta_{mn} \equiv \begin{cases} 1 & , \ m = n \\ 0 & , \ m \neq n \end{cases} \qquad (17)$$

then they can be used to define a transformation between the primitive variables and the one-dimensional characteristic variables.

$$U = \sum_{n=1}^{N} c_n w_n^R, \qquad (18)$$

where

$$c_n = w_n^L U. \qquad (19)$$

Expressed in terms of the characteristic variables, the boundary condition is simply that $c_n = 0$ for each incoming wave.

2.4 Exact, two-dimensional, steady b.c.'s

The exact, two-dimensional steady boundary conditions may be considered to be the limit of the ideal boundary conditions as $\omega \to 0$. Performing a Fourier decomposition of the solution on the boundary (which is assumed to be periodic with period 2π),

$$U(0, y, t) = \sum_{-\infty}^{\infty} \hat{U}_l(t) e^{ily}, \qquad (20)$$

where

$$\hat{U}_l(t) = \frac{1}{2\pi} \int_0^{2\pi} U(0, y, t) e^{-ily} \, dy. \qquad (21)$$

The boundary conditions for $l \neq 0$ are

$$s_n^L \hat{U}_l = 0 \qquad (22)$$

for each incoming wave n, where

$$s_n^L = \lim_{\lambda \to \infty} v_n^L(\lambda). \qquad (23)$$

The boundary condition for the $l = 0$ mode, which is the solution average at the boundary, is

$$v_n^L(0) \hat{U}_0 = 0 \ \Rightarrow \ w_n^L \hat{U}_0 = 0 \qquad (24)$$

for each incoming wave n. The right-hand-side of Eq. (24) can be modified by the user to specify the value of the incoming average characteristics. Further discussion of this point will be delayed until the section on the application to the Euler equations.

2.5 Approximate, two-dimensional, unsteady b.c.'s

A sequence of approximate non-reflecting boundary conditions can be obtained by expanding v_n^L in a Taylor series as a function of $\lambda = l/\omega$ [1].

$$v_n^L(\lambda) = v_n^L\big|_{\lambda=0} + \lambda \frac{dv_n^L}{d\lambda}\bigg|_{\lambda=0} + \frac{1}{2}\lambda^2 \frac{d^2 v_n^L}{d\lambda^2}\bigg|_{\lambda=0} + \cdots \quad (25)$$

The first order approximation obtained by just keeping the leading term just gives the one-dimensional boundary conditions. The second order approximation is

$$\bar{v}_n^L(\lambda) = v_n^L\big|_{\lambda=0} + \frac{l}{\omega} \frac{dv_n^L}{d\lambda}\bigg|_{\lambda=0} \qquad (26)$$

The overbar denotes the fact that $\bar{v}$ is an approximation to v. This produces the boundary condition

$$\left(v_n^L\big|_{\lambda=0} + \frac{l}{\omega} \frac{dv_n^L}{d\lambda}\bigg|_{\lambda=0} \right) U = 0. \qquad (27)$$

Multiplying by ω, and replacing ω and l by $i\frac{\partial}{\partial t}$ and $-i\frac{\partial}{\partial y}$ respectively gives,

$$v_n^L\big|_{\lambda=0} \frac{\partial U}{\partial t} - \frac{dv_n^L}{d\lambda}\bigg|_{\lambda=0} \frac{\partial U}{\partial y} = 0 \qquad (28)$$

This is a local boundary condition, with the same differential order as the governing equations, and so can in general be implemented without difficulty.

2.6 Wellposedness and Reflection Analysis

Well-posedness is the requirement that a solution exists, is unique, and is bounded in the sense that small perturbations in the boundary data produce small changes in the solution. Any hyperbolic system arising from a model of a physical problem ought to be well-posed and so it is critical that any far-field boundary conditions which are used to truncate the solution domain must give a well-posed problem. Higdon has written an excellent review [8] of the work of Kreiss [2] and others, and in particular gives a physical interpretation of the theory in terms of wave propagation.

Due to space limitations the theory is not presented here. The basic idea behind the theory is that if there is an incoming wave which exactly satisfies the boundary conditions, then it can grow without bound and so the problem is ill-posed. Using an energy argument, it can be shown that if A and B are symmetric and can be simultaneously symmetrised, the one-dimensional boundary conditions are always well-posed. However, for the higher order nonreflecting boundary conditions, no such general result exists, and each application must be analysed separately. In the case

of the Euler equations, there are difficulties in the analysis due to two different types of degeneracy. Additional theory to overcome these problems is presented in one of the two original reports [5].

A slight variation on the well-posedness analysis assesses the effectiveness of the boundary conditions, by considering a general solution which is a sum of incoming and outgoing modes. The amplitudes of the incoming modes can be expressed as a function of the amplitudes of the outgoing modes, using reflection coefficients. In the ideal case, these coefficients are zero. Using one-dimensional boundary conditions the coefficients are $O(l/\omega)$, and using the approximate unsteady boundary conditions they are in general $O(l/\omega)^2$.

3 Application to Euler Equations

3.1 Fourier analysis

The linearized two-dimensional Euler equations written in primitive form are

$$\frac{\partial U}{\partial t} + A\frac{\partial U}{\partial x} + B\frac{\partial U}{\partial y} = 0, \qquad (29)$$

where

$$U = \begin{pmatrix} \delta\rho \\ \delta u \\ \delta v \\ \delta p \end{pmatrix}, \qquad (30)$$

and

$$A = \begin{pmatrix} u & \rho & 0 & 0 \\ 0 & u & 0 & \frac{1}{\rho} \\ 0 & 0 & u & 0 \\ 0 & \gamma p & 0 & u \end{pmatrix}, \quad B = \begin{pmatrix} v & 0 & \rho & 0 \\ 0 & v & 0 & 0 \\ 0 & 0 & v & \frac{1}{\rho} \\ 0 & 0 & \gamma p & v \end{pmatrix}. \qquad (31)$$

The elements of the vector U represent perturbations from a uniform flow, and the matrices A and B are evaluated using those same uniform flow conditions. The analysis is greatly simplified if the unsteady perturbations and the steady variables in A and B are all non-dimensionalised using the steady density and speed of sound. With this choice of non-dimensionalisation the final form of the matrices A and B is

$$A = \begin{pmatrix} u & 1 & 0 & 0 \\ 0 & u & 0 & 1 \\ 0 & 0 & u & 0 \\ 0 & 1 & 0 & u \end{pmatrix}, \quad B = \begin{pmatrix} v & 0 & 1 & 0 \\ 0 & v & 0 & 0 \\ 0 & 0 & v & 1 \\ 0 & 0 & 1 & v \end{pmatrix}, \qquad (32)$$

and the variables u and v in the above matrices are now the Mach numbers in the x and y directions.

Following the analytic theory described earlier, we first obtain the dispersion relation.

$$(uk + vl - \omega)^2 \left((uk + vl - \omega)^2 - k^2 - l^2\right) = 0 \qquad (33)$$

Two of the four roots are clearly identical.

$$k_{1,2} = \frac{\omega - vl}{u} \qquad (34)$$

For $u > 0$ these both correspond to right-travelling waves.

The other two roots are given by

$$\left(1 - u^2\right) k^2 - 2u(vl - \omega)k - \left(vl - \omega\right)^2 + l^2 = 0 \qquad (35)$$

Hence the third and fourth roots are defined by,

$$k_3 = \frac{(\omega - vl)(-u + S)}{1 - u^2} \qquad (36)$$

$$k_4 = \frac{(\omega - vl)(-u - S)}{1 - u^2} \qquad (37)$$

where

$$S = \sqrt{1 - (1 - u^2)l^2/(\omega - vl)^2} \qquad (38)$$

For $0 < u < 1$, which corresponds to subsonic flow normal to the boundary, the third root is a right-travelling wave, and the fourth root is a left-travelling wave, provided the correct branch of the complex square root function is used in defining S. It can be shown [5], that if ω is real and S^2 is real and positive, then the positive root must be taken, while if ω and/or S are complex then the comlex root must be chosen such that k_3 has a positive imaginary component and k_4 has a negative imaginary component.

3.2 Eigenvectors

Root 1: entropy wave

$$k_1 = \frac{\omega - vl}{u} \qquad (39)$$

After some algebra [5], it can be shown that appropriate right and left eigenvectors are

$$u_1^R = \begin{pmatrix} -1 \\ 0 \\ 0 \\ 0 \end{pmatrix}, \qquad (40)$$

and

$$v_1^L = \begin{pmatrix} -1 & 0 & 0 & 1 \end{pmatrix} \qquad (41)$$

This choice of eigenvectors corresponds to the entropy wave. This can be verified by noting that the only non-zero term in the right eigenvector is the density, so that the wave has varying entropy, no vorticity and constant pressure. Also, the left eigenvector 'measures' entropy in the sense that $v_1^L U$ is equal to the linearised entropy, $\delta p - \delta \rho$ (remembering that $c = 1$ because of the non-dimensionalisation).

Root 2: vorticity wave

$$k_2 = \frac{\omega - vl}{u} \tag{42}$$

The second set of right and left eigenvectors for the multiple root is given by

$$u_2^R = \begin{pmatrix} 0 \\ -ul/\omega \\ uk_2/\omega \\ 0 \end{pmatrix} = \begin{pmatrix} 0 \\ -u\lambda \\ 1-v\lambda \\ 0 \end{pmatrix}, \tag{43}$$

and

$$v_2^L = \begin{pmatrix} 0 & -u\lambda & 1-v\lambda & -\lambda \end{pmatrix} \tag{44}$$

This root corresponds to the vorticity wave, which can be verified by noting that the right eigenvector gives a wave with vorticity, but uniform entropy and pressure.

Root 3: downstream running pressure wave

$$k_3 = \frac{(\omega - vl)(S - u)}{1 - u^2} \tag{45}$$

The eigenvectors are

$$u_3^R = \frac{1+u}{2\omega} \begin{pmatrix} \omega - uk_3 - vl \\ k_3 \\ l \\ \omega - uk_3 - vl \end{pmatrix} = \frac{1}{2(1-u)} \begin{pmatrix} 1-(1-v\lambda)uS \\ (1-v\lambda)(S-u) \\ (1-u^2)\lambda \\ 1-(1-v\lambda)uS \end{pmatrix}, \tag{46}$$

and

$$v_3^L = \begin{pmatrix} 0 & (1-v\lambda) & u\lambda & (1-v\lambda)S \end{pmatrix} \tag{47}$$

This root corresponds to an isentropic, irrotational pressure wave, travelling downstream.

Root 4: upstream running pressure wave

$$k_4 = -\frac{(\omega - vl)(S + u)}{1 - u^2} \tag{48}$$

The eigenvectors are

$$u_4^R = \frac{1-u}{2\omega} \begin{pmatrix} \omega - uk_4 - vl \\ k_4 \\ l \\ \omega - uk_4 - vl \end{pmatrix} = \frac{1}{2(1+u)} \begin{pmatrix} 1+(1-v\lambda)uS \\ -(1-v\lambda)(S+u) \\ (1-u^2)\lambda \\ 1+(1-v\lambda)uS \end{pmatrix}, \tag{49}$$

and

$$v_4^L = \begin{pmatrix} 0 & -(1-v\lambda) & -u\lambda & (1-v\lambda)S \end{pmatrix} \tag{50}$$

This root corresponds to an isentropic, irrotational pressure wave, travelling upstream provided $u < 1$.

3.3 One-dimensional, unsteady b.c.'s

If the computational domain is $0 < z < 1$, and $0 < u < 1$, then the boundary at $z = 0$ is an inflow boundary with incoming waves corresponding to the first three roots, and the boundary at $z = 1$ is an outflow boundary with just one incoming wave due to the fourth root.

When $\lambda = 0$, $S = 1$, and so the right eigenvectors w^R are

$$w_1^R = \begin{pmatrix} -1 \\ 0 \\ 0 \\ 0 \end{pmatrix}, \qquad w_2^R = \begin{pmatrix} 0 \\ 0 \\ 1 \\ 0 \end{pmatrix},$$

$$w_3^R = \begin{pmatrix} \frac{1}{2} \\ \frac{1}{2} \\ 0 \\ \frac{1}{2} \end{pmatrix}, \qquad w_4^R = \begin{pmatrix} \frac{1}{2} \\ -\frac{1}{2} \\ 0 \\ \frac{1}{2} \end{pmatrix}, \tag{51}$$

and the left eigenvectors w^L are

$$w_1^L = \begin{pmatrix} -1 & 0 & 0 & 1 \end{pmatrix}$$

$$w_2^L = \begin{pmatrix} 0 & 0 & 1 & 0 \end{pmatrix}$$

$$w_3^L = \begin{pmatrix} 0 & 1 & 0 & 1 \end{pmatrix} \tag{52}$$

$$w_4^L = \begin{pmatrix} 0 & -1 & 0 & 1 \end{pmatrix}.$$

Hence the transformation to, and from, 1-D characteristic variables is given by the following two matrix equations.

$$\begin{pmatrix} c_1 \\ c_2 \\ c_3 \\ c_4 \end{pmatrix} = \begin{pmatrix} -1 & 0 & 0 & 1 \\ 0 & 0 & 1 & 0 \\ 0 & 1 & 0 & 1 \\ 0 & -1 & 0 & 1 \end{pmatrix} \begin{pmatrix} \delta\rho \\ \delta u \\ \delta v \\ \delta p \end{pmatrix} \tag{53}$$

$$\begin{pmatrix} \delta\rho \\ \delta u \\ \delta v \\ \delta p \end{pmatrix} = \begin{pmatrix} -1 & 0 & \frac{1}{2} & \frac{1}{2} \\ 0 & 0 & \frac{1}{2} & -\frac{1}{2} \\ 0 & 1 & 0 & 0 \\ 0 & 0 & \frac{1}{2} & \frac{1}{2} \end{pmatrix} \begin{pmatrix} c_1 \\ c_2 \\ c_3 \\ c_4 \end{pmatrix} \tag{54}$$

$\delta\rho, \delta u, \delta v$ and δp are the perturbations from the uniform flow about which the Euler equations were linearized, and c_1, c_2, c_3 and c_4 are the amplitudes of the four characteristic waves. At the inflow boundary the correct unsteady, non-reflecting, boundary conditions are

$$\begin{pmatrix} c_1 \\ c_2 \\ c_3 \end{pmatrix} = 0, \tag{55}$$

while at the outflow boundary the correct non-reflecting boundary condition is

$$c_4 = 0. \tag{56}$$

The standard numerical method for implementing these is to calculate or extrapolate the outgoing characteristic values from the interior domain, and then use Eq. (54) to reconstruct the solution on the boundary.

3.4 Exact, two-dimensional, steady b.c.'s

The exact, two-dimensional steady boundary conditions are essentially the ideal boundary conditions in the limit $\omega \rightarrow 0$. One begins by performing a Fourier decomposition of U along the boundary.

$$U(0, y, t) = \sum_{-\infty}^{\infty} \hat{U}_m(t) e^{i l_m y}, \qquad (57)$$

where

$$\hat{U}_m(t) = \frac{1}{P} \int_0^P U(0, y, t) e^{-i l_m y} \, dy, \qquad (58)$$

and

$$l_m = \frac{2\pi m}{P}. \qquad (59)$$

Boundary conditions are now constructed for each Fourier mode. If the mode number m is non-zero, then

$$\lim_{\lambda \to \infty} S(\lambda) = \sqrt{1 - \frac{1 - u^2}{v^2}}$$

$$= -\frac{\beta}{v} \qquad (60)$$

where

$$\beta = \begin{cases} i \, \text{sign}(l)\sqrt{1 - u^2 - v^2}, & u^2 + v^2 < 1 \\ -\text{sign}(v)\sqrt{u^2 + v^2 - 1}, & u^2 + v^2 > 1 \end{cases} \qquad (61)$$

The reason for the choice of sign functions in the definition of β, is that for supersonic flow S must be positive, as discussed when S was first defined, and for subsonic flow S must be consistent with $Im(k_3) > 0$.

The next step is to construct the steady-state left eigenvectors s^L. Since it is permissible to multiply the eigenvectors by any function of λ, we will slightly modify the definition given in the theory section in order to keep the limits finite as $\lambda \to \infty$.

$$s_1^L = \lim_{\lambda \to \infty} v_1^L = (\, -1 \;\; 0 \;\; 0 \;\; 1\,)$$

$$s_2^L = \lim_{\lambda \to \infty} \tfrac{1}{\lambda} v_2^L = (\, 0 \;\; -u \;\; -v \;\; -1\,)$$

$$s_3^L = \lim_{\lambda \to \infty} \tfrac{1}{\lambda} v_3^L = (\, 0 \;\; -v \;\; u \;\; \beta\,) \qquad (62)$$

$$s_4^L = \lim_{\lambda \to \infty} \tfrac{1}{\lambda} v_4^L = (\, 0 \;\; v \;\; -u \;\; \beta\,)$$

Using these vectors, the exact, two-dimensional, steady-state, non-reflecting boundary conditions at the inflow are

$$\begin{pmatrix} -1 & 0 & 0 & 1 \\ 0 & -u & -v & -1 \\ 0 & -v & u & \beta \end{pmatrix} \hat{U}_m = 0, \qquad (63)$$

and at the outflow the boundary condition is

$$\begin{pmatrix} 0 & v & -u & \beta \end{pmatrix} \hat{U}_m = 0. \qquad (64)$$

For subsonic flow, β depends on l and hence the mode number m. For supersonic flow, β does not depend on l and so the boundary conditions are the same for each Fourier mode other than $m = 0$.

In order to discuss the approach in implementing these conditions, we now transform from primitive variables into characteristic variables. The inflow boundary condition becomes

$$\begin{pmatrix} 1 & 0 & 0 & 0 \\ 0 & -v & -\tfrac{1}{2}(1+u) & -\tfrac{1}{2}(1-u) \\ 0 & u & \tfrac{1}{2}(\beta - v) & \tfrac{1}{2}(\beta + v) \end{pmatrix} \begin{pmatrix} \hat{c}_1 \\ \hat{c}_2 \\ \hat{c}_3 \\ \hat{c}_4 \end{pmatrix} = 0, \qquad (65)$$

and the outflow equation becomes

$$\begin{pmatrix} 0 & -u & \tfrac{1}{2}(\beta + v) & \tfrac{1}{2}(\beta - v) \end{pmatrix} \begin{pmatrix} \hat{c}_1 \\ \hat{c}_2 \\ \hat{c}_3 \\ \hat{c}_4 \end{pmatrix} = 0, \qquad (66)$$

Solving to obtain the incoming characteristics as a function of the outgoing ones gives

$$\begin{pmatrix} \hat{c}_1 \\ \hat{c}_2 \\ \hat{c}_3 \end{pmatrix} = \begin{pmatrix} 0 \\ -\left(\dfrac{\beta + v}{1 + u}\right) \hat{c}_4 \\ \left(\dfrac{\beta + v}{1 + u}\right)^2 \hat{c}_4 \end{pmatrix}, \qquad (67)$$

and

$$\hat{c}_4 = \left(\frac{2u}{\beta - v}\right) \hat{c}_2 - \left(\frac{\beta + v}{\beta - v}\right) \hat{c}_3. \qquad (68)$$

It has already been stated that if the incoming one-dimensional boundary conditions are set to zero then the initial-boundary-value problem is well-posed. This suggests that the evolutionary process for the steady-state problem will be well-posed if we lag the updating of the incoming characteristics.

$$\frac{\partial}{\partial t}\begin{pmatrix} \hat{c}_1 \\ \hat{c}_2 \\ \hat{c}_3 \end{pmatrix} = \alpha \begin{pmatrix} -\hat{c}_1 \\ -\left(\dfrac{\beta + v}{1 + u}\right) \hat{c}_4 - \hat{c}_2 \\ \left(\dfrac{\beta + v}{1 + u}\right)^2 \hat{c}_4 - \hat{c}_3 \end{pmatrix} \qquad (69)$$

$$\frac{\partial \hat{c}_4}{\partial t} = \alpha \left(\left(\frac{2u}{\beta - v}\right) \hat{c}_2 - \left(\frac{\beta + v}{\beta - v}\right) \hat{c}_3 - \hat{c}_4 \right) \qquad (70)$$

Numerical experience indicates that a suitable choice for α is $1/P$. This completes the formulation of the boundary conditions for all of the Fourier modes except $m = 0$,

which corresponds to $l = 0$ which is the average mode. For this mode the user specifies the changes in the incoming one-dimensional characteristics in order to achieve certain average flow conditions. In the turbomachinery program developed by the author, at the inflow the three incoming characteristics are determined by specifying the average entropy, flow angle and stagnation enthalpy, and at the outflow boundary the one incoming characteristic is determined by specifying the average exit pressure. Full details of this numerical procedure are given in a report [6]. It explains the problems caused by the fact that because we have used a linear theory we can get second-order non-uniformities in entropy and stagnation enthalpy across the inflow boundary. These are undesirable, and are avoided by modifying one of the inflow boundary conditions, and replacing another by the constraint of uniform stagnation enthalpy. The report also shows how the same boundary condition approach can be used to match together two stator and rotor calculations, so that the interface is treated in an average, conservative manner.

3.5 Approximate, two-dimensional, unsteady b.c.'s

Second-order b.c.'s

Following the theory presented earlier, the second order non-reflecting boundary conditions are obtained by taking the second-order approximation to the left eigenvectors v^L in the limit $\lambda \approx 0$. In this limit $S \approx 1$ and so one obtains the following approximate eigenvectors.

$$\bar{v}_1^L = (-1 \quad 0 \quad 0 \quad 1)$$
$$\bar{v}_2^L = (0 \quad -u\lambda \quad 1-v\lambda \quad -\lambda)$$
$$\bar{v}_3^L = (0 \quad 1-v\lambda \quad u\lambda \quad 1-v\lambda) \quad (71)$$
$$\bar{v}_4^L = (0 \quad -(1-v\lambda) \quad -u\lambda \quad 1-v\lambda)$$

Actually, the first two eigenvectors are exact since the only approximation which has been made is $S \approx 1$ in the third and fourth eigenvectors. Consequently, the inflow boundary conditions will be perfectly non-reflecting for both of the incoming entropy and vorticity characteristics.

The second step is to multiply by ω and replace ω by $-\frac{\partial}{\partial t}$ and l by $\frac{\partial}{\partial y}$. This gives the inflow boundary condition

$$\begin{pmatrix} -1 & 0 & 0 & 1 \\ 0 & 0 & 1 & 0 \\ 0 & 1 & 0 & 1 \end{pmatrix} \frac{\partial U}{\partial t} + \begin{pmatrix} 0 & 0 & 0 & 0 \\ 0 & u & v & 1 \\ 0 & v & -u & v \end{pmatrix} \frac{\partial U}{\partial y} = 0, \quad (72)$$

and the outflow boundary condition

$$(0 \quad -1 \quad 0 \quad 1) \frac{\partial U}{\partial t} + (0 \quad -v \quad u \quad v) \frac{\partial U}{\partial y} = 0. \quad (73)$$

For implementation purposes it is preferable to rewrite these equations using one-dimensional characteristics.

$$\frac{\partial}{\partial t} \begin{pmatrix} c_1 \\ c_2 \\ c_3 \end{pmatrix} + \begin{pmatrix} 0 & 0 & 0 & 0 \\ 0 & v & \frac{1+u}{2} & \frac{1-u}{2} \\ 0 & -u & v & 0 \end{pmatrix} \frac{\partial}{\partial y} \begin{pmatrix} c_1 \\ c_2 \\ c_3 \\ c_4 \end{pmatrix} = 0 \quad (74)$$

$$\frac{\partial c_4}{\partial t} + (0 \quad u \quad 0 \quad v) \frac{\partial}{\partial y} \begin{pmatrix} c_1 \\ c_2 \\ c_3 \\ c_4 \end{pmatrix} = 0. \quad (75)$$

Before actually implementing these boundary conditions, a wellposedness analysis was performed. This revealed that the outflow b.c. is wellposed, but the inflow b.c is ill-posed with an incoming wave which grows exponentially. Hence, it was necessary to modify the inflow boundary conmdition.

Modified boundary conditions

To overcome the ill-posedness of the inflow boundary conditions we modified the third inflow boundary condition. To do this we noted that we are overly restrictive in requiring v_3^L to be orthogonal to u_1^R and u_2^R. Since the first two inflow boundary conditions already require that $a_1 = a_2 = 0$, we only really require that v_3^L is orthogonal to u_4^R. Thus we proposed a new definition of $\bar{v}_3^L$ which is equal to $(\bar{v}_3^L)_{old}$ plus λ times some multiple of the leading order term in $\bar{v}_2^L$.

$$\bar{v}_3^L = (0 \quad 1 \quad u\lambda \quad 1) + \lambda m(0 \quad 0 \quad 1 \quad 0) \quad (76)$$

The variable m was chosen to minimize $\bar{v}_3^L u_4^R$, which controls the magnitude of the reflection coefficient. The motivation for this approach was that the second approximation to the scalar wave equation is well-posed and produces fourth order reflections [1]. Carrying out this procedure resulted in the following modified inflow boundary condition.

$$\begin{pmatrix} -1 & 0 & 0 & 1 \\ 0 & 0 & 1 & 0 \\ 0 & 1 & 0 & 1 \end{pmatrix} \frac{\partial U}{\partial t} + \begin{pmatrix} -v & 0 & 0 & v \\ 0 & u & v & 1 \\ 0 & v & \frac{1-u}{2} & v \end{pmatrix} \frac{\partial U}{\partial y} = 0. \quad (77)$$

A wellposedness analysis confirmed that this is wellposed.

Finally, it is helpful to express this boundary condition in characteristic form.

$$\frac{\partial}{\partial t} \begin{pmatrix} c_1 \\ c_2 \\ c_3 \end{pmatrix} + \begin{pmatrix} v & 0 & 0 & 0 \\ 0 & v & \frac{1+u}{2} & \frac{1-u}{2} \\ 0 & \frac{1-u}{2} & v & 0 \end{pmatrix} \frac{\partial}{\partial y} \begin{pmatrix} c_1 \\ c_2 \\ c_3 \\ c_4 \end{pmatrix} = 0. \quad (78)$$

The numerical implementation of this boundary condition is straightforward. In the program developed by the author, the changes in the outgoing characteristics are obtained from the changes distributed by Ni's version of the Lax-Wendroff algorithm which is used to solve the unsteady Euler equations on the interior domain. The changes in the incoming characteristics are calculated by integrating the boundary conditions using a one-dimensional Lax-Wendroff algorithm. The combined characteristic changes are then converted back into changes in the primitive variables, and hence the conservation variables [6]. The outflow boundary condition is implemented in a similar fashion.

3.6 Dimensional boundary conditions

For convenience, this section lists all of the boundary conditions in the original dimensional variables.

a) Transformation to, and from, one-dimensional characteristic variables.

$$\begin{pmatrix} c_1 \\ c_2 \\ c_3 \\ c_4 \end{pmatrix} = \begin{pmatrix} -c^2 & 0 & 0 & 1 \\ 0 & 0 & \rho c & 0 \\ 0 & \rho c & 0 & 1 \\ 0 & -\rho c & 0 & 1 \end{pmatrix} \begin{pmatrix} \delta\rho \\ \delta u \\ \delta v \\ \delta p \end{pmatrix} \quad (79)$$

$$\begin{pmatrix} \delta\rho \\ \delta u \\ \delta v \\ \delta p \end{pmatrix} = \begin{pmatrix} -\frac{1}{c^2} & 0 & \frac{1}{2c^2} & \frac{1}{2c^2} \\ 0 & 0 & \frac{1}{2\rho c} & -\frac{1}{2\rho c} \\ 0 & \frac{1}{\rho c} & 0 & 0 \\ 0 & 0 & \frac{1}{2} & \frac{1}{2} \end{pmatrix} \begin{pmatrix} c_1 \\ c_2 \\ c_3 \\ c_4 \end{pmatrix} \quad (80)$$

b) One-dimensional, unsteady b.c.'s.
Inflow:

$$\begin{pmatrix} c_1 \\ c_2 \\ c_3 \end{pmatrix} = 0. \quad (81)$$

Outflow:

$$c_4 = 0. \quad (82)$$

c) Exact, two-dimensional, steady b.c.'s.
Inflow:

$$\frac{\partial}{\partial t} \begin{pmatrix} \tilde{c}_1 \\ \tilde{c}_2 \\ \tilde{c}_3 \end{pmatrix} = \alpha \begin{pmatrix} -\tilde{c}_1 \\ -\left(\frac{c\beta+v}{c+u}\right)\tilde{c}_4 - \tilde{c}_2 \\ \left(\frac{c\beta+v}{c+u}\right)^2 \tilde{c}_4 - \tilde{c}_3 \end{pmatrix}. \quad (83)$$

Outflow:

$$\frac{\partial \tilde{c}_4}{\partial t} = \alpha \left(\left(\frac{2u}{c\beta-v}\right)\tilde{c}_2 - \left(\frac{c\beta+v}{c\beta-v}\right)\tilde{c}_3 - \tilde{c}_4 \right), \quad (84)$$

where

$$\beta = \begin{cases} i\,\mathrm{sign}(l)\sqrt{1-M^2}, & M < 1 \\ -\mathrm{sign}(v)\sqrt{M^2-1}, & M > 1 \end{cases} \quad (85)$$

d) Fourth order, two-dimensional, unsteady, inflow b.c.

$$\frac{\partial}{\partial t} \begin{pmatrix} c_1 \\ c_2 \\ c_3 \end{pmatrix} + \begin{pmatrix} v & 0 & 0 & 0 \\ 0 & v & \frac{c+u}{2} & \frac{c-u}{2} \\ 0 & \frac{c-u}{2} & v & 0 \end{pmatrix} \frac{\partial}{\partial y} \begin{pmatrix} c_1 \\ c_2 \\ c_3 \\ c_4 \end{pmatrix} = 0. \quad (86)$$

e) Second order, two-dimensional, unsteady, outflow b.c.

$$\frac{\partial c_4}{\partial t} + \begin{pmatrix} 0 & u & 0 & v \end{pmatrix} \frac{\partial}{\partial y} \begin{pmatrix} c_1 \\ c_2 \\ c_3 \\ c_4 \end{pmatrix} = 0. \quad (87)$$

4 Results

4.1 Steady non-reflecting b.c.'s

To verify the effectiveness of the steady-state non-reflecting boundary conditions, Figs. 1 and 2 show results for a high-turning turbine cascade. The first figure shows results for subsonic outflow conditions, with two different locations of the far-field boundaries. The results are almost identical. The second figure shows the corresponding results for a supersonic outflow condition which has two weak, oblique shocks extending from the trailing edge. The agreement in this case in not quite as good due to second-order nonlinear effects which are not considered by the linear theory. However, under the standard boundary conditions which impose uniform exit pressure, the outgoing shocks produce reflected expansion waves which greatly contaminate the solution on the blade. This behavior is shown in Fig. 3. Thus the non-reflecting boundary conditions give a major improvement in accuracy.

4.2 Unsteady non-reflecting b.c.'s

The unsteady test case is a relatively simple linear test case, the addition of a low amplitude sinusoidal wake to a steady uniform flow past an unloaded flat plate cascade. This case was chosen because the results can be compared to those obtained using LINSUB, a program developed by Whitehead [9] based upon the linear singularity theory of Smith [10]. The steady flow has a Mach number of 0.7 and a flow angle of 30°, parallel to the flat plates which have a pitch/chord ratio of 0.577. The unsteady wakes have a pitch which is a factor 0.9 smaller, and an angle of −30° which corresponds to the outflow angle relative to the upstream

blade row. Figure 4 shows contour plots of the entropy and pressure at one instant in time.

To obtain a quantitative comparison the unsteady pressures from UNSFLO were Fourier transformed, and then non-dimensionalized in exactly the same manner as in LIN-SUB. Figure 5 shows the real and imaginary components of the complex amplitude of the first Fourier mode of the pressure jump across the blade. The agreement between the UNSFLO computation and the LINSUB theory is good except at the leading edge where the $z^{-\frac{1}{2}}$ singularity causes some minor oscillations. The integrated lift and moment also agree to within 5%. This test case shows that the computational method is capable of correctly predicting the unsteady forces due to a wake/vortex interaction. However, the level of agreement is no poorer if the standard quasi-one-dimensional boundary conditions are used. It appears that in this case it is the truncation error of the numerical scheme on the interior of the domain which is responsible for the dominant error term. Thus, unlike the steady-state case, we are unable at present to demonstrate any large improvements in accuracy due to the improved, unsteady, non-reflecting boundary conditions.

5 Conclusions

A unified linear theory for the construction of non-reflecting boundary conditions has been developed and applied to the Euler equations.

Analytically, the steady-state boundary conditions are exact, within the assumptions of the linear theory, which means that in practice the only errors are second order nonlinear effects which are quadratic in the amplitude of the nonuniformity at the inflow or outflow boundary. Numerical results show that they are extremely effective in a turbomachinery application.

The unsteady boundary conditions are based upon a second order approximation of the ideal nonreflecting boundary conditions, whereas the standard 'quasi-one-dimensional' boundary conditions correspond to the first order approximation. This means that if the wavecrests of outgoing waves are at an angle θ to the boundary then the amplitude of the artificially reflected wave is $O(\theta^2)$ for the new boundary conditions, as opposed to $O(\theta)$ for the standard boundary conditions. However, numerical results are unable to demonstrate this improvement, due to the dominance of the truncation error of the numerical algorithm.

References

[1] B. Engquist and A. Majda. Absorbing Boundary Conditions for the Numerical Simulation of Waves. *Mathematics of Computation*, 31:629–651, July 1977.

[2] H.-O. Kreiss. Initial Boundary Value Problems for Hyperbolic Systems. *Communications on Pure and Applied Mathematics*, 23:277–298, 1970.

[3] L. Ferm. *Open Boundary Conditions for External Flow Problems*. Dept. of Computing Science Report 108. Uppsala University, Feb 1987.

[4] B. Gustafsson. *Far Field Boundary Conditions for Time-Dependent Hyperbolic Systems*. Center for Large Scale Scientific Computation CLaSSiC-87-16, Stanford University, Feb 1987.

[5] M. B. Giles. *Non-Reflecting Boundary Conditions for the Euler Equations*. Technical Report TR-88-1, MIT Computational Fluid Dynamics Laboratory, 1988.

[6] M. B. Giles. *UNSFLO: A Numerical Method for Unsteady Flow in Turbomachinery*. Technical Report 195, MIT Gas Turbine Laboratory, 1988.

[7] G. B. Whitham. *Linear and Nonlinear Waves*. John Wiley & Sons, 1974.

[8] R. L. Higdon. Initial-Boundary Value Problems for Linear Hyperbolic Systems. *SIAM Review*, 28:177–217, 1986.

[9] D. S. Whitehead. *LINSUB User's Guide*. Personal communication, 1986.

[10] S. N. Smith. *Discrete Frequency Sound Generation in Axial Flow Turbomachines*. University of Cambridge, Department of Engineering Report CUED/A-Turbo/TR 29, 1971.
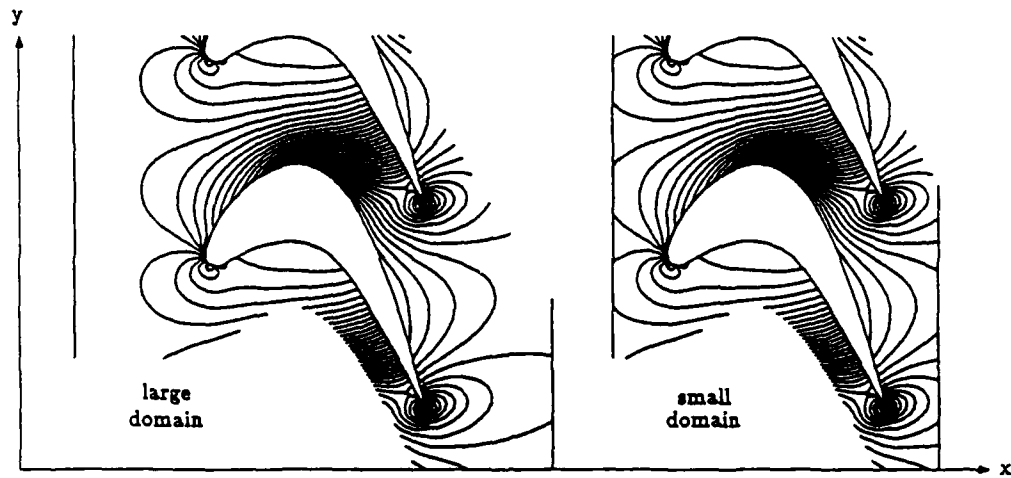
Figure 1: Pressure contours using non-reflecting b.c.'s, $M_{exit} = 0.75$
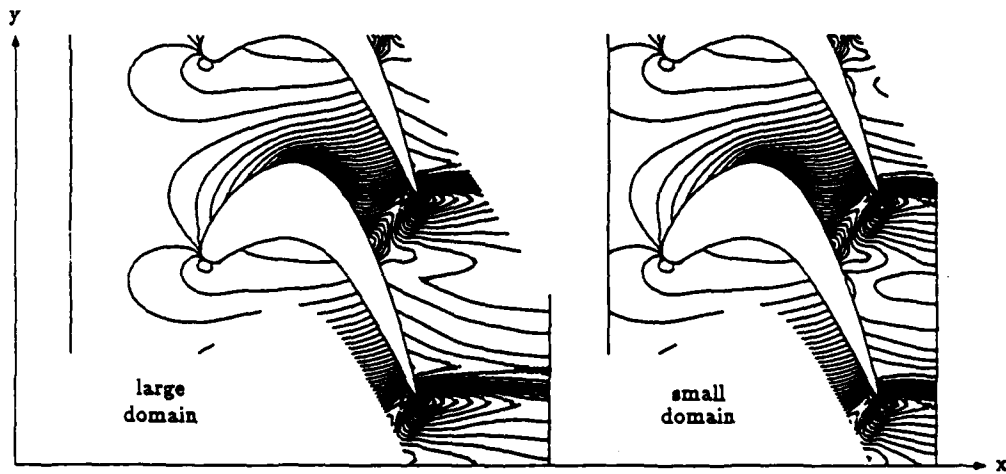

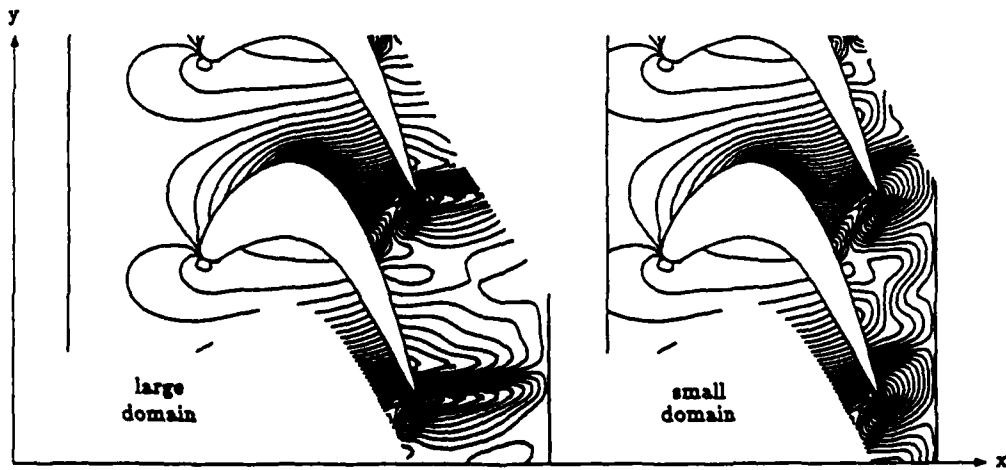Figure 2: Pressure contours using non-reflecting b.c.'s, $M_{exit} = 1.1$

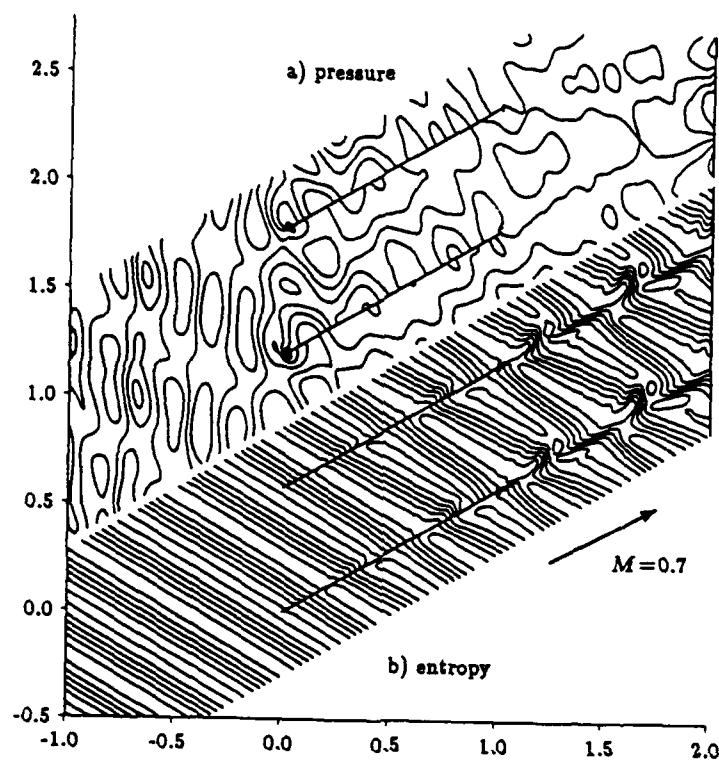Figure 3: Pressure contours using reflecting b.c.'s, $M_{exit} = 1.1$
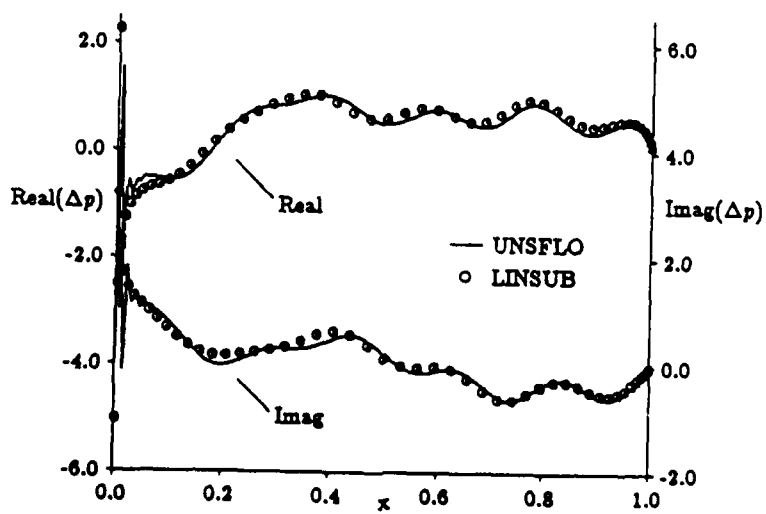
Figure 4: Flat plate pressure and entropy contours

Figure 5: Complex amplitude of flat plate pressure jump

AIAA'89

AIAA 89-0556

A Coupled Euler/Navier-Stokes Algorithm
for 2-D Unsteady Transonic Flows

Steven R. Allmaras and Michael B. Giles
Massachusetts Institute of Technology
Cambridge, MA

27th Aerospace Sciences Meeting
January 9-12, 1989/Reno, Nevada

A Coupled Euler/Navier-Stokes Algorithm
for 2-D Unsteady Transonic Flows

Steven R. Allmaras[*]
Michael B. Giles[†]

Department of Aeronautics and Astronautics
Massachusetts Institute of Technology
Cambridge, MA 02139

Abstract

This paper presents a coupled Euler/Navier-Stokes algorithm for solving 2-D unsteady transonic flows. Separate Euler and Navier-Stokes algorithms are used on overlapping grids and are coupled through wall transpiration fluxes. The Navier-Stokes algorithm uses two-point differencing across the boundary layer; this is second order accurate for both inviscid and viscous terms on nonsmooth grids. Flux-splitting is used for the streamwise discretization to capture shocks. The spatial discretization admits no decoupled modes and does not require added artificial dissipation. A semi-implicit time integration is employed. As is shown by a stability analysis, this allows a time step that is determined by the streamwise grid spacing only. The algorithm uses a dynamic coordinate rescaling to evolve the viscous grid to the changing boundary layer thickness. Results are presented for a subsonic laminar compression duct and an unsteady transonic turbulent diffuser.

Introduction

Transonic flows at high Reynolds numbers are often dominated by the interaction of shocks with boundary layers. This interaction can also be naturally unsteady. Examples of such flows are engine inlets, where the shock and boundary layer in the diffuser section of the inlet can interreact with the compressor face in an oscillating manner. These oscillations are typically small but depending on geometries and flight conditions, they may become large, seriously degrading performance. Pressure oscillations of 20% magnitude have been observed experimentally [9].

Today prediction of 2-D unsteady, strongly interacting flowfields is becoming possible with the tools of CFD. Because of the strength of the shock/boundary layer interaction and extent of viscous regions, these flowfields are presently simulated by algorithms solving the full Navier-Stokes equations everywhere. In principle, all relevant physics will be present in such solutions, but this is not necessarily the case. Within boundary layers significant

flow variations exist, which must be resolved to be accurately predicted. This requires local grid refinement, which in turn requires a priori knowledge of the boundary layer thickness—something that is part of the solution. Furthermore, these Navier-Stokes solvers typically use the same discretization throughout the flowfield. This has the advantage of simplicity in implementation, but it has several drawbacks. For example, viscous effects are calculated everywhere even though they are negligible throughout most of the flowfield. This results in wasted computing effort. Another drawback is that flowfields often include different features, such as shocks, boundary layers, acoustic waves, which are predicted by the same discretization. Each of these could be more efficiently solved by different algorithms.

We present an alternative method for the solution of such flowfields with unsteady, strong viscous/inviscid interaction—a coupled 2-D Euler/Navier-Stokes algorithm. Separate but coupled algorithms are developed to solve the inviscid and viscous regions of the flowfield; each algorithm is tailored to the important physics of that region.

This paper concentrates on the development of a new Thin-Shear-Layer Navier-Stokes algorithm and the coupling procedure. The Euler algorithm, previously presented by Allmaras and Giles [2], is briefly discussed here. The Euler algorithm, the TSL Navier-Stokes algorithm, and the coupling procedure are all developed in detail by Allmaras [3].

Governing Equations

The Thin-Shear-Layer Navier-Stokes equations are written in vector form as,

$$\frac{\partial \mathbf{U}}{\partial t} + \frac{\partial \mathbf{F}}{\partial x} + \frac{\partial \mathbf{G}}{\partial y} = \frac{1}{R_t}\frac{\partial \mathbf{S}}{\partial y}, \qquad (1)$$

where the inviscid conservation and flux vectors are,

$$\mathbf{U} = \begin{pmatrix} \rho \\ \rho u \\ \rho v \\ \rho E \end{pmatrix} \quad \mathbf{F} = \begin{pmatrix} \rho u \\ \rho u^2 + p \\ \rho u v \\ \rho u H \end{pmatrix} \quad \mathbf{G} = \begin{pmatrix} \rho v \\ \rho u v \\ \rho v^2 + p \\ \rho v H \end{pmatrix}. \quad (2)$$

In these vectors ρ is density, p is pressure, E is total internal energy, H is total enthalpy, and $u\hat{\imath} + v\hat{\jmath}$ is the velocity

[*]Research Assistant, Member AIAA
[†]Harold E. Edgerton Assistant Professor, Member AIAA

vector (u and v are the Cartesian components in the x and y directions, respectively). Viscous effects are represented by the vector S given by,

$$S = \begin{pmatrix} 0 \\ \tau \\ 0 \\ -q + u\tau \end{pmatrix},\qquad(3)$$

where the shear stress τ and heat transfer q are defined as,

$$\tau = (\mu + \mu_t)\frac{\partial u}{\partial y},$$
$$q = -\left(\frac{\mu}{Pr} + \frac{\mu_t}{Pr_t}\right)\left(\frac{\partial H}{\partial y} - u\frac{\partial u}{\partial y}\right). \qquad(4)$$

The molecular viscosity μ is determined by Sutherland's law. The turbulent viscosity μ_t is obtained from the Cebeci-Smith two-layer algebraic turbulence model [8].

The governing equations are nondimensionalised by a reference length L_{ref}, density ρ_{ref}, velocity c_{ref}, molecular viscosity μ_{ref}, thermal conductivity coefficient k_{ref}, and specific heat coefficient $c_{p_{ref}}$. In the resulting nondimensionalised governing equations, the reference Reynolds and Prandtl numbers appear; these are defined as,

$$Re = \frac{\rho_{ref}c_{ref}L_{ref}}{\mu_{ref}}, \qquad Pr = \frac{\mu_{ref}c_{p_{ref}}}{k_{ref}}. \qquad(5)$$

For air the laminar and turbulent Prandtl numbers are assumed constant ($Pr = 0.72$, $Pr_t = 0.9$).

The Thin-Shear-Layer Navier-Stokes equations are obtained from the full Navier-Stokes equations by neglecting streamwise gradients of the viscous stresses and all viscous terms in the y-momentum equation. If the inviscid y-momentum equation is replaced by the condition that pressure is constant through the boundary layer then the equation set reduces to the Prandtl Boundary Layer equations.

Turbulence Model

The Cebeci-Smith turbulence model is composed of inner (law-of-the-wall) and outer (law-of-the-wake) regions. In the inner region, the turbulent viscosity is given by,

$$\mu_t^{(i)} = \rho l^2\left|\frac{\partial u}{\partial y}\right|Re, \qquad l = \kappa y\left[1 - e^{-y^+/A^+}\right],$$
$$y^+ = \frac{yu_\tau}{\nu}\sqrt{Re}, \qquad u_\tau = \sqrt{\frac{|\tau|}{\rho}}. \qquad(6)$$

where $\kappa = 0.40$ and $A^+ = 26$. In this implementation of the model, the shear velocity u_τ is based on the local shear rather than the wall shear. In the outer region, the turbulent viscosity is given by,

$$\mu_t^{(o)} = \alpha\rho u_e\delta_i^*\gamma Re, \qquad \gamma = \left[1 + 5.5(y/\delta)^6\right]^{-1}. \qquad(7)$$

where $\alpha = 0.0168$, δ_i^* is the incompressible displacement thickness, δ is the boundary layer thickness, and γ is Klebanoff's intermittency factor.

Starting from the wall, the inner model is used up to the point where the outer model first exceeds the inner; the outer model is used from there.

No transition model or mechanism for changing from laminar to turbulent boundary layers is incorporated into the present algorithm.

Defect Formulation

Away from the wall, viscous effects become negligible and the Navier-Stokes equations asymptote to the Euler equations. Thus, solving the Navier-Stokes equations everywhere is inefficient since most of the flowfield is effectively inviscid. This section presents an alternative formulation of the problem involving a composite solution using both the Euler and TSL Navier-Stokes equations.

Probably the most obvious means of obtaining a composite solution is to solve the TSL equations from the wall to the edge of the boundary layer and patch to a solution of the Euler equations in the outer flow. In this approach, the domain is divided into two regions and the solution in each represented by different equations sets. The final solution is then a patch of the viscous and inviscid solutions. We choose instead to describe the flowfield by the Defect formulation of Le Balleur [15,16]. Here, two equation sets, both applicable throughout the entire domain, are used to describe the flowfield; the composite solution is the sum of the two solutions.

In the Defect formulation the governing equations are split into an inviscid contribution described by the Euler equations (8a) and a viscous contribution described by the Defect equations (8b),

$$\frac{\partial\hat{U}}{\partial t} + \frac{\partial\hat{F}}{\partial x} + \frac{\partial\hat{G}}{\partial y} = 0, \qquad(8a)$$

$$\frac{\partial}{\partial t}(\hat{U}-U) + \frac{\partial}{\partial x}(\hat{F}-F) + \frac{\partial}{\partial y}(\hat{G}-G) + \frac{1}{Re}\frac{\partial S}{\partial y} = 0. \qquad(8b)$$

Far from the wall, the viscous solution U asymptotes to the inviscid solution $\hat{U}$,

$$U \to \hat{U} \qquad \text{as} \qquad y \to \infty. \qquad(9)$$

Outside the boundary layer, the Defect is zero, leaving only the Euler equations. Within the boundary layer, equation (8a) results in an inviscid solution which has no physical significance. Le Balleur refers to this as the pseudo-inviscid solution. It does not satisfy inviscid solid wall boundary conditions; instead, the fluxes at the wall are driven by the viscous contribution.

Analytically, this approach is no different if the Defect equations (8b) are replaced by the full TSL equations (1) within the boundary layer. The real advantage of the Defect equations is in the quality of numerical results when different algorithms are used to determine the pseudo-inviscid solution $\hat{U}$ and the viscous solution U or $\hat{U} - U$, as is done in this paper. The source of the difference is numerical truncation error, and its resulting effect is a mismatch between

the inviscid and viscous components of the solution outside the boundary layer.

In fact, solution of the Defect equations may be viewed as an elegant means of truncation error manipulation. To see this the truncation error is analysed using operator notation. Let the operator L_{TSL} denote the analytic TSL Navier-Stokes equations (1) and L_{EUL} the analytic Euler equations (8a). Let U be the analytic solution of the TSL equations with no slip boundary conditions, and $\hat{U}$ be the associated pseudo-inviscid solution,

$$L_{TSL}(U) = 0, \qquad L_{EUL}(\hat{U}) = 0. \qquad (10)$$

By construction, U asymptotes to $\hat{U}$ far from the wall. Similarly, assume two different numerical operators, L^h_{EUL} and L^h_{TSL}, for the solution of the Euler and TSL equations, respectively, and let $\hat{U}^h$ and U^h be their solutions with appropriate boundary conditions,

$$L^h_{TSL}(U^h) = 0, \qquad L^h_{EUL}(\hat{U}^h) = 0. \qquad (11)$$

It is desired that U^h asymptote to $\hat{U}^h$, just as the analytic solutions do, but this is not necessarily the case. Far from the wall, the analytic solution U of the TSL equations is also a solution of the Euler equations,

$$L_{EUL}(U) \to 0 \qquad \text{as} \qquad y \to \infty. \qquad (12)$$

However, the exact solution U^h of the discretised TSL operator does not asymptote to an exact solution of the discretised Euler operator,

$$L^h_{EUL}(U^h) \to \epsilon^h \neq 0 \qquad \text{as} \qquad y \to \infty. \qquad (13)$$

The reason is differing truncation errors between the two numerical operators or algorithms. The result will be a mismatch between U^h and $\hat{U}^h$ outside the boundary layer. A computational example of this is shown in Fig. 4. Fortunately, this situation can be rectified by altering the viscous solution, giving $\underline{U}^h$, so that it does asymptote to an exact solution of the Euler operator,

$$L^h_{EUL}(\underline{U}^h) \to 0 \qquad \text{as} \qquad y \to \infty, \qquad (14)$$

thereby allowing $\underline{U}^h$ to asymptote to $\hat{U}^h$ (see Fig. 5). This altered viscous solution is no longer a solution of the discretised TSL operator; in fact,

$$L^h_{TSL}(\underline{U}^h) \to \epsilon^h \qquad \text{as} \qquad y \to \infty, \qquad (15)$$

but it is an exact solution of the discretised Defect operator,

$$L^h_{DEF}(\hat{U}^h - \underline{U}^h) \equiv L^h_{TSL}(\hat{U}^h) - L^h_{TSL}(\underline{U}^h) = 0. \qquad (16)$$

Hence, solution of the Defect equations is a means of subtracting off the undesired difference in truncation error between the discretised Euler and TSL operators.

This conclusion can alternately be obtained by noting that $\hat{U} - U = 0$ is both an analytic solution of the Defect equations (8b) and an exact solution of any properly discretised form of the Defect equations.

Two approaches to the discretisation of the Defect equations (8b) become apparent. The first is to discretise the

equations as written and solve for a viscous defect $\hat{U} - U$ given a known pseudo-inviscid solution $\hat{U}$. The second approach emerges from the above discrete operator analysis. A discretised TSL operator or algorithm is first developed. Then the discrete Defect operator (16) is constructed by taking the difference of the TSL operator operating on the viscous solution U and the known inviscid solution $\hat{U}$. We have chosen this second approach to discretise the Defect equations.

Euler Algorithm

The 2-D Euler algorithm, initially developed by Allmaras and Giles [2] and further detailed and improved in Ref. [3], has been designed for unsteady transonic flows. In particular, it has been developed with the objectives of crisp resolution of unsteady shocks combined with low truncation error even on nonsmooth grids. Moving shocks are captured crisply and without oscillations using upwinding, more specifically, van Leer's flux-splitting [28]. The flux through each face is obtained by first extrapolating two solutions to the face, one from either side; the split-flux vector is then calculated from these two solutions. In upwind methods it is the accuracy of these extrapolated solutions that determines the overall spatial accuracy of the solution. In the present algorithm, these extrapolations are made second order accurate by using a linear solution approximation within each cell. Both averages ($\overline{U}$) and gradients ($\overline{U_X}$, $\overline{U_Y}$) are stored for each cell as shown in Fig. 1, and a linear Taylor expansion used to extrapolate the solution to the faces of the cell,

$$U(x, y) = \overline{U} + (x - x_e)\overline{U_X} + (y - y_e)\overline{U_Y}. \qquad (17)$$

The averages on each cell are evolved in time by a finite volume solution of the unsteady Euler equations. In a similar manner, the gradients are evolved in time by solving the first moments of the unsteady Euler equations. Two-point Gauss quadrature is used to calculate the flux on each face of the cells. This gives second order accurate gradients for steady flow. It also eliminates all decoupled modes and any need for explicitly added artificial dissipation. In addition, nonlinear consistency in the discretised first moment equations has been found to be crucial for convergence near shocks. This nonlinear consistency is obtained using Roe's parametric vector [23]. An explicit 3-stage Runge-Kutta scheme is used to integrate both the discrete Euler equations and the first moments of the Euler equations in time. The resulting upwind algorithm has grid independent second order accuracy for both steady and unsteady flows.

Thin Shear Layer Navier-Stokes Algorithm

Before presentation of the algorithm, a few comments are in order. This algorithm is developed from the start with the intent to use it only in viscous regions and to couple it with an outer inviscid solver. As will be discussed later, the form of coupling used in this paper is new for Euler/Navier-Stokes algorithms. To reduce unnecessary geometric complexity

in the coupling, the TSL Navier-Stokes equations (1) are discretized on a grid with one set of coordinate lines parallel to the y-axis, rather than on a body normal grid. Errors in the TSL equations are introduced by this assumption, particularly in the definition of the shear stress and heat transfer. These errors small for the duct cases presented, since their walls are nearly parallel to the z-axis.

Objectives

The present TSL Navier-Stokes algorithm is developed with three major objectives or goals in mind. The first is high spatial accuracy across the boundary layer. Within boundary layers, the viscous terms are as important as the inviscid terms normal to the wall. In this algorithm, both inviscid and viscous terms across the boundary layer are discretized to second order accuracy for the stretched grids typical of viscous calculations.

The second objective is to avoid impractical time step restrictions imposed on fully explicit time integration techniques. This algorithm uses semi-implicit time integration to circumvent this problem.

The third major objective is to adapt the viscous grid to the changing boundary layer thickness. This is accomplished by a dynamic transformation of the y-coordinate.

Coordinate Rescaling

The extent of the viscous region is not known a priori; hence, the computational grid cannot be specified. Since it changes both along the wall and in time, some form of adaptation must be used to determine the extent of the viscous region and the grid. The technique used here has been used in the boundary layer schemes of Carter [7] and Drela [10]. The y-coordinate is rescaled by the local boundary layer thickness, and the resulting transformed equations solved on a fixed grid in computational space.

Define the coordinate transformation to computational space,

$$\tau = t, \qquad \xi = z, \qquad \eta = \frac{y - \bar{y}(z)}{\Delta(z,t)}, \qquad (18)$$

where $\Delta(z,t)$ is a scaling parameter which depends on the local boundary layer thickness, and $\bar{y}(z)$ is the location of the stationary wall. Including $\bar{y}$ in the definition of η accounts for wall curvature effects. Derivatives with respect to z, y and t then become,

$$\frac{\partial}{\partial z} = \frac{\partial \xi}{\partial z}\frac{\partial}{\partial \xi} + \frac{\partial \eta}{\partial z}\frac{\partial}{\partial \eta} = \frac{\partial}{\partial \xi} - \left(\frac{\eta \Delta_z}{\Delta} + \frac{\bar{y}_z}{\Delta}\right)\frac{\partial}{\partial \eta},$$

$$\frac{\partial}{\partial y} = \qquad \frac{\partial \eta}{\partial y}\frac{\partial}{\partial \eta} = \frac{1}{\Delta}\frac{\partial}{\partial \eta}, \qquad (19)$$

$$\frac{\partial}{\partial t} = \frac{\partial \tau}{\partial t}\frac{\partial}{\partial \tau} + \frac{\partial \eta}{\partial t}\frac{\partial}{\partial \eta} = \frac{\partial}{\partial \tau} - \frac{\eta \Delta_t}{\Delta}\frac{\partial}{\partial \eta},$$

where

$$\Delta_z \equiv \frac{\partial \Delta}{\partial z}, \qquad \Delta_t \equiv \frac{\partial \Delta}{\partial t}, \qquad \bar{y}_z \equiv \frac{d\bar{y}}{dz}. \qquad (20)$$

The transformed TSL Navier-Stokes equations (1) can then be written in conservation form as,

$$\frac{\partial}{\partial \tau}(\Delta U) + \frac{\partial}{\partial \xi}(\Delta F) \qquad (21)$$

$$+ \frac{\partial}{\partial \eta}\left(G - \frac{1}{Re}S - (\Delta_z \eta + \bar{y}_z)F - \Delta_t \eta U\right) = 0.$$

Hereafter, the time coordinate τ will be replaced by t to avoid confusion with the shear stress.

Cross-Stream Discretization (η-direction)

Typical approaches to discretizing the Navier-Stokes equations use 3-point differencing assuming a uniform grid to discretize viscous terms [1,4,26,27]. For the stretched grids commonly used in viscous calculations, this fails to be second order accurate. In the present algorithm, both inviscid and viscous terms across the boundary layer are discretized to second order accuracy for nonsmooth grids.

Among algorithms for solution of the boundary layer equations is the highly successful Keller Box scheme [14]. In this scheme second order accuracy is obtained for both inviscid and viscous terms across the boundary layer (η-direction). The key to this scheme is rewritting the governing equations as a system of first order equations and using two-point differencing to evaluate all η-derivatives. This is the approach taken in the present algorithm.

The TSL Navier-Stokes equations are solved as a system of six first order equations as written in (21) and (4), where the vectors U, F, G and S are given by (2) and (3). Thus, the shear stress τ and heat transfer q are stored along with the conservation variables U. These six unknowns are stored at face midpoints as shown in Fig. 1b. With unknowns stored in this manner, two-point differencing is used to evaluate η-derivatives on each cell. For example,

$$\left.\frac{\partial G}{\partial \eta}\right|_{i,j+1/2} = \frac{G_+ - G_-}{\Delta \eta} + O(\Delta \eta^2), \qquad (22)$$

where the convention $(\ )_+ = (\ )_{i,j+1}$ and $(\ )_- = (\ )_{i,j}$ is used throughout this section. This discretization is second order accurate for nonsmooth spacing in the η-direction. Derivatives with respect to t and ξ will remain undefined for the present, except to say that $\partial U/\partial t$ is evaluated at the center of the cell using the midpoint rule in η (which is also second order accurate),

$$\left.\frac{\partial U}{\partial t}\right|_{i,j+1/2} = \frac{\partial}{\partial t}\left(\frac{U_+ + U_-}{2}\right) + O(\Delta \eta^2). \qquad (23)$$

The resulting semi-discrete TSL Navier-Stokes equations in conservation form on each cell are given by,

$$\frac{\partial}{\partial t}\left[\Delta_i\left(\frac{U_+ + U_-}{2}\right)\right] + \frac{\partial}{\partial \xi}(\Delta F) + \frac{1}{\Delta \eta}\left[(G_+ - G_-)\right.$$

$$- \frac{1}{Re}(S_+ - S_-) - \Delta_{z,i}(\eta_+ F_+ - \eta_- F_-) \qquad (24)$$

$$\left. - \bar{y}_{z,i}(F_+ - F_-) - \Delta_{t,i}(\eta_+ U_+ - \eta_- U_-)\right] = 0,$$

where Δ_i, Δ_{s_i} and Δ_{t_i} are the scaling parameter and its derivatives at the cell center. The Δ_t and Δ_s derivatives are given by,

$$\Delta_{t_i} = \frac{\Delta_i^{n+1} - \Delta_i^n}{\Delta t}, \quad \Delta_{s_i} = \frac{\Delta_{i+1/2} - \Delta_{i-1/2}}{\Delta \xi}. \quad (25)$$

The scaling parameter at the left and right faces of the cell is obtained by interpolating the values at the midpoints of the two adjacent cells.

The definitions of shear stress τ and heat transfer q on each cell complete the system. They are discretised in the same manner as the conservation equations. For example, the shear stress definition is,

$$\frac{\tau_+ + \tau_-}{2} - (\mu + \mu_t)\frac{u_+ - u_-}{\Delta\Delta\eta} = 0, \quad (26)$$

where μ and μ_t are evaluated at the cell center.

Streamwise Discretisation (ξ-direction)

The ξ-derivative in the conservation equations is evaluated by differencing the fluxes at the midpoints of the left and right faces of the cell (the subscript $j + 1/2$ is assumed in the following analysis),

$$\frac{\partial \Delta \mathbf{F}}{\partial \xi}\bigg|_i = \frac{(\Delta \mathbf{F})_{i+1/2} - (\Delta \mathbf{F})_{i-1/2}}{\Delta \xi} + O(\Delta\eta^2). \quad (27)$$

This formula is second order in $\Delta\eta$ due to the midpoint rule. The fluxes at the faces are evaluated using flux-splitting for capturing shocks in the outer portion of the boundary layer,

$$\mathbf{F}_{i\pm 1/2} = \mathbf{F}^+(\mathbf{U}_{i\pm 1/2}^-) + \mathbf{F}^-(\mathbf{U}_{i\pm 1/2}^+), \quad (28)$$

where $\mathbf{F}^\pm$ are the split flux vectors developed by van Leer [28]. $\mathbf{U}^+$ is the solution at the face interpolated from the right, and $\mathbf{U}^-$ that interpolated from the left. Since streamwise accuracy is not as important as the cross-stream discretisation in this preliminary development, a first order interpolation is used,

$$\mathbf{U}_{i+1/2}^+ = \frac{1}{2}(\mathbf{U}_{i,j+1} + \mathbf{U}_{i,j}),$$
$$\mathbf{U}_{i+1/2}^- = \frac{1}{2}(\mathbf{U}_{i+1,j+1} + \mathbf{U}_{i+1,j}), \quad (29)$$

and similarly for $\mathbf{U}^\pm$ at the left face. These interpolations are $O(\Delta\xi, \Delta\eta^2)$ accurate, resulting in a first order accurate streamwise discretisation.

Artificial Dissipation

Given sufficient grid density to resolve the gradients of the boundary layer solution, the present spatial discretisation admits no decoupled sawtooth modes. Hence, no added artificial dissipation is required; this is an advantage over most other Navier-Stokes algorithms which do admit decoupled modes. Artificial dissipation adds user adjustable constants, requires additional nonphysical boundary conditions, and if not properly done can contaminate solutions as indicated in Ref. [1].

Furthermore, the use of flux-splitting in the streamwise direction allows shocks to be captured without explicitly added artificial dissipation.

Time Integration

Resolution of the large gradients within the viscous region can result in very small grid spacing normal to the wall, particularly for turbulent cases. To avoid impractical time step restrictions on a fully explicit scheme resulting from this small spacing, the equations are integrated in time using a semi-implicit formulation. Discretisation normal to the wall (η-direction) is evaluated implicitly, whereas streamwise discretisation (ξ-direction) is evaluated explicitly. As will be shown by a stability analysis, this allows the solution to be integrated using a time step Δt determined by the streamwise resolution Δz only.

In the present implementation, the equations are integrated using a single stage backward Euler for η-derivatives and forward Euler for ξ-derivatives to advance the solution from time t (level n) to $t + \Delta t$ (level $n + 1$). Thus, in the conservation equations, streamwise fluxes derivatives (27) are evaluated explicitly using the solution a level n. The remaining spatial derivatives in the conservation equations are evaluated completely at the new time (level $n+1$), giving

$$\frac{1}{\Delta t}\left[\Delta^{n+1}\left(\frac{\mathbf{U}_+ + \mathbf{U}_-}{2}\right)^{n+1} - \Delta^n\left(\frac{\mathbf{U}_+ + \mathbf{U}_-}{2}\right)^n\right]$$
$$+ \frac{1}{\Delta\xi}\left[(\Delta\mathbf{F})_{i+1/2}^n - (\Delta\mathbf{F})_{i-1/2}^n\right] \quad (30)$$
$$+ \frac{1}{\Delta\eta}\left[(\mathbf{G}_+ - \mathbf{G}_-)^{n+1} - \frac{1}{Re}(\mathbf{S}_+ - \mathbf{S}_-)^{n+1}\right.$$
$$- \Delta_{s_i}^n(\eta_+\mathbf{F}_+ - \eta_-\mathbf{F}_-)^{n+1} - \bar{y}_{s_i}(\mathbf{F}_+ - \mathbf{F}_-)^{n+1}$$
$$\left. - \Delta_{t_i}(\eta_+\mathbf{U}_+ - \eta_-\mathbf{U}_-)^{n+1}\right] = 0.$$

Likewise, the shear stress and heat transfer definitions (26) are evaluated completely at the new time level. These equations form an implicit nonlinear system for the evolution of the solution in time. The nonlinear system at each streamwise and time step is solved by Newton's method.

Discrete Defect Equations

In this section the discretisation of the Defect equations (8b) is discussed. We use the approach suggested by the operator analysis leading to the discrete Defect operator (16). In this approach the discrete Defect operator is constructed from the discrete TSL Navier-Stokes operator (30), where the explicit streamwise discretisation is given by (27–29).

A proper discretisation of the Defect equations would result by taking the difference of (30) operating on the viscous solution $\mathbf{U}^h$ and the known pseudo-inviscid solution $\hat{\mathbf{U}}^h$ interpolated to every cell of the viscous grid. We have not done this. Instead, we have constructed a simplified discretisation using the fact that the discrete Defect equations are a means of manipulating the relative truncation errors of the viscous and inviscid algorithms.

The outer Euler algorithm developed in Refs. [2,3] is spatially second order accurate even for nonsmooth grids. The

TSL algorithm developed in this section is spatially second order accurate in the η-direction but only first order in the streamwise direction. Thus, the major contribution to solution mismatch at the edge is the first order interpolation (29) in the streamwise discretization (27). This component of the relative truncation error is largely eliminated by substituting the inviscid edge solution into the discrete TSL equations of the outermost viscous cell and subtracting the result from all cells at that streamwise station. Hence, the simplified discrete Defect operator on each cell is given by,

$$\left[L_{Def}(U^k - \hat{U}^k)\right]_{i,j+1/2} \qquad (31)$$

$$= \left[L_{TSL}(U^k)\right]_{i,j+1/2} - \left[L_{TSL}(\hat{U}^k)\right]_{i,J-1/2},$$

where $j = 1$ to $J - 1$, and L_{TSL} is the operator notation for (30). This is a proper discretization of the Defect equations only for the outermost cell.

The pseudo-inviscid solution and its gradients are known at the edge at both the n and $n + 1$ time levels. Thus, $\hat{U}$ is known at the upper and lower faces of the outermost cell by interpolation,

$$\hat{U}^k_+ = \hat{U}^k_{i,J} = \hat{U}^k_e, \qquad (32a)$$

$$\hat{U}^k_- = \hat{U}^k_{i,J-1} = \hat{U}^k_e - (\Delta^k \Delta\eta_J)\frac{\partial\hat{U}}{\partial y}\Big|_e^k, \quad (32b)$$

where $\hat{U}_e$ is the inviscid edge solution, $k = n$ or $n + 1$, and $\Delta\eta_J = \eta_J - \eta_{J-1}$. Substitution of these values into the discrete TSL equations (30) gives the pseudo-inviscid component of the simplified discrete Defect operator (31).

This simplification is essentially an approximation that the pseudo-inviscid solution is linear across the boundary layer and given by the solution and gradients at the edge.

Wall and Outer Edge Boundary Conditions

At each streamwise station, containing $(J - 1)$ cells across the grid, there are $6J$ unknowns and $6(J - 1)$ equations. This leaves 6 boundary conditions to be specified to close the numerical system. At the wall, no-slip and adiabatic wall conditions are specified,

$$u(\xi, 0, t) = 0, \quad v(\xi, 0, t) = 0, \quad q(\xi, 0, t) = 0. \qquad (33)$$

The outer edge of the viscous grid is a nonphysical boundary where three conditions need to be specified; these are chosen to be pressure, shear stress and total enthalpy,

$$p(\xi, \eta_J, t) = \hat{p}_e, \quad \tau(\xi, \eta_J, t) = 0, \quad H(\xi, \eta_J, t) = \hat{H}_e, \qquad (34)$$

Here $\hat{p}_e$ and $\hat{H}_e$ are the values of the outer inviscid flow interpolated to the edge of the viscous grid.

Inlet/Exit Boundary Conditions

The inlet and exit planes are nonphysical boundaries resulting from truncation of the computational domain. Boundary conditions at these planes are enforced using 1-D characteristic theory in the x-direction.

For supersonic flow at the inlet, all flow variables are specified from an inlet profile. For subsonic inflow, the entropy, total enthalpy, and v velocity are specified; and the Riemann invariant $u - \frac{2}{\gamma-1}c$ is extrapolated from the interior. At the inlet, the specified viscous profile is generated by an assumed flat plate similarity boundary layer solution. Equation (21) is solved with the assumptions of steady flow, constant pressure through the boundary layer and $\partial F/\partial \xi = 0$. The scaling parameter Δ for the similarity profile is given by (36) and a power law assumption used to evaluate Δ_s.

At the exit, all flow variables are extrapolated from the interior for supersonic flow. For subsonic flow, the entropy, v velocity and Riemann invariant $u + \frac{2}{\gamma-1}c$ are extrapolated from the interior; the exit pressure is specified.

Scaling Parameter

As previously stated, the governing equations are transformed by scaling the y-coordinate with the local boundary layer thickness. Since the edge of the boundary layer is not well defined, relations for the scaling parameter $\Delta(x, t)$ must be chosen empirically. Here it is defined in terms of the incompressible (or kinematic) displacement and momentum thicknesses,

$$\delta_k^* = \int_0^\infty \left(1 - \frac{u}{u_e}\right) dy, \qquad \theta_k = \int_0^\infty \frac{u}{u_e}\left(1 - \frac{u}{u_e}\right) dy, \qquad (35)$$

where u_e is the x-component of velocity at the edge of the boundary layer.

As suggested by Drela [10], one method is to express the scaling parameter as a linear combination of δ_k^* and θ_k,

$$\Delta(x, t) = \sigma\theta_k + \frac{1 - \sigma}{H}\delta_k^*, \qquad (0 \le \sigma \le 1) \qquad (36)$$

where H is the value of the shape parameter for incompressible flat plate flow ($H = 2.6$ for laminar and $H = 1.2$ for turbulent). Defined in this manner, Δ is independent of σ for flat plate flow.

Unfortunately, this definition of the scaling parameter is not adequate. The major reason is that (36) results in nearly discontinuous grids when shocks are encountered, leading to solution divergence. Resolution of this problem lies in smoothing the scaling parameter. Here, we employ an analogy to the 1-D heat equation to evolve the scaling parameter in time,

$$\frac{\partial\Delta}{\partial t} = \nu_1 (\Delta_{eq} - \Delta) + \nu_2 \frac{\partial^2\Delta}{\partial x^2}, \qquad (37)$$

where the coefficients ν_1 and ν_2 control the relative amount of smoothing as well as the relaxation of Δ in time. The previous definition (36) is used as the source term Δ_{eq}, and explicit second differences used for the dissipation term $\partial^2\Delta/\partial x^2$. Thus,

$$\Delta_i^{n+1} = \Delta_i^n + \nu_1 \left[\sigma\theta_k + \frac{1 - \sigma}{H}\delta_k^* - \Delta_i^{n+1}\right] \qquad (38)$$

$$+ \nu_2 \left[\Delta_{i+1}^n - 2\Delta_i^n + \Delta_{i-1}^n\right],$$

where θ_k and δ_k^* are evaluated at the $n + 1$ time level. A von Neumann stability analysis [22] requires $\nu_2 < 1/2$ for stability. All test cases presented in this paper use the values $\nu_1 = 0.1$, $\nu_2 = 0.45$ and $\sigma = 0.8$.

Newton Solution Procedure

At each streamwise station, a time step consists of the solution of the following nonlinear system:

Unknowns: U, r, q at nodes   6J
           Δ, δ_k^* 2

Equations: Conservation on cells $4(J-1)$
            r and q defns. on cells $2(J-1)$
            Boundary conditions   6
            Δ, δ_k^* defns.   2

Here, J is the total number of nodes and $(J-1)$ is the total number of cells. The unknown δ_k^* is introduced through the turbulence model. This system is solved by Newton's method, which is quadratically convergent.

The Newton procedure is conceptually straightforward. The system of nonlinear equations may be written as,

$$\mathbf{F}(\mathbf{X}) = 0, \qquad (39)$$

where $\mathbf{F}$ is the vector of equations and $\mathbf{X}$ is the vector of unknowns. Given a guess for the solution at some iteration level k, the next guess $\mathbf{X}^{k+1}$ is obtained by setting the linear Taylor series expansion for $\mathbf{F}(\mathbf{X}^{k+1})$ to zero,

$$\mathbf{F}(\mathbf{X}^{k+1}) \simeq \mathbf{F}(\mathbf{X}^k) + \left(\frac{\partial \mathbf{F}}{\partial \mathbf{X}}\right)^k \delta \mathbf{X}^k = 0, \qquad (40a)$$

$$\mathbf{X}^{k+1} = \mathbf{X}^k + \delta \mathbf{X}^k. \qquad (40b)$$

The term $\partial \mathbf{F}/\partial \mathbf{X}$ is the Jacobian matrix whose entries $(\partial \mathbf{F}/\partial \mathbf{X})_{m,n}$ are the partial derivative of the mth equation $\mathbf{F}_m$ with respect to the nth unknown $\mathbf{X}_n$. These entries are evaluated at the kth iterate. Because $\partial \mathbf{F}/\partial \mathbf{X}$ is a matrix, a linear system must be solved to obtain the changes $\delta \mathbf{X}^k$.

In the present algorithm, the linear system resulting from the Newton procedure is a block tri-diagonal matrix with 6×6 blocks. The linear system is solved by Gaussian elimination.

Stability Analysis

The stability boundary of the present algorithm is determined by a von Neumann stability analysis of the 2-D advection-diffusion equation,

$$\frac{\partial u}{\partial t} + a\frac{\partial u}{\partial z} + b\frac{\partial u}{\partial y} - \frac{\partial \tau}{\partial y} = 0, \qquad \tau = \nu\frac{\partial u}{\partial y}. \qquad (41)$$

Consistent with the present algorithm, this equation is discretised using a single-stage time integration with implicit two-point differencing in the y-direction and explicit upwind differencing in the z-direction. The discretised equations can be written compactly using the following translation operators:

$$Zu^n \equiv u^{n+1}, \quad Tu_j \equiv u_{j-1}, \quad Ku_j \equiv u_{j+1}. \qquad (42)$$

With these translation operators the discrete equations may be written as,

$$\frac{1}{2}(K+1)(Z-1)u_{i,j}^n + \frac{a\Delta t}{2\Delta z}(K+1)(1-T)u_{i,j}^n \qquad (43)$$

$$+ \frac{b\Delta t}{\Delta y}(K-1)Zu_{i,j}^n - \frac{\Delta t}{\Delta y}(K-1)Z\tau_{i,j}^n = 0,$$

where $\tau_{i,j}^n$ is obtained from the shear definition,

$$\tau_{i,j}^n = \frac{2\nu}{\Delta y}\left(\frac{K-1}{K+1}\right)u_{i,j}^n = \frac{2\nu}{\Delta y}\tilde{K}\tilde{u}. \qquad (44)$$

Substitution for $\tau_{i,j}^n$ gives the final result,

$$(Z-1) + \lambda_z(1-T) + 2\lambda_y Z\tilde{K} - 4\sigma Z\tilde{K}^2 = 0, \qquad (45)$$

where

$$\lambda_z \equiv \frac{a\Delta t}{\Delta z}, \quad \lambda_y \equiv \frac{b\Delta t}{\Delta y}, \quad \sigma \equiv \frac{\nu\Delta t}{\Delta y^2}. \qquad (46)$$

Equation (45) is now examined for the Fourier mode,

$$u_{i,j}^n = g^n e^{i(i\theta + j\phi)}, \qquad \begin{array}{c} -\pi < \theta \le +\pi \\ -\pi < \phi \le +\pi \end{array} \qquad (47)$$

where $i = \sqrt{-1}$. For this mode the translation operators become $Z = g$, $T = e^{-i\theta}$, and $K = e^{+i\phi}$. Substitution of this Fourier mode into (45) gives the amplification factor g,

$$g = \frac{1 - \lambda_z(1 - e^{-i\theta})}{1 + i2\lambda_y \tan(\phi/2) - 4\sigma \tan^2(\phi/2)}. \qquad (48)$$

For stability, we require that $|g| \le 1$.

Note that the numerator is a function of θ only and the denominator a function of ϕ only; hence, their amplitudes can be analysed independently. The denominator has a magnitude greater than 1 for all positive λ_y and σ, except at $\phi = 0$ where it has a magnitude of 1. Thus, for stability the numerator must have a magnitude that is not greater than 1; this requires $\lambda_z \le 1$. For the Navier-Stokes equations, the wave speed a is replaced by $|u| + c$, giving the stability restriction,

$$\lambda_z = \frac{(|u| + c)\Delta t}{\Delta z} \le 1. \qquad (49)$$

This shows that the numerical stability of the algorithm depends only on the streamwise spacing Δz.

Euler/Navier-Stokes Coupling

Separation of the flowfield into inviscid and viscous regions requires a procedure for coupling the respective solutions. In this section, a procedure is described for coupling the Euler and Thin-Shear-Layer Navier-Stokes algorithms.

Previous methods for coupling Euler and Navier-Stokes regions of a flowfield have used patched grids or slightly overlapping grids; both approaches are used by Rai [21]. Coupling is through conservative flux evaluation at the interface in the former and solution interpolation within the overlap region in the latter. Positioning of interfaces and overlap regions require a priori knowledge of the extent of

viscous regions if they are fixed, and regridding of the entire flowfield if they are adapted. Furthermore, a smooth matching of solutions is not guaranteed if different algorithms are used to solve the inviscid and viscous regions.

We have chosen to couple the inviscid and viscous algorithms by the technique of wall transpiration fluxes. This technique has proven very successful with boundary layer schemes coupled with potential or Euler algorithms [15,13,29]. The present work represents the first extension of this coupling technique to the solution of the TSL Navier-Stokes equations, both for steady and unsteady flows. The fundamental issues addressed in this extension are the matching of the inviscid and viscous solutions with this equation set and the performance of the technique for boundary layers which may have substantial thickness. To better isolate these issues, geometric complexity is removed by making simplifying assumptions on the Euler and viscous grids. These are that j grid lines are vertical, even for curved walls, and coincide for the two grids as shown in Fig. 1.

In review, the flowfield is solved using the Defect formulation of Le Balleur [15,16]. At each point in the flowfield two equation sets are used to represent the solution. The first are the Euler equations and the second are the TSL Navier-Stokes equations written in the form of Defect equations. The Euler equations are solved on a fixed grid, while the viscous grid dynamically evolves with the boundary layer thickness. The Defect equations reduce to an identity in the outer inviscid portion of the flow. Thus, they are solved to the edge of the boundary layer and outer boundary conditions imposed by the solution of the Euler equations. Within the boundary layer, the solution of the Euler equations has no physical significance. This pseudo-inviscid solution does not satisfy the zero mass flux condition at the wall. Instead, it satisfies boundary conditions driven by the viscous solution; these are referred to as wall transpiration conditions. Hence, coupling the two solutions involves determining outer or edge boundary conditions for the viscous equations and boundary conditions at the wall for the Euler equations.

Interpolation of Edge Solution

To implement the outer boundary conditions for the viscous solver, the inviscid solution is needed at the edge of the viscous grid. This solution is interpolated from the inviscid grid in a rather straightforward manner. The assumption that j grid lines coincide for the Euler and viscous grids reduces the geometric complexity of finding the edge of the viscous grid; it also makes the interpolation essentially one dimensional.

Wall Transpiration Fluxes

The inviscid solution $\hat{U}$ satisfies boundary conditions at the wall driven by the viscous solution, rather than the solid wall slip conditions. These boundary conditions are transpiration fluxes or surface blowing constructed to reproduce the viscous effects on the outer inviscid solution. As first

• Geometry: x, y o Solution: $\overline{U}, \overline{U_X}, \overline{U_Y}$

a) Euler Grid

• Geometry: ξ, η o Solution: U, τ, q
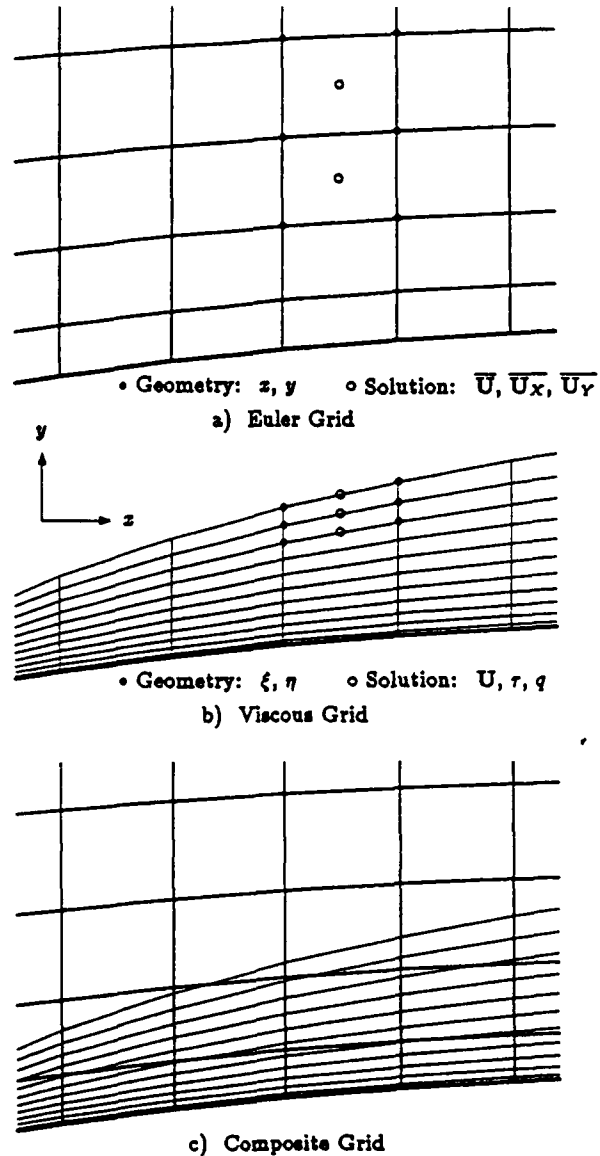
b) Viscous Grid

c) Composite Grid

Figure 1: Composite Grid Topology for Coupling

suggested by Johnston and Sockol [13], these wall transpiration fluxes can be derived by integrating the Defect equations in transformed coordinates across the boundary layer. The integration is performed subject to the no-slip conditions on U at the wall and the constraint that the viscous solution U asymptotes to the inviscid solution $\hat{U}$. Written in transformed coordinates, the transpiration fluxes are,

$$\hat{G}_w - \hat{y}_x \hat{F}_w = G_w - \hat{y}_x F_w - \frac{1}{Re} S_w \qquad (50)$$

$$+ \frac{\partial}{\partial x} \int_0^\infty \Delta(\hat{F} - F)\, d\eta + \frac{\partial}{\partial t} \int_0^\infty \Delta(\hat{U} - U)\, d\eta,$$

where ( )$_w$ indicates values at the wall.

The unsteady Euler equations describe acoustic and convective wave propagation; therefore, it is physically incor-

rect to impose all four of the transpiration fluxes. The proper choice of boundary conditions has been addressed by Murman and Bussing [20] using a 1-D characteristic analysis normal to the wall. Their recommendation was to specify three conditions, the mass, x-momentum and energy fluxes, for the usual case of flow into the domain. Conversely, for flow out of the domain only the mass transpiration flux should be specified.

In the present coupling procedure, we impose only the mass transpiration flux, allowing all other flow quantities at the wall to float to values predicted by the Euler algorithm. This choice is motivated by the following reasoning, based on Lighthill's analysis for steady flow [17]. The primary effect of the boundary layer on the outer inviscid flow is a displacement of the streamlines away from the surface of the body. For the solution of the outer inviscid flow, this effect can be produced by physically thickening the body by the displacement thickness δ^* of the boundary layer. It can be equivalently produced by a distribution of sources on the surface of the body (i.e. the mass transpiration flux). In this case the streamline located at the displacement thickness of the boundary layer divides the outer flow from all fluid injected at the surface. Hence, properties of this fluid that are convected along streamlines, such as the entropy and vorticity, have little or no effect on the outer inviscid solution.

The same discretization developed for the solution of the Defect equations (31) is used to numerically integrate the mass Defect equation across the boundary layer. Hence, at a given streamwise station, the discrete counterpart of (50) is,

$$\left(\hat{G} - \tilde{y}_s\hat{F}\right)_0^{n+1} = \left(G - \frac{1}{Re}S - \tilde{y}_s F\right)_{i,1}^{n+1}$$

$$+ \frac{1}{\Delta\xi}\sum_{j=1}^{J-1}\left[\left(\Delta^n\delta F\right)_{i+1/2} - \left(\Delta^n\delta F\right)_{i-1/2}\right]_{j+1/2} \quad (51a)$$

$$+ \frac{1}{\Delta t}\sum_{j=1}^{J-1}\left[\left(\Delta\delta U\right)_i^{n+1} - \left(\Delta\delta U\right)_i^{n}\right]_{j+1/2}.$$

The equations are written here in vector form, but only the mass equation is used. Consistent with the approximations used in the discrete Defect equations, the pseudo-inviscid profile is assumed to be linear and given by the edge solution and its gradients. Thus, the Defect integrands δF and δU are given by,

$$\delta F_{j+1/2} = \hat{F}_{J-1/2}^{n+1} - F_{j+1/2}^n,$$
$$\delta U_{j+1/2} = \hat{U}_{J-1/2} - U_{j+1/2}. \quad (51b)$$

Since the discretization of these equations is the same as that used to integrate the Defect equations one step in time, all terms are known. In particular the split-flux vectors at $i \pm 1/2$ are known and do not need to be recomputed.

In the present coupling procedure, the time derivative term in (51) has been found to have a destabilizing effect for the more difficult cases attempted. In these circumstances, this term is neglected and a quasi-steady assumption for the mass transpiration flux is used. This assumption is minor since the time term is usually small physically (although it can cause unbounded numerical growth).

Numerical Coupling Procedure

Evolution of the flowfield in time is by means of an explicit coupling procedure between the Euler and TSL Navier-Stokes algorithms. At each time step the inviscid and viscous solutions are integrated separately. Communication between the two is through the viscous outer edge boundary conditions and inviscid wall transpiration fluxes. The procedure is schematically presented in Fig. 2. Given the transpiration fluxes at time level n, the Euler algorithm is integrated one time step to produce the updated inviscid solution $\hat{U}^{n+1}$. Based on the position of the viscous grid at the previous time step, the inviscid edge solution $\hat{U}_e^{n+1}$ and its gradients are interpolated from the updated inviscid solution. With the updated edge solution, the TSL Navier-Stokes algorithm is then integrated one time step; this gives the updated viscous solution U^{n+1}. Finally, the mass Defect equation is integrated across the boundary layer by (51) to produce the updated mass transpiration flux at the wall for the next time step.
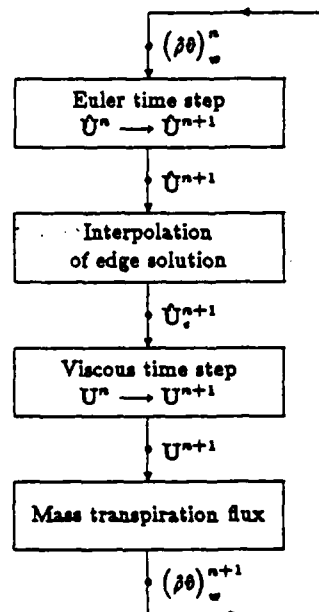

Figure 2: Flow Chart for Numerical Coupling Procedure

The present coupling procedure uses no under-relaxation of the interpolated edge solution or mass transpiration flux. In addition, the procedure is not iterated at each time step to converge the edge solution and transpiration fluxes. Hence, these quantities are first order accurate in time.

Proper vs. Approximate Transpiration Fluxes

A proper discretization of the Defect equations (8b) results if the pseudo-inviscid solution is interpolated to each point in the viscous grid and substituted into the discrete viscous equations on each viscous cell. It is proper in the sense that no approximations in the pseudo-inviscid profile through the boundary layer are made. Likewise, this is

also the proper way to numerically integrate the mass Defect equation across the boundary layer to obtain the mass transpiration flux. This has not been done in the present research. Instead, a linear pseudo-inviscid profile given by the edge solution and its gradients is assumed.

The distinction between proper and approximate discretisation of the Defect equations and mass transpiration flux is important in that approximate integrations cannot guarantee complete matching of the inviscid and viscous solutions at the edge of the boundary layer. Furthermore, these mismatches will remain in the limit of infinite grid resolution.

The assumption of a linear or even constant pseudo-inviscid profile through the boundary layer is typical of viscous/inviscid coupling techniques appearing in the literature. In practice a linear assumption is actually quite good. Only for cases of thick or rapidly changing boundary layers in conjunction with severe geometries or shocks is there any appreciable variation of the pseudo-inviscid profile. Numerically, nonlinear variations can only occur for large boundary layer thicknesses measured in terms of the number of inviscid cells in the boundary layer. For example, if the boundary layer is completely contained within a single inviscid cell, there will be essentially no difference between a proper and approximate discretization of the Defect equations.

Discussion of Results

Subsonic Compression Duct

The first case presented is a steady subsonic compression duct with a laminar boundary layer on the lower wall. Its purpose is to demonstrate the improvement in numerical results obtained with the solution of the Defect equations (8b) rather than the TSL Navier-Stokes equations (1) within viscous regions.
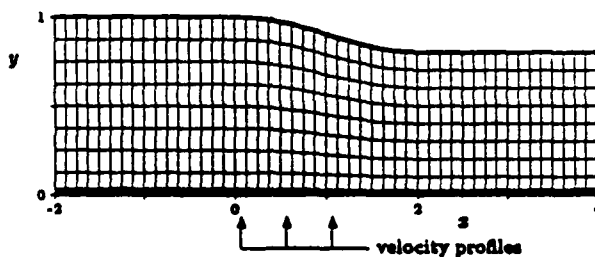
Figure 3: Subsonic Compression Duct Geometry and Grid (vertical scale doubled)

Figure 3 shows the geometry and composite grid for this case. The duct has an exit to inlet area ratio of 0.8, with a $\cos(z)$ variation in the upper wall from $z = 0$ to $z = 2$. The Reynolds number is $Re = 10^6$ and the exit Mach number is $M_{exit} = 0.5$. Inviscid slip boundary conditions are imposed on the upper wall, and no-slip conditions on the lower. At the inlet, a flat plate similarity boundary layer profile is specified with a thickness of 3.4% of the inlet height. The

fixed Euler grid is 48×8, and the lower wall viscous grid is 16 cells across.

This case was first run with the discretised TSL Navier-Stokes equations (30) solved within the boundary layer. Velocity profiles at three streamwise stations are shown in Fig. 4. The stations are located in the constriction where the flow is accelerating as indicated in Fig. 3. The plots in Fig. 4 show both the viscous profile U and the pseudo-inviscid profile $\hat{U}$ through the boundary layer. The plots show that the viscous and inviscid solutions do not quite match at the the edge of the viscous grid. Although the viscous solution asymptotes to an inviscid solution towards the outer edge of the viscous grid, it is not the same as that predicted by the outer Euler solver. Also worth noting is the difference in $\partial v/\partial y$ between the viscous and inviscid profiles; this indicates a difference in the streamwise velocity gradient, $\partial u/\partial x$.
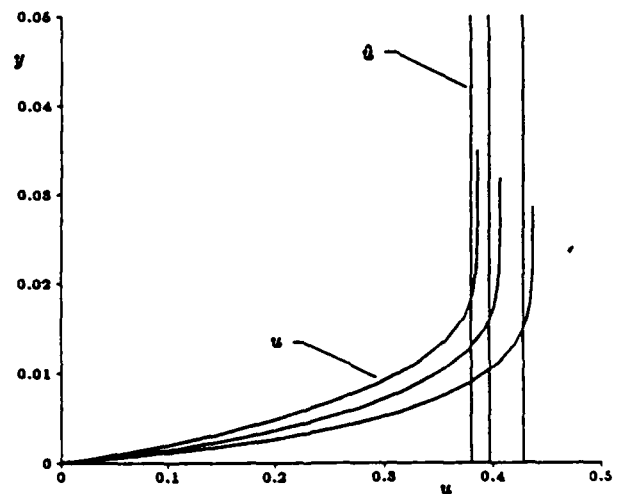
a) Axial Velocity
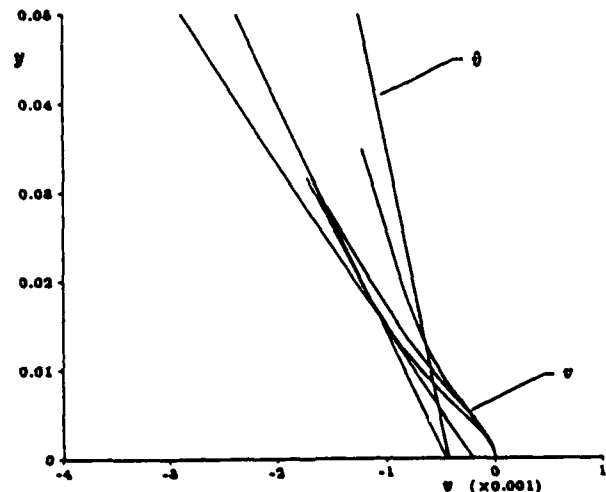
b) Vertical Velocity

Figure 4: Velocity Profiles Using TSL Naver-Stokes Equations

As previously stated, the cause of the mismatch is the difference in truncation errors between the Euler and TSL Navier-Stokes algorithms. Hence, solution of the Defect equations should cancel the difference in truncation errors, allowing the the solutions to match. Because the Defect equations have been approximately discretized, assuming a linear pseudo-inviscid profile, we cannot expect to match the solutions precisely. However, they should be close since the viscous grid is completely contained within the first Euler cell. Figure 5 shows the velocity profiles obtained from the solution of the discrete Defect equations (16) within the boundary layer. The resulting velocity profiles are shown in Fig. 5. The plots show a dramatic improvement over those in Fig. 4. The u velocities match to within plotting accuracy, and the v velocities are very close. In addition, $\partial v/\partial y$ matches between the viscous and inviscid solutions. The v velocity is the most difficult solution component to match because it is typically quite small, and matching is almost completely dependent on the mass transpiration flux rather than edge boundary conditions on the viscous solution.

a) Axial Velocity

b) Vertical Velocity
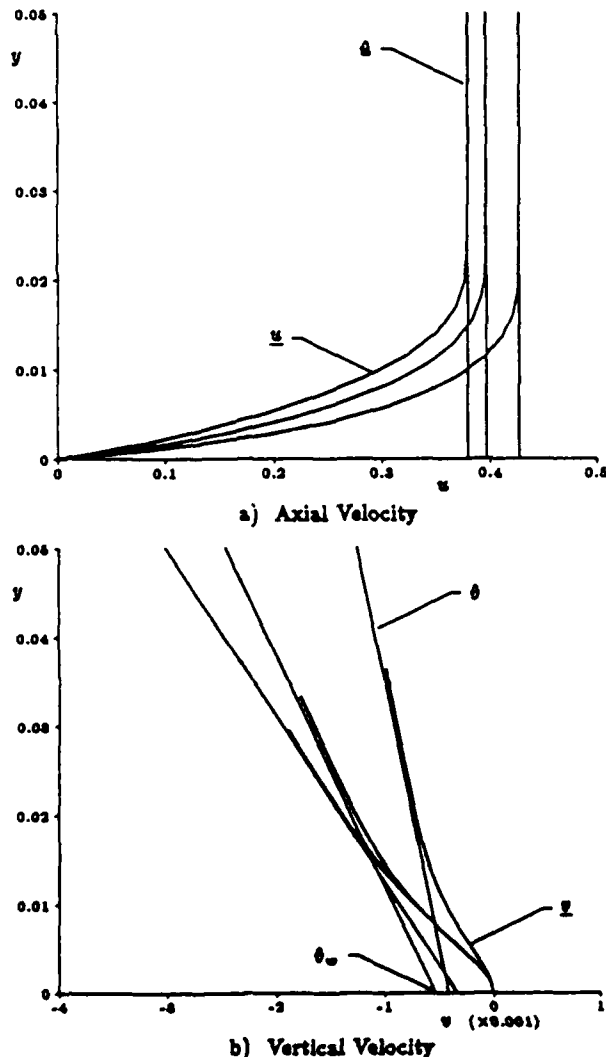
Figure 5: Velocity Profiles Using Defect Equations

Transonic Diffuser

The second test case for the coupled Euler/Navier-Stokes algorithm is a 2-D transonic diffuser with turbulent boundary layers. The geometry, depicted in Fig. 6, has been the subject of extensive experimental investigations at McDonnell-Douglas [5,6,24,25] into the nature of 2-D unsteady shock/boundary layer interaction. The experimental studies have included both self-induced and forced oscillations of the diffuser flowfield. For all cases containing terminal shocks in the diffuser section, low amplitude natural oscillations were observed in the experimental investigations. The physical mechanisms responsible for the unsteadiness were found to depend on the strength of the terminal shock.
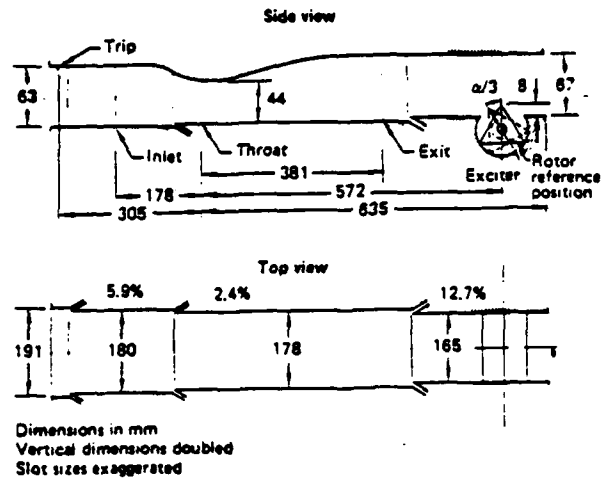

Figure 6: Experimental Geometry (from [25])

The geometry has also been the subject of Navier-Stokes simulations [11,12,18] using MacCormack's algorithm [19]. These simulations also investigated both forced and self-induced oscillations. Reference [12] included self-induced oscillations for a strong shock case, in which the boundary layers separate. To these authors' knowledge, computational results for the natural oscillations of the weak shock case presented in this paper have not been reported previously.

The specific case presented in this paper is an exit pressure of $R_p = 0.826$ (exit static to inlet stagnation), producing a weak shock with a pre-shock Mach number of $M = 1.235$. The Reynolds number is 1.1×10^6 based on the throat height h_* and stagnation conditions at the inlet. For this case the turbulent boundary layers on the upper and lower surfaces remain attached throughout the diffuser. Low amplitude self-induced oscillations have been experimentally observed downstream of the shock. These were identified as longitudinal acoustic modes resulting from the interaction of the shock and the diffuser exit. The frequency and number of observed modes changed with the diffuser length [5].

This case is computationally difficult for three reasons. The first is that the unsteadiness is naturally occurring rather than forced. Hence, the physics causing the unsteadiness must be correctly modeled. The second reason is is that

the upper and lower wall boundary layers grow by an order of magnitude downstream of the shock. This presents difficulties for any viscous solver, and is an excellent test of the coordinate rescaling in the present algorithm. The third reason is that the boundary layers nearly merge at the exit, pushing the limit of applicability of viscous/inviscid coupling in general. It also presents a test of the present coupling technique, and the approximations made herein, since several inviscid cells are located within each boundary layer near the exit.

Quasi-Steady Results

The case was initially run using steady-state acceleration techniques discussed in Ref. [3] until the residuals leveled off (this occurred two orders above single-precision machine zero). The quasi-steady results for the diffuser section are presented in the contour plots of Fig. 7 and the wall distribution plots of Fig. 8.

a) Composite Grid

(Euler 71 × 8, Viscous 71 × 31 lower and upper)

b) Mach Contours ($\Delta = 0.02$)

c) Static Pressure Contours ($\Delta = 0.01$)
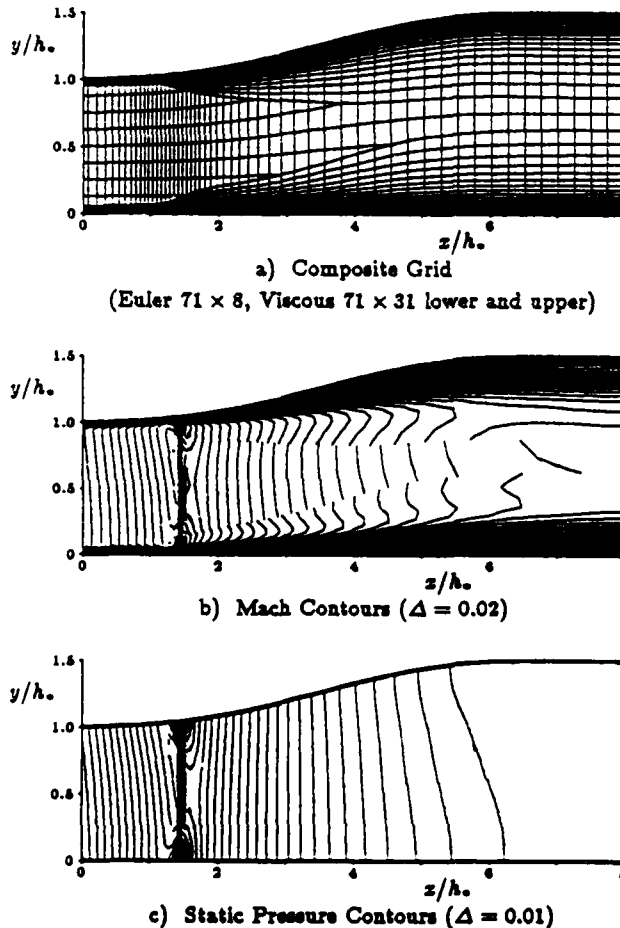
Figure 7: Transonic Diffuser: Quasi-Steady Grid and Contour Plots (vertical scale doubled)

Figure 7a shows the composite grid (with inviscid cells inside the boundary layers hidden). The computational domain extends from the experiment's nominal inlet station at $z/h_* = -4$ upstream of the throat to the nominal exit

station at $z/h_* = 8$. The Euler grid is constructed from a uniformly spaced 48 × 8 cell background grid with streamwise clustering in the vicinity of the shock increasing the resolution to 71 × 8. The upper and lower wall viscous grids, each 31 cells across, are exponentially stretched away from the wall. The minimum grid spacing for the upper wall grid is $\Delta y^+_{min} = 1.5$ from the inlet to the shock and increases to 5 at the exit. Likewise, the minimum lower wall grid spacing is 1.5 from the inlet to the shock and increases to 7.5 at the exit. This places the first few cells well within the laminar sublayer which extends to approximately $y^+ \simeq 30$. The viscous grids are thin upstream of the shock and grow dramatically downstream of the shock. The initial guesses for the upper and lower wall viscous grids were flat plate turbulent boundary layers beginning at the specified inlet profiles.

The contour and wall distribution plots show that the flow accelerates through sonic conditions at the throat with a terminal shock located at $z/h_* = 1.45$. The experimentally determined mean shock position was located at $z/h_* = 1.47$. The grid plot and some of the wall plots indicate that the presence of the shock is felt upstream within the boundary layers, beginning at about $z/h_* = 1.1$. In accordance with experimental observation, the skin friction coefficient on the upper and lower walls (Fig. 8c) show that the boundary layers remain attached throughout the diffuser section. Downstream of the shock, the boundary layers grow by almost a factor of ten as shown in Figs. 8d–e. Because the y-coordinate rescaling in the viscous grid is dynamically dependent on the local displacement and momentum thicknesses, these growths are accurately duplicated by the viscous grid.

The Mach contours (Fig. 7b) indicate an overshoot in the viscous profiles downstream of the shock on both walls. These are the result of shear layers originating at the base of the shock. Within both boundary layers, the shock becomes a compression fan, and at the shock-fan junction, a shear layer forms. Although the grid is not fine enough to resolve the fan at the base of the shock, the shear layer is captured.

Results of the present computation are compared with experimental data in Fig. 8. In general the agreement is quite good. The major reason for any discrepancies is the lack of experimental data on the boundary layers at the inlet. Bogar et al [5] give displacement and momentum thickness data for the upper wall at the inlet; however, the nominal inlet station at $z/h_* = -4$ is in accelerating flow. Hence, it is difficult to specify an inlet profile replicating these values. No data is given for the lower wall. Reference [5] states that a suction slot is located upstream of the throat producing a new laminar boundary layer off its lip. This boundary layer remains laminar until it transitions at the shock. This causes problems for the present algorithm since no transition mechanism is built into it. In previous computations, Hsieh et al [11] specified flat plate turbulent profiles for the inlet upper and lower wall boundary layers; the thicknesses were reported to be from experimental data and specified to be 9% and 4.5% of the throat height. We specify these same conditions.

The contour plots of Fig. 7 give an indication of the qual-

a) Core Axial Velocity

b) Wall Static Pressure

c) Wall Skin Friction Coefficient

d) Upper Wall Displacement and Momentum Thicknesses

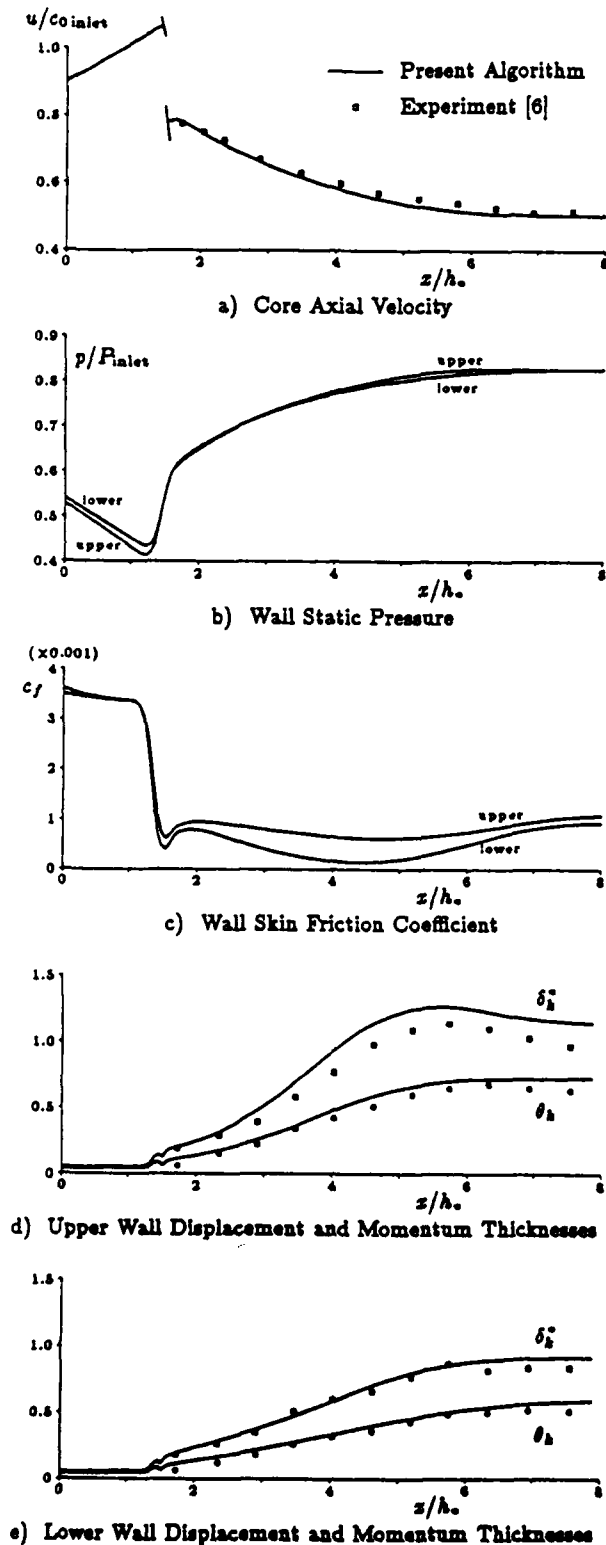e) Lower Wall Displacement and Momentum Thicknesses

Figure 8: Transonic Diffuser: Quasi-Steady Core and Wall Distribution Plots

ity of solution matching at the edge of the viscous grid. The pressure is correctly matched throughout the diffuser since it is a prescribed boundary condition at the outer edge of the viscous grid; it also transitions smoothly through the interface. The Mach number, along with other flow quantities that are not prescribed at the edge, matches fairly well ahead and just aft of the shock. Farther downstream, the mismatch becomes more noticeable as the boundary layer grows rapidly. Part of the reason for the mismatch is the rapid growth of the boundary layers and the fact that they becomes several inviscid cells thick at the exit. As a result the linear inviscid profile assumption in the discrete Defect equations and the mass transpiration flux is beginning to break down. Another reason may be the lack of cross-stream resolution in the outer portion of the viscous grid.

Unsteady Results

For the weak shock case ($R_p = 0.826$), unsteady results were reported for two diffuser lengths by Bogar et al [5]. For a diffuser length of $z_{exit}/h_e = 14.4$, two natural frequencies in the shock motion were observed; these correlated well with measured wall static pressures. The two frequencies where 60 and 230 Hz, which correspond to reduced frequencies of 0.046 and 0.178, respectively, based on the throat height h_e and inlet stagnation speed of sound $c_{0 inlet}$. The amplitude (rms) of the shock motion was measured to be 1.4% of the throat height. For a diffuser length of $z_{exit}/h_e = 30.5$, three natural frequencies were observed.

In the present computations, the constant-pressure exit plane was specified at $z/h_e = 8$, which was the nominal exit station in the experiments. Starting with the quasi-steady solution, the flowfield was marched in time at a CFL of $\lambda = 0.55$ (and a Δt based on the Euler grid) for approximately 90,000 iterations.

Figure 9 shows a trace of the unsteady pressure component on the upper wall at $z/h_e = 5.4$. The unsteady component was taken as the difference between the instantaneous and time-averaged pressures. This trace is typical of streamwise stations downstream of the shock. It shows distinct periodic oscillations that reach a constant amplitude after 5 or 6 periods. The last 20 periods of the trace was Fourier transformed and the resulting power-spectral-density plotted in Fig. 10. A peak is present at a reduced frequency of 0.135, and a second, smaller peak is present at 0.275.

The computed natural frequencies are difficult to compare to the experiments. The reason is the effect of the differing experimental and computational diffuser lengths. Since the experimentally observed oscillations were identified as longitudinal acoustic modes, their frequencies would vary inversely with the diffuser length. Thus, the values of 0.046 and 0.178 experimental observed with the exit at $z/h_e = 14.4$ should increase for a shorter diffuser. By how much they should increase for a diffuser of length 8 is clouded by the presence of boundary layer suction and the unused exciter downstream of $z/h_e = 8$ in Fig. 6.

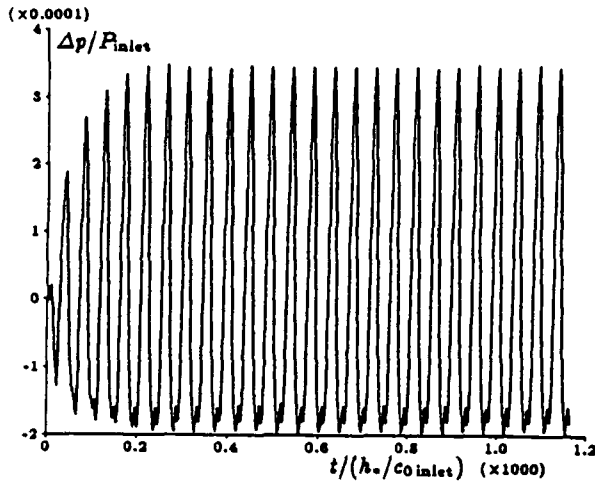An additional uncertainty is the constant-pressure exit

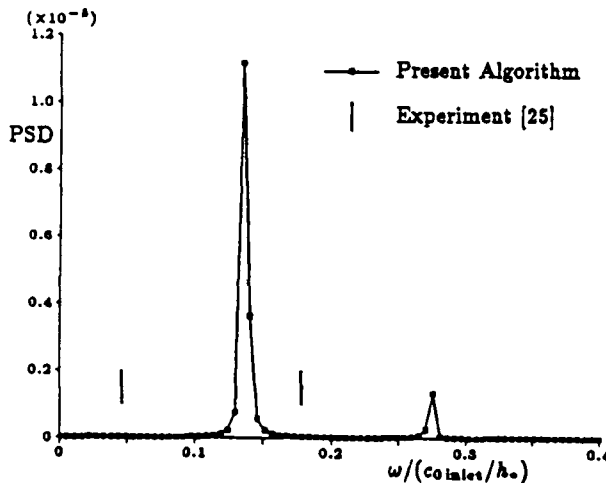Figure 9: Transonic Diffuser: Unsteady Pressure Trace on Upper Wall at $z/h_* = 5.4$

Figure 10: Transonic Diffuser: Power-Spectral-Density of Unsteady Pressure on Upper Wall at $z/h_* = 5.4$
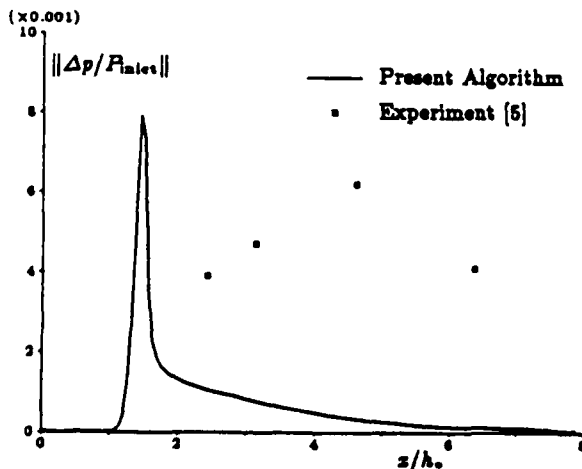

Figure 11: Transonic Diffuser: Amplitude (rms) of Unsteady Pressure Along Upper Wall

boundary condition, chosen for practical reasons, in the computation. It does not correctly model the physical wave reflection and attenuation at the open exit. This should affect both the strength of reflected waves at the exit and the effective length of the diffuser.

Figure 11 shows the amplitude (rms) of the unsteady pressure component along the diffuser. The amplitude is greatest in the immediate vicinity of the shock ($z/h_* = 1.45$), producing a sharp peak there. Downstream of this peak, the amplitude decreases slowly to zero at the exit, where constant pressure is prescribed. Essentially no oscillations occur upstream of $z/h_* = 1$, which from the quasi-steady results is approximately the farthest upstream point in the boundary layer that is affected by the shock. Experimental amplitudes are also plotted in Fig. 11; the values are approximately an order of magnitude higher than predicted by the computations. This difference may be caused by the fact that the unsteady shock motion is not resolved on the present grid. The experimentally measured shock motion was $0.014 h_*$, but the streamwise resolution is only $\Delta z/h_* = 0.063$ at the shock in the present computations. This calculation was also performed on a coarser grid composed of a 48×8 uniform Euler grid with a streamwise resolution of $\Delta z/h_* = 0.25$ at the shock; the resulting flow was completely steady. This suggests that as the shock motion is resolved, the amplitude of the pressure fluctuations will increase.

Conclusions

This paper has presented a new coupled Euler/Navier-Stokes algorithm for the solution of 2–D unsteady transonic flows. The flowfield is separated into viscous and inviscid regions and solved using a Defect formulation. Separate Euler and Navier-Stokes algorithms are solved on overlapping grids, with the Euler grid extending to the wall. Coupling between the Euler and Navier-Stokes solutions is through outer edge boundary conditions on the viscous solution and a mass transpiration flux at the wall for the Euler solution. Evolution of the flowfield is by an explicit coupling procedure.

In the Navier-Stokes algorithm, the inviscid solution along with the shear stress and heat transfer are stored at horizontal face midpoints. Two-point differencing is used to discretise the equations across the boundary layer; this is second order accurate for both inviscid and viscous terms on nonsmooth grids. Streamwise discretisation is by first order accurate flux-splitting to capture shocks. The spatial discretisation of this algorithm admits no decoupled modes. Thus, it requires no added artificial dissipation.

The viscous equations are integrated in time using a single-stage semi-implicit time-marching technique. Discretisation across the boundary layer is integrated implicitly and streamwise discretisation is integrated explicitly. The nonlinear implicit system at each streamwise station and time step is solved by Newton's method. A stability analysis shows that the time step Δt is dependent only on the streamwise grid spacing Δz. Thus, the scheme avoids

impractical time step restrictions imposed on fully explicit techniques by the small grid spacing normal to the wall.

The viscous grid evolves with the changing boundary layer thickness by a dynamic coordinate transformation. Thus, a priori knowledge of the boundary layer thickness is no necessary to specify the grid.

Two test cases have been presented. The first is a steady subsonic laminar compression duct. The results demonstrate the improvement in numerical results, in particular the inviscid/viscous solution matching, obtained by solving the Defect equations within viscous regions. The second test case is a transonic turbulent diffuser. The flowfield has been experimentally observed to be naturally unsteady, and this unsteadiness is detected by the present algorithm. This case demonstrates the algorithm's ability to predict shock/boundary layer interaction and boundary layers which grow by an order of magnitude. Quasi-steady computational results compare well with experimental time-averaged results.

Acknowledgements

References

[1] Agarwal, R. K., and Deese, J. E., "Computation of Transonic Viscous Airfoil, Inlet, and Wing Flowfields," AIAA Paper 84-1551, June 1984.

[2] Allmaras, S. R., and Giles, M. B., "A Second Order Flux Split Scheme for the Unsteady 2-D Euler Equations on Arbitrary Meshes," *Proceedings of the AIAA 8th Computational Fluid Dynamics Conference*, Paper 87-1119, June 1987.

[3] Allmaras, S. R., "A Coupled Euler/Navier-Stokes Algorithm for 2-D Unsteady Transonic Shock/Boundary Layer Interaction," Ph.D. Thesis, Department of Aeronautics and Astronautics, Massachusetts Institute of Technology, January 1989.

[4] Beam, R. M., and Warming, R. F., "An Implicit Factored Scheme for the Compressible Navier-Stokes Equations," *AIAA Journal*, vol 16, no 4, April 1978, pp. 393-402.

[5] Bogar, T. J., Sajben, M., and Kroutil, J. C., "Characteristic Frequencies of Transonic Diffuser Flow Oscillations," *AIAA Journal*, vol 21, no 9, September 1983, pp. 1232-1240.

[6] Bogar, T. J., Sajben, M., "Response of Transonic Diffuser Flows to Abrupt Increase in Back Pressure: Wall Pressure Measurements," AIAA Paper 87-1356, June 1987.

[7] Carter, J. E., "Inverse Solutions for Laminar Boundary-Layer Flows With Separation and Reattachment," NASA TR R-447, 1975.

[8] Cebeci, T., and Smith, A. M. O., *Analysis of Turbulent Boundary Layers*, Academic Press, New York, 1974.

[9] Clark, W. H., "Experimental Investigation of Pressure Oscillations in a Solid Dump Ramjet Combustor," *Journal of Spacecraft*, vol 19, no 1, January-February 1982, pp. 47-53.

[10] Drela, M., "A New Transformation and Integration Scheme for the Compressible Boundary Layer Equations, and Solution Behavior at Separation," S.M. Thesis, Department of Aeronautics and Astronautics, Massachusetts Institute of Technology, May 1983. Also *Numerical and Physical Aspects of Aerodynamic Flows II*, T. Cebeci ed., Springer-Verlag, New York, 1984, pp. 327-335.

[11] Hsieh, T., Wardlaw, A. B. Jr., Collins, P., and Coakley, T. J., "Numerical Investigation of Unsteady Inlet Flow Fields," AIAA Paper 84-0031, January 1984.

[12] Hsieh, T., and Coakley, T. J., "Downstream Boundary Effects on the Frequency of Self-Excited Oscillations in Transonic Diffuser Flows," AIAA Paper 87-0161, January 1987.

[13] Johnston, W., and Sockol, P., "Matching Procedure for Viscous-Inviscid Interactive Calculations," *AIAA Journal*, vol 17, no 6, June 1979, pp. 661-663.

[14] Keller, H. B., "Accurate Numerical Methods for Boundary Layer Flows: I. Two Dimensional Laminar Flows," *Proceedings of the Second International Conference on Numerical Methods in Fluid Dynamics*, Von Karman Institute for Fluid Dynamics, Sept. 1970.

[15] Le Balleur, J. C., "Strong Matching Method for Computing Transonic Viscous Flows Including Wakes and Separations. Lifting Airfoils," *La Recherche Aerospatiale*, no 1981-3 (English ed.), pp. 21-45.

[16] Le Balleur, J. C., "Numerical Viscous-Inviscid Interaction in Steady and Unsteady Flows," *Numerical and Physical Aspects of Aerodynamic Flows II*, T. Cebeci ed., Springer-Verlag, New York, 1984, pp. 259-284.

[17] Lighthill, M. J., "On Displacement Thickness," *Journal of Fluid Mechanics*, vol 4, pt 4, January 1958, pp. 383-392.

[18] Liou, M.-S., and Coakley, T. J., "Numerical Simulations of Unsteady Transonic Flow in Diffusers," *AIAA Journal*, vol 22, no 8, August 1984, pp. 1139-1145.

[19] MacCormack, R. W., "An Efficient Numerical Method for Solving the Time-Dependent Compressible Navier-Stokes Equations at High Reynolds Number," *Computing in Applied Mechanics*, ASME, AMD, vol 18, 1976.

[20] Murman, E. M., and Bussing, T. R. A., "On the Coupling of Boundary Layer and Euler Equation Solutions," *Numerical and Physical Aspects of Aerodynamic Flows II*, T. Cebeci ed., Springer-Verlag, New York, 1984, pp. 313-325.

[21] Rai, M. M., "Navier-Stokes Simulations of Rotor-Stator Interaction Using Patched and Overlaid Grids," *Proceedings of the AIAA 7th Computational Fluid Dynamics Conference*, Paper 85-1519, June 1985.

[22] Richtmeyer, R. D., and Morton, K. W., *Difference Methods for Initial-Value Problems*, 2nd ed., John Wiley & Sons, New York, 1967, p. 189.

[23] Roe, P. L., "Approximate Riemann Solvers, Parametric Vectors, and Difference Schemes," *Journal of Computational Physics*, vol 43, 1981, pp. 357-372.

[24] Sajben, M., Bogar, T. J., and Kroutil, J. C., "Forced Oscillation Experiments in Supercritical Diffuser Flows with Application to Ramjet Instabilities," AIAA Paper 81-1487, July 1981.

[25] Salmon, J. T., Bogar, T. J., and Sajben, M., "Laser Velocimeter Measurements in Unsteady, Separated, Transonic Diffuser Flows," AIAA Paper 81-1197, June 1981.

[26] Swanson, R. C., and Turkel, E., "A Multistage Time-Stepping Scheme for the Navier-Stokes Equations," AIAA Paper 85-0035, January, 1985.

[27] Thomas, J. L., and Walters, R. W., "Upwind Relaxation Algorithms for the Navier Stokes Equations," *Proceedings of the AIAA 7th Computational Fluid Dynamics Conference*, Paper 85-1501, June 1985.

[28] van Leer, B., "Flux-vector Splitting for the Euler Equations," ICASE Report No. 82-30, September 1982.

[29] Whitfield, D. L., Thomas, J. L., Jameson, A., and Schmidt, W., "Computation of Transonic Viscous-Inviscid Interacting Flow," *Numerical and Physical Aspects of Aerodynamic Flows II*, T. Cebeci ed., Springer-Verlag, New York, 1984, pp. 285-295.

TASK III: UNSTEADY PHENOMENA, INLET DISTORTION, AND FLOW INSTABILITIES IN MULTISTAGE COMPRESSORS

(Investigators: E.M. Greitzer, C.S. Tan, R. Plumley)

Introduction

This task is focussed on the basic instabilities which set fundamental limits to the performance of turbomachines; specifically, on the travelling wave type of disturbances that grow into the large amplitude limit cycle motions that are known as rotating stall and, more globally, surge. During the past several years, under other sponsorship, we have developed new approaches (using pseudo-spectral computational techniques) for modelling the evolution of these wave transients. This has allowed us to examine instability inception with uniform flow and with inlet distortion, the latter being a case of more practical interest.

An interesting result of the computations has been an elucidation of the not well understood phenomena of coupling between imposed propagating disturbances and the propagating disturbances that are the natural eigenmodes of the system. This is somewhat analogous to the resonance which occurs in simple dynamical systems, but is fluid dynamically more complex. Such imposed disturbances can arise, for example, from one compressor in rotating stall feeding another, as occurs in two-spool engines.

Where there has been comparison with data, the models seem to give good results, at least qualitatively, but the data generally concerns only an overall behavior. While this is useful, there is little fundamental information that addresses the key unsteady fluid dynamic effects that are being modelled.

The present program is aimed at providing data of this type. The experimental work is carried out in cooperation with Dr. D.C. Wisler's group from the General Electric Aircraft Engine Group and uses the GE low speed research compressor facility. This facility is extremely well-suited for carrying out the type of experiments that are envisioned. The instrumentation is extensive, the rig has rapid-acting throttle capability for transient studies, and the large size is conducive to detailed unsteady and three-dimensional fluid dynamic measurements. A cross-

section of the low speed research compressor is shown in Fig. 1 and detailed information about the rig is given in Ref. [1].

Experiment Definition and Design

The initial efforts were focussed on defining, in a conceptual sense, the experiments to be carried out. The basic ground rules were to obtain a clear demonstration of the wave interaction phenomena described, in a situation that is relevant in a parametric sense. Beyond this, we have specifically defined the fluid mechanic situations that are of interest. This, in turn, involves computations of the effect of rotating distortions on compressor stability, as well as computations for defining the inlet distortion generator, based on the former.

In the design of the distortions to be used, there were two different screen parameters to be selected: distortion sector size and distortion amplitude. To choose these, an extensive set of computations were carried out to define the regimes over which the compressor was predicted to show a significant effect due to the distortion. This involved an analysis of not only the non-axisymmetric screen flow field but also the distorted flow through the compressor.

These computations were described in the Annual Report of December 1988 and will not be covered here in any detail. The main point is that a screen was selected of 120 degree extent and having a pressure drop at design of $0.12 \rho U^2$. Figure 2 shows stagnation (total) pressure versus circumferential position downstream of the screen. The goal of the design and the experimental measurements are both indicated and it can be seen that the computation procedure (essentially that given in Ref. [2]) does a good job.

The rotating mechanism and support ring for the actual distortion screen were designed at General Electric. An aluminum support ring of 5-foot diameter and 5.5-foot outer diameter was used to hold the screens. This ring was placed in a housing and held in place by retainer bearings. It was tapped every 10 degrees to allow insertion of support cylinders which extended radially inward toward the center of the ring, with the screen safety wired to the cylinders. The screen and

support cylinders were weighed, and an equal mass of sheet metal was screwed into the inside edge of the ring 180 degrees away from the center of the screen to balance the ring.

The aluminum support ring was driven by a rubber drive pulley, contact friction being adequate to drive the aluminum ring. A motor drive regulated the power supplied to the electric motor and a photo detector was chosen to sense and control the speed of the screen. The distortion screen could be rotated either with the rotor or against it, up to 70% rotor speed at the normal rotor velocity and up to 130% of rotor speed if the rotor velocity were reduced. The device performed well throughout the program.

The design and setup of the experiment, however, is just the means to the end, and what is of more interest is the unsteady response of the compressor. We wished to look at several basic questions concerning this unsteady behavior:

1) Is there an identifiable "precursor" to rotating stall, both with and without inlet distortion?

2) Is the response to a rotating distortion different than to a stationary one?

3) If so, how?

These issues are discussed below.

Rotating Stall Precursor

This part of the experiment addressed the structure of disturbances occurring prior to stall. The data were recorded by 8 evenly spaced single element hot films located at plane 0.4, (0.7 radii upstream of IGV's). The procedure was to set the compressor throttle at a position very close to stall, and then begin logging data, with the goal to have the compressor stall while data were being recorded. It was also important to take data at a point far from stall, to verify that what was seen near stall was indeed present *only* near stall.

To look for a precursor, the technique used by Garnier [3] was employed. At each point in time, an FFT was done on the 8 signals,

$$C_k = \frac{1}{8}\sum_{j=1}^{8} V_j \exp\left[\frac{-2ijk\pi}{8}\right]$$

and the magnitude and phase of the first harmonic plotted against rotor revolutions. In Fig. 3, the growth of the amplitude of the first harmonic is shown. Rotating stall can be seen clearly towards the end of the trace where the stall is fully developed and the magnitude is much larger. (The oscillations in this regime reflect differences in probe calibration which have been deliberately set to be accurate in the small amplitude range of interest. The oscillations are an artifact of these calibrations; the magnitude of the first harmonic, while in rotating stall, should be constant.) There is a hump at about 17 revolutions, as well as 2 smaller humps between 20 and 30 revolutions; these represent a coherent first harmonic signal that we can identify.

From just beyond 10 revolutions to 30 revolutions, a wave appears to be travelling around the annulus at about 20% of rotor speed. In Fig. 4, the signal is shown for a shorter data sample which does not include the fully developed rotating stall. The time interval brackets the bump that occurs near 17 revolutions in Fig. 3. Two peaks can be identified: one at 8.59 Hz represents the frequency of the rotor, and the other (the highest peak), at a frequency of 1.56 Hz, corresponds to a travelling disturbance at 18% of rotor speed. The data thus show that a wave travels around the annulus prior to stall onset although, because of probe location, the signal to noise level is not adequate for further definition.

Another aspect of wave behavior prior to stall is the influence of the distortion on the waveform. The qualitative behavior was predicted in Ref. [4], where it was suggested that the amplitude of the fluctuating wave would increase (with θ) in the low velocity region and decay in the undistorted region. The wave shape thus gives another point of reference with the modelling, and we can examine distorted inlet flow data to investigate this idea.

The recording procedure was identical to the one described above; we record a data trace that included unstalled as well as stalled data and the regime prior to rotating stall was examined. The velocity signals were processed for this portion of the analysis in the same manner as described earlier. The time average velocity for each probe is plotted in Fig. 5 as a triangle. Also shown are calculated velocity profiles for a stationary distortion at the same measurement plane and at the compressor inlet.

With reference to Fig. 5, we now examine the data in Fig. 6, which shows the maximum cross correlation for each set of adjacent wires. The cross-correlation was obtained by first subtracting out the mean velocity from each trace and multiplying the resulting velocity fluctuations for adjacent wires using different time delays. These were summed along the length of the data trace and then divided by the total number of points in the data trace. The maximum cross-correlation for that range is plotted at the circumferential point corresponding to the midpoint of the two probes used to do the correlation. The calculated line is the square of the fluctuation of the most unstable eigenmode predicted by the model, adjusted so that theory and data would have the same peak. The agreement between the two plots is quite good. As predicted by the theory, the maximum cross-correlation actually occurs in the high total pressure region after growing in the low velocity sector.

Data from Steady State Instrumentation

All of the steady performance data were taken using the in-place instrumentation coverage. Data were obtained on compressor performance (speed lines) including stall onset and cessation points. These data were obtained over screen rotations of 0 to 120% of rotor RPM.

Effect of Screen Rotation on Stall Points

To determine the stall points, the screen was brought up to the desired rotation speed with the compressor running at a stable throttle position. The compressor was then slowly throttled until stall occurred, and throttle position was then recorded. This was done for a range of rotation speeds and three different compressor speeds, 500, 350, and 275 rpm. The resulting flow coefficient vs. rotation speed curves can be seen plotted in Fig. 7 along with the results of the calculations.

Figure 7 demonstrates the dependence of the instability point on rotation speed. The compressor is most stable for negative distortion rotation rates (i.e. counter-rotation). The flow coefficient at instability increases steadily with positive rotation until the smallest stable flow range is reached at about 30% of compressor speed, and then drops with further increase in screen

rotation rate. A smaller increase in instability flow also appears at a rotation rate of about 70% of compressor speed. At high negative distortion rotations, the compressor is more stable. The stability decreases with the minimum stability (i.e. maximum stalling flow coefficient) occuring at roughly 0.3 experimentally compared to 0.5 theoretically. The calculated stalling flow coefficient becomes constant above about 70% of rotor speed.

The stalling flow coefficient for high distortion rotation rates differs for experiment and theory. To examine whether the discrepancy results are due to inadequate representation of the low flow side of the axisymmetric characteristic used in the theory, calculations have been carried out to determine neutral stability points for the two other characteristics with different steepness. As discussed in [5], changing the low flow side does change the constant stall point for both large negative and large positive rotation rates and may account for some of the difference, but this is clearly not all of the story. More importantly, it cannot explain the differences in the high rotation rate values.

Summary of the Work Done to Date

Sparse experimental evidence had shown that a compressor subjected to a rotating inlet distortion suffers a degradation of performance. General trends had been demonstrated experimentally and theoretically, but no direct comparisons between experiment and theory had been done.

A stability assessment of a compressor with a rotating inlet distortion was therefore carried out on a four-stage compressor. The results, which were consistent with qualitative trends seen in earlier experimental work, gave a clearer quantitative picture of the phenomenon. The unsteady flow model was able to predict the stability trends, but there are discrepancies; at high positive rotation rates, the model predicts greater stability than what was seen experimentally.

The pre-stall flowfield investigation showed travelling waves at about 60% of fully developed stall cell speed, although more detailed experimental investigations are needed. The results of the experimental investigation of pre-stall travelling waves in distorted flow showed

excellent agreement with the predictions of the model concerning travelling wave growth in the low velocity region and decay in the high velocity region.

References

1. Wisler, D.C.,"Loss Reductions in Axial-Flow Compressors Through Low Speed Model Testing," *ASME J,Eng.Gas Turbines and Power,* Vol. 107, April 1985.

2. Koo, J.-K. and James, D.F., "Fluid Flow Around and Through a Screen," *J. Fluid Mechanics,* Vol. 60, part 3, 1973.

3. Garnier, V.H., "Experimental Investigation of Rotating Waves as a Rotating Stall Inception Indication in Compressors," MIT GTL Report #198, June 1989.

4. Hynes, T.P. and Greitzer, E.M. "A method for Assessing Effects of Inlet Distortion on Compressor Instabiity," *ASME J. Turbomachinery* 1987, Vol. 109, 371-379.

5. Plumley, R.E., "Unsteady Compressor Distortion Response and Compressor Instability," M.S. Thesis, MIT Department of Aeronautics and Astronautics, February 1990.

Flow Direction

Inlet Screen

Bellmouth

Plane 0.1 Bellmouth Flow Measurement Plane

Plane 0.5 IGV Inlet

Plane 1.0 Rotor 1 Inlet

Plane 1.5 Rotor 1 Exit
Plane 2.0
Plane 2.5
Plane 3.0
Plane 3.5
Plane 4.0
Plane 4.5
Plane 5.0

1.0 m

Laboratory Floor

Throttle
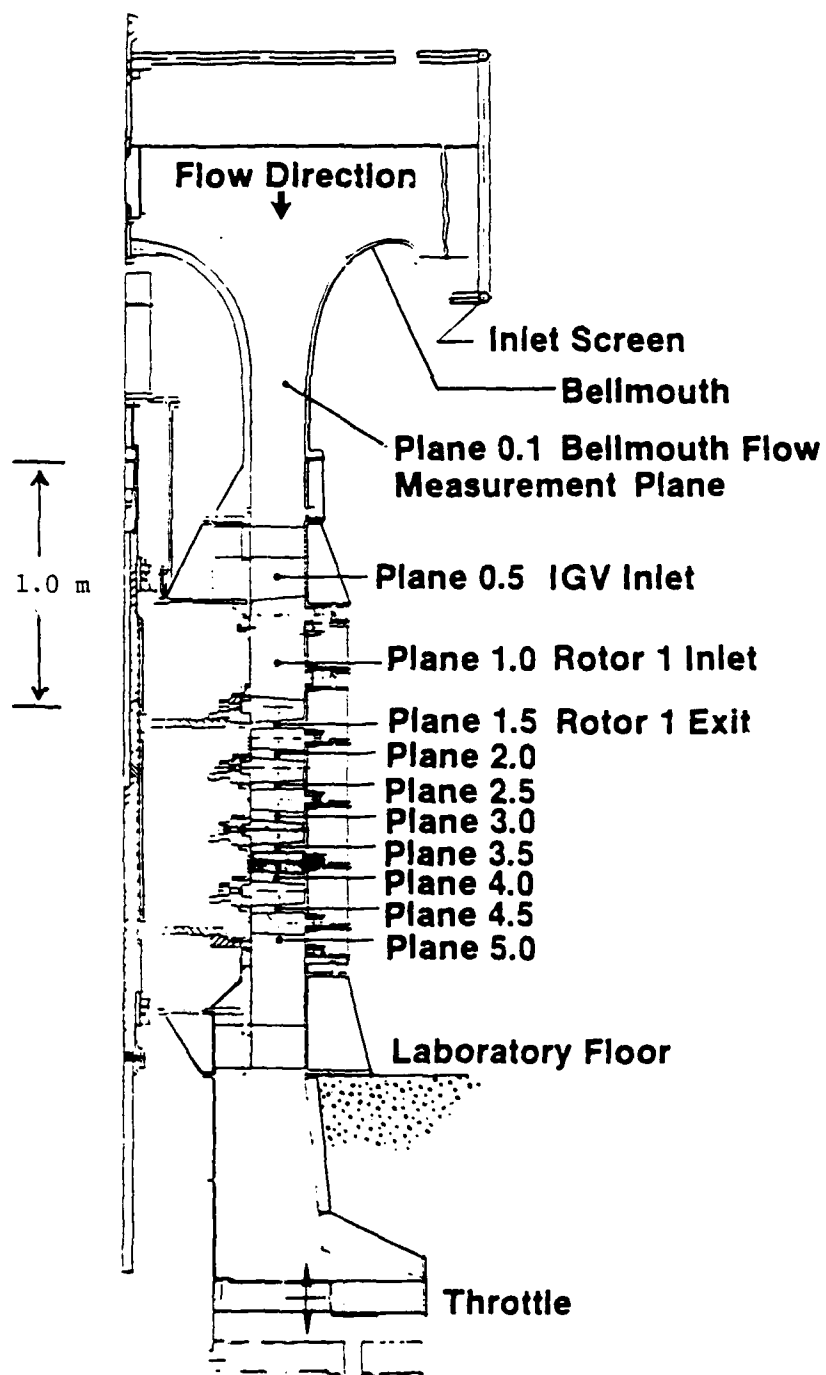
Fig. 1: Cross-section of General Electric low-speed research compressor in 0.7 radius ratio configuration.
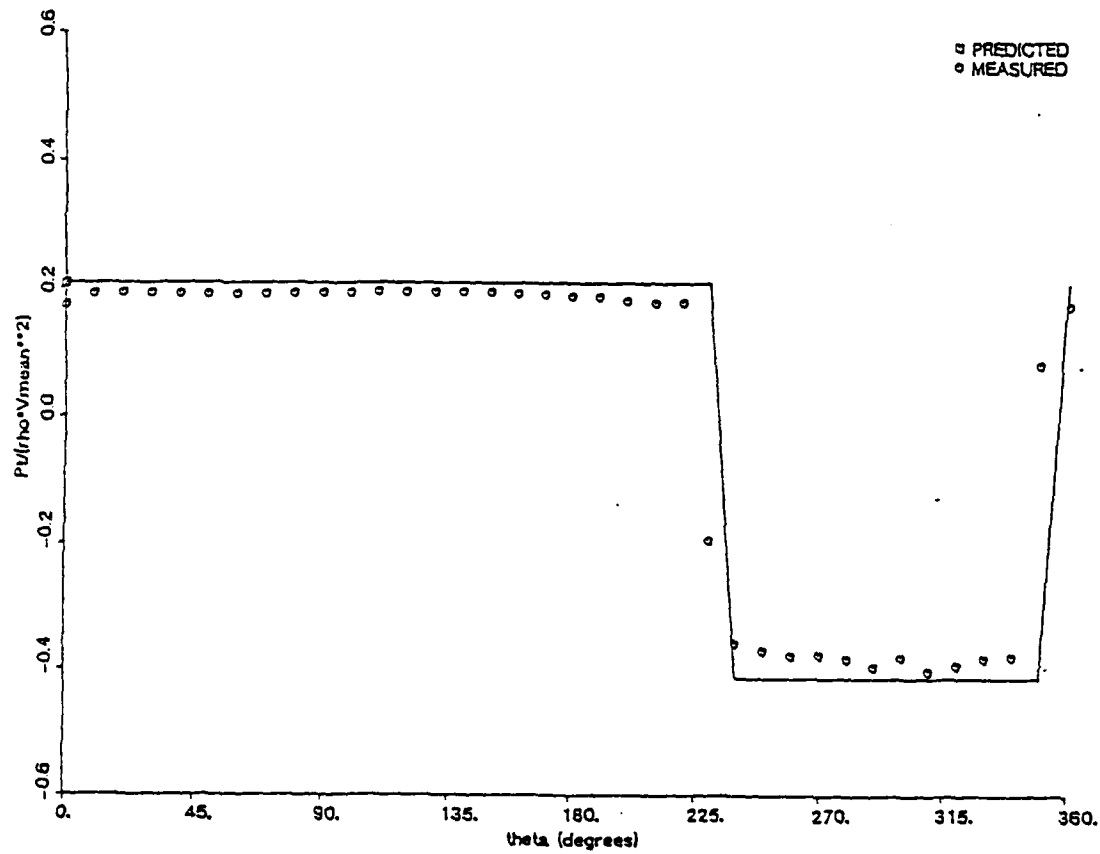
Figure 2: Total Pressure Comparison: Post Test Kiel Probe Measurement Versus Distortion Screen Design Goal, Standard Distortion.
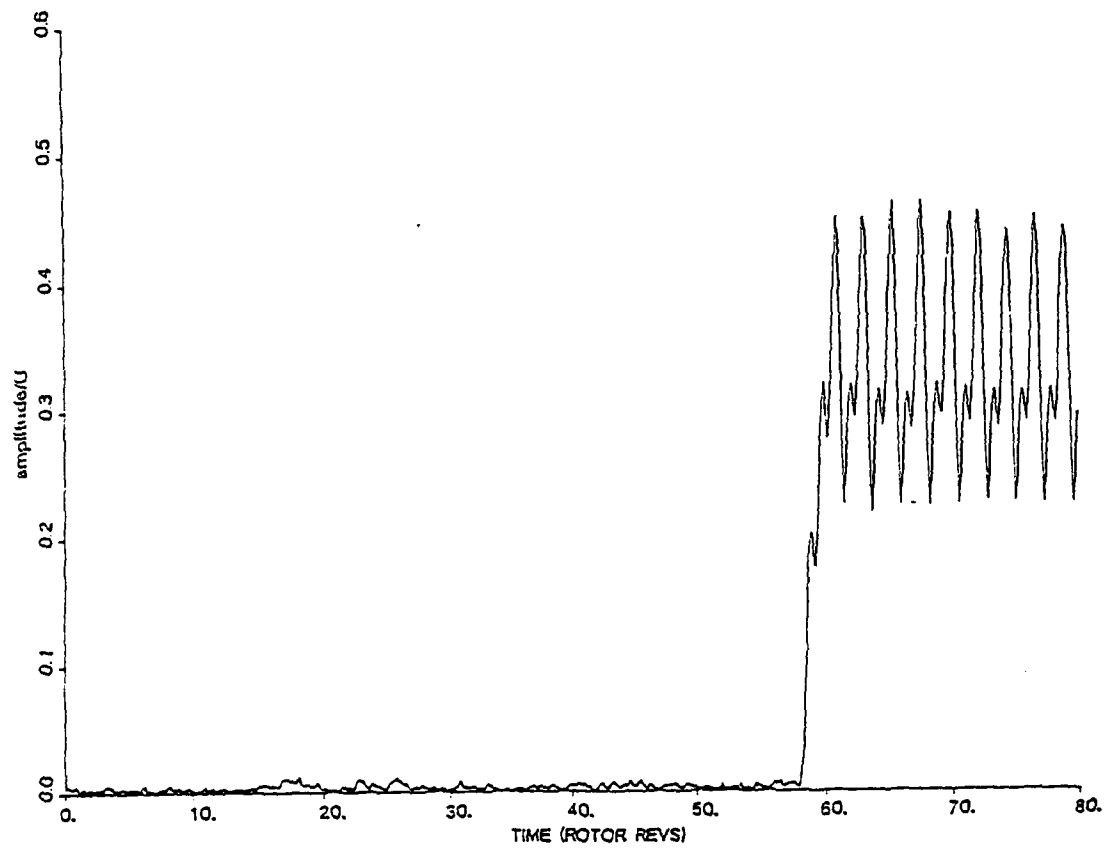
Figure 3: Growth of Amplitude of First Circumferential Harmonic, Undistorted
Flow (Probe sensitivity differences are causing oscillation. In stall,
actual amplitude is constant.)
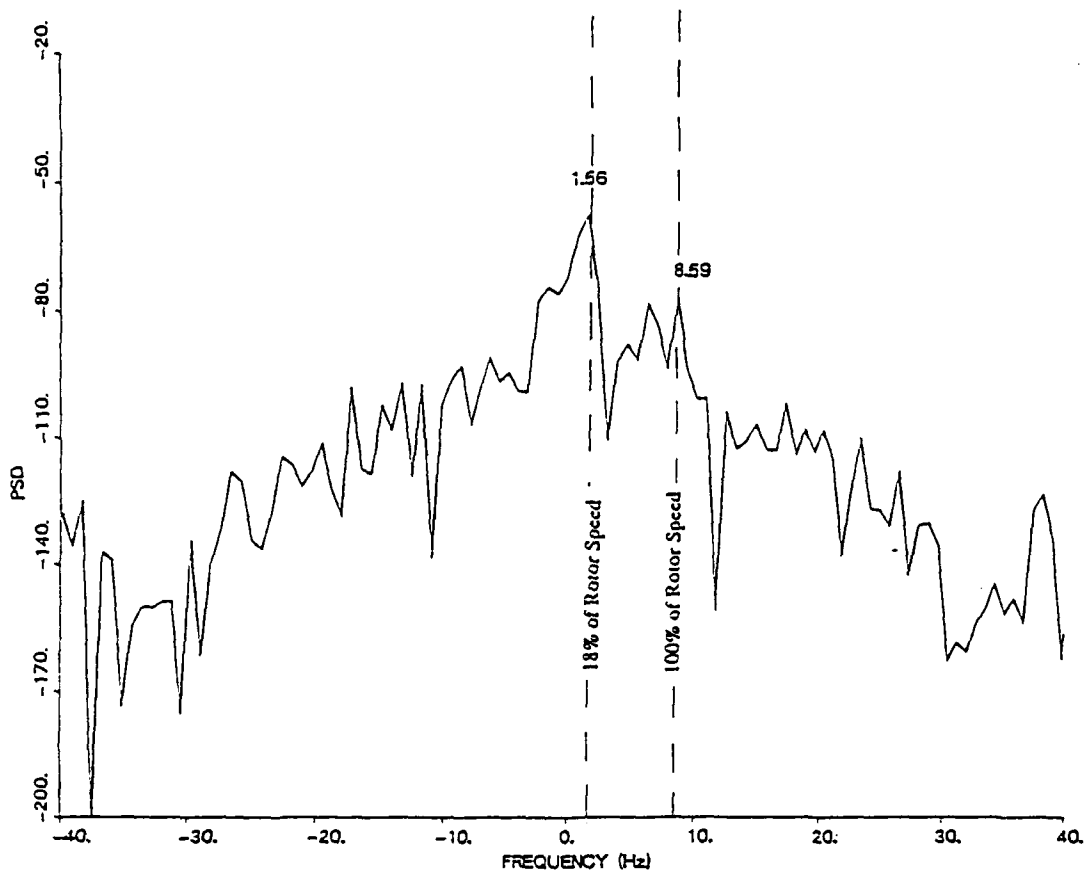
Figure 4: Power spectral Density for Range of 10.5 to 21 Compressor Revolutions.

63
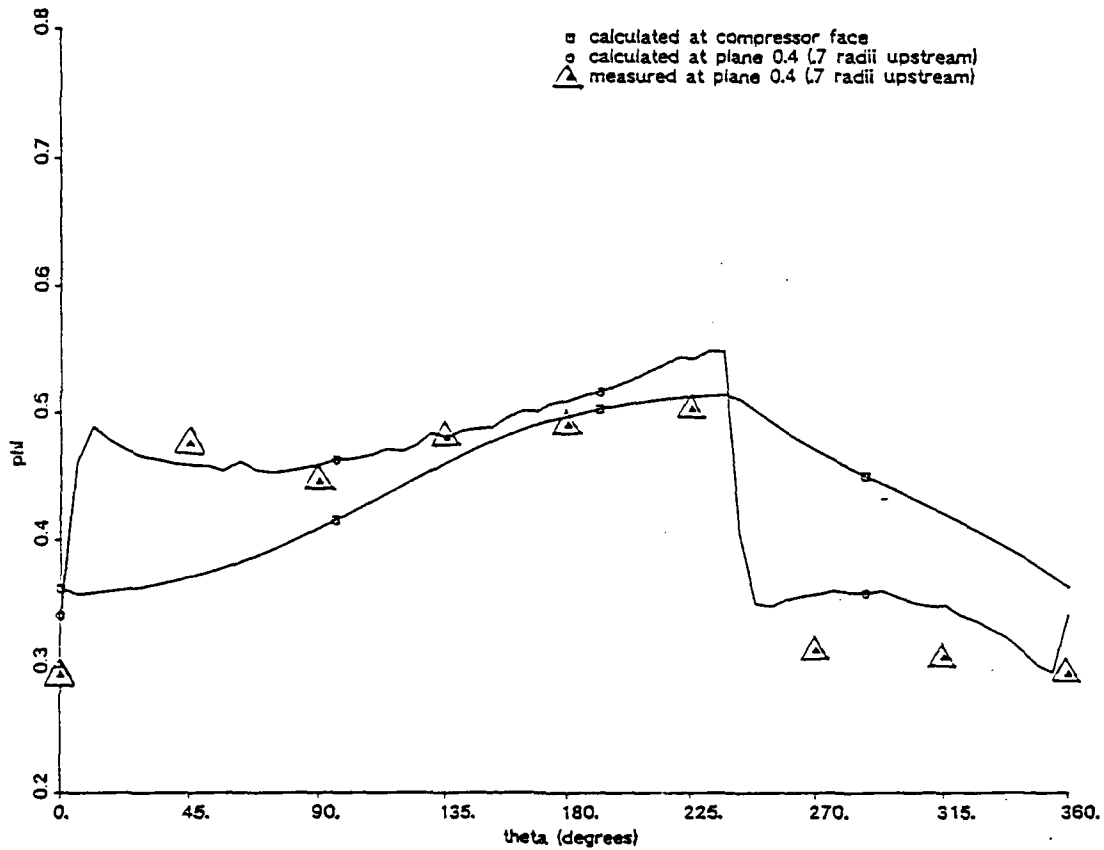
Figure 5   Phase Relationship for Calculated and Measured Velocity Profiles
Used in Cross Correlation. Stationary Distortion
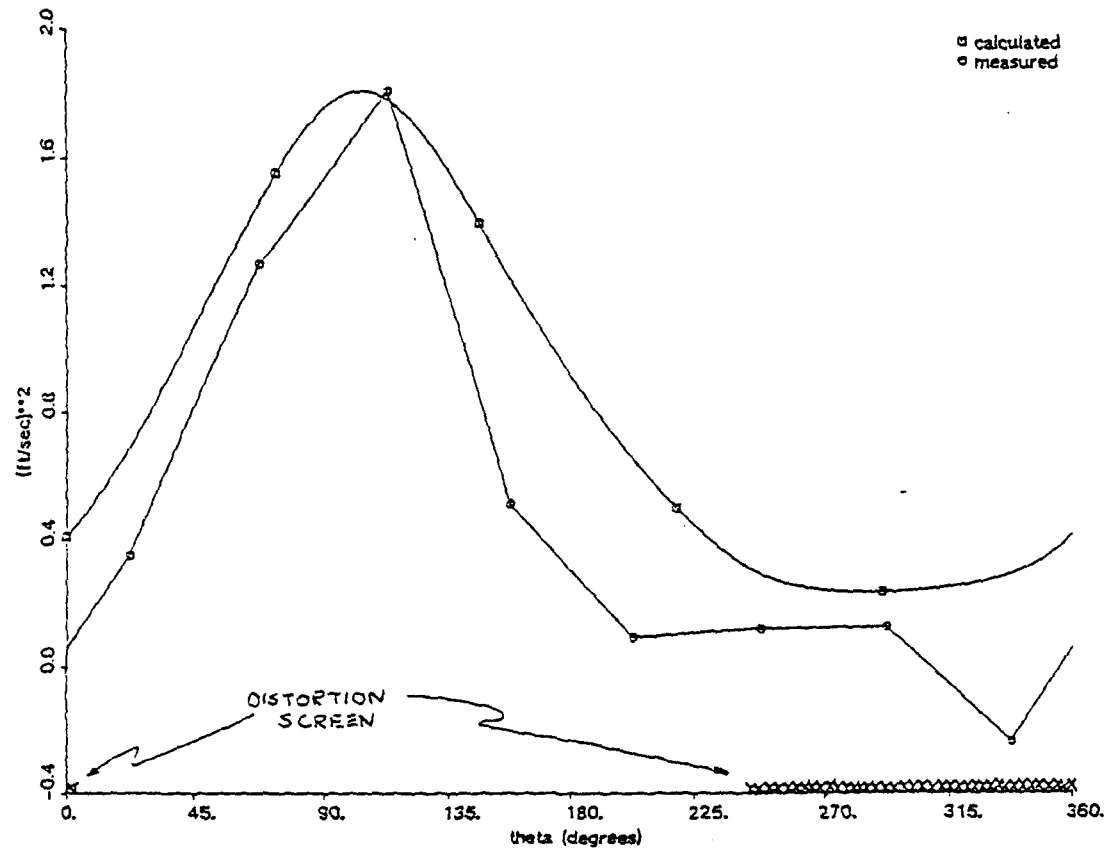
Figure 6: Calculated Square of Unsteadiness and Maximum Measured Cross
Correlation for Stationary Distortion Near Stall
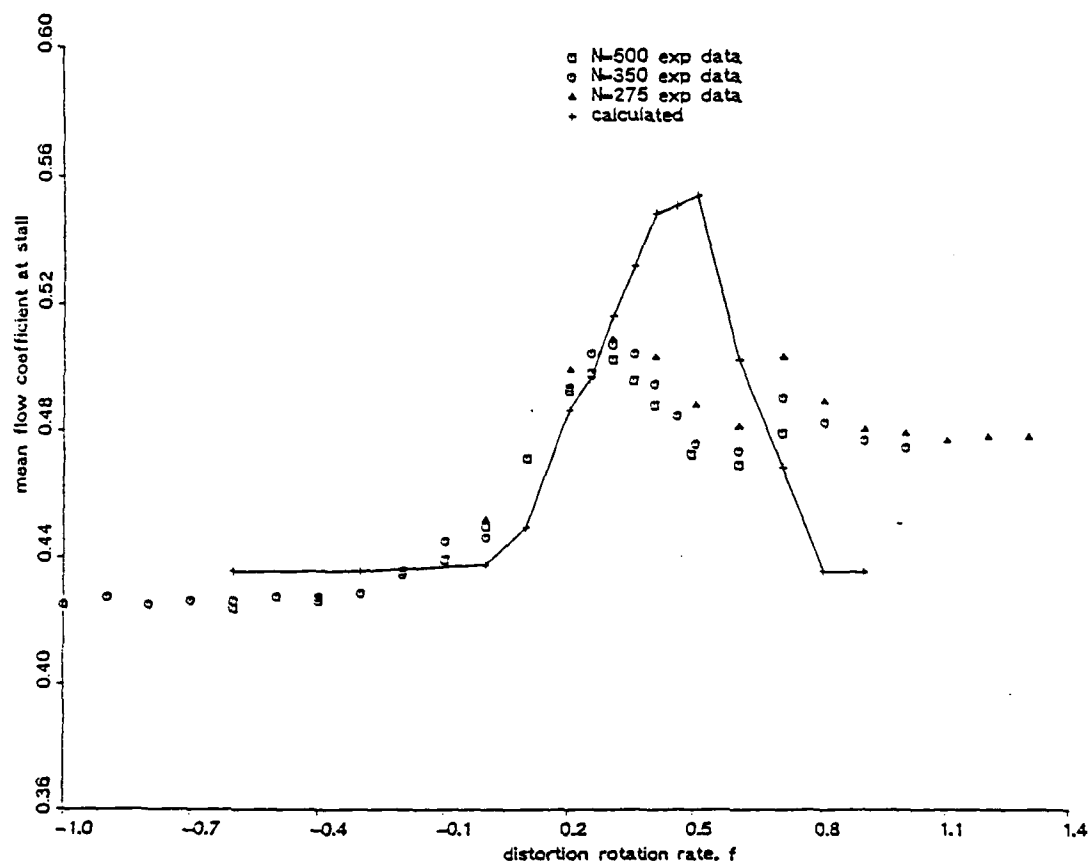
Figure 7: Calculated and Experimental Neutral Stability Flow Coefficients for Standard Distortion

TASK IV: VORTEX WAKE-COMPRESSOR BLADE INTERACTION IN CASCADES: A NEW RAPID METHOD FOR UNSTEADY SEPARATION AND VORTICITY FLUX CALCULATIONS

(Investigators: J.E. McCune, H. Benson, A. Gioulekas, G. Lam)

1   Introduction

In flow involving streamlined airfoils or cascade blades, use of the Kutta condition as a part of the potential flow calculation provides a means by which blade circulation (and hence lift or mean turning) can be determined, thus eliminating the need for complex viscous calculations. For bluff bodies and blades with rounded trailing edges, however, this classical approach must be modified [19] to include the interaction between the body boundary layers and the wake behind the body.

In the steady flow case, the blade circulation is determined by setting the net vorticity flux leaving the blade equal to zero ¬' [16]. The position of the separation points on both top and bottom surfaces is calculated, taking

into account the interference effect of the wakes, and the blade circulation is chosen so that the velocities in the main stream at the points of separation are equal.

In the unsteady flow case, the rate of change of the blade circulation is equal to the net vorticity flux leaving the blade. It is then necessary to determine the boundary layer developments on the blade, and in particular the location and the motion of the separation points, since these determine the net vorticity flux into the wakes. The calculation in addition to the unsteadiness of the incoming flow, must also take into account the interaction of the blades with their wakes.

A principal goal of this research has been to devise a simplified method of determining blade-wake interaction by providing a quick and accurate method for determining separation point location and movement. Promisig new results have been obtained in the past period; these are summarized briefly in the following sections, together with a description of how they are going to be applied in the planned next steps.

2 Prediction of the location of separation

2.1 Use of the Stratford criterion in the steady flow case

In the case of steady boundary layers, particularly on blades in turbomachines, remarkable success has been achieved by Stratford [22] and others

[2] in devising a simplified method for predicting the location of boundary layer separation, for both laminar [22] and turbulent [23] boundary layers. Stratford's procedure avoids detailed calculation of the boundary layer development by using in the prediction of the separation location key flow properties known to control boundary layer behaviour. His method is often used quite effectively, for example, in predicting blade losses and refining blade design in cascades.

Early in our research on this topic, we decided to apply Stratford's idea to the prediction of steady lift versus incidence on bodies with rounded trailing edges where the Kutta condition cannot be expected to apply. In particular, we applied this procedure to the prediction of the lift on an ellipse at various angles of attack, a problem first discussed by Howarth [6]. Moore [17] improved Howarth's calculation in more recent work, employing improved calculation methods and apparently correcting an error in the earlier study. We discovered that the Stratford criterion worked very well indeed for such an application and we were able to duplicate Moore's results right up to the stall of the ellipse. The calculation was done for both turbulent and laminar flows. Thus, under the right circumstances, the Stratford approach seems to provide a means of determining blade performance with almost the same ease as the Kutta condition at least in steady flow.

2.2 Prediction of unsteady separation

The next step was to investigate whether a similar method could be devised for unsteady flow. The flow past compressor blades in actual oper-

3

ation varies periodically with time. The general unsteady boundary layer equations can be applied to the problem. However, the difficulty for carrying out a general analysis is great, because of the inertia terms in the equation of motion. These terms give rise to periodic variations at higher harmonics of the frequency of the changing outside stream.

In the case of turbomachinery the flow unsteadiness occurs at moderate to high reduced frequencies, based either on blade chord or cascade pitch [3]. In that case, a very good approximate analysis due to C. C. Lin [10] and his students [4] can be applied. The basis of this analysis is the following. If the reduced frequency of the oscillation is high, the local acceleration is much larger than the time-dependent part of the convection of momentum. Then, to a first approximation the time-dependent part of the motion can be treated by a linear theory (Stokes second problem). The oscillatory motion in the boundary layer influences the time-mean component of the flow, because there is a Reynolds stress associated with it (in analogy with turbulent flow).

We find that such an approach offers a remarkable opportunity to generalize the Stratford criterion to unsteady flows in turbomachines. The flow is divided into two parts : the 'Prandtl layer' and the 'Stokes layer'. The 'Stokes layer' responds primarily to the unsteady component of the external flow, whereas the 'Prandtl layer' corresponds primarily to the mean component. The two layers interact most strongly at the blade surface where they together must satisfy a no-slip condition.

This picture of the unsteady boundary layer is very useful for our pur-

4

poses in several ways. First of all, it simplifies the identification of separation in the unsteady case. Adopting the classical generic definition of separation of Landau and Lifshitz [8], valid for both steady and unsteady flows, we look for a dramatic increase in the normal component of the velocity in the boundary layer, or equivalently a dramatic increase in the displacement thickness. The condribution of the 'Stokes layer' to the displacement thickness is closely limited, bounded by an inverse power of the Reynolds number, in contrast with the contribution of the 'Prandtl layer'. Focussing on the Prandtl layer behaviour, and assuming that the dramatic increase in the normal velocity component near separation is the manifestation of a square-root singularity in the coordinate along the wall [20], [14] we derive two conditions for unsteady separation. If we add the 'Stokes' to the 'Prandtl' velocity so as to reconstruct the full boundary layer velocity these conditions yield the Moore-Rott-Sears criterion for unsteady separation [17], [18], [20].

A second major advantage to Lin's approach is that both the steady and the unsteady components of the Prandtl velocity can be expressed in terms of the steady flow driven by the mean part of the free stream velocity ('basic flow') and key unsteady flow parameters. If we use Stratford's ideas to describe the development of the 'basic flow' (a steady problem), the generalization of Stratford's criterion to unsteady flows follows naturally.

3 Flow in a boundary layer with a rapidly oscillating free-stream velocity

3.1 The 'Splitting' of the Solution

The system of the unsteady boundary layer equations and boundary conditions is:

$$\frac{\partial u}{\partial t} + (u\frac{\partial}{\partial x} + v\frac{\partial}{\partial y})u - \nu\frac{\partial^2 u}{\partial y^2} = \frac{\partial U}{\partial t} + U\frac{\partial U}{\partial x}$$

$$\frac{\partial u}{\partial x} + \frac{\partial v}{\partial y} = 0$$

$$y = \infty : u = U(x,t); \quad y = 0 : u = v = 0$$

The solution (u, v) is split into two components ,the 'Prandtl' velocity distribution (u_p, v_p) associated with the component $\overline{U}(x)$ of $U(x,t)$, and the 'Stokes' velocity distribution (u_s, v_s) corresponding to the $\tilde{U}(x,t)$ component of $U(x,t)$:

$$u = u_p + u_s; \quad v = v_p + v_s$$

These velocity components satisfy the following boundary conditions :

$$y = \infty : u_p = \overline{U}(x), u_s = \tilde{U}(x,t); \quad y = 0 : u_p + u_s = 0, v_p = v_s = 0$$

Appendix A explains how the boundary layer equations are split. The end result is :

$$\frac{\partial u_p}{\partial t} - \nu\frac{\partial^2 u_p}{\partial y^2} + (u_p\frac{\partial}{\partial x} + v_p\frac{\partial}{\partial y})u_p + (u_p\frac{\partial}{\partial x} + v_p\frac{\partial}{\partial y})\tilde{U} +$$

$$+(\tilde{U}\frac{\partial}{\partial x} + V_s\frac{\partial}{\partial y})u_p = \overline{U}\frac{\partial\overline{U}}{\partial x} + \frac{\partial\overline{U}\tilde{U}}{\partial x}$$

6

$$\frac{\partial u_p}{\partial x} + \frac{\partial v_p}{\partial y} = 0$$

$$y = \infty : u_p = \overline{U}(x); \quad y = 0 : u_p + u_s = 0, v_p = 0 \qquad (1)$$

$$\frac{\partial u_s}{\partial t} - \nu \frac{\partial^2 u_s}{\partial y^2} + (u_s \frac{\partial}{\partial x} + v_s \frac{\partial}{\partial y})u_s + [(u_s - \tilde{U})\frac{\partial}{\partial x} + (v_s - V_s)\frac{\partial}{\partial y}]u_p +$$

$$+(u_p \frac{\partial}{\partial x} + v_p \frac{\partial}{\partial y})(u_s - \tilde{U}) = \frac{\partial \tilde{U}}{\partial t} + \tilde{U}\frac{\partial \tilde{U}}{\partial x}$$

$$\frac{\partial u_s}{\partial x} + \frac{\partial v_s}{\partial y} = 0$$

$$y = \infty : u_s = \tilde{U}(x,t); \quad y = 0 : u_s + u_p = 0, v_s = 0 \qquad (2)$$

3.2 The Non-dimensional Form of the Equations

We introduce the dimensionless variables:

$$x^* = \frac{x}{l}, \quad y_p^* = \frac{y}{\delta_p}, \quad y_s^* = \frac{y}{\delta_s}, \quad t^* = \omega t$$

and the dimensionless functions :

$$u_p^*(x^*, y_p^*, t^*) = \frac{u_p}{V}, \quad v_p^*(x^*, y_p^*, t^*) = \frac{l}{V\delta_p}v_p = \sqrt{Re}\frac{v_p}{V},$$

$$u_s^*(x^*, y_s^*, t^*) = \frac{u_s}{V}, \quad v_s^*(x^*, y_s^*, t^*) = \frac{l}{V\delta_s}v_s,$$

$$U^*(x^*, t) = \frac{U(x,t)}{V}, \quad \overline{U^*}(x^*) = \frac{\overline{U}(x)}{V}, \quad \widetilde{U^*}(x^*, t^*) = \frac{\tilde{U}(x,t)}{V},$$

$$V_s(x,y,t) = \frac{V\delta_s}{l}V_s^* = \frac{V\delta_s}{l}[-y_s^*\frac{\partial \tilde{U}^*}{\partial x^*} + W_s^*(x^*, t^*)] = \frac{V\delta_p}{l}[-y_p^*\frac{\partial \tilde{U}^*}{\partial x^*} + \frac{1}{\lambda}W_s^*(x^*, t^*)]$$

(Reminder : $\delta_p = \frac{l}{\sqrt{Re}}, \delta_s = \sqrt{\frac{\nu}{\omega}}, \lambda = \frac{\delta_p}{\delta_s} = \sqrt{\frac{\omega l}{V}}$)

The system (1) in non-dimensional form is:

$$V\omega\frac{\partial u_p^*}{\partial t^*} - \underbrace{\frac{\nu V Re}{l^2}}_{\frac{V^2}{l}}\frac{\partial^2 u_p^*}{\partial y_p^{*2}} + \frac{V^2}{l}(u_p^*\frac{\partial}{\partial x^*} + v_p^*\frac{\partial}{\partial y_p^*})u_p^* + \frac{V^2}{l}(u_p^*\frac{\partial}{\partial x^*} + v_p^*\frac{\partial}{\partial y_p^*})\tilde{U}^* +$$

$$+(\frac{V^2}{l}\tilde{U}^*\frac{\partial}{\partial x^*} + \underbrace{\frac{V\delta_s}{l}\frac{\sqrt{Re}}{l}V V_s^*\frac{\partial}{\partial y_p^*}}_{\frac{V^2}{\lambda l}})u_p^* = \frac{V^2}{l}\overline{U}^*\frac{\partial\overline{U}^*}{\partial x^*} + \frac{V^2}{l}\frac{\partial\overline{U}^*\tilde{U}^*}{\partial x^*}$$

$$\frac{\partial u_p^*}{\partial x^*} + \frac{\partial v_p^*}{\partial y_p^*} = 0$$

$$y_p^* = \infty : u_p^* = \overline{U}^*(x); \quad y_p = 0 : u_p^* + u_s^* = 0, v_p^* = 0$$

Dividing by $V\omega$ and dropping the asterisks:

$$\frac{\partial u_p}{\partial t} + \frac{1}{\lambda^2}\left[-\frac{\partial^2 u_p}{\partial y_p^2} + (u_p\frac{\partial}{\partial x} + v_p\frac{\partial}{\partial y_p})u_p + (u_p\frac{\partial}{\partial x} + v_p\frac{\partial}{\partial y_p})\tilde{U} +\right.$$

$$\left.+(\tilde{U}\frac{\partial}{\partial x} + \frac{1}{\lambda}V_s\frac{\partial}{\partial y_p})u_p\right] = \frac{1}{\lambda^2}\left(\overline{U}\frac{d\overline{U}}{dx} + \frac{\partial\overline{U}\tilde{U}}{\partial x}\right)$$

$$\frac{\partial u_p}{\partial x} + \frac{\partial v_p}{\partial y_p} = 0$$

$$y_p = \infty : u_p = \overline{U}(x); \quad y_p = 0 : u_p + u_s = 0, v_p = 0 \qquad (3)$$

The system (2) in non-dimensional form is:

$$V\omega\frac{\partial u_s^*}{\partial t^*} - \nu\frac{V}{\delta_s^2}\frac{\partial^2 u_s^*}{\partial y_s^{*2}} + \frac{V^2}{l}(u_s^*\frac{\partial}{\partial x^*} + v_s^*\frac{\partial}{\partial y_s^*})u_s^* +$$

$$+\frac{V^2}{l}[(u_s^* - \widetilde{U}^*)\frac{\partial}{\partial x^*} + (v_s^* - V_s^*)\frac{\partial}{\partial y_s^*}]u_p^* +$$

$$+(\frac{V^2}{l}u_p^*\frac{\partial}{\partial x^*} + \frac{V\delta_p}{l}v_p^*\frac{1}{\delta_s}\frac{\partial}{\partial y_s^*}V)(u_s^* - \widetilde{U}^*) - V\omega\frac{\partial\widetilde{U}^*}{\partial t^*} - \frac{V^2}{l}\widetilde{U}^*\frac{\partial\widetilde{U}^*}{\partial x^*} = 0$$

$$\frac{\partial u_s^*}{\partial x^*} + \frac{\partial v_s^*}{\partial y_s^*} = 0$$

$$y_s^* = \infty : u_s^* = \widetilde{U}^*(x,t); y_s^* = 0 : u_s^* + u_p^* = 0, v_s^* = 0$$

Dividing by $V\omega$ and dropping the asterisks :

$$\frac{\partial u_s}{\partial t} - \frac{\partial \tilde{U}}{\partial t} - \frac{\partial^2 u_s}{\partial y_s^2} + \frac{1}{\lambda^2} \left\{ (u_s \frac{\partial}{\partial x} + v_s \frac{\partial}{\partial y_s}) u_s + \right.$$

$$+ \left[(u_s - \tilde{U}) \frac{\partial}{\partial x} + (v_s - V_s) \frac{\partial}{\partial y_s} \right] u_p +$$

$$+ (u_p \frac{\partial}{\partial x} + \lambda v_p \frac{\partial}{\partial y_s})(u_s - \tilde{U}) \left. \right\} = \frac{1}{\lambda^2} \tilde{U} \frac{\partial \tilde{U}}{\partial x}$$

$$\frac{\partial u_s}{\partial x} + \frac{\partial v_s}{\partial y_s} = 0$$

$$y_s = \infty : u_s = \tilde{U}(x,t); \quad y_s = 0 : u_s + u_p = 0, v_s = 0 \qquad (4)$$

Since $\frac{\delta_s}{\delta_p} = \sqrt{\frac{V}{\omega l}} = \frac{1}{\lambda} \ll 1$, u_p and v_p are replaced in (4) by their series expansions which are valid for small values of y_p :

$$u_p = \sum_{n=0}^{\infty} \frac{1}{\lambda^n} \frac{y_s^n}{n!} \frac{\partial^n u_p}{\partial y_p^n}(x,0)$$

$$v_p = \sum_{n=0}^{\infty} \frac{1}{\lambda^n} \frac{y_s^n}{n!} \frac{\partial^n v_p}{\partial y_p^n}(x,0)$$

The boundary condition at the wall requires that $v_p(x,0) = 0$, while $u_p(x,0) \neq 0$ is allowed by the coupling condition .

Appendix B describes how these substitutions lead to the final form of (4):

$$\frac{\partial u_s}{\partial t} - \frac{\partial \tilde{U}}{\partial t} - \frac{\partial^2 u_s}{\partial y_s^2} + \frac{1}{\lambda^2} \left\{ -(\tilde{U} + u_p(x,0)) \frac{\partial(\tilde{U} + u_p(x,0))}{\partial x} + \right.$$

$$+ \left[(u_s + u_p(x,0)) \frac{\partial}{\partial x} + (v_s + y_s \frac{\partial v_p}{\partial y_p}(x,0)) \frac{\partial}{\partial y_s} \right] (u_s + u_p(x,0)) \left. \right\} +$$

$$+ \sum_{n=1}^{\infty} \frac{1}{\lambda^{n+2}} \left\{ \left[(\frac{y_s^n}{n!} \frac{\partial^n u_p}{\partial y_p^n}(x,0) \frac{\partial}{\partial x} + \frac{y_s^{n+1}}{(n+1)!} \frac{\partial^{n+1} v_p}{\partial y_p^{n+1}}(x,0) \frac{\partial}{\partial y_s} \right] (u_s - \tilde{U}) + \right.$$

9

$$+ \left[(u_s - \tilde{U}) \frac{\partial}{\partial x} + (v_s - V_s) \frac{\partial}{\partial y_s} \right] \frac{y_s^n}{n!} \frac{\partial^n u_p}{\partial y_p^n}(x, 0) \Big\} = 0$$

$$\frac{\partial u_s}{\partial x} + \frac{\partial v_s}{\partial y_s} = 0$$

$$y_s = \infty : u_s = \tilde{U}(x, t); \quad y_s = 0 : u_s + u_p = 0, v_s = 0 \tag{5}$$

3.3 The solution

The solution to $(E_p) \equiv (3)$ and $(E_s) \equiv (5)$ is obtained by expanding u_p and u_s in powers of $\frac{1}{\lambda}$:

$$u_p = \sum_{n=0}^{\infty} \frac{1}{\lambda^n} u_{p,n}, \quad u_s = \sum_{n=0}^{\infty} \frac{1}{\lambda^n} u_{s,n}$$

At each step the time average and the fluctuating part of the velocity, $u_{p,n} = \overline{u}_{p,n} + \tilde{u}_{p,n}, \quad u_{s,n} = \overline{u}_{s,n} + \tilde{u}_{s,n}$ are calculated by solving four coupled systems : $(\tilde{E}_{p,n}), (\overline{E}_{p,n}), (\tilde{E}_{s,n}), (\overline{E}_{s,n})$.

3.4 First approximation

$$\tilde{u}_{p,0} \equiv 0$$

$$\frac{\partial \tilde{u}_{s,0}}{\partial t} - \frac{\partial^2 \tilde{u}_{s,0}}{\partial y_s^2} - \frac{\partial \tilde{U}}{\partial t} = 0$$

$$y_s = \infty, \tilde{u}_{s,0} = \tilde{U}; \quad y_s = 0, \tilde{u}_{s,0} + \tilde{u}_{p,0} = 0, \tilde{v}_{s,0} = 0$$

Solution : $\tilde{u}_{s,0} = \Re\{ \frac{1}{2}(1 - e^{-y_s\sqrt{i}})\tilde{U}e^{it} \}$

$$\overline{u}_{s,0} \equiv 0$$

10

$$(\overline{u}_{p,0}\frac{\partial}{\partial x} + \overline{v}_{p,0}\frac{\partial}{\partial y_p})\overline{u}_{p,0} - \frac{\partial^2 \overline{u}_{p,0}}{\partial y_p^2} - \overline{U}\frac{d\overline{U}}{dx} = 0$$

$$y_p = \infty : \overline{u}_{p,0} = \overline{U}; \quad y_p = 0 : \overline{u}_{p,0} + \overline{u}_{s,0} = 0, \overline{v}_{p,0} = 0$$

The solution to $(\overline{E}_{p,0})$ is called the 'basic' flow (u_b, v_b). It is the velocity profile which corresponds to the steady free-stream velocity $\overline{U}(x)$.

3.5 Third approximation

The potential oscillation $(\tilde{U}, -y_p\frac{\partial \tilde{U}}{\partial x})$ interacts with (u_b, v_b) and creates an unsteady Prandtl flow $(\tilde{u}_{p,2}, \tilde{v}_{p,2})$. Since there is no viscous action, $\tilde{u}_{p,2}$ does not reduce to zero at the wall.

$$\frac{\partial \tilde{u}_{p,2}}{\partial t} = \frac{\partial}{\partial x}[\tilde{U}(\overline{U} - u_b)] + y_p\frac{\partial u_b}{\partial y_p}\frac{\partial \tilde{U}}{\partial x}$$

$$y_p = \infty : \tilde{u}_{p,2} = 0; \quad y_p = 0 : \tilde{u}_{p,2} + \tilde{u}_{s,2} = 0, \tilde{v}_{p,2} = 0$$

Solution :

$$\tilde{u}_{p,2} = \Re\{\frac{e^{it}}{i}\{\frac{\partial}{\partial x}[\tilde{U}(\overline{U} - u_b)] + y_p\frac{\partial u_b}{\partial y_p}\frac{\partial \tilde{U}}{\partial x}\}\}$$

The resultant slip velocity , $\tilde{u}_{p,2}(x,0) = \Re\{\frac{e^{it}}{i}\frac{\partial}{\partial x}(\tilde{U}\overline{U})\}$, is balanced by the unsteady Stokes flow when the coupling boundary condition at the wall is applied.

In the Stokes layer, the Reynolds stress associated with the shear oscillations gives rise to $(\tilde{u}_{s,2}, \tilde{v}_{s,2})$, which by viscous diffusion adjusts to the wall boundary condition.

11

$$\frac{\partial \tilde{u}_{s,2}}{\partial t} - \frac{\partial^2 \tilde{u}_{s,2}}{\partial y_s^2} + \tilde{u}_{s,0}\frac{\partial \tilde{u}_{s,0}}{\partial x} + \tilde{v}_{s,0}\frac{\partial \tilde{u}_{s,0}}{\partial y_s} - \tilde{U}\frac{\partial \tilde{U}}{\partial x} = 0$$

$$y_s = \infty, \tilde{u}_{s,2} = 0; \quad y_s = 0, \tilde{u}_{s,2} + \tilde{u}_{p,2} = 0, \tilde{v}_{s,2} = 0$$

Solution :

$$\tilde{u}_{s,2} = \Re\{ -\frac{e^{it}}{i}\frac{\partial}{\partial x}(\overline{U}\tilde{U})e^{-y_s\sqrt{i}} \}$$

The Reynolds stress creates a steady Stokes flow (acoustic streaming), which the viscous forces cannot reduce to zero at the wall.

$$-\frac{\partial^2 \overline{u}_{s,2}}{\partial y_s^2} + \overline{(\tilde{u}_{s,0}\frac{\partial \tilde{u}_{s,0}}{\partial x} + \tilde{v}_{s,0}\frac{\partial \tilde{u}_{s,0}}{\partial x} - \tilde{U}\frac{\partial \tilde{U}}{\partial x})} = 0$$

Solution :

$$\overline{u}_{s,2} = -\Re\{ \frac{1}{2i}[(3 - i + y_s\sqrt{i})e^{y_s\sqrt{i}} - e^{y_s\sqrt{i^*}} - \frac{1+i}{2}e^{y_s\sqrt{2}}]\overline{\tilde{U}\frac{\partial \tilde{U}}{\partial x}} \}$$

On the wall there is a non-vanishing u-component, which is responsible for $(\overline{u}_{p,2}, \overline{v}_{p,2})$.

$$\overline{u}_{p,2}(x,0) = -\overline{u}_{s,2}(x,0) = -\frac{3}{4}\overline{\tilde{U}\frac{\partial \tilde{U}}{\partial x}}$$

The steady Prandtl flow of order $\frac{1}{\lambda^2}$ is induced by the coupling at the wall.

$$\frac{\partial u_b\overline{u}_{p,2}}{\partial x} + v_b\frac{\partial \overline{u}_{p,2}}{\partial y_p} + \overline{v}_{p,2}\frac{\partial u_b}{y_p} - \frac{\partial^2 \overline{u}_{p,2}}{\partial y_p^2} = 0$$

$$y_p = \infty : \overline{u}_{p,2} = 0; \quad y_p = 0 : \overline{u}_{p,2} + \overline{u}_{s,2} = 0, \overline{v}_{p,2} = 0$$

Solution :

$$\overline{u}_{p,2} = \frac{\partial}{\partial y_p}(h(x)u_b), \quad \overline{v}_{p,2} = -\frac{\partial}{\partial x}(h(x)u_b)$$

where : $h(x) = \dfrac{\overline{u}_{p,2}(x,0)}{\tau_b(x,0)} = \dfrac{-\frac{3}{4}\overline{\widetilde{U}\frac{\partial\widetilde{U}}{\partial x}}}{\tau_b(x,0)}$

The presence of $(\overline{u}_{p,2}, \overline{v}_{p,2})$ can be interpreted as a vertical displacemnt of the 'basic' flow by the distance $\frac{h(x)}{\lambda^2}$, because $\overline{u}_p = u_b + \frac{\overline{u}_{p,2}}{\lambda^2} = u_b(x, y_p + \frac{h(x)}{\lambda^2})$.

4 Unsteady separation

4.1 Conditions for the velocity profile at the position of unsteady separation

The wall-stress (in non-dimensional variables) is :

$$\tau_w = \tau_{p,w} + \tau_{s,w} = \underbrace{\frac{\partial u_b}{\partial y}\Big|_w + O(\frac{1}{\lambda^2}) +}_{\tau_{p,w}}$$

$$+\underbrace{\Re\{\lambda\sqrt{i}\widetilde{U}e^{it} + \frac{1}{\lambda\sqrt{2}}\overline{\widetilde{U}\frac{d\widetilde{U}}{dx}} + \frac{1}{\lambda\sqrt{i}}\frac{d}{dx}(\widetilde{U}\overline{U})e^{it} + O(\frac{1}{\lambda^2})\}}_{\tau_{s,w}}$$

The mass flux defect is :

$$\Delta\dot{m} = \int_0^\infty (U - u)dy = \overline{U}\,\widetilde{\delta}^* + \Re\{[\frac{\widetilde{U}}{\lambda\sqrt{i}} + O(\frac{1}{\lambda^2})]e^{it}\}$$

where $\overline{\delta}^*$ is the displacement thickness of the mean flow.

The contribution of Stokes flow in τ_w is of order $O(\lambda)$, whereas in $\Delta\dot{m}$ of order $O(\frac{1}{\lambda})$.

For high frequencies, τ_w oscillates with large amplitude (of $O(\lambda)$), while the fluctuations in $\Delta\dot{m}$ are small (of $O(\frac{1}{\lambda})$). At separation, there is a sharp increase in δ^* and consequently in $\Delta\dot{m}$. The Stokes flow is mainly

responsible for the sign reversal of τ_w; on the other hand its contribution to $\Delta\dot{m}$ is small. We conclude therefore, that backflow may be present in the Stokes layer without affecting the occurence of separation.

For this reason, we focus on the 'Prandtl' component of the flow in our effort to derive the conditions for unsteady separation.

The equation for the 'Prandtl' component of the velocity is in non-dimensional form :

$$\frac{\partial u_p^*}{\partial t^*} + \frac{1}{\lambda^2}\left[\,-\frac{\partial^2 u_p^*}{\partial y_p^{*2}} + (u_p^*\frac{\partial}{\partial x^*} + v_p^*\frac{\partial}{\partial y_p^*})u_p^* + (u_p^*\frac{\partial}{\partial x^*} + v_p^*\frac{\partial}{\partial y_p^*})\widetilde{U}^* + \right.$$

$$\left. + (\widetilde{U}^*\frac{\partial}{\partial x^*} + \frac{1}{\lambda}V_s^*\frac{\partial}{\partial y_p^*})u_p^* - \overline{U}^*\frac{d\overline{U}^*}{dx^*} - \frac{\partial\overline{U}^*\widetilde{U}^*}{\partial x^*}\,\right] = 0$$

$$\frac{\partial u_p^*}{\partial x^*} + \frac{\partial v_p^*}{\partial y_p^*} = 0$$

$$y_p^* = \infty : u_p^* = \overline{U}^*(x^*); \quad y_p^* = 0 : u_p^* + u_s^* = 0, v_p^* = 0 \tag{6}$$

Far upstream of the point of separation : $\frac{v_p}{u_p} \sim \frac{1}{\sqrt{Re}}$.

As the position of separation is approached, the flow breaks away from the wall. In other words, the normal velocity component becomes of the same order as the tagential velocity component, $\frac{v_p}{u_p} \sim 1$.

The ratio of the dimensionless velocity components, near separation is, $\frac{v_p^*}{u_p^*} = \frac{v_p\sqrt{Re}}{u_p} \sim \sqrt{Re}$.

Let us examine how the derivatives of the velocity components change in magnitude, as separation is approached.

Far upstream : $\frac{\partial u_p^*}{\partial v_p^*} \sim \sqrt{Re}$, at separation : $\frac{\partial u_p^*}{\partial v_p^*} \sim \sqrt{Re}$ (remains the same).

Far upstream : $\frac{\partial v_p^*}{\partial v_p^*} \sim 1$, at separation : $\frac{\partial v_p^*}{\partial v_p^*} \sim \sqrt{Re}$ (because v_p^*

increases by a factor $\sqrt{Re}$).

Far upstream : $\frac{\partial u_p^*}{\partial x^*} \sim 1$. Because of continuity, the magnitude of this term at separation is : $\frac{\partial u_p^*}{\partial x^*} \sim \frac{\partial v_p^*}{\partial y_p^*} \sim \sqrt{Re}$.

Since the magnitude of u_p^* does not change as separation is approached, then $\frac{\partial}{\partial x^*} \sim \sqrt{Re}$. Thus, changes in the x-direction become dramatic near separation [21].

Far upstream : $\frac{\partial v_p^*}{\partial x^*} \sim \frac{1}{\sqrt{Re}}$, at separation : $\frac{\partial v_p^*}{\partial x^*} \sim \sqrt{Re}$, because both v_p^* and $\frac{\partial}{\partial x^*}$ increase by a factor of $\sqrt{Re}$ near separation.

If $x^* = x^*(u_p^*, v_p^*, t^*)$, $y_p^* = y_p^*(u_p^*, v_p^*, t^*)$, $t^* = t^*$, are considered to be the independent variables, then :

$$\frac{\partial x^*}{\partial u_p^*} = J\left(\frac{\partial v_p^*}{\partial y_p^*}\frac{\partial t^*}{\partial t^*} - \frac{\partial v_p^*}{\partial t^*}\frac{\partial t^*}{\partial y_p^*}\right) = \frac{\frac{\partial v_p^*}{\partial v_p^*}}{\frac{\partial u_p^*}{\partial x^*}\frac{\partial v_p^*}{\partial v_p^*} - \frac{\partial u_p^*}{\partial v_p^*}\frac{\partial v_p^*}{\partial x^*}}$$

Near separation the magnitude of this expression is : $\frac{\partial x^*}{\partial u_p^*} \sim \frac{\sqrt{Re}}{\sqrt{Re}\sqrt{Re} - 1\sqrt{Re}} = \frac{1}{\sqrt{Re}}$, as $x \rightarrow x_0(t)$.

The asterisks are dropped, and in what follows, all symbols represent dimensionless quantities.

Let the coordinates of the 'centre of separation' be $(x_0(t), y_0(t))$ and the x-component of the 'Prandtl' velocity at the station of separation be $u_p(x_0(t), y_p, t) \equiv u_0(y_p, t)$ for $y_p \geq y_0(t)$.

Near the 'centre of separation' the differences $u_p - u_0$ and $x_0(t) - x$ are small, and $x_0(t) - x$ can be expanded in powers of $u_p - u_0$.

Since $\frac{\partial x}{\partial u_p} \rightarrow \frac{1}{\sqrt{Re}}$ as $u_p \rightarrow u_0$, the first term in this expansion is $\frac{u_p - u_0}{\sqrt{Re}}$.

The expression for $u_p - u_0$, if second degree terms are retained is:

$$x - x_0(t) = \frac{u_p - u_0}{\sqrt{Re}} + f(y_p, t)(u_p - u_0)^2 \Rightarrow$$

$$u_p - u_0 = -\frac{-\frac{1}{\sqrt{Re}} + \sqrt{\frac{1}{Re} + 4f(x_0(t) - x)}}{2f} = -\frac{1}{2f\sqrt{Re}} + \frac{1}{\sqrt{f}}\sqrt{\frac{1}{4fRe} + (x_0(t) - x)} \Rightarrow$$

$$u_p - u_0 = -\epsilon_1(y_p, t) + a(y_p, t)\sqrt{\epsilon_2(y_p, t) + (x_0(t) - x)}$$

where : $a(y,t) = \frac{1}{\sqrt{f(y,t)}}$, $\epsilon_1 = \frac{1}{2f(y,t)\sqrt{Re}}$, $\epsilon_2 = \frac{1}{4f(y,t)Re}$.

Thus,

$$u_p(x, y_p, t) = u_0(y_p, t) + a(y_p, t)\sqrt{x_0(t) - x + O(\frac{1}{Re})} \qquad (7)$$

From continuity

$$\frac{\partial v_p}{\partial y_p} = -\frac{\partial u_p}{\partial x} = \frac{a(y_p, t)}{2\sqrt{x_0(t) - x + O(\frac{1}{Re})}}$$

therefore,

$$v_p(y_p, t) = \frac{b(y_p, t)}{\sqrt{x_0(t) - x + O(\frac{1}{Re})}} \qquad (8)$$

where : $b(y_p, t) = \frac{1}{2}\int_{y_0(t)}^{y} a(y, t)dy$.

The dominant terms in (6) are those of order $\frac{1}{\sqrt{x_0(t) - x + O(\frac{1}{Re})}}$.

The terms in (6) that contribute to the dominant balance near separation are:

$$\frac{\partial u_p}{\partial t} = \frac{\partial u_0}{\partial t} + \frac{a(y_p, t)}{2\sqrt{x_0(t) - x + O(\frac{1}{Re})}}\frac{dx_0}{dt} + \frac{\partial a}{\partial t}\sqrt{x_0(t) - x + O(\frac{1}{Re})}$$

$$u_p\frac{\partial u_p}{\partial x} = -u_p\frac{\partial v_p}{\partial y_p} = -[u_0 + a(y_p, t)\sqrt{x_0(t) - x + O(\frac{1}{Re})}]\frac{\frac{\partial b}{\partial v_p}}{\sqrt{x_0(t) - x + O(\frac{1}{Re})}}$$

16

$$v_p \frac{\partial u_p}{\partial y_p} = \frac{b(y_p, t)}{\sqrt{x_0(t) - x + O(\frac{1}{Re})}} [\frac{\partial u_0}{\partial y_p} + \frac{\partial a}{\partial y_p} \sqrt{x_0(t) - x + O(\frac{1}{Re})}]$$

$$\tilde{U} \frac{\partial u_p}{\partial x} = -\tilde{U} \frac{\partial v_p}{\partial y_p} = -\tilde{U} \frac{\frac{\partial b}{\partial y_p}}{\sqrt{x_0(t) - x + O(\frac{1}{Re})}}$$

After multiplying by $\sqrt{x_0(t) - x + O(\frac{1}{Re})}$ and using the fact that $\frac{a}{2} = \frac{\partial b}{\partial y_p}$ we get:

$$\frac{a}{2} \frac{dx_0}{dt} - u_0 \frac{\partial b}{\partial y_p} + b \frac{\partial u_0}{\partial y_p} - \tilde{U} \frac{\partial b}{\partial y_p} = 0 \Rightarrow$$

$$\frac{\partial b}{\partial y_p} (u_0 + \tilde{U} - \frac{dx_0}{dt}) = b \frac{\partial}{\partial y_p} - \quad (9)$$

At $x = x_0(t)$ for $y \gg y_0$, $v_p \sim \sqrt{Re}\, u_p$ (in nondimensional variables).

On the other hand, v_p must satisfy the boundary condition at the wall, $v_p = 0$ for $y_p = 0$. Thus, there must be a connecting region, which extends from the position of the 'centre fo separation' to the wall, where $v_p \sim u_p \sim 1 \Rightarrow b(y_p, t) \sim \frac{1}{\sqrt{Re}}$.

From (9) it follows that

$$b(y_p, t) = C(t)[u_0(y_p, t) + \tilde{U} - \frac{dx_0}{dt}]$$

The expressions for the velocity components, valid as $x \to x_0(t)$, become:

$$u_p(x, y_p, t) = u_0(y_p, t) + 2C(t) \frac{\partial u_0}{\partial y_p}(y_p, t) \sqrt{x_0(t) - x + O(\frac{1}{Re})} \quad (10)$$

$$v_p(x, y_p, t) = \frac{C(t)[u_0(y_p, t) + \tilde{U} - \frac{dx_0}{dt}]}{\sqrt{x_0(t) - x + O(\frac{1}{Re})}} \quad (11)$$

Since $\frac{\partial u_0(0,t)}{\partial x} = -\frac{3}{8}\frac{d}{dx}[|\tilde{U}|\frac{d|\tilde{U}|}{dx}]$ is finite, it is reasonable to expect $\frac{\partial u_0(y,t)}{\partial x}$ to be finite in a region which extends from the wall to the 'centre of separation' $(0 < y < y_0(t))$. Using (10),

$$\frac{\partial u_p}{\partial x} = \frac{\frac{\partial u_0}{\partial y_p}}{\sqrt{x_0(t) - x + O(\frac{1}{Re})}}$$

This expression is finite at $(x_0(t), y_0(t))$ when

$$\frac{\partial u_0}{\partial y_p} = 0 \tag{12}$$

Furthermore, $v_p(x_0(t), y_0(t))$ is finite if

$$u_0(y_0, t) + \tilde{U}_0 - \frac{dx_0}{dt} = 0 \tag{13}$$

The 'Stokes' equation imposes the constraint $y_0(t) > \delta_s$ on the location of the 'centre of separation'.

In the 'Stokes' equation,

$$\frac{\partial u_s}{\partial t} - \frac{\partial \tilde{U}}{\partial t} - \frac{\partial^2 u_s}{\partial y_s^2} + \frac{1}{\lambda^2}(u_s\frac{\partial}{\partial x} + v_s\frac{\partial}{\partial y_s})u_s +$$

$$+ \frac{1}{\lambda^2}[(u_s - \tilde{U})\frac{\partial}{\partial x} + (v_s - V_s)\frac{\partial}{\partial y_s}]u_p +$$

$$+ \frac{1}{\lambda^2}(u_p\frac{\partial}{\partial x} + \lambda v_p\frac{\partial}{\partial y_s})(u_s - \tilde{U}) - \frac{1}{\lambda^2}\tilde{U}\frac{\partial \tilde{U}}{\partial x} = 0$$

$$\frac{\partial u_s}{\partial x} + \frac{\partial v_s}{\partial y_s} = 0$$

$$y_s = \infty : u_s = \tilde{U}(x,t); \quad y_s = 0 : u_s + u_p = 0, v_s = 0 \tag{14}$$

the terms of order $\frac{1}{\sqrt{x_0(t)-x+O(\frac{1}{Re})}}$ are :

$$(u_s - \tilde{U})\frac{\partial u_p}{\partial x} = (u_s - \tilde{U})(-\frac{\partial v_p}{\partial y_p}) = -(u_s - \tilde{U})\frac{\frac{\partial b}{\partial y_p}}{\sqrt{x_0(t) - x + O(\frac{1}{Re})}}$$

$$\lambda v_p \frac{\partial(u_s - \tilde{U})}{\partial y_s} = \lambda v_p \frac{\partial(u_s - \tilde{U})}{\lambda \partial y_p} = \frac{b(y_p, t)}{\sqrt{x_0(t) - x + O(\frac{1}{Re})}} \frac{\partial u_s}{\partial y_p}$$

After multiplying (14) by $\sqrt{x_0(t) - x + O(\frac{1}{Re})}$:

$$(u_s - \tilde{U})\frac{\partial b}{\partial y_p} = b\frac{\partial(u_s - \tilde{U})}{\partial y_p}$$

This equation is identically satisfied if $y_0(t) > \delta_s$, because then $u_s = \tilde{U}$.

The boundary layer velocity, at the 'centre of separation' is : $u = u_p + u_s = u_p + \tilde{U}$.

Using (12) and (13) we find that the boundary layer velocity must satisfy the following relations at the position of separation $(x_0(t), y_0(t))$:

$$\frac{\partial u}{\partial y} = 0$$
$$u = \frac{dx_0}{dt}$$

This is the Moore-Rot-Sears criterion for unsteady separation [17], [18],[20].

4.2 Unsteady separation criterion

In deriving the unsteady separation criterion we use many of the ideas that led Stratford to his separation criterion for steady flows. It is useful, therefore, before getting into the unsteady separation criterion to discuss the steady case first.

We consider a steady flow with uniform pressure between $x = 0$ and $x = x_m$ and an adverse pressure gradient downstream.

In the outer part of the boundary layer, the flow is nearly inviscid, and Bernoulli's equation yields:

$$(p + \frac{1}{2}\rho u_{out}^2)_{x_m,\psi} = (p + \frac{1}{2}\rho u_{out}^2)_{x,\psi} + \Delta H \qquad (15)$$

where $\delta H = \int_{x_m}^{x} \frac{\partial \tau}{\partial y}(x,\psi)ds$ represents a (small) correction for the effects of viscosity. The term $\frac{\partial \tau}{\partial y}$ does not change very rapidly along a streamline in the outer part of the boundary layer, and is approximately the same as if the pressure had remained constant. Stratford [22] assumed that the loss of total head along a streamline in the the outer part of the boundary layer is independent of the pressure rise, and is the same as for the corresponding streamline in the Blasius case, where the pressure remains constant.

$$(p + \frac{1}{2}\rho u_{out}^2)_{x_m,\psi} = (p + \frac{1}{2}\rho u_f^2)_{x,\psi} + \Delta H = p_m + \frac{1}{2}\rho(u_f^2)_{x,\psi} + \Delta H \quad (16)$$

Subtracting (16) from (15) we get:

$$(p + \frac{1}{2}\rho u_{out}^2)_{x,\psi} = p_m + \frac{1}{2}\rho(u_f^2)_{x,\psi} \qquad (17)$$

By differentiating this result with respect to ψ we get:

$$(u_{out}\frac{\partial u_{out}}{\partial \psi})_{x,\psi} = (u_f\frac{\partial u_f}{\partial \psi})_{x,\psi},$$

or

$$(\frac{\partial u_{out}}{\partial y})_{x,\psi} = (\frac{\partial u_f}{\partial y})_{x,\psi} \qquad (18)$$

If we differentiate once more with respect to ψ, we get:

$$(\frac{\partial^2 u_{out}}{\partial y^2})_{x,\psi} = (\frac{u_{out}}{u_f}\frac{\partial^2 u_f}{\partial y^2})_{x,\psi} \qquad (19)$$

Equations (17), (18), and (19) give the significant properties of the 'outer profile', which must be joined to an 'inner profile' at a distance y_j from the wall. The 'inner profile' is assumed to extend over only a small part of the total boundary layer thickness, and this requires that the pressure rise $(p - p_m)$ be small. In this case ψ_j is small, and in the range of interest the Blasius profile is almost linear.

$$u_f(x, \psi) \approx \sqrt{\frac{2\tau_f}{\mu}\psi}$$

$$\left(\frac{\partial u_f}{\partial y} \right)_{x,\psi} \approx \frac{\tau_f}{\mu}$$

$$\left(\frac{\partial^2 u_f}{\partial y^2} \right)_{x,\psi} \approx 0$$

where $\tau_f = 0.33206 \frac{\mu \overline{U}_m}{x} \sqrt{Re_x}$ is the Blasius skin friction.

With these approximations the 'outer profile' at the junction becomes:

$$\frac{1}{2} u_{out,j}^2(x, \psi) = \frac{\tau_f}{\mu}\psi - \frac{p - p_m}{\rho}$$

$$\left(\frac{\partial u_{out,j}}{\partial y} \right)_{x,\psi} = \frac{\tau_f}{\mu}$$

$$\left(\frac{\partial^2 u_{out,j}}{\partial y^2} \right)_{x,\psi} = 0$$

In the 'inner layer' the fluid inertial forces are small and can be neglected. The pressure force is balanced by the gradient of the shear force, and the 'inner profile' has the form:

$$\mu u_{in} = \tau_w y + \frac{1}{2}p'y^2 + B(x)y^3$$

which satisfies the boundary condition at the wall, $\left(\frac{\partial^2 u_{in}}{\partial y^2} \right)_w = \frac{1}{\mu}\frac{dp}{dx}$.

21

Now we consider an unsteady flow with free steam velocity : $U(x,t) = \overline{U}(x) + \tilde{U}(x,t) = \overline{U}(x) + \hat{U}(x)cos(\omega t)$, which has the properties : $\overline{U}' = \hat{U}' = 0$ from $x = 0$ to $x = x_m$, and $\overline{U}', \hat{U}' < 0$ downstream of $x = x_m$. We have shown that if the unsteady part of the free stream velocity, oscillates with a high reduced frequency, the occurence of unsteady separation can be identified by focussing attention primarily on the behaviour of the 'Prandtl' part of the flow as the overall boundary layer develops along the wall.

The steady part of the Prandtl layer is [4]:

$$\overline{u}_p(x,y) = u_b(x, y + h(x)) \tag{20}$$

where $h(x)$ is chosen so as to satisfy the boundary condition at the wall:

$$\overline{u}_p(x,0) = u_b(x, h(x)) = -\frac{3\mu}{8\omega}\hat{U}\hat{U}'$$

By expanding $u_b(x, h(x))$ in Taylor series we obtain:

$$h(x) = \frac{-\tau_w + \sqrt{\tau_w^2 - \frac{3\mu}{4\omega}\overline{p}'\hat{U}\hat{U}'}}{\overline{p}'}$$

Since $h(x) > 0$, the mean Prandtl velocity profile has a smaller shape parameter than the 'basic' flow (Figure 1); therefore, the mean position of separation is displaced downstream, a prediction which agrees with experimental findings [7].

According to (20), the 'inner profile' satisfies the relations:

$$\mu\psi_{in} = \frac{1}{2}\tau_w(y+h)^2 + \frac{1}{6}\overline{p}'(y+h)^3 + \frac{1}{4}B(x)(y+h)^4 - \frac{1}{2}\tau_w h^2 - \frac{1}{6}\overline{p}'h^3 - \frac{1}{4}B(x)h^4$$

$$\mu u_{in} = \tau_w(y+h) + \frac{1}{2}\overline{p}'(y+h)^2 + B(x)(y+h)^3$$

It must be patched to an 'outer profile', which is linear at the junction, as in the steady case. The difference is that the joining occurs now at a larger value of y_j. Near the junction, the 'outer profile' has the following form:

$$u_f(x, \psi) \approx \sqrt{\frac{2\tau_f}{\mu}\psi}$$

$$\left(\frac{\partial u_f}{\partial y}\right)_{x,\psi} \approx \frac{\tau_f}{\mu}$$

$$\left(\frac{\partial^2 u_f}{\partial y^2}\right)_{x,\psi} \approx 0$$

The joining conditions are the requirement for continuity in ψ, u, $\frac{\partial u}{\partial y}$, $\frac{\partial^2 u}{\partial y^2}$:

$$\mu\psi_j = \frac{1}{2}\tau_w(y_j+h)^2 + \frac{1}{6}\overline{p}'(y_j+h)^3 + \frac{1}{4}B(x)(y_j+h)^4 - \frac{1}{2}\tau_w h^2 - \frac{1}{6}\overline{p}'h^3 - \frac{1}{4}B(x)h^4$$

(21)

$$\mu u_j = \tau_w(y_j+h) + \frac{1}{2}\overline{p}'(y_j+h)^2 + B(x)(y_j+h)^3 \qquad (22)$$

$$\tau_f = \tau_w + \overline{p}'(y_j+h) + 3B(x)(y_j+h)^2 \qquad (23)$$

$$0 = \overline{p}' + 6B(x)(y_j+h) \qquad (24)$$

$$\frac{1}{2}u_j^2 = \frac{\tau_f}{\mu}\psi_j - \frac{\overline{p}-\overline{p}_m}{\rho} \qquad (25)$$

If we eliminate successively a, y_j, ψ_j, and u_j from the above system of equations we get:

$$\frac{\overline{p}-\overline{p}_m}{\rho}\mu^2\frac{(\overline{p}')^2}{\tau_f^4} = \frac{1}{9}(1-\frac{\tau_w}{\tau_f})^3(1+2\frac{\tau_w}{\tau_f}) - \frac{1}{2}\frac{\tau_w}{\tau_f}A^2 - \frac{1}{6}A^3 + \frac{1}{48}\frac{\tau_f}{\tau_f-\tau_w}A^4 \quad (26)$$

where :

$x_0(t)$: location of unsteady separation point

$\overline{p} = \overline{p}(x_0(t)), \overline{p}' = \overline{p}'(x_0(t))$: mean pressure and mean pressure gradient at the position of separation

$$A = A(\omega, Re) \equiv -\frac{\tau_m}{\tau_f} + \sqrt{(\frac{\tau_m}{\tau_f})^2 - \frac{3\mu}{4\omega\tau_f^3}\overline{p}'\hat{U}\hat{U}'}$$

τ_w : wall shear of the 'basic flow' at $x_0(t)$

$\overline{p}_m, \overline{U}_m$: mean pressure, mean velocity at the suction peak

$\tau_f = 0.33206\frac{\mu\overline{U}_m}{x_0(t)}\sqrt{Re_{x_0(t)}}$: 'Blasius' shear

$\tilde{U}(x,t) = \hat{U}(x)cos(\omega t)$: unsteady component of external flow

If the flow is steady, the above equation reduces to $c_p(x\frac{dc_x}{dx})^2 = 0.0108(1 - \frac{\tau_m}{\tau_f})^2(1 + 2\frac{\tau_m}{\tau_f})$, which is the relation for the variation of skin friction of Curle and Davies [1], Eq. (6.77).

Figure 2 depicts the evolution of the mean 'Prandtl velocity' along with the trajectory of the 'centre of separation'.

The unsteady component of the 'Prandtl velocity' is:

$$\tilde{u}_{p,2} = \frac{sin(\omega t)}{\omega}\{ \frac{\partial}{\partial x}[\tilde{U}(\overline{U} - u_b)] + y_p\frac{\partial u_b}{\partial y_p}\frac{\partial \tilde{U}}{\partial x} \} =$$

$$= \frac{sin(\omega t)}{\omega\mu} [\mu(\hat{U}\overline{U})' - \hat{U}\tau_w'y_0 + \frac{1}{2}(\hat{U}'\overline{p}' - \hat{U}\overline{p}'')y_0^2 + (2\hat{U}'B - \hat{U}B')y_0^3]$$

where $B = -\frac{(\overline{p}')^2}{12(\tau_f - \tau_w)}$

Now, by using t' above expressions for the mean and the unsteady part of the 'Prandtl velocity', we derive from the general conditions for unsteady separation the remaining two equations of our practical separation criterion.

The first condition, $\frac{\partial u_n}{\partial v_p} = 0$, in dimensional form is:

$$0 = [\tau_w + \overline{p}'(y_0 + h) + 3B(y_0 + h)^2] +$$
$$+\frac{sin(\omega t)}{\omega} [-\hat{U}\tau_w' + (\hat{U}'\overline{p}' - \hat{U}\overline{p}'')y_0 + 3(2\hat{U}'B - \hat{U}B')y_0^2] \quad (27)$$

24

The second condition, $u_0(y_0, t) + \tilde{U}_0 - \frac{dx_0}{dt} = 0$, yields in dimensional variables:

$$\frac{dx_0}{dt} - \hat{U}cos(\omega t) =$$
$$= \frac{(y_0 + h)}{\mu} \left[\tau_w + \frac{\overline{p}'}{2}(y_0 + h) + B(y_0 + h)^2 \right] + \qquad (23)$$
$$+ \frac{sin(\omega t)}{\omega\mu} \left[\mu(\hat{U}\overline{U})' - \hat{U}\tau_w'y_0 + \frac{1}{2}(\hat{U}'\overline{p}' - \hat{U}\overline{p}'')y_0^2 + (2\hat{U}'B - \hat{U}B')y_0^3 \right]$$

Boundary conditions:

$$x_0(t) = x_0(t + \frac{2\pi}{\omega})$$
$$y_0(t) = y_0(t + \frac{2\pi}{\omega})$$
$$\tau_w(t) = \tau_w(t + \frac{2\pi}{\omega}) \qquad (29)$$

In the absence of unsteadiness (26), (27), and (28) reduce to the steady Stratford's criterion. Indeed, (28) becomes $u = 0$, with solution $y_0 = 0$, (27) becomes $\frac{\partial u}{\partial y} = 0$, or $\tau_w = 0$, and (26) yields $\frac{\overline{p}-\overline{p}_m}{\rho}\mu^2\frac{\overline{p}'}{\tau_f^4} = \frac{1}{9}$, which, upon differentiation with respect to x, and use of the expression $\tau_f = 0.33206\frac{\mu\overline{U}_m}{x_0}\sqrt{Re_{x_0}}$, yields the relation:

$$c_p \left(x\frac{dc_p}{dx} \right)^2 = 0.0108$$

which is the initial form of the Stratford relation [22]. However, Curle and Skan [2] have shown that the value 0.0104 for the constant gives results that agree better with all the known accurate computations for flow with separation.

The system of equations (26), (27), and (28), subject to the boundary conditions (29), are solved by a Newton-Raphson method. Complete results for the cases of pulsating flow over a circular arc, and past the Howarth ellipse at an angle of attack, will be available early in January, and will be compared to experimental data [7], [12].

5 Next steps

We plan to use our method for determining the location and motion of the blade separation points in our calculations of unsteady blade-wake interaction. The importance of describing the influence of the unsteadiness on the the boundary layer behaviour by means of a number of key flow parameters emerges at this stage. Our method, combined with new efficient techniques for describing the coupling between the wake and the approaching the blade flow [13], [9], enables us to perform a first-of-a-kind analysis of the interaction between the unsteady separated flow over blades in cascade and their wakes.

In the 2-D case, we will be able to determine the 'natural' frequency, or Strouhal number, of cascade vortex shedding, a task analogous to determining the properties of a Karman vortex street behind a cylinder or a bluff body at lower Reynolds numbers. We will also be able to investigate the effects of blade shape, incidence, and spacing, mean cascade turning, pressure use, mean flow Mach number, and other key cascade parameters on the natural oscillations. Study of the trends will lead to useful comparisons

with available experimental results [3], [5].

In the 3-D case, the information obtained in the above rapid interactive calculations is vital to the analysis of the spanwise variations in the actual vortical structure. For example, variations along the blade span of relative Mach number, blade incidence, and loading are of essential importance to a realistic determination of the wake 3-D patterns. Without a rapid parametric treatment of boundary layer separation, such a computer-aided analytic study of unsteady wake formation behind a cascade might well be prohibitively difficult or lengthy. At present, a pure CFD approach is also unlikely to be successful because of resolution problems at realistic Reynolds numbers.

The work of developing a program which will implement our method in the case of a 2-D compressor cascade is proceeding well. The computational treatment of the problem should be possible by the end of spring 1990 or in the early summer. As the proceedure is refined, we expect to be able to thoroughly investigate the predicted trends and to develop checks with experiment and other computational work.

A   Appendix

The splitting of the solution is a two-step proceedure.

First step:

Separate the forcing terms :

$$\frac{\partial u_p}{\partial t} - \nu \frac{\partial^2 u_p}{\partial y^2} + (u_p \frac{\partial}{\partial x} + v_p \frac{\partial}{\partial y}) u_p = \overline{U} \frac{\partial \overline{U}}{\partial x} + \frac{\partial \overline{U} \tilde{U}}{\partial x}$$

$$\frac{\partial u_s}{\partial t} - \nu\frac{\partial^2 u_s}{\partial y^2} + (u_s\frac{\partial}{\partial x} + v_s\frac{\partial}{\partial y})u_s + (u_s\frac{\partial}{\partial x} + v_s\frac{\partial}{\partial y})u_p +$$

$$+(u_p\frac{\partial}{\partial x} + v_p\frac{\partial}{\partial y})u_s = \frac{\partial\tilde{U}}{\partial t} + \tilde{U}\frac{\partial\tilde{U}}{\partial x}$$

Second step :

In order to cancel out the term $\frac{\partial\overline{U}\tilde{U}}{\partial x}$ and thus satisfy the boundary condition, $u_p = \overline{U}(x)$ at $y = \infty$, add to E_p and subtract from E_s the terms:

$$(u_p\frac{\partial}{\partial x} + v_p\frac{\partial}{\partial y})\tilde{U} + (\tilde{U}\frac{\partial}{\partial x} + V_s\frac{\partial}{\partial y})u_p$$

E_p becomes:

$$\frac{\partial u_p}{\partial t} - \nu\frac{\partial^2 u_p}{\partial y^2} + (u_p\frac{\partial}{\partial x} + v_p\frac{\partial}{\partial y})u_p + (u_p\frac{\partial}{\partial x} + v_p\frac{\partial}{\partial y})\tilde{U}$$

$$+(\tilde{U}\frac{\partial}{\partial x} + V_s\frac{\partial}{\partial y})u_p = \overline{U}\frac{\partial\overline{U}}{\partial x} + \frac{\partial\overline{U}\tilde{U}}{\partial x}$$

and E_s becomes:

$$\frac{\partial u_s}{\partial t} - \nu\frac{\partial^2 u_s}{\partial y^2} + (u_s\frac{\partial}{\partial x} + v_s\frac{\partial}{\partial y})u_s + [(u_s - \tilde{U})\frac{\partial}{\partial x} + (v_s - V_s)\frac{\partial}{\partial y}]u_p$$

$$+(u_p\frac{\partial}{\partial x} + v_p\frac{\partial}{\partial y})(u_s - \tilde{U}) = \frac{\partial\tilde{U}}{\partial t} + \tilde{U}\frac{\partial\tilde{U}}{\partial x}$$

It turns out that the boundary condition $u_s = \tilde{U}(x,t)$ is identically satisfied at $y = \infty$.

Note : E_p contains no (u_s, v_s), only $(\tilde{U}, V_s)$.

28

B Appendix

E_s can be rewritten as :

$$\frac{\partial u_s}{\partial t} - \frac{\partial \tilde{U}}{\partial t} - \frac{\partial^2 u_s}{\partial y_s^2} + \frac{1}{\lambda^2} \left\{ \left[(u_s + u_p)\frac{\partial}{\partial x} + (v_s + \lambda v_p)\frac{\partial}{\partial y_s} \right] (u_s + u_p) \right.$$

$$\left. -(\tilde{U} + u_p)\frac{\partial}{\partial x}(\tilde{U} + u_p) - (\wedge v_p + V_s)\frac{\partial u_p}{\partial y_s} \right\} = 0$$

By substituting in E_s

$$u_p = \sum_{n=0}^{\infty} \frac{1}{\lambda^n} \frac{y_s^n}{n!} \frac{\partial^n u_p}{\partial y_p^n}(x,0) \equiv u_p(x,0) + S_1$$

$$v_p = \sum_{n=0}^{\infty} \frac{1}{\lambda^n} \frac{y_s^n}{n!} \frac{\partial^n v_p}{\partial y_p^n}(x,0) \equiv \frac{y_s}{\lambda}\frac{\partial v_p}{\partial y_p}(x,0) + S_2$$

we get:

$$\frac{\partial u_s}{\partial t} - \frac{\partial \tilde{U}}{\partial t} - \frac{\partial^2 u_s}{\partial y_s^2} +$$

$$+\frac{1}{\lambda^2} \left\{ \left[(u_s + u_p(x,0))\frac{\partial}{\partial x} + (v_s + \lambda\frac{y_s}{\lambda}\frac{\partial v_p}{\partial y_p}(x,0))\frac{\partial}{\partial y_s} \right] (u_s + u_p(x,0)) - \right.$$

$$-(\tilde{U} + u_p(x,0))\frac{\partial}{\partial x}(\tilde{U} + u_p(x,0)) + (S_1\frac{\partial}{\partial x} + \lambda S_2\frac{\partial}{\partial y_s})(u_s + u_p(x,0)) +$$

$$+ \left[(u_s + u_p(x,0))\frac{\partial}{\partial x} + v_s\frac{\partial}{\partial y_s} \right] S_1 + (S_1\frac{\partial}{\partial x} + \lambda S_2\frac{\partial}{\partial y_s})S_1 - S_1\frac{\partial}{\partial x}(\tilde{U} + u_p(x,0)) -$$

$$\left. -(\tilde{U} + u_p(x,0))\frac{\partial S_1}{\partial x} - S_1\frac{\partial S_1}{\partial x} - (\lambda S_2 + V_s)\frac{\partial S_1}{\partial y_s} \right\} = 0 \Rightarrow$$

$$\frac{\partial u_s}{\partial t} - \frac{\partial \tilde{U}}{\partial t} - \frac{\partial^2 u_s}{\partial y_s^2} +$$

$$+\frac{1}{\lambda^2} \left\{ \left[(u_s + u_p(x,0))\frac{\partial}{\partial x} + (v_s + \lambda\frac{y_s}{\lambda}\frac{\partial v_p}{\partial y_p}(0))\frac{\partial}{\partial y_s} \right] (u_s + u_p(x,0)) - \right.$$

$$-(\tilde{U} + u_p(x,0))\frac{\partial}{\partial x}(\tilde{U} + u_p(x,0)) + (S_1\frac{\partial}{\partial x} + \lambda S_2\frac{\partial}{\partial y_s})u_s + S_1\frac{\partial u_p(x,0)}{\partial x} +$$

$$+ [\ (u_s + u_p(x,0))\frac{\partial}{\partial x} + v_s\frac{\partial}{\partial y_s}\ ]\ S_1 + (S_1\frac{\partial}{\partial x} + \lambda S_2\frac{\partial}{\partial y_s})S_1 - S_1\frac{\partial}{\partial x}(\tilde{U} + u_p(x,0)) -$$

$$-(\tilde{U} + u_p(x,0))\frac{\partial S_1}{\partial x} - S_1\frac{\partial S_1}{\partial x} - (\lambda S_2 + V_s)\frac{\partial S_2}{\partial y_s}\ \} = 0 \Rightarrow$$

$$\frac{\partial u_s}{\partial t} - \frac{\partial \tilde{U}}{\partial t} - \frac{\partial^2 u_s}{\partial y_s^2} +$$

$$+ \frac{1}{\lambda^2}\ \{\ [\ (u_s + u_p(x,0))\frac{\partial}{\partial x} + (v_s + \lambda\frac{y_s}{\lambda}\frac{\partial v_p}{\partial y_p}(0))\frac{\partial}{\partial y_s}\ ]\ (u_s + u_p(x,0)) -$$

$$-(\tilde{U} + u_p(x,0))\frac{\partial}{\partial x}(\tilde{U} + u_p(x,0)) + (S_1\frac{\partial}{\partial x} + \lambda S_2\frac{\partial}{\partial y_s})(u_s - \tilde{U}) +$$

$$+ [\ (u_s - \tilde{U})\frac{\partial}{\partial x} + (v_s - V_s)\frac{\partial}{\partial y_s}\ ]\ S_1\ \} = 0 \Rightarrow$$

$$\frac{\partial u_s}{\partial t} - \frac{\partial \tilde{U}}{\partial t} - \frac{\partial^2 u_s}{\partial y_s^2} + \frac{1}{\lambda^2}\ \{\ -(\tilde{U} + u_p(x,0))\frac{\partial(\tilde{U} + u_p(x,0))}{\partial x} +$$

$$+ [\ (u_s + u_p(x,0))\frac{\partial}{\partial x} + (v_s + y_s\frac{\partial v_p}{\partial y_p}(x,0)\frac{\partial}{\partial y_s}\ ]\ (u_s + u_p(x,0))\ \} +$$

$$+ \sum_{n=1}^{\infty}\frac{1}{\lambda^{n+2}}\ \{\ [\ (\frac{y_s^n}{n!}\frac{\partial^n u_p}{\partial y_p^n}(x,0)\frac{\partial}{\partial x} + \frac{y_s^{n+1}}{(n+1)!}\frac{\partial^{n+1} v_p}{\partial y_p^{n+1}}(x,0)\frac{\partial}{\partial y_s}\ ]\ (u_s - \tilde{U}) +$$

$$+ [\ [(u_s - \tilde{U})\frac{\partial}{\partial x} + (v_s - V_s)\frac{\partial}{\partial y_s}\ ]\ \frac{y_s^n}{n!}\frac{\partial^n u_p}{\partial y_p^n}(x,0)\ \} = 0$$

References

[1] Curle, N. and Davies, H. J., 1969, *Modern Fluid Mechanics*, Van Nostrand, 217-222.

[2] Curle, N. and Skan, S. W., 1957, Approximate methods for predicting separation properties of laminar boundary layers, *Aeronaut. Quart. Vol. 8*, 278-289.

[3] Gertz, J. B., 1986, Unsteady design-point phenomena in transonic compressors, *GTL Report No. 188*, MIT.

[4] Gibson, W. E., 1957, Unsteady laminar boundary layers, *MIT Ph. D. Thesis*, Department of Mathematics.

[5] Gioulekas, A., 1990, *MIT Ph. D. Thesis* (in preparation).

[6] Howarth, L., 1935, The theoretical prediction of the lift coefficient for a thin elliptic cylinder, *Proc. Royal Society A, Vol. 149*, 558-586.

[7] Koromilas, C. A., and Telionis, D. P., 1980, Unsteady laminar separation : an experimental study, *J. Fluid Mech.*, Vol. 97, part 2, 347-384.

[8] Landau, L. D., and Lifshitz, E. M., 1959, *Fluid Mechanics*, 2nd edition, Pergamon Press, 163-167.

[9] Lam C.-M. G., 1989, Non-linear unsteady vortex wake evolution behind Joukowski airfoils including explicit free panel method, *MIT M. Sc. Thesis*, Department of Aeronautics and Astronautics.

[10] Lin, C. C., 1956, Motion in the boundary layer with a rapidly oscillating external flow, *9th International Congress of Applied Mechanics*, University of Brussels.

[11] Mathioulakis, D. S. and Telionis, D. P., 1987, Velocity and vorticity distributions in periodic separating laminar flow, *J. Fluid Mech.*, Vol. 184, 303-333.

[12] Mathioulakis, D. S. and Telionis, D. P., 1989, Pulsating flow over an ellipse at an angle of attack, *J. Fluid Mech.*, Vol. 201, 99-121.

[13] McCune, J. E., Scott, M. T. and Lam, C-M. G., 1989, Nonlinear aerodynamics of two-dimensional airfoils in severe maneuver, *AIAA J.*, (to be published).

[14] Messiter, A. F., 1983, Boundary-layer interaction theory, *J. Appl. Mech.*, 50, 1104-1113.

[15] Mezaris, T. B., Barbi, C., Jones, G. S. and Telionis, D. P., 1987, Separation and wake of pulsating laminar flow, *Phil. Trans. R. Soc. Lond.*, A 322, 493-523.

[16] Moore, F. K., 1955, *Lift hysteresis at stall as an unsteady boudary layer phenomenon*, *NACA TN-3571*.

[17] Moore, F. K., 1958, On the separation of the unsteady boundary layer, *Boundary Layer Research*, (ed. H. Görtler), Springer, 296-311.

[18] Rott, N., 1964, in *Theory of Laminar Flows*, (ed. Moore, F. K.), Princeton University Press, 395-397.

[19] Sears, W. R., 1976, Unsteady motion of airfoils with boundary layer separation, *AIAA J.*, Vol.14, No. 2, 210- 220.

[20] Sears, W. R. and Telionis, D. P., 1975, Boundary layer separation in unsteady flow, *SIAM J. Appl. Maths* , 28, 215-235.

[21] Shen, S.-F., 1968, Unsteady separation according to the boundary layer equation, *Adv. in Appl. Mech.*, Vol 18, 117-220.

[22] Stratford, B. S., 1954, Flow in the laminar boundary layer near separation, *Rep. and Mem. Aero. Res. Cou. Lond.*, No. 3002.

[23] Stratford, B. S., 1957, The prediction of separation of the turbulent boundary layer, *J. Fluid Mech.*, Vol.15, 1-17.

[24] Telionis, D. P., 1981, *Unsteady Viscous Flows* , Springer, Chs 5 and 7.

3. AIR FORCE RESEARCH IN AERO PROPULSION TECHNOLOGY (AFRAPT) PROGRAM

The research at MIT is strongly tied in with the AFRAPT Program. At present, there are 11 students working in the Gas Turbine Laboratory under this training program. The students, advisors, and research projects are:

Trainee: Steven Allmaras (finished Ph.D. thesis, 1/89)
Advisor: Prof. M.B. Giles
Project: Computation Techniques for Turbomachines (Unsteady Flows in Turbomachinery) (AFOSR)

Trainee: Scott Barton
Advisor: Prof. A.H. Epstein
Project: Distortion Amelioration in Centrifugal Pumps (ONR)

Trainee: Jonathan Elliott
Advisor: Prof. E.M. Greitzer/Dr. C.S. Tan
Project: Computation Procedures for Convoluted Trailing Edge Flows (NAVAIR)

Trainee: Victor Filipenco
Advisor: Prof. E.M. Greitzer
Project: Unsteady Flows in Diffusers for High Performance Centrifugal Compressors (GE)

Trainee: Daniel Gysling (finished M.S. Thesis, 9/89)
Advisor: Prof. J. Dugundji/Prof. E.M. Greitzer
Project: Active Control of Aeromechanical Systems (AFOSR)

Trainee: Dana Lindquist
Advisor: Prof. M.B. Giles
Project: Development of Adaptive Procedures for Turbomachinery Flow Computations

Trainee: Douglas Loose (finished M.S. Thesis, 10/89)
Advisor: Prof. M. Martinez-Sanchez
Project: Tip Clearance Excited Turbomachine Rotordynamic Instabilities (NASA MSFC)

Trainee: Theodore Manning
Advisor: Prof. E.M. Greitzer/Dr. C.S. Tan
Project: Vortical Structures from Convoluted Trailing Edges (NAVAIR)

Trainee: Knox Millsaps
Advisor: Prof. M. Martinez-Sanchez
Project: Rotor Dynamic Instability Due to Alford Forces (NASA MSFC)

Trainee: George Pappas
Advisor: Prof. A.H. Epstein
Project: Radial Temperature Distribution Effects on Turbine Rotor Heat Transfer

Trainee: Judith Pinsley (finished M.S. Thesis, 11/88)
Advisor: Prof. E.M. Greitzer
Project: Smart Engines - Active Stabilization of Aeromechanical Systems (ARO)

Trainee: Robert Plumley (finished M.S. Thesis, 11/89)
Advisor: Prof. E.M. Greitzer/Dr. C.S. Tan
Project: Unsteady Phenomena and Flow Instabilities in Multistage Turbomachines (AFOSR)

Trainee: Earl Renaud
Advisor: Dr. C.S. Tan
Project: Three-Dimensional Vortical Flows in Axial Turbines (NASA LeRC)

Trainee: Peter Silkowski
Advisor: Prof. E.M. Greitzer/Dr. C.S. Tan/Prof. N.A. Cumpsty (Cambridge University)
Project: Unsteady Phenomena and Flow Instabilities in Multistage Turbomachines (AFOSR)

Trainee: William Steptoe (finished M.S. Thesis, 10/89)
Advisor: Prof. A.H. Epstein
Project: Influence of Radial Temperature Distribution on Turbine Heat Transfer
            Aerodynamics (RRI)

Trainee: Eric Strang
Advisor: Dr. C.S. Tan/Prof. E.M. Greitzer
Project: Inlet Distortion Effects in Multistage Turbomachines (NASA)

A more detailed description of the work carried out on these projects is given in Refs. 3.1

and 3.2.

References

3.1 Greitzer, E.M., Dugundji, J., Epstein, A.H., Giles, M.B., Martinez-Sanchez, M., Tan,
     C.S., "Air Force Research in Aero Propulsion Technology," Annual Technical Report on
     Grant AFOSR-85-0288, September 1988.

3.2 Greitzer, E.M., Dugundji, J., Epstein, A.H., Giles, M.B., Martinez-Sanchez, M., Tan,
     C.S., "Air Force Research in Aero Propulsion Technology," Annual Technical Report on
     Grant AFOSR-85-0288, September 1989.

4. PUBLICATIONS AND PRESENTATIONS

Epstein, A.H., Greitzer, E.M., Tan, C.S., Giles, M.B.,"Advanced Three-Dimensional and Time Varying Turbomachinery Problems," Short Course presented at Concepts, ETI, November 1988.

Giles, M.B., "Developments in the Calculation of Unsteady Turbomachinery Flow," invited paper at ICFD conference held at Oxford University, March 1988 (CFDL-TR-88-11).

Giles, M.B., "Non-Reflecting Boundary Conditions for the Euler Equations," seminar presented at Princeton University, November 1988.

Giles, M.B., "Non-Reflecting Boundary Conditions for the Euler Equations," CFDL Report TR-88-1.

Giles, M.B., "UNSFLO: A Numerical Method for Unsteady Inviscid Flow in Turbomachinery," GTL Report No. 195, October 1988.

Giles, M.B., Tan, C.S., "An Introduction to Computational Fluid Dynamics," 2-day AIAA short course, July 1988 and July 1989.

Greitzer, E.M., "Advances in Turbomachinery Stability," seminar presented at Concepts ETI Seventh Anniversary Symposium on State-of-the-Art in Turbomachinery, December 1987.

Greitzer, E.M., "Effects of Unsteadiness on Multistage Compressor Instability," presentation at General Electric Aircraft Engine Group, March 1988.

Greitzer, E.M., "Unsteady Flows in Turbomachines: Recent Advances and Opportunities for Control," seminar presented at United Technologies Research Center, April 1988; also presented at NASA Lewis Research Center, August 1988; also, invited presentation at US-Korea Joint Fluids Engineering Seminar, September 1989.

Greitzer, E.M., 3-lecture series in AGARD Seminar on "Gas Turbine Engine Instability," Cranfield Institute of Technology, Cranfield, England, October 1989.

Kotidis , P.A., Epstein, A.H., "Unsteady Radial Transport in a Transonic Compressor Stage," to be presented at 1990 ASME Gas Turbine Conference, Brussels, June 1990.

Lee, N.K.W., "Effects of Compressor Endwall Suction and Blowing on Stability Enhancement," MIT Gas Turbine Laboratory Report #192, January 1988; also presentation made at Allison Gas Turbine Division, February 1988, on this topic by E.M. Greitzer. Paper presented at 1989 ASME Gas Turbine Conference, and accepted for publication in *ASME J. Turbomachinery.*

5. PROGRAM PERSONNEL

Principal Investigator:

Edward M. Greitzer
H.N. Slater Professor of Aeronautics and Astronautics
Director, Gas Turbine Laboratory

Co-Investigators:

Alan H. Epstein
Associate Professor of Aeronautics and Astronautics
Associate Director, Gas Turbine Laboratory

Michael B. Giles
Assistant Professor of Aeronautics and Astronautics

James E. McCune
Professor of Aeronautics and Astronautics

Choon S. Tan
Principal Research Engineer

Graduate Research Assistants:

9/83 - 11/88	Petros Kotidis**
9/86 - 1/89	Steve Allmaras** (AFRAPT student)
9/87 - 10/89	Rob Plumley* (AFRAPT student)
6/88 - 6/89	Hewett Benson*
6/88 - present	Alexandros Gioulekas
6/88 - 9/89	Gordon Lam*

* M.S. Degree Completed
** Ph.D. Degree Completed

6. INTERACTIONS

As we have noted previously and as may be inferred from the presentations that were given, there are considerable interactions between Gas Turbine Laboratory personnel and industry and government. This occurs in several forms. One of these is support of research in the laboratory from industry and from government laboratories. This creates a direct link with those persons who are actively working in similar areas in other establishments, and aids considerably in helping transfer technology.

A second type of interaction is through presentations and discussions with industry or government agencies. These were listed in Section 4 covering the contract period. It should be noted that only those which involved discussion of AFOSR supported projects are given.

Finally, the Gas Turbine Laboratory has an active seminar program which brings speakers from industry and government. Listed below are the speakers for the period 10/19/88 to 10/18/89; those in the previous year were given in Ref. [1].

Dr. R.A. Delaney, Allison Gas Turbine Division
"Computations of Turbine Vane-Blade Interaction"

Mr. L.A. Gross, NASA MSFC
"Past, Present, and Future Problems in Space Propulsion Systems"

Dr. L.H. Smith, General Electric Aircraft Engine Business Group
"Unducted Fan Aerodynamic Design"

Mr. D.N. Herr, American Airlines
"Airline Maintenance Requirements and Programs for the GE CFC Family of Engines"

Dr. D.G. Holmes, General Electric Corporate Research and Development Center
"Solving the Euler and Navier-Stokes Equations on Unstructured Quadrilateral and Triangular Meshes"

Dr. R.W. Paterson, United Technologies Research Center
"Gas Turbine Applications of Streamwise Vorticity Flow Structures"

7. DISCOVERIES, INVENTIONS, AND SCIENTIFIC APPLICATIONS

During the present contract period, there have been no inventions.

8. OTHER RELATED ACCOMPLISHMENTS

In addition to the publications that have resulted directly from the research, there are also two survey lectures that deal with the general area of unsteady flows in turbomachines. The material in these lectures relates closely to the field of research, and reflects much of the work that has been funded by AFOSR, not only during the present contract but over a longer time period. As such, we feel it is appropriate to include these two lectures as Appendices to the main text of the Progress Report.

The lectures are entitled "Numerical Methods for Unsteady Turbomachinery Flow," by M.B. Giles, which appears as Appendix A, and "Unsteady Flow in Turbomachinery: Basic Phenomena and Practical Aspects," by E.M. Greitzer and C.S. Tan, which appears as Appendix B.

9. CONCLUDING REMARKS

The topic of unsteady flows in turbomachines is one that is of high intellectual and technological interest. With the availability of modern data processing and flow computation procedures, phenomena that were formerly just guessed at are becoming amenable to quantitative scrutiny and, as discussed by Wennerstrom [9.1], there is real potential for increased performance through including these phenomena in the design process in a rational way. Although the problems are complex, the aim here is a clear understanding of, and physical insight into, this general class of flows, rather than just case by case *ad hoc* examination of results. We believe that this can only occur if there is strong coupling between experiment, computation, and theory. The Multi-Investigator program and the interaction it fosters between different investigators is extremely useful in promoting just this type of interaction.

Reference

9.1   Wennerstrom, A.J., "Low Aspect Ratio Axial Flow Compressors: Why and What It Means," to appear in *ASME J. Turbomachinery*, Vol. 112, 1990.

APPENDIX A

Numerical Methods For
Unsteady Turbomachinery Flow

by

Michael Giles

CFDL-TR-89-3   April 1989

Chapter 1

Introduction

1.1 Objectives of Lectures

The intent of these lectures is to present an overview of the full diversity of approaches to calculating the unsteady flow in turbomachinery. The different approaches vary greatly in the accuracy of the physical model used to represent the very complicated fluid dynamics that occurs in a turbomachine. Therefore, one objective is to discuss what it is that one is interested in determining when performing a numerical calculation or simulation, and examine the extent to which relatively simple models can be used. The emphasis here will be on the formulation of the mathematical models, the assumptions and approximations which they involve, and the circumstances under which these remain valid.

As a direct consequence of the differing levels of accuracy of the physical models, there is an accompanying variation in the computational time required to numerically solve the mathematical equations produced by the physical model. This variation spans several orders of magnitude, from a few seconds on a MicroVax II to several days on a CRAY-XMP. In practical, industrial applications of unsteady flow calculations, there is a very definite need to keep numerical solutions as cheap and as quick as possible, while still providing solutions which are sufficiently accurate that they are useful. Thus, a second objective, very closely related to the first, is to give as much insight as possible into the trade-offs in time and accuracy between the different methods. This is an issue that it is not generally addressed in the research literature, and so it will necessarily be a rather personal viewpoint.

The third objective of these lectures is to discuss in some detail the key features of the different numerical methods. Unlike steady solution methods, the emphasis will usually not be on the basic numerical algorithm for solving the partial differential equation. Instead, the emphasis will usually be on the unsteady boundary conditions, both their mathematical formulation and their numerical implementation. In discussing current areas of research, different numerical algorithms being used by different researchers to solve the same mathematical model will be presented, and some of their relative advantages and disadvantages will be discussed. There is insufficient time to be comprehensive in discussing the numerical details of all of the algorithms, but the bibliography gives references to all the major research works in this area, and the reader is urged to read these.
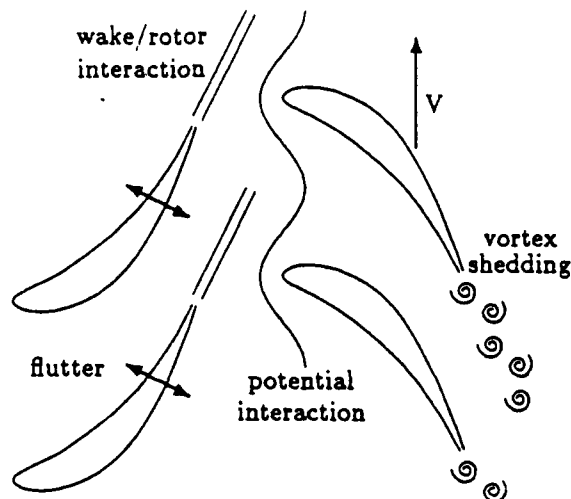
Figure 1.1: Sources of unsteadiness in turbomachinery flow

1.2 Sources of Unsteadiness in Turbomachinery

In this section we will intorduce the various different sources of unsteadiness in a turbomachine, and will discuss their characteristics and their particular features or consequences which are of engineering concern. As shown in Fig. 1.1 there are four principal two-dimensional sources of unsteadiness in a single stage of a turbomachine.

Wake/rotor interaction causes unsteadiness because the stator wakes, which one can assume to be approximately steady in the stator frame of reference, are unsteady in the rotor frame of reference since the rotor is moving through the wakes and chopping them into pieces. This causes unsteady forces on the rotor blades and generates unsteady pressure waves. Although the stator wakes are generated by viscosity, the kinematics of the subsequent interaction with the rotor blades is primarily an inviscid process and so much of the interaction can be modelled by the inviscid equations of motion.

There are two principal engineering concerns with regard to wake/rotor interaction. The first is the forced response of the rotor, the vibration of the rotor blade due to the unsteady loading and moment caused by the interaction [29]. When the gap between the stators and rotors is large, the wake/rotor interaction is the primary contributor to the unsteady forces on the rotor, and these can be of the order of 5% of the steady forces. At this level, the interaction is approximately linear, and so the simplest model which will capture the essential features would be a linear inviscid model which is able to treat both the vorticity and entropy variations in the wake.

The second concern is the effect on heat transfer and losses. Extensive experimental research on wake/rotor interaction in transonic turbines has shown that the passing stator

wakes can cause an intermittent transition in the rotor's boundary layer, causing the heat transfer to alternate between a low, laminar value and a high, turbulent value [13,..,16,6,25]. This greatly increases the mean heat transfer and also the mean overall loss of the turbine rotor [47]. Numerical prediction of this phenomena requires the solution of the unsteady Reynolds-averaged Navier-Stokes equations with a very sophisticated transition model and turbulence model.

A similar phenomenon to wake/rotor interaction is hot streak interaction. The flow leaving the combustor in a gas turbine is not temporally or spatially uniform. Streaks of hot, less dense gas, with the same static and total pressure as the surrounding colder gas, pass through the first stator row and become hot jets of fluid. These are the opposite of wakes in that their velocity is greater than the other, colder fluid. A second-order nonlinear effect [35] causes this fluid to preferentially "migrate" towards the pressure surface of the first rotor row [7,36,44]. This increases the mean temperature of the fluid at the edge of the boundary layer, and so increases the mean heat transfer. This is believed to be the reason for unexpected thermal damage on the pressure surface of the rotor, and is a current topic of interest in both experimental and computational research. Since the nonlinearity is a fundamental part of the problem, linear methods are unsuitable. However, the migration effect is an inviscid phenomenon and so inviscid methods may be suitable to calculate the increase in the mean stagnation temperature at the edge of the boundary layer, from which the increased heat transfer could be deduced.

Potential stator/rotor interaction causes unsteadiness due to the fact that the pressure in the region between the stator and rotor blade rows can be decomposed approximately into a part that is steady and uniform, a part that is non-uniform but steady in the rotor frame (due to the lift on the rotor blades) and a part that is non-uniform but steady in the stator frame (due to the lift on the stator blades). As the rotor blades move, the stator trailing edges experience an unsteady pressure due to the non-uniform part that is locked to the rotors, and the rotor leading edges experience an unsteady pressure due to the non-uniform part that is locked to the stators [14,34]. This is a purely inviscid interaction and the sole engineering concern is the unsteady forces and moments which it causes. When the gap between the stator and rotor is small, and when the stator outflow is supersonic, these unsteady forces can become very large, as much as 20% of the steady forces. In the design of a stage, this is the primary limitation on how the spacing between the stator and rotor, and so fast, accurate methods of predicting the forces are required to avoid serious design problems. There are two approaches to modelling this interaction. The first is an unsteady, inviscid calculation of the stator and rotor blade rows. The second is an unsteady, inviscid calculation of just one of the blade rows, either the stator or the rotor, with the unsteady pressure being specified as a boundary condition. The latter approach is more efficient, but when the spacing between the stator and rotor rows is extremely small, and/or there

are shock waves moving in the region between them, one may not know what to specify as unsteady boundary conditions and so one may have to adopt the first approach.

The first two sources of unsteadiness were both due to the relative motion of the stator and rotor rows. The remaining two sources are not. The viscous flow past a blunt turbine trailing edge results in vortex shedding, very similar to the Karman vortex street shed behind a cylinder. In fact real wakes lie somewhere between the two idealized limits of a Karman vortex street and a turbulent wake with a steady mean velocity profile. It is believed that provided the integrated loss is identical the choice of model does not affect the subsequent interaction with the downstream rotor blade row. However, this is an assumption which needs to be investigated sometime in the future. The importance of vortex shedding lies in the calculation of the average pressure around the blunt trailing edge, which determines the base pressure loss, a significant component of the overall loss. There is also experimental and computational evidence of vortex shedding in compressors [15].

Finally, there can be unsteadiness due to the motion of the stator or rotor blades. The primary concern here is the avoidance of flutter. This is a condition in which a small oscillation of the blade produces an unsteady force and moment on the blade which due to its phase relationship to the motion does work on the blade and so increases the amplitude of the blade's unsteady motion. This can rapidly lead to very large amplitude blade vibrations, and ultimately blade failure. Since the unsteadiness is initially of low amplitude, linear methods are clearly appropriate. Inviscid assumptions are also perfectly acceptable until one is concerned about stall flutter, in which case unsteady separation of the boundary layer becomes very important and a viscous model is necessary.

There are several other sources of unsteadiness which deserve to be mentioned briefly. Shock/boundary layer interaction can cause a boundary layer to separate, and the free shear layer is then unstable. Under the correct conditions the shear layer instability can couple acoustically to an oscillation in the shock position, which in turn drives an oscillation in the separation position. This is known to occur in transonic inlet diffusers, and may also cause unsteadiness in transonic compressors. In bypass fans, the thick pylons can have an associated potential field which extends far upstream ahead of the outlet guide vanes, and cause unsteady forces on the fan. In three dimensions, there is unsteadiness due to rotors interacting with passage vortices and inlet flow distortions, and due to stators interacting with passage and tip vortices. Also, there is the large subject of rotating stall and surge. The direct simulation of these highly unsteady, viscous, three-dimensional, large-scale flows lies well beyond our current capabilities. Instead, a completely different approach to the mathematical modelling of the whole fluid dynamic compression system is required. The state-of-the-art in the analysis of these problems is reviewed by Greitzer in Ref. [24].

Chapter 2

Linear Methods

2.1 Flat Plate Analysis

The flat plate analysis method was developed in the early 1970's. Although various people contributed to its development, the first complete analysis of the subsonic problem, together with a numerical method for the solution of the resulting integral equation, is due to Smith [48]. A unified presentation of the theory for both subsonic and supersonic cases is given by Ni [40].

The analysis considers linear perturbations to a uniform flow (at zero incidence) past a cascade of flat plate airfoils. The airfoils can have an arbitrary stagger and pitch, and the uniform flow can have an arbitrary Mach number although it will be assumed in the discussion below that the flow is axially subsonic. Thus, the principal effects which are neglected in this model are the thickness of real compressor or fan airfoils, and the steady loading on the airfoils.

The two-dimensional Euler equations in the so-called "primitive" form are

$$\frac{\partial U}{\partial t} + A\,\frac{\partial U}{\partial x} + B\,\frac{\partial U}{\partial y} = 0 \tag{2.1}$$

where

$$U = \begin{pmatrix} \bar{\rho} \\ \bar{u} \\ \bar{v} \\ \bar{p} \end{pmatrix},\ A = \begin{pmatrix} u & \rho & 0 & 0 \\ 0 & u & 0 & 1/\rho \\ 0 & 0 & u & 0 \\ 0 & \gamma p & 0 & u \end{pmatrix},\ B = \begin{pmatrix} v & 0 & \rho & 0 \\ 0 & v & 0 & 0 \\ 0 & 0 & v & 1/\rho \\ 0 & 0 & \gamma p & v \end{pmatrix} \tag{2.2}$$

ρ, u, v, p are the density, velocity components and pressure respectively. γ is the constant ratio of specific heats for the gas which is assumed to be ideal. U is the vector of perturbation from the uniform steady flow-field, and A and B are constant matrices based upon the uniform flow variables.

The eigenmodes of this equation are wave-like solutions of the form

$$U(x,y,t) = \exp(ikx + ily - i\omega t)\,\hat{U}. \tag{2.3}$$

Substituting this equation into the governing differential equations yields

$$(-\omega I + kA + lB)\hat{U} = 0. \tag{2.4}$$

This has a non-trivial solution only if the matrix is singular.

$$\det(-\omega I + kA + lB) = 0 \tag{2.5}$$

5

This equation is the dispersion relation, relating the frequency ω to the wavenumbers k, l.

For a particular problem, each (real) frequency component is analyzed separately, since by linearity these components can be added to form the general linear solution. l has a discrete set of real values to satisfy the periodicity constraint. The dispersion equation then gives the axially wavenumber.

$$k = k(\omega, l) \tag{2.6}$$

For each ω, l there are four values of k and four corresponding eigenmodes $\hat{U}$. Assuming axially subsonic flow these have the following features.

- $\hat{U}_1$ is an entropy wave which affects only the density. This wave is convected at the local steady fluid velocity, and so k is always real.

- $\hat{U}_2$ is a vorticity wave which affects only the two velocity components. Like the entropy, it is convected at the local steady fluid velocity.

- $\hat{U}_3$ is a downstream running pressure wave, which affects density, pressure, and both velocity components. If the steady flow is subsonic then k is real only when l is within a finite range. Outside this range k is complex implying that the pressure wave decays exponentially downstream. If the flow is supersonic then the reverse occurs. k is complex for a finite range of values of l, and real otherwise

- $\hat{U}_4$ is an upstream running pressure wave, which again affects density, pressure, and both velocity components. k behaves in a similar manner to the downstream running pressure wave, except then when it is complex the imaginary component has the opposite sign so that the pressure wave decays exponentially upstream.

The next step in the analysis is to perform an actuator disk analysis to calculate the outgoing waves due to a point force normal to an infinitesimal part of every blade. This is shown schematically in Fig. 2.1. The multiple point forces are first decomposed into a Fourier series in y, using the following identity.

$$\sum_n \delta(y - nP) \exp(in\sigma) = \frac{1}{P} \sum_m \exp\left(i(2\pi m + \sigma)\frac{y}{P}\right) \tag{2.7}$$

P is the blade pitch, and σ is the inter-blade phase angle, the phase difference between the unsteady forces on two neighboring blades. Each Fourier mode in y is treated separately in the actuator disk analysis which matches the mass flow and entropy on the two sides of the disk, and changes the momentum according to the distributed forces along the disk. This gives four equations from which the amplitudes of the four outgoing waves are determined. Because of the isentropic matching condition the outgoing entropy wave has zero amplitude, and so the solution is a combination of a vorticity wave and a pressure wave going downstream, and a pressure wave going upstream.

114
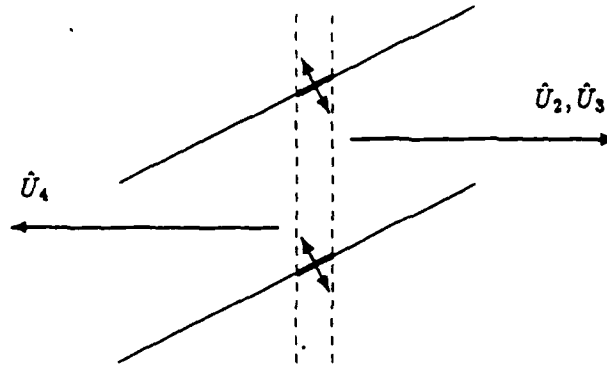
Figure 2.1: Outgoing waves in actuator disk analysis

Summing over the different Fourier modes produces a vector Green's function for the response shown in Fig. 2.1 due to the unit force on the infitesimal blade element. Integrating over the whole blade, using this Green's function, gives the unsteady flow due to distributed unsteady loading on the blade.

$$\hat{U}(x, y, t) = \int_0^c G(x - s\cos\theta, y - s\sin\theta)\,\Delta p(s)\,ds \qquad (2.8)$$

The total unsteady flow field is obtained by adding incoming external disturbances, due to either incoming vorticity waves or incoming pressure waves.

$$\hat{U}(x, y, t) = \int_0^c G(x - s\cos\theta, y - s\sin\theta)\,\Delta p(s)\,ds \; + \; \hat{U}_{ext} \qquad (2.9)$$

At the blade surface there is no flow normal to the blade. If the blade is moving (as in a flutter calculation) then this statement is modified to say that there is no normal flow relative to the moving blade. This produces an equation of the following form.

$$\int_0^c g(s' - s)\,\Delta p(s)\,ds = f_{ext}(s') \; + \; f_{blade}(s') \qquad (2.10)$$

$g(s)$ is another Green's function corresponding to the flow normal to the blade produced by $G(s)$. f_{ext} is the normal flow produced by the incoming, external perturbation, and f_{blade} is the contribution due to the moving blade.

The final step is to solve this equation to obtain $\Delta p(s)$. This cannot be done analytically and so is done by a numerical method which turns the integral equation into a matrix equation in which the unknowns are the pressure jumps at various points along the blade. This numerical solution is extremely accurate and can be considered for practical purposes

7

to be exact. It is also an extremely cheap procedure, requiring on the order of 1 CPU min. on a MicroVax II.

In addition to its low cost, there are three good points about this method. It can handle all two-dimensional inviscid phenomena, including wake/rotor and potential/rotor interactions and flutter in compressors and fans. Also, according to Verdon [49] the analysis has proven to be very useful in the prediction of supersonic fan flutter. The final point is that it can be used as an analytic test case to validate the other computational methods to be presented in this review. Due to the difficulty in obtaining good experimental unsteady flow data for code validation, analytic test cases such as these are invaluable.

The limitations in the method are due to the fact that it completely ignores the effects of thickness and loading, which change the mean flow, about which the unsteady perturbation is being calculated. In the same review article, Verdon states that this renders it ineffective in predicting flutter at transonic or subsonic speeds, and prevents the forced response prediction from being any more than an order-of-magnitude answer.

2.2 Linear Potential Methods

This class of methods was developed in the late 1970's, with major contributions coming from Verdon and Caspar [50,8] and Whitehead [51]. This approach begins by assuming that a steady, isentropic, irrotational flow field has already been determined through the solution of the steady, nonlinear full potential equations by some appropriate numerical method. The analysis then considers linear, unsteady, irrotational, isentropic perturbations to the steady flow. Since linearity allows the superposition of unsteady flows of different frequencies, it can be further assumed that there is only one frequency and so the unsteady component varies harmonically.

The description that follows is for the simplest case of subsonic, isentropic, irrotational, two-dimensional flow. Extensions to include the effects of three-dimensionality, transonic flow, and incoming entropy and vorticity will be discussed briefly later.

The nonlinear, unsteady mass equation for an isentropic, irrotational, two-dimensional flow is

$$\frac{\partial \rho}{\partial t} + \nabla \cdot (\rho \, \nabla \Phi) = 0 \qquad (2.11)$$

The linear, harmonic mass equation is obtained by expressing the density, ρ, as the sum of the steady density and a harmonically oscillating unsteady component.

$$\rho = \bar{\rho} + \exp(-i\omega t) \, \hat{\rho} \qquad (2.12)$$

$\hat{\rho}$ is the complex amplitude of the unsteady density. In this equation and others that will

follow, it is implicitly understood that the density is actually the real part of the right-hand-side of the equation..

Similarly the potential Φ is expressed as a sum of a steady component and a harmonically varying unsteady component.

$$\Phi = \overline{\Phi} + \exp(-i\omega t)\,\hat{\phi} \qquad (2.13)$$

Substituting these into the unsteady mass equation, and ignoring all second order products of the linear perturbations, yields the linearized, unsteady mass equation.

$$-i\omega\,\hat{\rho} + \nabla \cdot (\overline{\rho}\,\nabla\hat{\phi}) + \nabla \cdot (\hat{\rho}\,\nabla\overline{\Phi}) = 0 \qquad (2.14)$$

For irrotational, isentropic flows the unsteady Bernoulli equation is

$$\frac{\partial \Phi}{\partial t} + \frac{1}{2}\,|\nabla\Phi|^2 + \int \frac{dp}{\rho} = \text{const.} \qquad (2.15)$$

Linearizing this equation gives

$$\frac{\overline{D}\,\hat{\phi}}{Dt} = \frac{\hat{p}}{\overline{\rho}}, \qquad (2.16)$$

where

$$\frac{\overline{D}}{Dt} = -i\omega + \nabla\overline{\Phi}\cdot\nabla \qquad (2.17)$$

Finally, the isentropic assumption means that the density and pressure perturbations are related through

$$\hat{p} = \overline{c}^2\hat{\rho}. \qquad (2.18)$$

Combining the three linear equation to eliminate the density and pressure variables yields the final form of the linear, harmonic, unsteady potential equation.

$$\frac{\overline{D}}{Dt}\left(\overline{c}^{-2}\,\frac{\overline{D}\,\hat{\phi}}{Dt}\right) - \overline{\rho}^{-1}\nabla\cdot\left(\overline{\rho}\,\nabla\,\hat{\phi}\right) = 0 \qquad (2.19)$$

Before addressing methods for solving this equation, we must address the boundary conditions required to complete the specification of the problem.

The boundary condition at the surface of the moving blade is that there is no normal flow relative to the blade, or equivalently that the flow velocity normal to the blade is equal to the blade's velocity normal to its surface.

$$\nabla\Phi\cdot n = u_n \qquad (2.20)$$

In this equation n is the unit vector normal to the surface of the blade.

This boundary condition, in the form in which it is written, must be applied at the instantaneous location of the moving blade surface. Thus, as the blade moves the location
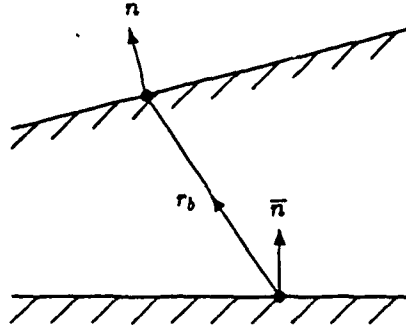
Figure 2.2: Geometry for unsteady wall boundary condition

at which the boundary condition must be enforced varies too. It is much more convenient however to reformulate the boundary condition so that it is enforced at the fixed, mean blade position. To do this, a Taylor-series expansion of the potential Φ is used. If the location of a point on the blade's moving surface is given by

$$r = \bar{r} + \exp(-i\omega t)\,\hat{r}_b, \tag{2.21}$$

then

$$\Phi(r) \;\approx\; \Phi(\bar{r}) + (r - \bar{r})\cdot\nabla\Phi \;\approx\; \overline{\Phi}(\bar{r}) + \exp(-i\omega t)\left(\hat{\phi} + \hat{r}_b\cdot\nabla\widetilde{\Phi}\right) \tag{2.22}$$

The other step in linearizing the wall boundary condition is to express the unsteady normal vector as

$$n = \bar{n} + \exp(-i\omega t)\,\hat{n}. \tag{2.23}$$

The vector $\hat{n}$ is normal to the vector $\bar{n}$ (since the magnitude of n is always unity), and represents the rotation of n due to the blade's motion. Fig. 2.2 illustrates the geometry of the moving wall. Inserting these equations into Eq. (2.20), with the wall's velocity being given by $-i\omega\exp(-i\omega t)\,\hat{r}_b$, gives the linearized, harmonic wall boundary condition.

$$\nabla\hat{\phi}\cdot\bar{n} + \hat{r}_b\cdot\nabla(\nabla\overline{\Phi}\cdot\bar{n}) + \nabla\overline{\Phi}\cdot\hat{n} = -i\omega\hat{r}_b\cdot\bar{n} \tag{2.24}$$

The unsteady boundary condition along the wake is simply that there is no pressure jump across the wake.

$$[p] = 0 \tag{2.25}$$

Linearizing this equation, in the same manner as the wall boundary condition, leads to

$$[\hat{p} + \hat{r}_w\cdot\nabla\overline{p}] = 0, \tag{2.26}$$

where $\hat{r}_w$ is the amplitude of the oscillation in the wake position. This equation is simplified by noting that in a steady potential flow there is no discontinuity in the pressure gradient

or velocity across the wake. Hence, the linearized wake boundary condition is

$$[\hat{p}] = \frac{\overline{D}}{Dt}\left[\dot{\phi}\right] = 0. \tag{2.27}$$

At the inflow, a Fourier eigenmode analysis, similar to that discussed earlier for the flat plate analysis, reveals that the harmonic unsteady potential is a sum of incoming and outgoing parts, each of which is a sum of modes with differing values of l, the circumferential wavenumber.

$$\hat{\phi}(x,y) = \sum_l \exp(ik_{in}x + ily)\,\hat{\phi}_{in} + \sum_l \exp(ik_{out}x + ily)\,\hat{\phi}_{out} \tag{2.28}$$

The incoming modes are prescribed by the user, and the outgoing modes are to be determined by the calculation. Fourier transforming the potential yields a simple algebraic equation relating the Fourier amplitudes at two different axial locations.

$$\mathcal{F}\hat{\phi}(x_1,l) - \exp(ik_{in}x_1)\hat{\phi}_{in} = \exp(ik_{out}(x_1-x_2))\left(\mathcal{F}\hat{\phi}(x_2,l) - \exp(ik_{in}x_2)\hat{\phi}_{in}\right). \tag{2.29}$$

There is a similar equation at the outflow, but in this case there is an additional term due to the unsteady vortex sheet that is shed along the wake by the airfoil due its varying circulation.

The final boundary condition is the periodic boundary condition, which is simply

$$\hat{\phi}(x,y+P) = \exp(-i\sigma)\,\hat{\phi}(x,y), \tag{2.30}$$

where P and σ are again the blade pitch and the inter-blade phase angle, respectively.

There are different approaches to the numerical solution of the linear, harmonic, unsteady potential equation. In the method used by Caspar and Verdon [8], $\hat{\phi}$ is defined to be quadratic in the neighborhood of each node of the computational grid.

$$\hat{\phi} = a + bx + cy + dx^2 + exy + fy^2 \tag{2.31}$$

The coefficients in this definition are chosen to match the local nodal values of $\hat{\phi}$ in a "least-squares" best fit. They refer to this procedure as an "implicit least-squares interpolation". Substituting this local quadratic formulation into the unsteady potential partial differential equation yields an algebraic equation at each interior node, and on one side of the wake.

The same basic method is used to discretize the surface and wake boundary conditions, and the periodic boundary condition is easily incorporated. The inlet and outlet boundary conditions are implemented by replacing the continuous Fourier transforms by discrete Fourier transforms, assuming the computational grid has been constructed such that the inlet and outlet nodes are uniformly spaced. The axial locations x_1 and x_2 correspond to the boundary plane and the first plane of nodes interior to the boundary.

The entire set of interior and boundary equations can be written as a block tridiagonal system and are then solved by Gaussian elimination.

Figures 2.3–2.5 show results computed by Verdon, with comparison against experimental results obtained by Carta. The cascade is a NACA 65 series cascade which was tested at UTRC. Fig. 2.3 shows the steady pressure distribution calculated using a nonlinear full potential code. To obtain good agreement with the experimental data, the inflow angle in the calculation was modified slightly. Fig. 2.4 shows the real and imaginary components of the complex surface pressure amplitude due to a torsional oscillation of the airfoils, for one particular frequency and inter-blade phase angle. The agreement is fairly good, but not excellent, particularly near the leading and trailing edges.

Fig. 2.5 shows the resultant moment as a function of the inter-blade phase angle. Although the qualitative trends are correct, there are now significant quantitative differences between the calculation and the experiment. However, the calculation is accurate in predicting the flutter boundaries, which correspond to the imaginary component of the moment being zero. When the imaginary component is positive the product of the moment and the torsion rate is positive on average, and so during one period of the oscillation the fluid does net work on the airfoil and increases the amplitude of its oscillation, leading ultimately to structural failure.

The linear potential method has been extended by several researchers to analyze transonic flow. In these applications, a conservative full potential transonic solver is used first to calculate the steady transonic flow field. This includes "capturing" any shocks in the flow field, meaning that they are not modelled as a line discontinuity in the flow field but instead simply appear in the flow field as part of the solution. In formulating the linear unsteady flow problem, the shocks are then "fit" and treated as an internal boundary. The corresponding boundary condition is the linearized form of the isentropic equivalent of the Rankine-Hugoniot moving shock relations. In form it is similar to both the solid wall and wake conditions. The other change for transonic flow is in the numerical discretization in the supersonic region. For reasons of numerical stability it is necessary to use an upwind-biased approximation to the streamwise second derivative operators.

Linear potential methods are about ten times more expensive than a flat plate analysis, taking of the order of 10 CPU mins. on a MicroVax II. In return for this additional expense, they are considerably more accurate, due to the inclusion of the effects of both airfoil thickness and airfoil loading. In particular, the linear, potential analysis is the simplest model which gives an accurate prediction of the very large changes in lift and moment due to shock motion in transonic applications. Engineering experience shows that these methods are very effective in predicting subsonic and transonic flutter, provided any shocks are not so strong that they significantly violate the isentropic assumption.

The limitations of potential method are all associated with the irrotational and isentropic assumptions. Computational results for steady flow past isolated airfoils have shown that potential solutions can be totally incorrect once the pre-shock Mach number exceeds 1.3. Also, the standard formulation of the linear, potential analysis does not allow for incoming vorticity or entropy waves, and so does not allow for the caluclation of wake/rotor interaction. Verdon [49] has shown that there is a more general formulation which allows for wake/rotor interactions by separating the unsteady velocity into a rotational part and a potential part, but no results have yet been published using this approach, and the increase in complexity suggests that one might be better advised to proceed instead to the next development, the linear, Euler methods.
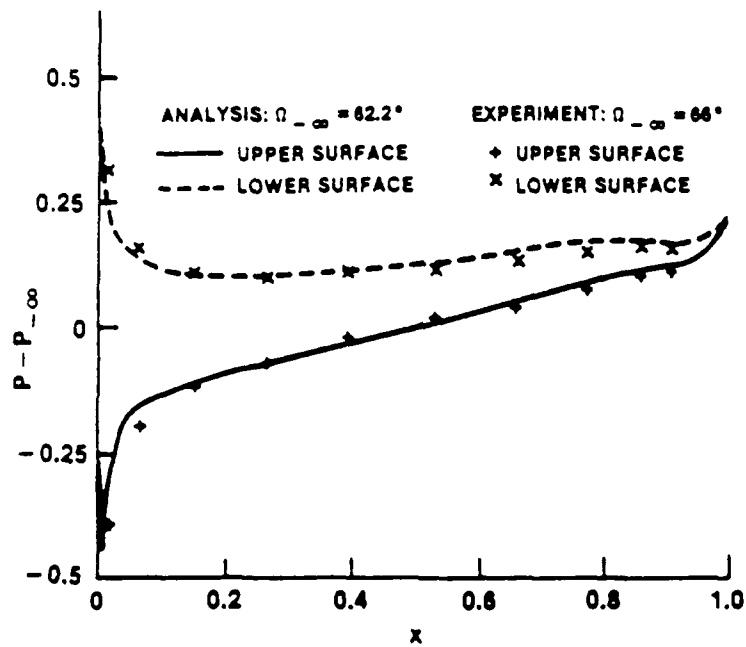
Figure 2.3: Steady pressure distribution on NACA 65 series cascade
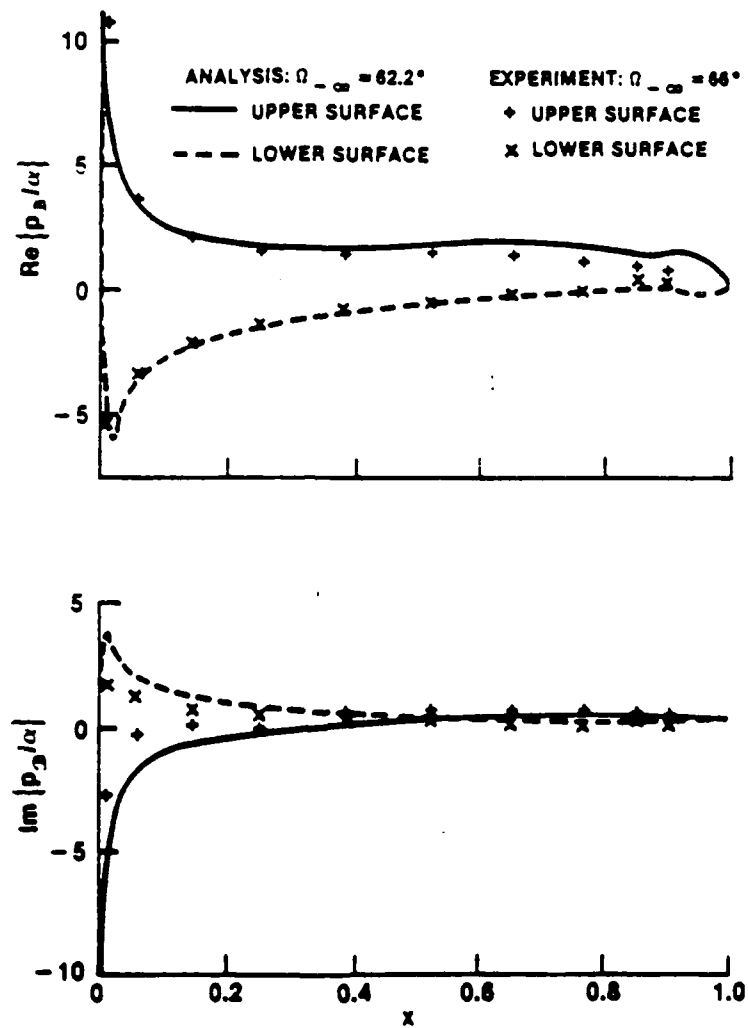
Figure 2.4: Unsteady pressure distribution due to torsional oscillation
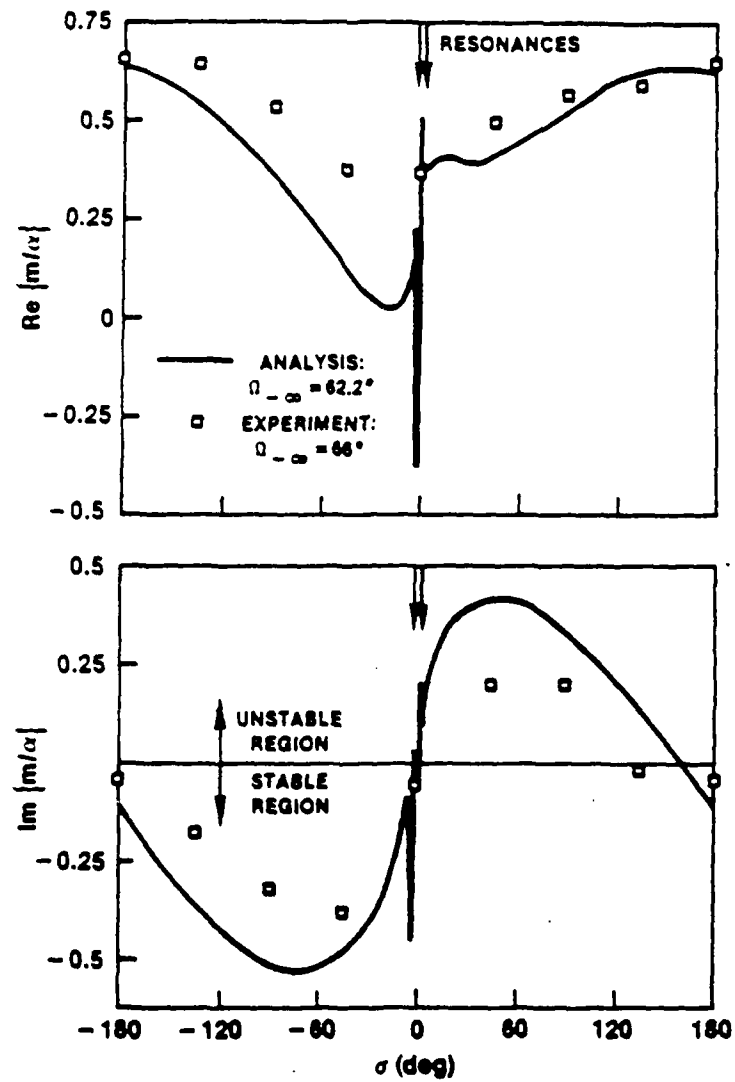
Figure 2.5: Unsteady moment due to torsional oscillation

2.3   Linear Euler Methods

Linear Euler methods are an idea whose time is coming. I am personally convinced that there is an important place for this class of methods in the toolkit of aerodynamic designers. They promise the efficiency of linear potential methods, without the restrictions of the isentropic and irrotational assumptions.

The current literature on the subject is limited to two pioneering Ph.D. theses. The first, by Ni in 1974 [39,41], used the isentropic form of the Euler equations, replacing the energy equation by the condition of uniform entropy. He validated the concept by comparison with the linear flat plate analysis.

The second thesis, by Hall in 1987 [26,27], used the full Euler equations. Hall also developed a shock-fitting technique, for both the nonlinear, steady solution and the linear, unsteady solution, which is analogous to that used in linear, unsteady potential methods. Due to the complexities of shock-fitting, it was developed only for duct applications, although the rest of the thesis included cascade applications.

The development of the linear Euler methods begins with the conservative vector form of the unsteady, nonlinear Euler equations.

$$\frac{\partial U}{\partial t} + \frac{\partial F}{\partial x} + \frac{\partial G}{\partial y} = 0 \tag{2.32}$$

where

$$U = \begin{pmatrix} \rho \\ \rho u \\ \rho v \\ \rho E \end{pmatrix}, \; F = \begin{pmatrix} \rho u \\ \rho u^2 + p \\ \rho u v \\ \rho u H \end{pmatrix}, \; G = \begin{pmatrix} \rho v \\ \rho u v \\ \rho v^2 + p \\ \rho v H \end{pmatrix} \tag{2.33}$$

E and H are the total internal energy and stagnation enthalpy per unit mass, respectively. They are related to each other and the other flow variables through the following ideal gas equations.

$$H = E + \frac{p}{\rho}, \quad p = (\gamma - 1)\left(\rho E - \frac{1}{2}\rho(u^2 + v^2)\right) \tag{2.34}$$

To obtain the linear, unsteady equations, U is written as the sum of a steady part and a harmonically varying unsteady perturbation.

$$U = \overline{U} + e^{-i\omega t}\hat{U} \tag{2.35}$$

Performing a Taylor-series expansion gives

$$F \approx \overline{F} + e^{-i\omega t}\overline{A}\hat{U}, \quad \overline{A} \equiv \frac{\partial F}{\partial U} \tag{2.36}$$

and

$$G \approx \overline{G} + e^{-i\omega t}\overline{B}\hat{U}, \qquad \overline{B} \equiv \frac{\partial G}{\partial U} \tag{2.37}$$

Hence, the linear, harmonic, unsteady Euler equations are

$$-i\omega\hat{U} + \frac{\partial}{\partial x}(\overline{A}\,\hat{U}) + \frac{\partial}{\partial y}(\overline{B}\,\hat{U}) = 0 \tag{2.38}$$

The boundary conditions are very similar to the those for the potential method. Without going into any additional detail, the wall boundary condition is

$$\hat{u} \cdot \overline{n} + \overline{u} \cdot \hat{n} + \hat{r}_b \cdot \nabla\,\overline{u}_n = -i\omega\hat{r}_b \cdot \overline{n}. \tag{2.39}$$

There are two boundary conditions along the wake. The first comes from the fact that, by definition, no fluid crosses the wake.

$$\hat{u} \cdot \overline{n} + \overline{u} \cdot \hat{n} + \hat{r}_w \cdot \nabla\,\overline{u}_n = -i\omega\hat{r}_w \cdot \overline{n}. \tag{2.40}$$

This equation must be satisfied on both sides of the wake. The second condition comes from the fact that there cannot be a pressure jump across the wake.

$$[\hat{p} + \hat{r}_w \cdot \nabla\,\overline{p}] = [\hat{p}] + \hat{r}_w \cdot \nabla\,[\overline{p}] = 0 \tag{2.41}$$

The inflow, outflow and periodic boundary conditions are also very similar to the potential boundary conditions.

Ni and Hall used very different methods to solve these equations. Examining Hall's method first, on each quadrilateral cell, the unsteady equations are integrated to obtain

$$\iint -i\omega\hat{U}\,dx\,dy + \oint \overline{A}\,\hat{U}\,dy - \overline{B}\,\hat{U}\,dx = 0. \tag{2.42}$$

This equation is approximated by trapezoidal integration. The boundary conditions are then discretized in a straightforward fashion and are combined with the interior equations in a least squares formulation which tries to drive all residual errors to zero. Minimization of the resulting quadratic function gives a linear equation which is solved by banded Gaussian elimination.

Ni's approach is to go back to the basic formulation, and instead let

$$U(x,y,t) = \overline{U}(x,y) + \exp(-i\omega t)\hat{U}(x,y,t) \tag{2.43}$$

Substituting this into the unsteady, nonlinear Euler equations gives

$$\frac{\partial\hat{U}}{\partial t} + \frac{\partial}{\partial x}(\overline{A}\,\hat{U}) + \frac{\partial}{\partial y}(\overline{B}\,\hat{U}) = i\omega\hat{U}. \tag{2.44}$$

This looks like the regular, non-harmonic, linear, unsteady Euler equations, but with a source term on the right-hand-side of the equation. This equation can now by solved

by one of the standard time-marching methods used to calculate steady solution to the Euler equations, since the "steady-state" solution of this equation is simply the desired complex harmonic amplitude $\hat{U}$. The advantage of this approach is that multigrid and other acceleration techniques can be used to obtain the solution extremely quickly. This is particularly important in three dimensions where the direct solution method of Hall becomes very expensive.

Figures 2.6–2.9 show results computed by Hall. The first two figures compare Hall's calculations with those performed by Allmaras using a nonlinear finite-volume unsteady Euler method. The test case is a transonic diffuser in which the exit pressure is being oscillated sinusoidally. The nondimensional frequency, based on the throat height and the sonic speed of sound, is 3.125, and the exit pressure oscillation is equal to 10% of the inflow stagnation pressure. When comparing results in Fig. 2.6, it must be noted that in the linear results the shock position appears to be stationary since the graphics post-processing did not take into account the calculated shock motion amplitude. With this in mind, the agreement between the linear and nonlinear results is extremely good for this large amplitude unsteady case. Fig. 2.7 shows the corresponding complex amplitude of the pressure oscillations on the lower wall. The agreement is very impressive, and demonstrates the usefulness of the linear Euler method for cases with strong unsteady shocks. The computational cost of the linear method was approximately 50 times less than the nonlinear method, which illustrates the practical potential of these methods. This means that a single two-dimensional linear calculation takes about one minute on a CRAY; a three-dimensional calculation would take maybe fifteen minutes. Additional algorithm work would probably reduce this cost significantly.

Fig. 2.8 shows steady Mach contours and surface pressure data computed for an analytic incompressible test case due to Gostelow [23]. Hall's surface pressure results include a Prandtl-Glauert correction to remove the very weak compressibility effects in his calculation. Fig. 2.9 shows the surface complex pressure amplitude due to the airfoil oscillating in pitch, with reduced frequency $\omega = 0.4$ and inter-blade phase angle $\sigma = \pi$. The comparison is with results obtained by a semi-analytic incompressible theory [3].

Linear Euler
(Hall)

Nonlinear Euler
(Allmaras)
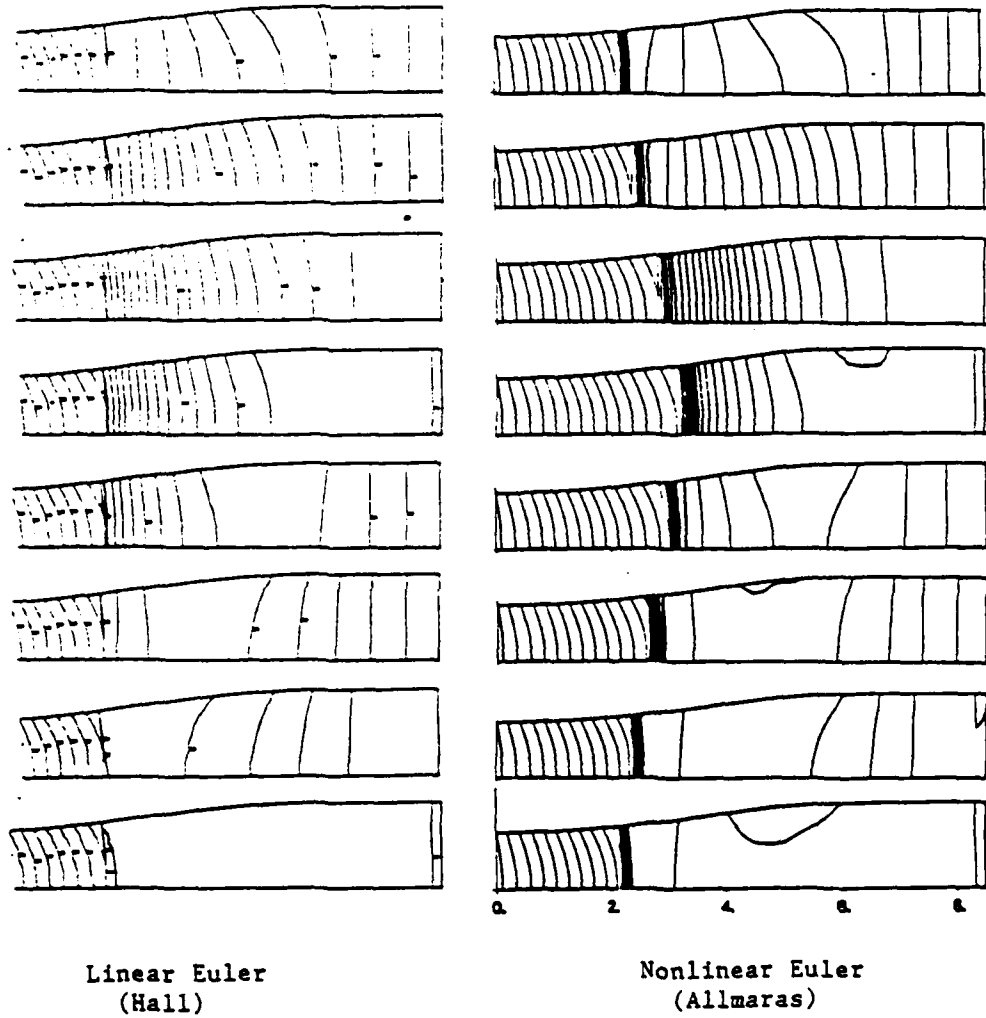
Figure 2.6: Comparison of nonlinear and linear calculations for duct with oscillating shock
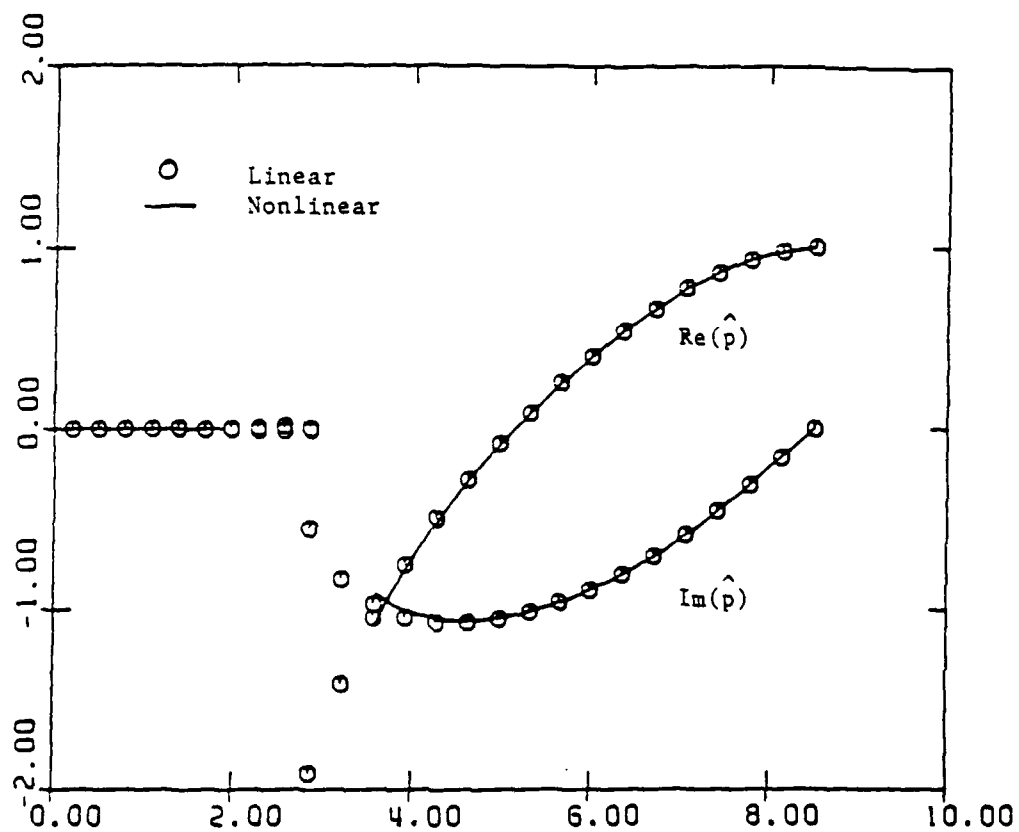
Figure 2.7: Comparison of surface complex pressure amplitudes
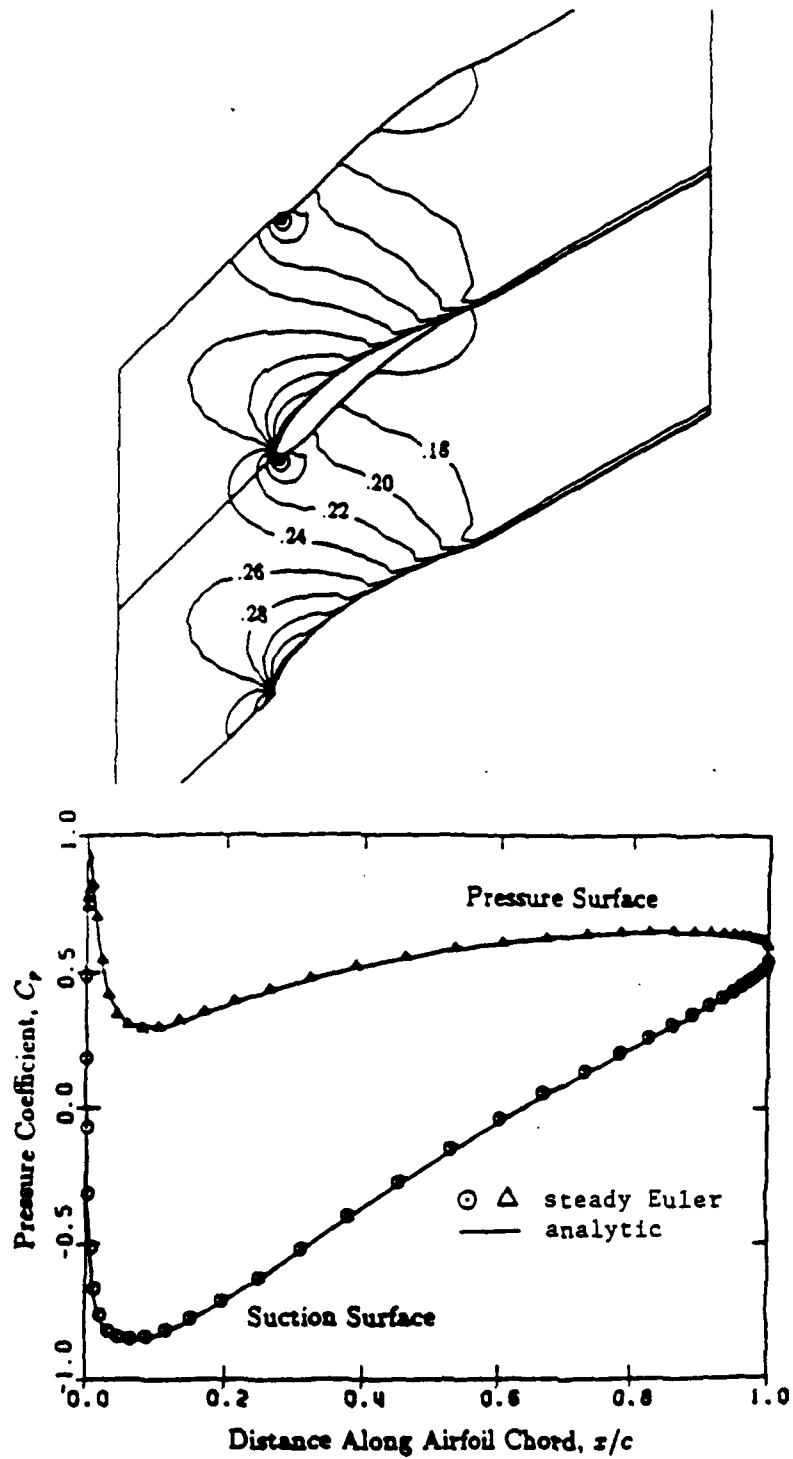
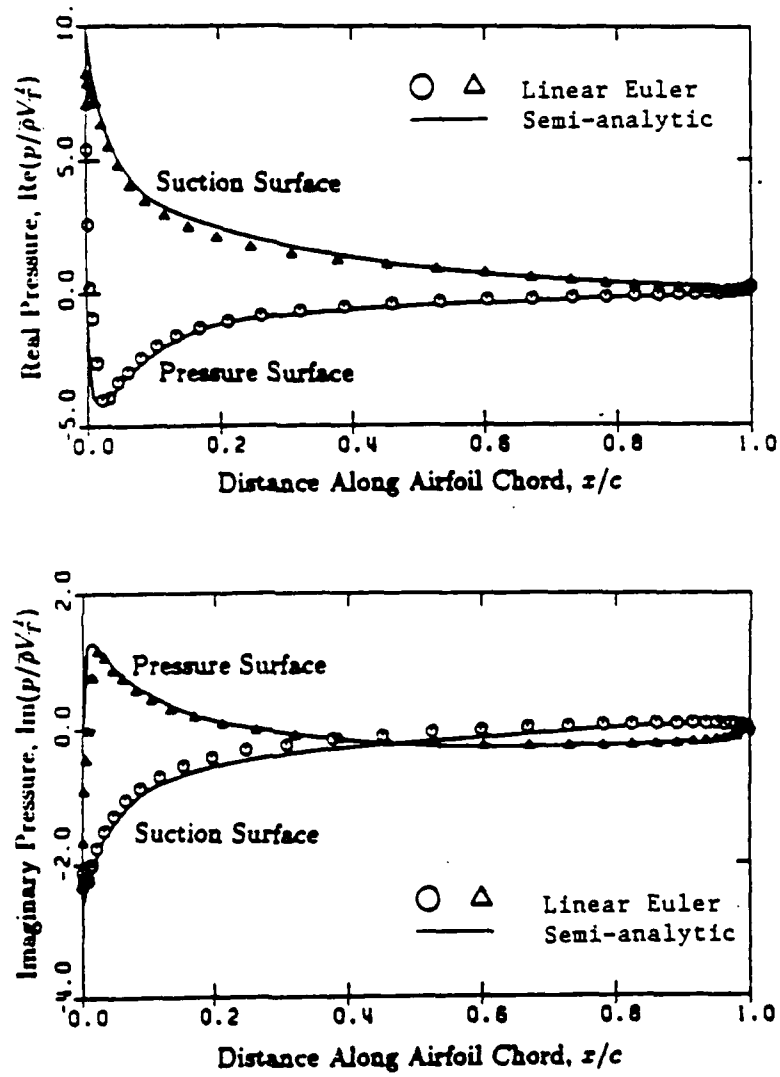Figure 2.8: Mach contours and pressure distribution for Gostelow cascade

Figure 2.9: Surface complex pressure amplitudes due to airfoil pitching

Chapter 3

Non-linear Unsteady Euler Methods

3.1 Basic Algorithms

It is assumed that the reader is already somewhat familiar with the most common explicit methods for solving the Euler equations. However, for the sake of completeness, and to define the notation which will be used, a brief review is given in this section.

The integral form of the nonlinear, unsteady Euler equations for a fixed, two-dimensional control volume Ω, is

$$\frac{d}{dt} \iint U\, dx\, dy + \oint_{\partial\Omega} Fn_x + Gn_y\, ds = 0 \tag{3.1}$$

where $(n_x, n_y)^T$ is the outward-pointing unit vector normal to the boundary $\partial\Omega$.

Jameson's cell-based and node-based Runge-Kutta algorithms are both based directly upon this integral formulation. The first step is the spatial discretization which yields the following semi-discrete system of ordinary differential equations for the flow variables at each grid node.

$$\text{Area} \times \frac{dU}{dt} = -\sum (Fn_x + Gn_y)\, \Delta s \tag{3.2}$$

The difference between the cell-based and node-based versions is in the definitions of the cell areas and the fluxes. Figure 3.1 shows the grid geometry for both algorithms. The solid circles correspond to the locations at which the flow variables are defined. In each case the appropriate area is the area of the shaded cell. In the cell-based scheme, the fluxes through the faces are based upon the averages of F and G at the cell centers of the cells on either side [31]. In the node-based scheme, they are based upon the averages of F and G at the

cell-centered scheme   node-based scheme
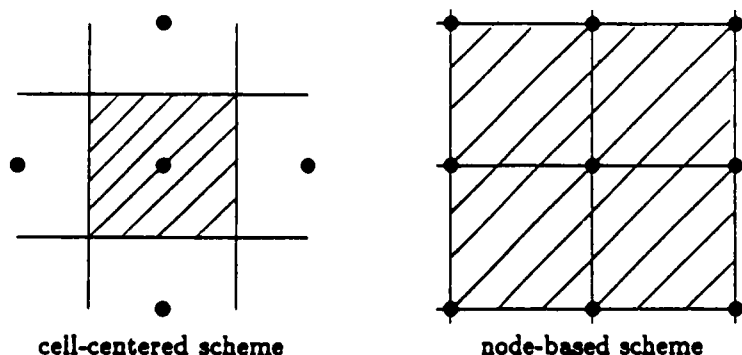
Figure 3.1: Grid geometry for Jameson's Euler algorithms

two ends of each face [30]. Eq. (3.2) can be re-written as

$$\frac{dU}{dt} = -R. \tag{3.3}$$

In general, the definition of R includes additional numerical smoothing, but details of the smoothing will not be presented here. The temporal discretization is performed using a Runge-Kutta approach.

$$
\begin{aligned}
U^{(1)} &= U^n - \tfrac{1}{4}\Delta t\, R^n \\
U^{(2)} &= U^n - \tfrac{1}{3}\Delta t\, R^{(1)} \\
U^{(3)} &= U^n - \tfrac{1}{2}\Delta t\, R^{(2)} \\
U^{n+1} &= U^n - \Delta t\, R^{(3)}
\end{aligned}
\tag{3.4}
$$

U^n and U^{n+1} are the state vectors at the old and new time levels, and $U^{(1)}, U^{(2)}, U^{(3)}$ are intermediate values of U in the multi-stage algorithm. $R^n, R^{n+1}, R^{(1)}, R^{(2)}, R^{(3)}$ are the corresponding values of R.

Figure 3.2 shows the grid geometry for Ni's Lax-Wendroff algorithm [38,28,11]. The change in U at node 1, for one timestep can be written as a sum of contributions from the four cells surrounding it.

$$\Delta U_1 = \delta U_{1A} + \delta U_{1B} + \delta U_{1C} + \delta U_{1D} \tag{3.5}$$

The sum of the contributions which cell A "distibutes" to its nodes is equal to the flux into cell A, divided by its area.

$$\delta U_{1A} + \delta U_{2A} + \delta U_{3A} + \delta U_{4A} = -\frac{\Delta t}{\text{Area}} \sum_{\text{cell A}} (Fn_x + Gn_y)\Delta s \tag{3.6}$$

The distributed changes have a first order component proportional to Δt, and a second order component proportional to Δt^2. The four first order components are equal, and so
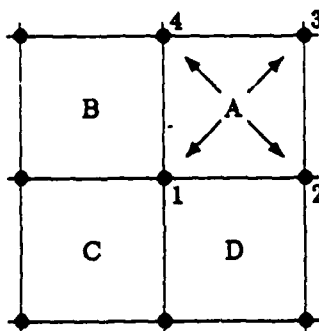
Figure 3.2: Geometry for Ni's Euler algorithm

for very small timesteps the algorithm has the same spatial discretization as Jameson's node-based algorithm. The second order terms introduce an element of upwinding which stabilizes the numerical procedure and makes it second order accurate. Further details can be obtained from the references.

3.2 Moving Grids

When calculating nonlinear flutter problems in which the unsteadiness is due to some prescribed motion of the blades in the cascade, it is necessary to perform the calculation on a grid which deforms to match the motion of the blades. This requires a generalization of the basic numerical algorithms.

The modifications can be derived by examining either the differential or integral forms of the Euler equations. Starting with the former approach, we define computational coordinates ξ, η, τ.

$$
\begin{aligned}
x &= x(\xi, \eta, \tau) & , & \qquad \xi = \xi(x, y, t) \\
y &= y(\xi, \eta, \tau) & , & \qquad \eta = \eta(x, y, t) \\
t &= \tau & , & \qquad \tau = t
\end{aligned}
\tag{3.7}
$$

ξ and η have been chosen such that the grid is steady in the computational (ξ, η) coordinates, and so the motion of the grid in the physical domain is fully contained in the time dependence of the x and y definitions.

Applying the chain rule gives

$$
\begin{aligned}
\frac{\partial U}{\partial t} &\equiv \frac{\partial \xi}{\partial t}\frac{\partial U}{\partial \xi} + \frac{\partial \eta}{\partial t}\frac{\partial U}{\partial \eta} + \frac{\partial U}{\partial \tau}, \\
\frac{\partial F}{\partial x} &\equiv \frac{\partial \xi}{\partial x}\frac{\partial F}{\partial \xi} + \frac{\partial \eta}{\partial x}\frac{\partial F}{\partial \eta}, \\
\frac{\partial G}{\partial y} &\equiv \frac{\partial \xi}{\partial y}\frac{\partial G}{\partial \xi} + \frac{\partial \eta}{\partial y}\frac{\partial G}{\partial \eta}.
\end{aligned}
\tag{3.8}
$$

Also, because the mapping from (x, y, t) to (ξ, η, τ) is the inverse of the mapping from (ξ, η, τ) to (x, y, t), the Jacobian matrices of the mappings in the two directions must be the inverse of each other.

$$
\begin{pmatrix} \frac{\partial \xi}{\partial x} & \frac{\partial \xi}{\partial y} & \frac{\partial \xi}{\partial t} \\ \frac{\partial \eta}{\partial x} & \frac{\partial \eta}{\partial y} & \frac{\partial \eta}{\partial t} \\ \frac{\partial \tau}{\partial x} & \frac{\partial \tau}{\partial y} & \frac{\partial \tau}{\partial t} \end{pmatrix} = \begin{pmatrix} \frac{\partial x}{\partial \xi} & \frac{\partial x}{\partial \eta} & \frac{\partial x}{\partial \tau} \\ \frac{\partial y}{\partial \xi} & \frac{\partial y}{\partial \eta} & \frac{\partial y}{\partial \tau} \\ \frac{\partial t}{\partial \xi} & \frac{\partial t}{\partial \eta} & \frac{\partial t}{\partial \tau} \end{pmatrix}^{-1}
\tag{3.9}
$$

Hence, after some tedious algebra, the transformed Euler equations become

$$
\frac{\partial (JU)}{\partial \tau} + \frac{\partial}{\partial \xi}\left[\left(F - U\frac{\partial x}{\partial \tau}\right)\frac{\partial y}{\partial \eta} - \left(G - U\frac{\partial y}{\partial \tau}\right)\frac{\partial x}{\partial \eta} \right]
$$

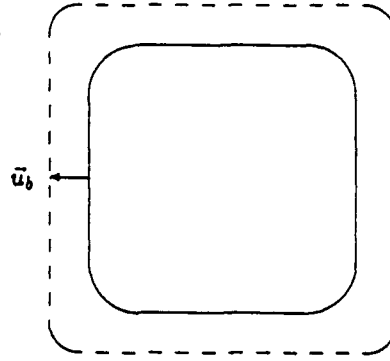Figure 3.3: Moving control volume

$$-\frac{\partial}{\partial \eta}\left[\left(F - U\underline{\frac{\partial x}{\partial \tau}}\right)\frac{\partial y}{\partial \xi} - \left(G - U\underline{\frac{\partial y}{\partial \tau}}\right)\frac{\partial x}{\partial \xi}\right] = 0 \qquad (3.10)$$

The four underlined terms are the additional terms due to the motion of the grid. $J(\tau)$ is the determinant of the mapping from (ξ, η) to (x, y) which is the ratio of the areas of corresponding infinitesimal volumes.

The integral approach to obtaining this same equation begins by integrating the Euler equations over a control volume Ω which is no longer assumed to be fixed.

$$\iint_\Omega \left(\frac{\partial U}{\partial t} + \frac{\partial F}{\partial x} + \frac{\partial G}{\partial y}\right) dx\, dy = 0 \qquad (3.11)$$

Now, because of the motion of the boundary $\partial\Omega$,

$$\frac{d}{dt}\iint_\Omega U\, dx\, dy = \iint_\Omega \frac{\partial U}{\partial t}\, dx\, dy + \int_{\partial\Omega} U\, \vec{u}_b\cdot\vec{n}\, ds \qquad (3.12)$$

As shown in Fig. 3.3, the second term corresponds to the volume being swept out by the moving boundary, with $\vec{u}_b$ being the velocity of the boundary. Hence,

$$\begin{aligned}
\frac{d}{dt}\iint_\Omega U\, dx\, dy &= -\iint_\Omega \frac{\partial F}{\partial x} + \frac{\partial G}{\partial y}\, dx\, dy + \int_{\partial\Omega} U\, u_b\cdot n\, ds \\
&= -\int_{\partial\Omega}(F - \underline{U u_{bx}})\, n_x + \left(G - \underline{U u_{by}}\right) n_y\, ds \qquad (3.13)
\end{aligned}$$

The underlined terms are again the extra terms due to the motion of the grid, with

$$\vec{u}_b = \left(\begin{array}{c} u_{bx} \\ u_{by} \end{array}\right) = \left(\begin{array}{c} \dfrac{dx}{dt} \\ \dfrac{dy}{dt} \end{array}\right) \qquad (3.14)$$

Comparing the forms of Eq. (3.10) and Eq. (3.14) it is apparent that they are equivalent.

The algorithm changes required as a consequence of these extra terms are relatively small. For Jameson's schemes, one needs to modify the flux terms and the time integration

since the cell areas are no longer constant. At least as much work is required in the grid generation task of producing a moving grid which conforms to the motion of the blades, and in the graphical post-processing of the results produced on the moving mesh.

A final note is that the wall b.c. is that there is no normal flow relative to the moving blade. Thus, the flux term for a wall face contains only pressure terms in the momentum equations (which are the same in steady flow) and in the energy equation there is a term corresponding to the work being done by pressure forces due to the motion of the surface.

$$((F-Uu_{bx})n_x + (G-Uu_{by})n_y)\Delta s = \begin{pmatrix} 0 \\ p\,n_x\Delta s \\ p\,n_y\Delta s \\ p\,\vec{u}_b\cdot\vec{n}\Delta s \end{pmatrix} \qquad (3.15)$$

3.3   Inlet/Outlet B.C.'s

There are two steps in the construction of inlet and outlet boundary conditions. The first is the construction of an appropriate phyical model for the flow at the inflow or outflow. This is simply a uniform flow if there are no incoming disturbances. If there are disturbances then these need to modelled. The procedure which I follow is to first model the incoming wakes by specifying that in the wake frame of reference the flow has uniform pressure, uniform flow angle and a prescribed velocity defect, which may have a Gaussian distribution or some other form. If the upstream blade row is approximately adiabatic then one could assume that the stagnation enthalpy is approximately constant. If one is concerned with cold wakes, or incoming hot streaks, then a variation in the stagnation enthalpy would have to be prescribed.

To model incoming potential disturbances at the inflow or outflow, a linear analysis in the potential frame of reference in which the disturbance is steady can be performed. This assumes uniform entropy, uniform stagnation enthalpy and a prescribed velocity variation based on linear eigenmodes. In subsonic cases the eigenmodes decay exponentially away from the boundary and so one can assume that only the dominant fundamental mode is important. In supersonic cases all modes propagate indefinitely, and so instead a linear shock/expansion fan model is employed.

The combined model is

$$\begin{aligned} U_{comb} \;=\; & U_{wake} \quad \text{unsteady nonlinear wake model} \\ + \;& \delta U_{pot} \quad \text{unsteady potential perturbation} \\ + \;& \delta U_{steady} \quad \text{steady perturbation.} \end{aligned} \qquad (3.16)$$

The steady perturbation term, which is taken from a previous steady calculation, is required to ensure that the steady flow is still a solution to the unsteady flow problem when there is no incoming disturbance.

The second step in formulating boundary conditions is their numerical implementation. This is accomplished using a characteristic treatment. The two-dimensional, linear Euler equations using primitive variables, and assuming no variations in the y-direction along the boundary, are

$$\frac{\partial}{\partial t}\begin{pmatrix} \rho \\ u \\ v \\ p \end{pmatrix} + \begin{pmatrix} u & \rho & 0 & 0 \\ 0 & u & 0 & 1/\rho \\ 0 & 0 & u & 0 \\ 0 & \gamma p & 0 & u \end{pmatrix} \frac{\partial}{\partial x}\begin{pmatrix} \rho \\ u \\ v \\ p \end{pmatrix} = 0 \qquad (3.17)$$

This can be diagonalized to obtain

$$\frac{\partial}{\partial t}\begin{pmatrix} c_1 \\ c_2 \\ c_3 \\ c_4 \end{pmatrix} + \begin{pmatrix} u & 0 & 0 & 0 \\ 0 & u & 0 & 0 \\ 0 & 0 & u+c & 0 \\ 0 & 0 & 0 & u-c \end{pmatrix} \frac{\partial}{\partial x}\begin{pmatrix} c_1 \\ c_2 \\ c_3 \\ c_4 \end{pmatrix} = 0 \qquad (3.18)$$

The equations defining the transformation to and from characteristic variables are

$$\begin{pmatrix} c_1 \\ c_2 \\ c_3 \\ c_4 \end{pmatrix} = \begin{pmatrix} -c^2 & 0 & 0 & 1 \\ 0 & 0 & \rho c & 0 \\ 0 & \rho c & 0 & 1 \\ 0 & -\rho c & 0 & 1 \end{pmatrix} \begin{pmatrix} \bar{\rho} \\ \bar{u} \\ \bar{v} \\ \bar{p} \end{pmatrix} \qquad (3.19)$$

and

$$\begin{pmatrix} \bar{\rho} \\ \bar{u} \\ \bar{v} \\ \bar{p} \end{pmatrix} = \begin{pmatrix} -\frac{1}{c^2} & 0 & \frac{1}{2c^2} & \frac{1}{2c^2} \\ 0 & 0 & \frac{1}{2\rho c} & -\frac{1}{2\rho c} \\ 0 & \frac{1}{\rho c} & 0 & 0 \\ 0 & 0 & \frac{1}{2} & \frac{1}{2} \end{pmatrix} \begin{pmatrix} c_1 \\ c_2 \\ c_3 \\ c_4 \end{pmatrix} . \qquad (3.20)$$

In standard non-reflecting b.c.'s in which the flow is assumed to be uniform far from the blade row, $\bar{U}$ is the perturbation from the uniform far-field steady flow. The characteristic variables c are set to zero for incoming waves and are extrapolated for outgoing waves. This ensures that the outgoing waves "pass cleanly through the boundary" without producing any spurious non-physical reflections.

When there are incoming wakes and potential disturbances $\bar{U}$ is the perturbation from the prescribed combined model. Again, the c's are set to zero for incoming waves and are extrapolated for outgoing waves. Further details on the numerical implementation can be obtained from Ref. [22].

3.4   Stator/Rotor Interface

In the current literature there are four different approaches to treating the stator/rotor interface for performing stator/rotor interaction caluclations.

The approach used by Rai is to use two grids, one fixed to the stator and the other fixed to the rotor, which meet each other at a sliding interface, a line which is common to both grids [42,43]. The numerical algorithm is constructed in a fully conservative manner, with the flux through each segment of the common interface being carefully calculated from values on either side.

Lewis also uses two grids which are steady in the stator and rotor frames respectively, but the grids overlap by a few cells [37]. The numerical coupling procedure forms boundary values for each grid's calculation by interpolation from the interior of the other grid. This is not a conservative formulation and so will give inaccurate, and incorrect, results for flows in which narrow wakes or shocks cross the interface.

Gibeling's approach uses just one grid which is attached two both the stator and rotor blades [17]. As the rotors move past the stators the grid deforms steadily. At the end of a blade-passing period, the flow solution is interpolated onto the computational grid which existed at the beginning of the period, and a new period is begun. This is also a non-conservative procedure, and the interpolation procedure will tend to smear any shocks and wakes. In addition there are some severe limitations on the stator/rotor gaps which can be analyzed, since very small gaps produce unacceptably high shearing of the computational grid.

My approach is similar to Rai's except that a one cell gap is left between the stator and rotor grids [21]. This gap is bridged by a line of shearing cells formed by connecting stator boundary nodes to the nearest rotor boundary nodes. This produces cells which become progressively more sheared until thay reconnect to different nodes. As shown in
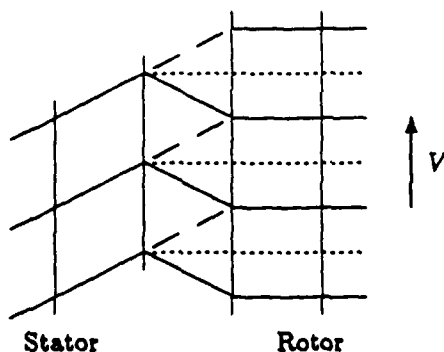
Figure 3.4: Shearing cells at stator/rotor interface
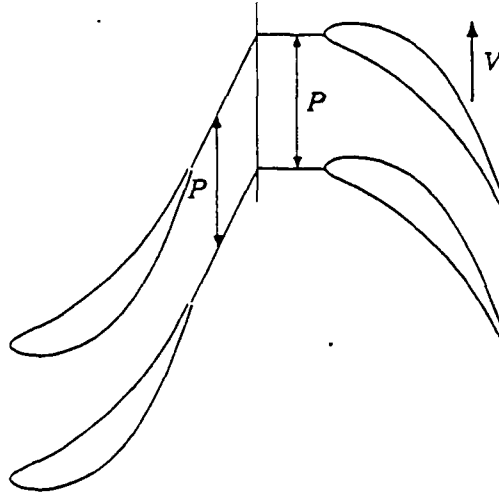
Figure 3.5: Periodic boundary conditions with equal pitches

Fig. 3.4, the shearing cells are initially in the position indicated with solid lines. As the rotor grid moves, they pass through a stage shown with dotted lines. Finally they end up in the position indicated with dashed lines, and at this moment they are readjusted, by changing the logical connections in the program, to the original solid-line cells. Since the shearing cells all have the same area, this process is completely conservative. The flow algorithm uses Ni's Lax-Wendroff scheme with moving-grid modifications for the shearing cells. For the maximum computational efficiency, the calculation on the main rotor grid uses rotor-relative flow variables so that the grid is steady. At the interface one must be careful in converting between stator-relative and rotor-relative variables, particularly in the construction of the numerical smoothing.

3.5   Periodic B.C.'s

When performing a stator/rotor calculation in which the stator and rotor blade pitches are equal, as shown in Fig. 3.5, the periodic boundary condition is very simple. It is assumed that what is happening on the upper periodic boundary is exactly the same as is happening on the lower perioidc boundary, at the same time.

$$U(x, y + P, t) = U(x, y, t) \tag{3.21}$$

In this equation P is the blade pitch. Strictly speaking this statement is an assumption, which may be incorrect for viscous flows. If there is vortex shedding at the trai ng edges there is no particular reason to believe that the shedding at neighboring blades will be in phase. Equation (3.21) prevents the possibility of non-synchronized shedding, but it is

139
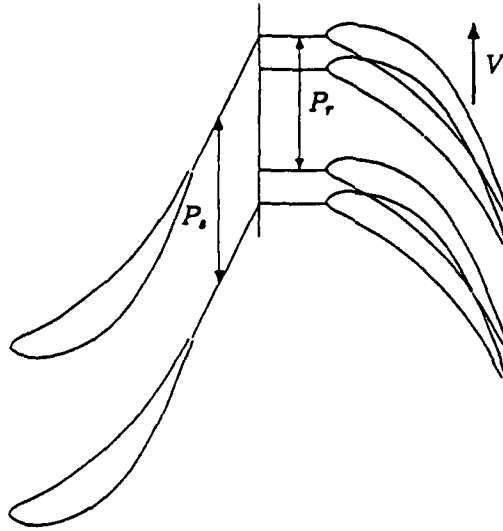
Figure 3.6: Periodic boundary conditions with unequal pitches

believed that this is not a serious error. To check this, calculations could be performed using multiple blade passages, for example with four stators and four rotors, with the periodic boundary condition having P replaced with $4P$. If there are no significant differences then it will show that our assumption is reasonably valid, or at least is a good approximation.

When performing a stator/rotor calculation in which the stator and rotor blade pitches are not equal, as shown in Fig. 3.6, the periodic boundary condition is much more complicated. If, as indicated, the rotor pitch is smaller than the stator pitch, then at one instant the lower rotor is aligned with the lower stator, and a little later the upper rotor is aligned with the upper stator. The time delay is equal to the difference in pitches divided by the rotor wheel speed.

$$\Delta T = (P_s - P_r)/V \tag{3.22}$$

The periodic boundary condition therefore has this time delay built in. On the stator side of the interface, the boundary condition is

$$U(x, y + P_s, t) = U(x, y, t + \Delta T), \tag{3.23}$$

while on the rotor side it is

$$U(x, y + P_r, t) = U(x, y, t + \Delta T). \tag{3.24}$$

The question now is how to implement the periodic boundary condition. In the equal pitch case it extremely simple. The boundary condition is exactly satisfied by logically
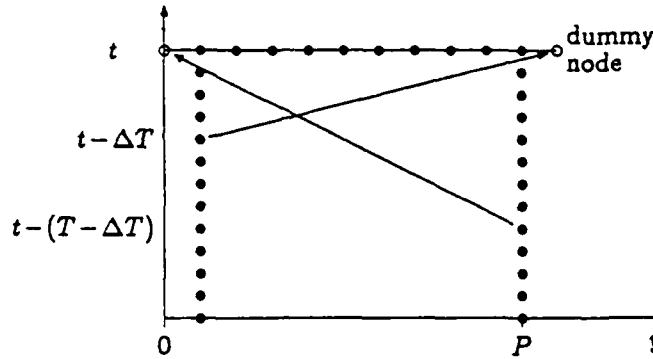
Figure 3.7: Erdos periodic boundary condition treatment

equating the nodes on the lower and upper periodic boundaries, saying that the corresponding periodic nodes are in fact the same node.

In the case of unequal pitches this no longer works. The first solution developed for this problem is due to Erdos [16]. As shown in Fig. 3.7, Erdos implemented the periodic boundary conditions by using a line of dummy nodes just outside the computational domain. The dummy nodes on the upper periodic boundary are updated by using the lagged boundary condition and setting their values equal to the values on the lower boundary at the time ΔT earlier. The dummy nodes on the lower periodic boundary are updated by assuming that the flow field is periodic in time, with period T equal to the blade-passing period. Thus,

$$U(x, y, t) = U(x, y, t - T) = U(x, y + P, t - (T - \Delta T)). \tag{3.25}$$

This allows the lower dummy nodes to be set from stored values along the upper boundary.

There are three problems with this approach. The first is it requires a lot of storage, which becomes a particular problem in three dimensions. The second is that the lagging of boundary information greatly delays convergence to a periodic state. The third, and most serious problem, is the assumption that a final temporally periodic state exists. This is not true in viscous applications with multiple frequencies, such as will occur when the blade passing and vortex shedding frequencies are independent. Thus Erdos' method is limited to inviscid applications.

I have developed an alternative approach of "time-inclined computational planes" which overcomes the limitations of Erdos' method. The basic concept is illustrated in Fig. 3.8. Whereas usually all of the nodes in a computational time-level are at the same physical time, in this technique the computational plane is "tilted" such that nodes at different values of y are at different times. In particular, the nodes on the upper periodic boundary
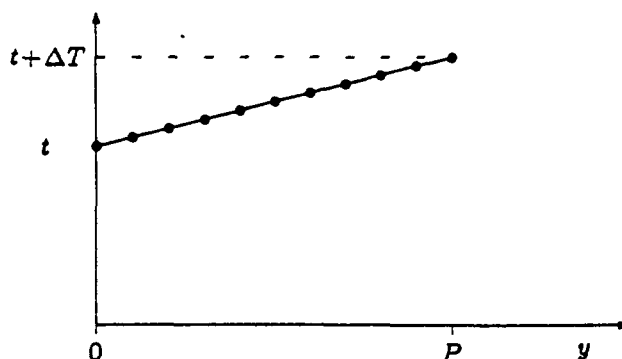
Figure 3.8: Giles periodic boundary condition treatment

are exactly ΔT later in time than the corresponding nodes on the lower periodic boundary. Thus the lagged periodic boundary condition can be trivially implemented again by logically identifying the upper and lower as being the same.

Mathematically this technique corresponds to a transformation to new computational coordinates.

$$
\begin{aligned}
x' &= x \\
y' &= y \\
t' &= t - \lambda y,
\end{aligned}
\tag{3.26}
$$

where

$$
\lambda = \Delta T / P.
\tag{3.27}
$$

Under this transformation, the periodic boundary condition becomes simply

$$
U(x', y' + P, t') = U(x', y', t'),
\tag{3.28}
$$

and the Euler equations become

$$
\frac{\partial}{\partial t'}(U - \lambda G) + \frac{\partial F}{\partial x'} + \frac{\partial G}{\partial y'} = 0
\tag{3.29}
$$

For a perfect gas U can be calculated directly from $U - \lambda G$, and so the modifications to the basic algorithm turn out to be relatively minor, involving at most an additional 15% computational effort.

Further information can be found in a number of references [22,20,19,18].

As an example of the kind of calculation which can be performed with an Euler method, Fig. 3.9 shows several snapshots of one period of a stator/rotor interaction. This a transonic turbine stage in which the stator and rotor outflow Mach numbers are both approximately 1.1. Consequently, there is an oblique shock system at the trailing edge of both stators and

rotors. In the case of the stators upstream, one oblique shock propagates upstream to the neighboring stator, and then reflects downstream. The other shock propagates downstream and strikes the downstream rotor. This produces a reflected shock, one part of which moves across to the neighboring rotor, and the other part of which moves upstream again to the next stator. This interaction leads to extremely large unsteady forces on the rotor, which in practice could lead to significant blade vibration. This calculation required slightly less than the equivalent of one hour of CRAY CPU time. At this speed and cost, it is still not practical to perform large numbers of calculations on a regular basis. However, it is a very practical tool for investigating specific engineering problems or for use as a research tool to understand specific physical phenomena. It is quite possible that within ten years the leading gas turbine manufacturers will be using such codes on a regular basis in their design systems for the assessment of unsteady forces in cases where the linear methods are considered to be not sufficiently accurate.
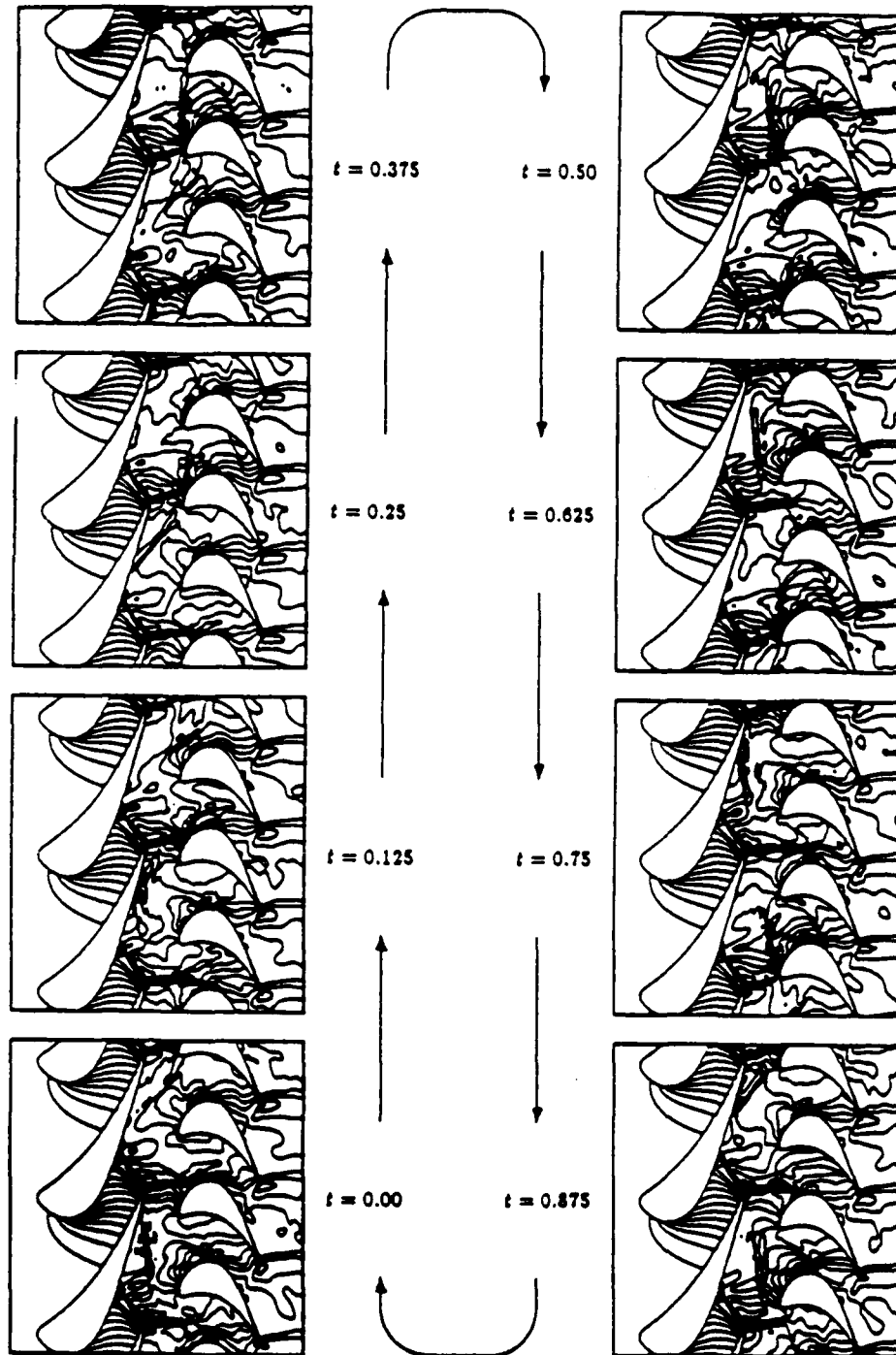
Figure 3.9: Pressure contours in unsteady stator/rotor interaction

Chapter 4

Unsteady N-S Methods

4.1 Basic Equations

The two-dimensional, compressible N-S equations are

$$\frac{\partial U}{\partial t} + \frac{\partial F}{\partial x} + \frac{\partial G}{\partial y} = 0 \tag{4.1}$$

where

$$F = \begin{pmatrix} \rho u \\ \rho u^2 + p - \tau_{xx} \\ \rho uv - \tau_{xy} \\ \rho uH - u\tau_{xx} - v\tau_{xy} + q_x \end{pmatrix}, \quad G = \begin{pmatrix} \rho v \\ \rho uv - \tau_{xy} \\ \rho v^2 + p - \tau_{yy} \\ \rho vH - u\tau_{xy} - v\tau_{xy} + q_y \end{pmatrix} \tag{4.2}$$

The following auxiliary equations are needed to define the stresses and heat conduction terms.

$$\tau_{xx} = \mu\left(\frac{4}{3}\frac{\partial u}{\partial x} - \frac{2}{3}\frac{\partial v}{\partial y}\right), \quad \tau_{yy} = \mu\left(\frac{4}{3}\frac{\partial v}{\partial y} - \frac{2}{3}\frac{\partial u}{\partial x}\right), \quad \tau_{xy} = \mu\left(\frac{\partial u}{\partial y} + \frac{\partial v}{\partial x}\right) \tag{4.3}$$

$$q_x = k\frac{\partial T}{\partial x}, \quad q_y = k\frac{\partial T}{\partial y} \tag{4.4}$$

To understand qualitatively the nature of a viscous flow it is helpful to form order-of-magnitude estimates of the length scales and time scales involved. Steady-state boundary layer length scales can be estimated using the following variables which represent typical values of certain important parameters.

- L = length scale for variations along boundary layer

- δ = length scale for variations across boundary layer

- U = typical magnitude of velocity along boundary layer

- V = typical magnitude of velocity across boundary layer

- ν = typical magnitude of kinematic viscosity

Matching viscous and convective terms in the x-momentum equation gives

$$U\frac{U}{L} \sim \nu\frac{U}{\delta^2} \implies \frac{\delta}{L} \sim \left(\frac{UL}{\nu}\right)^{-1/2} \equiv \text{Re}_L^{-1/2} \tag{4.5}$$

Similarly, matching terms in the mass equation gives

$$\frac{V}{U} \sim \frac{\delta}{L} \tag{4.6}$$

Three time scales can also be estimated on an order-of-magnitude basis. The first is the convection time scale which is the time taken to convect the distance L.

$$T_c = \frac{L}{U} \tag{4.7}$$

The second is the time scale for diffusion of momentum across the boundary layer.

$$T_d = \frac{\delta^2}{\nu} = \left(\frac{\delta}{L}\right)^2 \frac{UL}{\nu} \frac{L}{U} \sim T_c \tag{4.8}$$

As this equation shows, the diffusion time scale is comparable to the convection time scale. The final time scale is the time required for a pressure wave to cross the boundary layer. This time scale is important because it is the one which determines the maximum stable time-step for explicit algorithms, and it turns out that it is very much smaller than the convection time scale for the large Reynolds numbers which are typical in turbomachinery.

$$T_p = \frac{\delta}{c} = \frac{U}{c} \frac{\delta}{L} \frac{L}{U} \sim M \operatorname{Re}^{-1/2} T_c \ll T_c \tag{4.9}$$

Based on the fact that $\delta \ll L$, one often uses the thin-shear-layer version of the Navier-Stokes equations in which streamwise diffusion is ignored, and the definition of the remaining stress terms is simplified accordingly.

$$F = \begin{pmatrix} \rho u \\ \rho u^2 + p \\ \rho uv \\ \rho uH \end{pmatrix}, \quad G = \begin{pmatrix} \rho v \\ \rho uv - \mu u_y \\ \rho v^2 + p \\ \rho vH - \mu uu_y - kT_y \end{pmatrix} \tag{4.10}$$

It is important to note that using a coarse grid in the streamwise direction has a similar effect, since even if the full N-S equations are used the numerical smoothing terms in the streamwise direction will be substantially larger than the streamwise viscous stresses.

4.2 Turbulence Modelling

Turbulence modelling is an extremely important subject which has already been covered by other lectures in this series, and is also presented in an excellent review paper by Rubesin [45]. However, there are some brief comments which I would like to make on the subject as it relates to the calculation of unsteady flows.

There are three major classes of turbulence model which are used in engineering calculations of steady flows. The first class is algebraic models, of which the Cebeci-Smith [9]

and Baldwin-Lomax [4] models are probably the best known examples. In these models the effect of the turbulence is modelled by a turbulent "viscosity" μ_t which is based on the local boundary layer velocity profile. This approach is very good in the inner layer of a turbulent boundary layer (the so-called laminar sub-layer and the log-law region) because that part of the boundary layer is in a dynamic equilibrium between the generation, diffusion and dissipation of turbulence, with characteristic length scales and time scales which are so small that the turbulent mixing exhibits very little "history" of the nature of the boundary layer further upstream. In the outer (wake) region of the boundary layer, the time scales are much longer and so history effects are more significant, and the algebraic models are more in error.

The one-half equation models, of which the Johnson-King model [32] is a good example, attempt to rectify the principal weakness of the algebraic models by using the same inner layer defintion and an outer layer formulation in which an o.d.e. is integrated in the streamwise direction to provide time lag effects.

The third class of methods is based upon the solution of one or more partial differential equations. In the one equation models, such as the Wilcox-Rubesin model [52], μ_t is based on an algebraically specified mixing length l and a turbulent kinetic energy k which is calculated by solving a convection/diffusion p.d.e. In two equation models, such as the Jones-Launder model [33], μ_t is based on the turbulence dissipation rate ϵ and the turbulent kinetic energy k, both of which calculated by solving a convection/diffusion p.d.e.

Having briefly listed the main characteristics of the most popular turbulence models, let us now examine some of the problems which are encountered in unsteady flows in turbomachinery.

The first problem is wake/boundary layer interaction. Experiments by Doorly at Oxford have shown that the passage of a turbulent wake over a laminar boundary layer can cause that boundary to undergo premature transition [13,46]. Unsteady heat transfer measurements clearly show that the heat transfer changes from a laminar value, to a turbulent value as the wake passes by, and then later returns to a laminar value when the boundary layer re-laminarizes. None of the current turbulence models have been developed with such a situation in mind, and so extensive work may be required to extend them to include the effect of intermittent freestream turbulence. The models which are based upon a p.d.e. for the turbulent kinetic energy seem the most likely to succeed in this regard.

A second problem is shock/boundary layer interaction. Doorly's experiments also show a shock impinging near the leading edge of a downstream blade which produces a separation bubble which later collapses and appears to form a turbulent spot which grows and convects downstream. Another area of shock/boundary layer interactions is in transonic diffusers, in which the interaction with acoustic feedback can lead to a self-excited instability. It

seems very likely that the accurate calculation of this will depend critically on unsteady turbulence modelling incorporating the correct time delays and growth rates, but this is an area which has not been extensively studied.

A third problem is vortex shedding. The boundary layers at the trailing edges of turbines are turbulent, but the basic mechanism behind vortex shedding is not a turbulent process. However, turbulence models treat the extremely high velocity gradients in vortices as "turbulence producing" leading to large values of turbulent viscosity and therefore rapid diffusion. Experimentally, it is known that vortices can convect a large distance before breaking down into turbulence, but this is not what will be predicted by current turbulence models.

These personal comments are not meant to be overly critical of the current turbulence models. As stated at the beginning of this section, turbulence modelling is an extremely difficult area, and progress in validating new modelling concepts requires very time-consuming numerical testing. However, some of the above problem areas will need to be addressed in the future if we are to successfully predict the heat transfer and losses produced by unsteady flows in turbomachinery.

4.3 Periodic B.C.'s

As with the inviscid equations in the last chapter, there is a time lag in the periodic boundary condition in cases in which the stator and rotor pitches are not equal. This time lag is overcome by again using the concept of "time-inclined" computational planes, as introduced in the last chapter. The transformed N-S equations are

$$\frac{\partial Q}{\partial t'} + \frac{\partial F}{\partial x'} + \frac{\partial G}{\partial y'} = 0 \qquad (4.11)$$

where

$$Q = U - \lambda G \qquad (4.12)$$

The difference from the inviscid time-inclined equations is that now F and G include viscous stress terms, and so Q contains derivatives of U and there is no simple algebraic transformation from Q to U.

The solution to this problem is to simply ignore the derivative terms in Q, or equivalently to replace Q by $U - \lambda G_{inviscid}$. This procedure can be justified for large Reynolds numbers as follows. Time derivatives are comparable in magnitude to streamwise spatial derivatives, and so

$$\frac{\partial^2 u}{\partial t' \partial y'} = O\left(\frac{\partial^2 u}{\partial x' \partial y'}\right) = O\left(Re^{-\frac{1}{2}}\right) \times \frac{\partial^2 u}{\partial y'^2} \qquad (4.13)$$
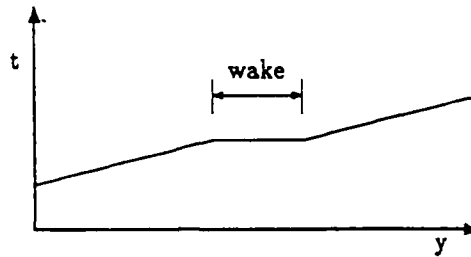
Figure 4.1: Alternati e inclined computational plane for viscous calculations
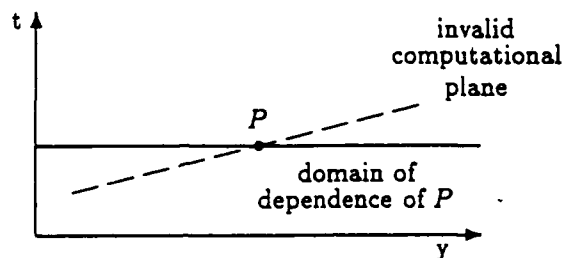

Figure 4.2: Low Reynolds number domain of dependence

Therefore, the neglected terms are comparable in magnitude to the terms which are dropped in the usual thin-shear-layer N-S equations, due to their being much smaller than the dominant diffusive terms in the boundary layer.

An alternative approach which would also work for high Reynolds numbers is to use "time-tilting" only outside the narrow viscous regions around each blade, and in each wake. This idea is illustrated in Fig. 4.1. The high-Reynolds number assumption is required to ensure that the wakes and boundary layers form a small fraction of the total domain.

Both of the above approaches fail at low Reynolds numbers. This is correct and proper since, as shown in Fig. 4.2, parabolic equations have infinite speed of propagation of information and any inclined computational plane will not fully include this domain of dependency, and so cannot produce the correct solution.

4.4   Algorithms

Several researchers have developed explicit algorithms for the Navier-Stokes equations which are a natural extension of corresponding methods for the Euler equations. For example, Chima [10] has developed a Navier-Stokes extension of Jameson's cell-centered scheme, and Davis [12] has developed a Navier-Stokes extension of Ni's Lax-Wendroff algorithm.

The primary advantages of these explicit methods are that they are relatively simple, very easily vectorized on today's vector and parallel computers, and can be used on unstructured meshes with grid adaptation.

The disadvantage with these methods for unsteady calculations is the timestep restriction. For a convective process, the timestep limit is

$$\Delta t < \frac{\Delta x}{L} T_c \qquad (4.14)$$

where T_c is the convective time-scale defined earlier in this chapter. For the process of diffusion across the boundary layer, the timestep limit is

$$\Delta t < \left(\frac{\Delta y}{\delta}\right)^2 T_d \qquad (4.15)$$

Since T_c is of the same order as T_d, these two restrictions are comparable, assuming the number of points across the boundary layer is not much more than 20. The limiting timestep restriction, however, is due to the propagation of pressure waves across the boundary layer. This limit is

$$\Delta t < \frac{\Delta y}{\delta} T_p \sim \frac{\Delta y}{\delta} \times O\left(M \, \mathrm{Re}^{-\frac{1}{2}} T_c\right) \qquad (4.16)$$

For typical Reynolds numbers of 10^6, this places a very severe restriction upon the maximum stable timestep. In steady calculations, this problem is overcome to a large extent by the use of local timesteps, implicit smoothing and multigrid acceleration techniques. However, typical unsteady calculations require 10^4 iterations per blade-passing period.

The only true solution to this difficulty is the use of an implicit method. To present the full spectrum of implicit algorithms, it is helpful to begin with the fully implicit nonlinear scheme. On a regular Cartesian mesh, as shown in Fig. 4.3, the Navier-Stokes equations

$$\frac{\partial U}{\partial t} + \frac{\partial F}{\partial x} + \frac{\partial G}{\partial y} = 0 \qquad (4.17)$$

can be approximated using Backward Euler time discretization as

$$U_{j,k}^{n+1} - U_{j,k}^n = -\frac{\Delta t}{\Delta x}\left(F_{j+\frac{1}{2},k}^{n+1} - F_{j-\frac{1}{2},k}^{n+1}\right) - \frac{\Delta t}{\Delta y}\left(G_{j,k+\frac{1}{2}}^{n+1} - G_{j,k-\frac{1}{2}}^{n+1}\right) \qquad (4.18)$$

It is important to note that the viscous fluxes F and G include derivative terms. These are evaluated using the nearest surrounding nodes. For example, the inviscid components of $F_{j+\frac{1}{2},k}$ are based on $U_{j,k}$ and $U_{j+1,k}$, while the viscous components also involve $U_{j,k-1}, U_{j+1,k-1}, U_{j,k+1}, U_{j+1,k+1}$. Thus, all nine sets of flow variables shown in Fig. 4.3 are involved in defining the fluxes into and out of cell (j,k).

The fully implicit scheme as it stands so far is a nonlinear system of equations for U at the new time-level. Since this system cannot be solved in closed form, the next step is to linearize it. Conceptually, linearizing gives

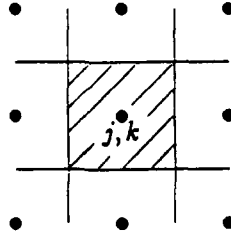$$F^{n+1} \approx F^n + A \, \Delta U, \qquad (4.19)$$

Figure 4.3: Flow variables used in cell-centered implicit N-S algorithms

where

$$A \equiv \frac{\partial F}{\partial U}, \qquad \Delta U \equiv U^{n+1} - U^n. \tag{4.20}$$

This equation is deceptively simple in appearance, since A is actually a 4×24 matrix representing the derivatives of each component of F with respect to each component of U at the six locations involved in the definition of F. Linearizing G^{n+1} in a similar manner gives the following, linearized, fully implicit scheme.

$$\left(I + \frac{\Delta t}{\Delta x} \, \delta_z A + \frac{\Delta t}{\Delta y} \, \delta_y B \right) \Delta U = -\frac{\Delta t}{\Delta x} \, \delta_z F^n - \frac{\Delta t}{\Delta y} \, \delta_y G^n \tag{4.21}$$

There are several good features to this scheme. The main one is that it is unconditionally stable for a linear, convection diffusion problem. Also, for the same linear problem with implicit boundary conditions in the limit $\Delta t \to \infty$ it gives the steady-state solution in one step. For unsteady calculations, the choice of Δt is limited only by the accuracy desired.

The bad news about this method is that because the implicit operator includes all nine neighboring ΔU's the number of operations required to solve the linear system of equations is $O(J^4)$ for a two-dimensional $J \times J$ grid, and $O(J^7)$ for a three-dimensional $J \times J \times J$ grid. This is considerably more than the $O(J^2)$ and $O(J^3)$ operations required per timestep for an explicit method in two and three dimensions, respectively.

To overcome this problem of efficiency, Beam and Warming developed the technique of approximate factorization [5]. Under this procedure the linear, fully implicit operator is factored approximately to give

$$\left(I + \frac{\Delta t}{\Delta x} \, \delta_z A \right) \left(I + \frac{\Delta t}{\Delta y} \, \delta_y B \right) \Delta U = -\frac{\Delta t}{\Delta x} \, \delta_z F^n - \frac{\Delta t}{\Delta y} \, \delta_y G^n \tag{4.22}$$

which can be rewritten in two steps as

$$\left(I + \frac{\Delta t}{\Delta x} \, \delta_z A \right) \Delta U^* = -\frac{\Delta t}{\Delta x} \, \delta_z F^n - \frac{\Delta t}{\Delta y} \, \delta_y G^n$$

$$\left(I + \frac{\Delta t}{\Delta y} \, \delta_y B \right) \Delta U = \Delta U^* \tag{4.23}$$

In two dimensions this algorithm is still unconditionally stable for the model linear problem. In three dimensions, it is unconditionally unstable for the model problem without any numerical smoothing. However, the instability is extremely weak, and is cured by the addition of the standard numerical smoothing. The implicit operators are now one-dimensional, and so the solution requires only block tri-diagonal inversions. Consequently, the computational cost is reduced to about 5 times more than an explicit scheme.

The efficiency gains have not been achieved without paying a cost. The factorization error which has been introduced is

$$\frac{\Delta t^2}{\Delta x \, \Delta y} \, \delta_x A \, \delta_y B \, \Delta U. \tag{4.24}$$

This is second-order when $\Delta t = O(\Delta x)$, but becomes much larger when $\Delta t \gg \Delta x, \, \Delta y$. In the limit as $\Delta t \to \infty$, the convergence rate actually goes to zero, and the optimal convergence occurs when

$$\Delta t \sim 5 \frac{\Delta x}{|u| + c} \tag{4.25}$$

This behavior means that implicit schemes have no significant advantages over explicit schemes for the Euler equations, and only emerge as winners in the solution of the Navier-Stokes equations because of their timestep being independent of the extremely tight grid spacing across the boundary layers.

One important point which needs to be mentioned is the potential ill-conditioning of the implicit operator. For the scalar convection equation the 1-D implicit operator obtained using central differencing has the following form.

$$A = \begin{pmatrix}
1 & \lambda & & & & & \\
-\lambda & 1 & \lambda & & & & \\
& -\lambda & 1 & \lambda & & & \\
& & -\lambda & 1 & \lambda & & \\
& & & -\lambda & 1 & \lambda & \\
& & & & -\lambda & 1 & \lambda \\
& & & & & -\lambda & 1
\end{pmatrix} \tag{4.26}$$

where

$$\lambda = \frac{u \Delta t}{2 \Delta x} \tag{4.27}$$

This matrix is ill-conditioned for $\lambda \gg 1$, and will lead to very large amplification of machine roundoff error. This potential problem is overcome by either adding implicit smoothing, or using upwind differencing [43].

To eliminate the splitting error introduced by the factorization, a number of researchers, such as Rai [43], use the technique of sub-iteration. What this means is that there is an

iterative process embedded within each timestep. The process begins by setting

$$\Delta U = 0 \tag{4.28}$$

The next step is to calculate δU using the following factorized discrete equation.

$$\left(I + \frac{\Delta t}{\Delta x}\delta_x A\right)\left(I + \frac{\Delta t}{\Delta y}\delta_y B\right)\delta U = -\Delta U - \frac{\Delta t}{\Delta x}\delta_x(F^n + A\Delta U) - \frac{\Delta t}{\Delta y}\delta_y(G^n + B\Delta U) \tag{4.29}$$

The third step is to define an improved value of ΔU by

$$\Delta U^{new} = \Delta U^{old} + \delta U. \tag{4.30}$$

One then can iterate by repeating the last two steps as often as one wishes.

Iterating once gives the standard factored algorithm. Iterating very many times converges to the ΔU which is the solution of the linear, fully implicit method. In practice, Rai usually iterates three times, and finds that this eliminates most of the factorization error.

Another algorithmic approach to solving the Navier-Stokes equations is a semi-implicit scheme in which an explicit algorithm is employed in the streamwise direction, and an implicit algorithm in employed in the normal direction [1]. In this scheme the timestep is restricted by the streamwise CFL limit, and so it retains the efficiency of implicit algorithms. One of the principal features of this method is that it allows the use of an unstructured mesh in the streamwise direction (and in the crossflow direction in three dimensions).

A completely different class of methods are hybrids, in which the Navier-Stokes equations are solved using one algorithm in the viscous regions, the boundary layers and possibly the wakes, while the Euler equations are solved with a different algorithm in the remaining majority of the flow field. The two calculations are coupled together by a conservative flux treatment at the interface. The reasons for this approach are that explicit node-based Euler algorithms are second order accurate on flexible unstructured grids, while the implicit cell-based Navier-Stokes algorithms are efficient and second order accurate on smooth structured grids which are easily generated for the boundary layer on blades. One example of this approach is an algorithm developed by Krouthèn [36]. This algorithm uses Jameson's cell-centered spatial discretization in both regions. In the inviscid region a multi-stage algorithm is used for the time integration, while in the viscous region the Beam-Warming approximate factorization method is used.

To illustrate the capabilities of unsteady viscous capabilities, Figs. 4.4 and 4.5 present results from a paper by Rai [44], in which he calculates a two-dimensional viscous stator/rotor interaction with an incoming hot streak from the combustor upstream. The first figure shows temperature contours at one particular instant. Note that there is clear indication of vortex shedding at the trailing edges of the rotors. The second figure is a comparison with an experiment performed by Butler *et al* [7]. The plotted variable is the difference
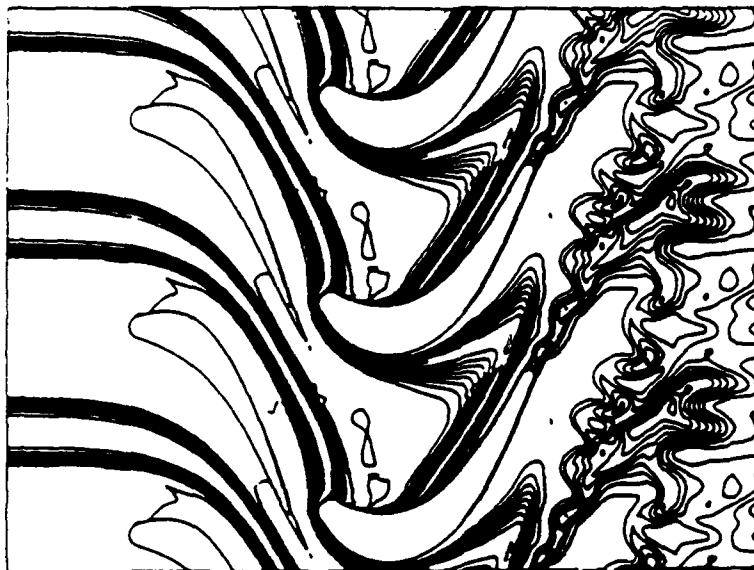
Figure 4.4: Temperature contours in unsteady hot streak calculation

between the average surface temperature and the temperature of the cold fluid, divided by the difference between the average temperature of the incoming fluid (including the hot streak) and the cold fluid temperature. A value of 1.0 is what would would be expected from a linear analysis. A value greater than 1.0 corresponds to an accumulation of hot fluid, and experimentally this is observed to occur on the pressure surface, and can lead to excessive temperatures on the rotor. Because of a number of differences, such as three-dimensionality, between the experiment and the calculation, there is very poor agreement between the two. Another numerical investigation by Krouthén [36] examined the role of various variables, but achieved only slightly better agreement. These calculations by required the equivalent of a few hours of CRAY CPU time. This large cost means that these methods are not yet suitable for regular 'production' use as part of an engineering design system. It is also partly resposible for the fact that much work remains to be done in the validation and application of Navier-Stokes methods for unsteady flows. However, the use of these methods will probably grow rapidly over the next ten years as computer speeds increase and the costs decrease.
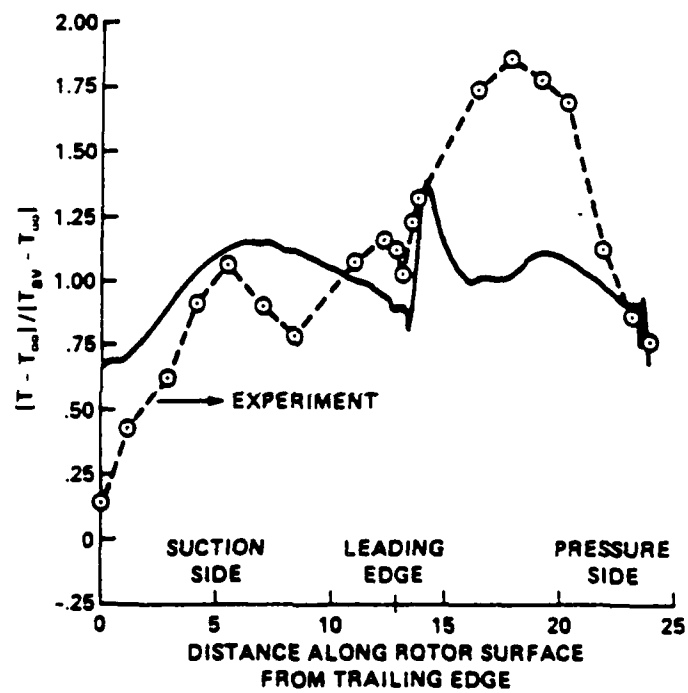
Figure 4.5: Average surface temperatures in unsteady hot streak calculation

Bibliography

[1] S. R. Allmaras and M. B. Giles. *A Coupled Euler/Navier-Stokes Algorithm For Unsteady 2-D Transonic Flows*. AIAA Paper 89-0556, 1989.

[2] D. A. Ashworth, J. E. LaGraff, D. L. Schultz, and K. J. Grindrod. Unsteady Aerodynamic and Heat Transfer Processes in a Transonic Turbine Stage. *Journal of Engineering for Gas Turbines and Power*, 107:1022–1030, 1985.

[3] H. Atassi and T. J. Akai. *Aerodynamic Force and Moment on Oscillating Airfoils in Cascade*. ASME Paper 79-GT-111, 1979.

[4] B. S. Baldwin and H. Lomax. *Thin-Layer Approximation and Algebraic Model for Separated Turbulent Flows*. AIAA Paper 78-257, 1978.

[5] R. Beam and R. Warming. An Implicit Factored Scheme for the Compressible Navier-Stokes equations. *AIAA Journal*, 16:393–403, 1978.

[6] A. Binder, W. Forster, H. Kruse, and H. Rogge. *An Experimental Investigation into the Effects of Wakes on the Unsteady Turbine Rotor Flow*. ASME Paper 84-GT-178, 1984.

[7] T.L. Butler, O.P. Sharma, H.D. Joslyn, and R.P. Dring. *Redistribution of an Inlet Temperature Distortion in an Axial Flow Turbine Stage*. AIAA Paper 86-1468, 1986.

[8] J.R. Caspar and J.M. Verdon. Numerical Treatment of Unsteady Subsonic Flow Past an Oscillating Cascade. *AIAA Journal*, 19:1531–1539, 1981.

[9] T. Cebeci and A. M. O. Smith. *Analysis of Turbulent Boundary Layers*. Academic Press, 1974.

[10] R. V. Chima. Explicit Multigrid Algorithm for Quasi-Three-Dimensional Viscous Flows in Turbomachinery. *AIAA Journal of Propulsion and Power*, 3(5):397–405, 1987.

[11] J. F. Dannenhoffer III and J. R. Baron. *Robust Grid Adaptation for Complex Transonic Flows*. AIAA Paper 86-0495, 1986.

[12] R. L. Davis and J. F. Dannenhoffer. *Adaptive Grid Embedding Navier-Stokes Technique for Cascade Flows*. AIAA Paper 89-0204, 1989.

[13] D. J Doorly, M. L. G. Oldfield, and C. T. J. Scrivener. *Wake-Passing in a Turbine Rotor Cascade.* Presented at the AGARD Symposium on Heat Transfer and Cooling in Gas Turbines, AGARD PEP CP-390, 1985.

[14] R. P. Dring, H. D. Joslyn, L. W. Hardin, and J. H. Wagner. Turbine Rotor-Stator Interaction. *Journal of Engineering for Power*, 104:1–14, October 1982.

[15] A. H. Epstein, J. B. Gertz, P. R. Owen, and M. B. Giles. Vortex Shedding in High-Speed Compressor Blade Wakes. *AIAA Journal of Propulsion and Power*, 4(3), May/June 1988.

[16] J. I. Erdos, E. Alzner, and W. McNally. Numerical Solution of Periodic Transonic Flow Through a Fan Stage. *AIAA Journal*, 15:1559–1568, Nov 1977.

[17] H. J. Gibeling, R. C. Buggeln, S. Y. Chen, and H. V. McConnaughey. *An Implicit Navier-Stokes Analyses of Turbine Rotor-Stator Interaction.* AIAA Paper 88-3090, 1988.

[18] M. B. Giles. Calculation of Unsteady Wake Rotor Interaction. *AIAA Journal of Propulsion and Power*, 4(4), July/August 1988.

[19] M. B. Giles. Developments in the Calculation of Unsteady Turbomachinery Flow. In K. W. Morton and M. J. Baines, editors, *Numerical Methods for Fluid Dynamics III*, pages 45–64, C ˉ ˉʲ University Press, 1988.

[20] M. B. Giles. *Generalized Conservation Cells for Finite Volume Calculations.* AIAA Paper 87-1118-CP, 1987.

[21] M. B. Giles. *Stator/Rotor Interaction in a Transonic Turbine.* AIAA Paper 88-3093, 1988.

[22] M. B. Giles. *UNSFLO: A Numerical Method for Unsteady Inviscid Flow in Turbomachinery.* Technical Report 195, MIT Gas Turbine Laboratory, 1988.

[23] J.P. Gostelow. *Cascade Aerodynamics.* Pergamon Press, 1984.

[24] E. Greitzer. The Stability of Pumping Systems – The 1980 Freeman Scholar Lecture. *Journal of Fluids Engineering*, 103:193–242, 1981.

[25] G. R. Guenette, A. H. Epstein, M. B. Giles, R. Haimes, and R. J. G. Norton. *Fully Scaled Transonic Turbine Rotor Heat Transfer Measurements.* ASME Paper 88-GT-171, 1988.

[26] K. C. Hall. *A Linearized Euler Analysis of Unsteady Flows in Turbomachinery.* PhD thesis, M.I.T., Sept 1987.

[27] K. C. Hall and E. F. Crawley. *Calculation of Unsteady Flows in Turbomachinery Using the Linearized Euler Equations.* Proceedings of Fourth Symposium on Unsteady Aerodynamics and Aeroelasticity of Turbomachines and Propellers, Sept 1987.

[28] M. G. Hall. *Cell-Vertex Multigrid Schemes for Solution of the Euler Equations.* Technical Report 2029, Royal Aircraft Establishment, Mar 1985.

[29] H. P. Hodson. *Measurements of Wake-Generated Unsteadiness in the Rotor Passages of Axial Flow Turbines.* ASME Paper 84-GT-189, 1984.

[30] A. Jameson. Current status and future directions of computational transonics. In A. K. Noor, editor, *Computational Mechanics - Advances and Trends*, pages 329–367, ASME, 1986.

[31] A. Jameson, W. Schmidt, and E. Turkel. *Numerical Solutions of the Euler Equations by Finite Volume Methods Using Runge-Kutta Time-Stepping Schemes.* AIAA Paper 81-1259, 1981.

[32] D. A. Johnson and L. S. King. A mathematically simple turbulence model for attached and separated turbulent boundary layers. *AIAA Journal*, 23:1684–1692, Nov. 1985.

[33] W. P. Jones and B. E. Launder. The prediction of laminarization with a two-equation model of turbulence. *International Developments in Heat Transfer*, 15:303–314, 1972.

[34] H.D. Joslyn, R.P. Dring, and O.P. Sharma. Unsteady Three-Dimensional Turbine Aerodynamics. *Journal of Engineering for Power*, 105:322–331, 1983.

[35] J. L. Kerrebrock and A. A. Mikolajczak. *Intra-Stator Transport of Rotor Wakes and Its effect on Compressor Performance.* ASME Paper 70-GT-39, 1970.

[36] B. Krouthén and M.B. Giles. *Numerical Investigation of Hot Streaks in Turbines.* AIAA Paper 88-3015, 1988.

[37] J. P. Lewis, R. A. Delaney, and E. J. Hall. *Numerical Prediction of Turbine Vane-Blade Interaction.* AIAA Paper 87-2149, 1987.

[38] R.-H. Ni. A Multiple Grid Scheme for Solving the Euler Equations. *AIAA Journal*, 20:1565–1571, Nov 1981.

[39] R.-H. Ni. *Nonstationary Aerodynamics of Arbitrary Cascades in Compressible Flow.* PhD thesis, Stevens Institute of Technology, June 1974.

[40] R.-H. Ni. *A Rational Analysis of Periodic Flow Perturbations in Supersonic Two-Dimensional Cascade.* ASME Paper 78-GT-176, 1978.

[41] R.-H. Ni and F. Sisto. *Numerical Computation of Nonstationary Aerodynamics of Flat Plate Cascades in Compressible Flow.* ASME Paper 75-GT-5, 1975.

[42] M. M. Rai. *Navier-Stokes Simulations of Rotor-Stator Interaction Using Patched and Overlaid Grids.* AIAA Paper 85-1519, 1985.

[43] M. M. Rai. *Unsteady Three-Dimensional Navier-Stokes Simulations of Turbine Rotor-Stator Interaction.* AIAA Paper 87-2058, 1987.

[44] M. M. Rai and R. P. Dring. *Navier-Stokes Analyses of the Redistribution of Inlet Temperature Distortions in a Turbine.* AIAA Paper 87-2146, 1987.

[45] M. W. Rubesin. *Turbulence Modeling for Aerodynamic Flows.* AIAA Paper 89-0606, 1989.

[46] D. L. Schultz, D. A. Ashworth, J. E. LaGraff, M. J. Rigby, and A. B. Johnson. *Wake and Shock Interactions in a Transonic Turbine Stage.* AGARD PEP CP-401, 1986.

[47] O. P. Sharma, E. Renaud, T. L. Butler, K. Millsaps, R. P. Dring, and H. D. Joslyn. *Rotor-Stator Interaction in Multi-Stage Axial-Flow Turbines.* AIAA Paper 88-3013, 1988.

[48] S. N. Smith. *Discrete Frequency Sound Generation in Axial Flow Turbomachines.* University of Cambridge, Department of Engineering Report CUED/A-Turbo/TR 29, 1971.

[49] J.M. Verdon. *Unsteady Aerodynamics for Turbomachinery Aeroelastic Applications.* UTRC Report R86-151774-1, United Technologies Research Center, June 1986.

[50] J.M. Verdon and J.R. Caspar. A Linearized Unsteady Aerodynamic Analysis for Transonic Cascades. *Journal of Fluids Mechanics*, 149:403–429, 1984.

[51] D. S. Whitehead. *The Calculation of Steady and Unsteady Transonic Flow in Cascades.* University of Cambridge, Department of Engineering Report CUED/A-Turbo/TR 118, 1982.

[52] D. C. Wilcox and M. W. Rubesin. *Progress in Turbulence Modelling for Complex Flow Fields Including Effects of Compressibility.* NASA TP-1517, 1980, 1981.

APPENDIX B

UNSTEADY FLOW IN TURBOMACHINERY: BASIC PHENOMENA AND PRACTICAL ASPECTS

E.M. Greitzer and C.S. Tan
Gas Turbine Laboratory
Massachusetts Institute of Technology
Cambridge, MA 02139 USA

ABSTRACT

A survey is presented of some of the unsteady flow phenomena associated with modern high performance turbomachinery. The central theme is that increases in performance can be achieved through improved understanding of unsteady flow and incorporation of this understanding into turbomachinery design. Within this overall theme, three main aspects are addressed: 1) the impact that unsteady phenomena can have on so-called steady state performance including interpretation of steady-state instrumentation results, 2) the considerable recent progress in one's ability to compute and to measure these flows, and 3) the new possibilities for using different types of non-uniformities (spatial as well as temporal) to control the flows of interest and thus to enhance the performance of advanced turbomachines and propulsion systems.

1. INTRODUCTION

It is a textbook item to state that turbomachines depend on unsteady fluid dynamic processes for operation and that turbomachinery flows are inherently unsteady. In spite of this, for the majority of current design procedures, unsteadiness tends either to be avoided, by adopting coordinate systems moving with the local blade row of interest, or neglected by assuming that the effects of upstream rows are "mixed out" and potential field effects of downstream rows are negligible. In situations where it is recognized that unsteadiness can impact performance, non-steady effects are often accounted for using correlative procedures, rather than by any truly unsteady calculation.

Work on unsteady fluid flow in turbomachines has thus been concentrated on areas where one cannot, even on the most basic level, avoid dealing with non-steady phenomena, for example aeroelasticity, flow instability, and noise. Even for these problems, however, much of the approach to "prediction" in the design process has been basically empirical. While the various correlations that have been developed provide very useful guidelines over certain regimes, they are often not based on a solid understanding of the fluid physics and hence not capable of extrapolation or extension.

There now appears to be growing recognition that to improve the performance of turbomachines further, one will have to better understand the unsteady flow effects. In this paper, we will discuss some of the unsteady phenomena that affect turbomachinery operation, review some of the progress that has been made over the past decade or so in these areas and,

where appropriate, attempt to point out relevant new research areas. The common thread is the view that increased performance can be obtained through a deeper understanding of unsteady effects.

2. GENERAL BACKGROUND AND SCOPE OF THE PAPER

Some brief comments should be made concerning the material to be presented. We stress that the paper is not meant as an all-inclusive survey, but rather as a more personal perspective on the topic of unsteady flow in turbomachines. As such, a large fraction of the examples and illustrations have been taken from work carried out at MIT and at Cambridge University, simply because the authors are most familiar with the research in these two institutions. The aim, however, is to present the reader with a view of the state of the art as far as research efforts and important problems to be attacked in the field. Throughout the paper, emphasis will be placed on giving useful, if introductory, descriptions of the phenomena that characterize these unsteady flows in advanced turbomachines and propulsion systems.

There were several good reviews of unsteady flows in turbomachines written in the mid 1970's [1], [2], and it is of interest to compare problems and approaches between then and now. First, the situation with respect to computations of unsteady flow has changed considerably. A decade ago, most unsteady computations were for inviscid flow past lightly loaded blades, with just the beginnings of procedures being developed to include loading. There now exist methods to compute (albeit with some questions concerning turbulence modelling) unsteady viscous flow past two- and even three-dimensional blade rows.

The difference in computational power is not just quantitative, for example, slightly better computations of pressure distribution. Rather, it is that one can now carry out "numerical experiments" using the computation to interrogate physical phenomena. This has been the situation for some time in other areas of fluid mechanics (two-dimensional vortex dynamics is one application) where the configurations are simpler, but the ability to do this in a turbomachine geometry is fairly new. We will see below several examples where numerical computations have provided at least tentative conclusions about phenomena which were previously not at all understood.

The situation is also different experimentally, because one can now routinely store and reduce a large amount of unsteady flow data, as well as conditionally sample an unsteady flow field so that data taking is keyed to times when interesting events occur. This has made it possible to examine topics such as the structure of rotating stall cells [3], [4], wake transport through blade passages [5], and unsteady transition in turbomachine boundary layers [6], [7], [8]. From an experimental as well as a theoretical/computational viewpoint, therefore, the situation is qualitatively different than at the point of [1] and [2], and we will attempt to further point up these differences with specific examples.

The organization of the review is as follows. The next section is a short discussion of some basic features of unsteady flows; this serves as an introductory framework from which to view the subsequent examples. We then describe some effects of unsteadiness in situations where the flow into the machine is (nominally) uniform and steady, and where the machine is at, or near, its design point. This includes mass flow capacity in transonic compressors, wake induced transition of blade boundary layers, and implications of flow unsteadiness for data analysis. Following this, several situations with operation at off-design conditions are examined, starting with non-uniform inlet flows (distortions). Instabilities in compressors and compression systems are then addressed, with respect to inception as well as to behavior subsequent to instability onset. This leads naturally into a discussion of the dynamic control of instability, either through active means or through tailoring of the system structural properties. The final topic examined is mixing in turbomachines, as regards both mechanisms and opportunities for its control.

3. SOME BASIC FEATURES OF UNSTEADY FLOWS

There are several features of unsteady flows that are of interest in the present context. First is the potential for the addition or abstraction of energy. In an inviscid, adiabatic flow with no body forces, unsteadiness provides the only mechanism for changing the stagnation enthalpy of a fluid particle, as shown in the equation for the rate of change of stagnation enthalpy along a pathline:

$$\frac{Dh_t}{Dt} = \frac{1}{\rho}\frac{\partial P}{\partial t}$$

A second feature, perhaps less well appreciated, concerns the variation in time average stagnation pressure seen in an unsteady flow. The point can be illustrated using the momentum equations for incompressible inviscid flow. If the velocity is written as a time mean plus a fluctuating part, with the former denoted by an overbar and the latter, which is not necessarily small, by a prime, the momentum equation can be written:

$$\frac{\partial v'}{\partial t} - (\bar{v} + v') \times (\overline{\omega \times \omega'}) = \frac{\nabla P_t}{\rho}$$

Taking the time average of this yields

$$\bar{v} \times \bar{\omega} + \overline{v' \times \omega'} = \frac{\overline{\nabla P_t}}{\rho}$$

If the time mean flow is irrotational, this is

$$\overline{v' \times \omega'} = \frac{\overline{\nabla P_t}}{\rho}$$

Time mean gradients in stagnation pressure due to unsteady flow will thus occur only if the unsteady velocity field is rotational*. Many of the unsteady phenomena of interest in turbomachinery are, in fact, associated with some type of vortical structure. The above two features are closely related since the second implies that the (unsteady) static pressure field associated with the change in stagnation enthalpy is due to some type of vortical structure, for example a row of "bound vortices" which represent a turbine or compressor blade row.

A third aspect, which we will see in several different applications, is the susceptibility of so-called steady-state flows to substantial alteration due to flow instability. This implies the possibility for qualitative, not just quantitative, changes in flow regime due to unsteady perturbations.

One additional point to be noted is that often one's "intuition", which has been developed for steady flow situations, does not apply in cases where there is strong unsteadiness. The stagnation enthalpy is no longer constant along a streamline, the blade force versus inlet angle relations from steady flow are not valid, and it is no longer sufficient that the square of the Mach number be small for compressibility effects to be absent.

It is useful in what follows to refer to some measure of how unsteady a given flow is. For this, an appropriate parameter is the so-called "reduced frequency", which can be introduced as a ratio between the time for the flow to change significantly and the time needed for a fluid particle to connect through the device of interest. If the unsteadiness is periodic

---

* An instructive discussion of this point in a quite different context is given in [9], where the idea of a vortex force, i.e. "an effective force on unit volume of fluid equal to density times vorticity times velocity", is introduced.

with predominant frequency, ω, the length of the device is L, and a characteristic velocity is U, this non-dimensional parameter can be written as

$$\text{Reduced frequency} \sim \frac{\text{flow through time}}{\text{flow change time}} \sim \frac{\omega L}{U}$$

Values of reduced frequency much less than unity imply that unsteady effects are small and that the flow can generally be considered quasi-steady, while those much larger than one mean that unsteady effects are dominant. Many turbomachinery applications have reduced frequency of order unity or higher.

4. UNSTEADY EFFECTS ON UNIFORM INLET FLOW PERFORMANCE: DESIGN POINT OPERATION

Even with nominally "uniform" inlet flow into a multi-row machine at the design point, it is apparent that there are sources of unsteadiness both upstream and downstream of a given row, due to the presence of neighboring blade rows. There are also unsteady effects that are self-excited, such as vortex shedding and motion of the separation location; these can occur even in an isolated rotor. For many of these effects, the reduced frequencies are of order unity or larger*. Also, in modern aircraft compressors, the trend of decreasing aspect ratios means that both wake and potential flow effects (the latter of which scale as the blade pitch) are more important than previously.

4.1 Flow Capacity Variations in Transonic Stages

The first example that we present has been described in connection with the performance of transonic stages (stages where the rotor Mach number is greater than one over a significant portion of the span) in multistage compressors [10]. Experiments are cited in which the flow into a stage was found to be too high by several percent. This is of concern because the stee,`ness of the speedlines in these types of stages means that overflowing leads to performance with low efficiency.

It was hypothesized that the higher flow capacity was linked to the circumferential non-uniformities at rotor inlet, which are seen by the rotor as an unsteady flow. A supporting circumstance was that the compressor had a low aspect ratio, which implied that the non-dimensional spacing between the blade rows was also low, and the wakes have much less opportunity to mix out. (As pointed out in [10], for a given level of diffusion, compressor wake thickness scales as blade chord.)

To investigate this idea, unsteady, two-dimensional, viscous flow computations were carried out [11] for the rotor, using the measured stator exit profiles as upstream conditions. The results of the computations (which one can regard as a numerical experiment in the spirit described above) are shown in Figure 1, where flow capacity of the blade row is seen to be increased over the situation for uniform inlet flow with equivalent mass averaged conditions.

The significance of this result is discussed very wel` ` n [10] where the central theme of this paper is also expressed. Adverse consequences - he· ` a mismatch of the stage - can result due to unsteadiness and present design methods do n· ` account for this. In addition, as shown in the computational studies reported in [12], the parametric dependence of the effect is not simple and its influence on new configurations is unknown.

---

* For problems of rotor-stator interaction, consider the rotor and stator to have roughly equal chords and solidity of unity. If the relative velocity is taken to be approximately equal to wheel speed, the value of the reduced frequency is 2π.
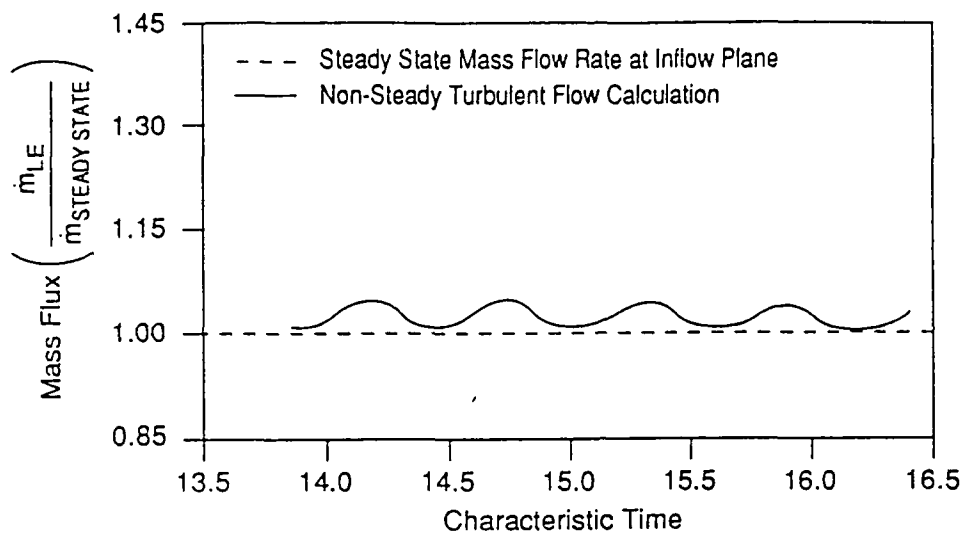
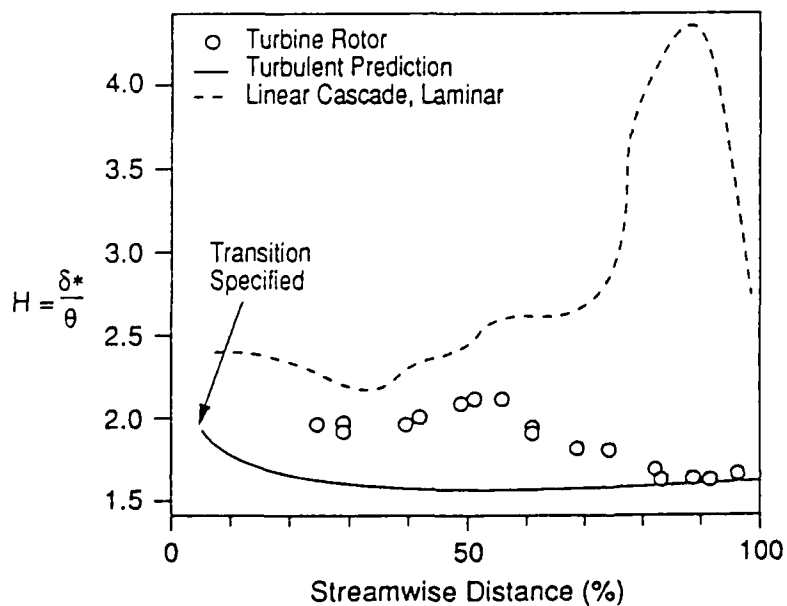FIGURE 1. Mass flow comparison at cascade leading edge plane [10].

FIGURE 2. Turbine blade suction surface boundary layer [6].

4.2 Wake Effects on Boundary Layer Transition, Loss, and Heat Transfer

When wakes pass through a following blade row one can show simply, from velocity triangles, that they will have a cross-passage "slip" velocity relative to the mean flow. Wakes will thus impinge on the pressure side of a compressor blade passage and the suction side of a turbine blade. One effect of the wake transport is redistribution of stagnation enthalpy [1]; another is the influence on laminar-turbulent transition. In turbomachinery, blade boundary layer transition is strongly linked to the periodic local variations in turbulence as the wakes pass.

The location of transition affects overall loss as well as heat transfer. As an example, comparison of losses for a turbine blade section tested in a linear cascade and as a rotor showed the loss to be approximately fifty percent higher in the latter. Boundary layer measurements from these tests are presented in Figure 2, which shows the time averaged shape factor, H, on the suction surface, for the turbine rotor and the linear cascade [6]. Results from a turbulent boundary layer calculation are also plotted. Over much of the blade surface, the time averaged shape factor has a value which is midway between the laminar and fully turbulent boundary layers. The same is true for the heat transfer as shown in Stanton number measurements (for another turbine section) in Figure 3 [13].

One view of the process leading to the data of Figures 2 and 3 is given schematically in Figure 4, which shows an x,t plane (i.e. the diagram refers to a two-dimensional blade/ wake configuration). In the figure, the shaded areas are regions in which the boundary layer is turbulent. Transition is taken as occurring at a location T whenever a wake passes. The process is seen as analogous, in many ways, to turbulent spots, which are created when the wakes impinge at T (although the turbulent spots seen in "natural transition" in conventional boundary layers occur irregularly across the span of the flow, while the structures here are two-dimensional). The analogy appears to be a useful one and has formed the basis for a heuristic model of unsteady transition, using the idea that the wake causes an initial production of turbulent "strips" which then propagate and grow along the blade surface independent of the subsequent wake motion [14], in similarity with the evolution of a turbulent spot.

At higher Mach numbers, unsteady shock impingement on the blades can also affect transition, not directly by shock wave-boundary layer interaction but by initiating a local separation which causes a turbulent "patch" that propagates downstream. Discussion of this is given in [7], using time resolved heat transfer data at different locations along an instrumented transonic turbine cascade, with bars moving in front of it.

The influence of wake passing on blade boundary layers has also been examined for compressor blades in a rig [15] and in a specially designed large, low speed cascade with an upstream grid of moving rods of it [16]. In constrast to the turbine, however, the presence of wakes did not have a significant effect on the exit boundary layer properties, compared to the situation without wakes, even though the detailed transition process was quite different in these cases [16].

The periodic transition process has a clear technological importance for turbomachinery. Its recognition, however, is even more important as far as phenomenology; accounting for unsteadiness, even in a simple fashion, leads one to results which are much closer to the actual machine behavior.

4.3 Modelling of Multistage Turbomachinery Performance

All the examples discussed so far are really parts of a broader problem, that of modelling the behavior of multistage turbomachines. If one starts from direct application of the equations of motion, it rapidly becomes clear that there are a wide range of length and time scales that must be dealt with, even if one excludes detailed description of the turbulence.
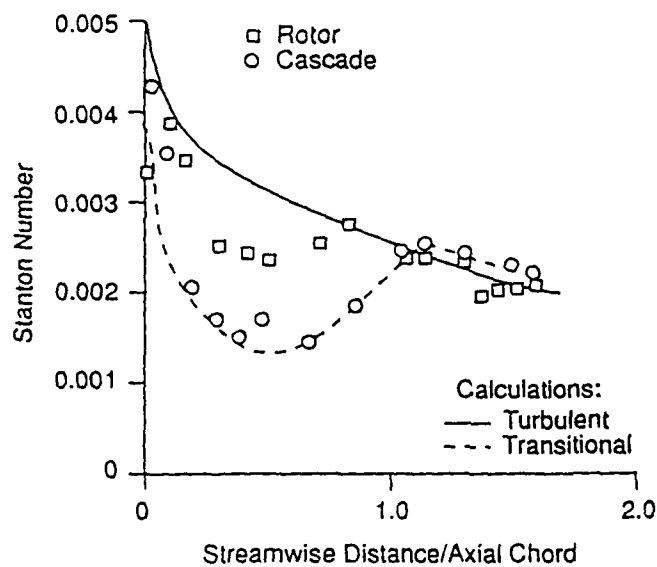
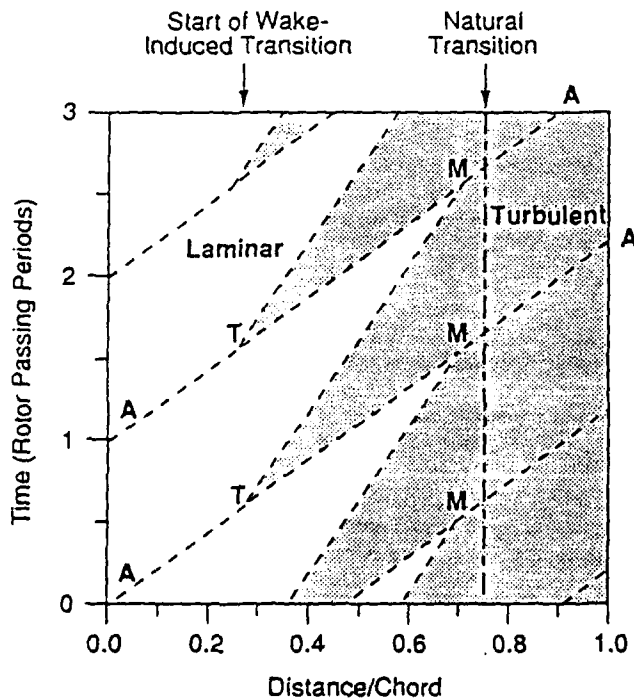FIGURE 3. Stanton Number distribution on rotor and cascade [13].

FIGURE 4. Schematic distance-time diagram of boundary layer states showing case of end of forced transition (at M) before natural transition (constant free-stream velocity). Line AA indicates free-stream velocity [8].

One approach to this task has been proposed in [17] and [18]; this provides the rigorous beginnings of a road map for an attack on this problem.

Although one can formally reduce the complexity of the flow field by averaging, either spatially or temporally, this brings in (unknown) correlation and body force terms, similar formally (although not in content) to Reynolds' stresses. Many of the terms in the correlations, however, do not appear to be important in a practical sense. Further, those that are important may well be able to be adequately modelled [19], i.e. this is not the turbulence closure problem in another guise. An important question is at what level one carries out the averaging and what must be done to model, in a generic manner, the dominant terms that appear in the correlations associated with this averaging. A key issue in developing improved predictive schemes for multistage turbomachine performance is thus modelling of unsteady flow effects; this has only recently started to be addressed in earnest.

5. IMPLICATIONS OF UNSTEADY FLOW PHENOMENA FOR DATA ANALYSIS

5.1 Unsteady Structure in "Real" Turbomachine Wakes

Wakes are often viewed as constant pressure regions with a velocity defect. Actual wakes, however, have a well-defined unsteady vortical structure because the steady wake velocity profile is strongly unstable. The instability is inviscid, associated with the presence of a maximum of vorticity, and growth rates tend to be much larger than those associated with amplification of Tollmien-Schlichting waves in boundary layers. The situation downstream of the trailing edge is thus often as shown schematically in Figure 5, with a vortex street forming downstream.

One result is that time resolved measurements of rotor exit flow will not show a periodic wake signal unless they are ensemble averaged. As an example, Figure 6 shows the relative flow angle determined by a high response probe at exit of a transonic rotor [20]. The upper trace is instantaneous data, the lower trace is for a 90 rotor revolution ensemble average.

Laser doppler anemometer measurements also reflect this unsteadiness, and can show a bimodal probability density distribution (p.d.d.) in the presence of vortex shedding, indicating that the wake may be more properly viewed as composed of two velocity states, one centered near the core flow velocity level and the other lower than the core flow level by nearly twice the time-mean wake velocity deficit.
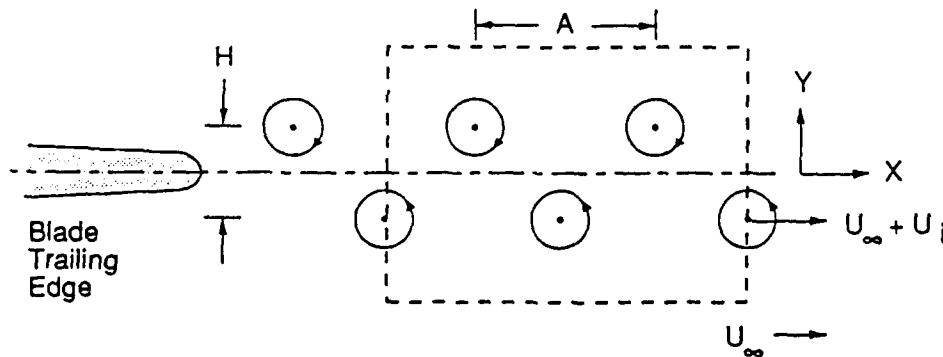

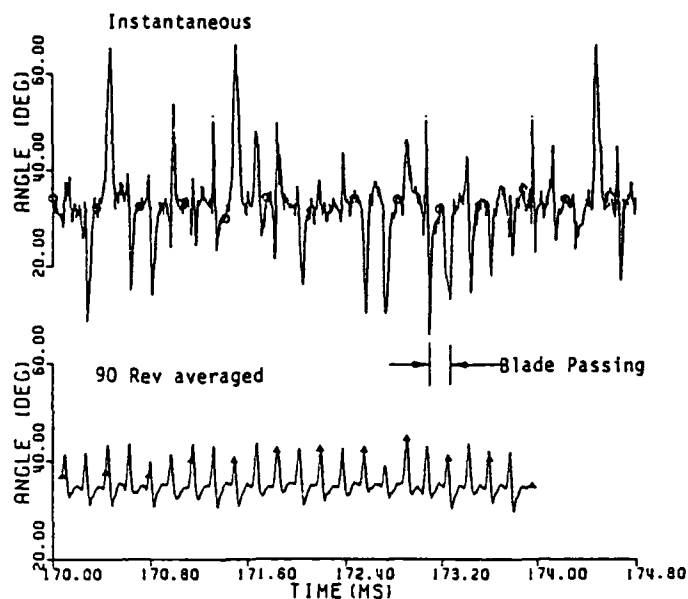FIGURE 5. Geometry of rotor blade vortex street.

FIGURE 6. Instantaneous and blade-by-blade ensemble
average rotor exit angle measurements [20].

Modelling the unsteady flowfield downstream of the rotor very simply as a two-dimensional vortex street appears to give a useful qualitative picture of the flowfield. This unsteady vortex model reproduces the wake shape and bimodal p.d.d., and accounts for the high level of blade to blade variation observed in several transonic compressors, which is now viewed as being due to intermittent sampling of the vortex street by the fixed frame probe [20].

5.2 Energy Separation in Unsteady Flow

Another effect of the wake vortex structure is the creation of a nonuniform relative (i.e., as measured in the blade fixed system) total temperature [21]. The situation is similar to that analyzed in the seminal paper on this topic by Preston [22], and can be demonstrated by examining the kinematics of a vortex row. Close to any vortex, the streamlines in the vortex fixed coordinate system are roughly circular. Velocity magnitude, pressure and temperature are roughly constant on these streamlines. To a stationary observer, fluid particles on one side of the vortex row have a high velocity and those on the other a low velocity, so particles on one side of the row have a higher total temperature than those on the other. Unsteadiness due to the vortex row is thus tied to total temperature differences.

The top part of Figure 7 shows a row of vortices moving to the right, and the solid line represents a particle path. Static pressure changes experienced by the particle are also shown. The terms "turbine" and "compressor" are appropriate because kinematically the vortices act like turbines for the passage of fluid across the row from the upper side and like compressors for the passage from below to above the row.

For a turbomachine wake which consists of two of these vortex rows, moving from the free stream to the wake has the same effect as going across a turbine blade row, i.e. a drop in total temperature (consider the circulation of the vortices shown in Figure 7). Neglecting dissipation and heat transfer, the relative total temperature difference would be expected to
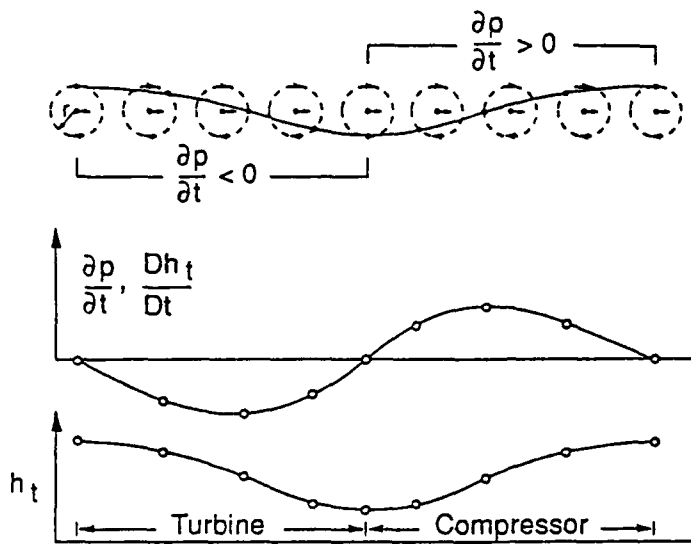
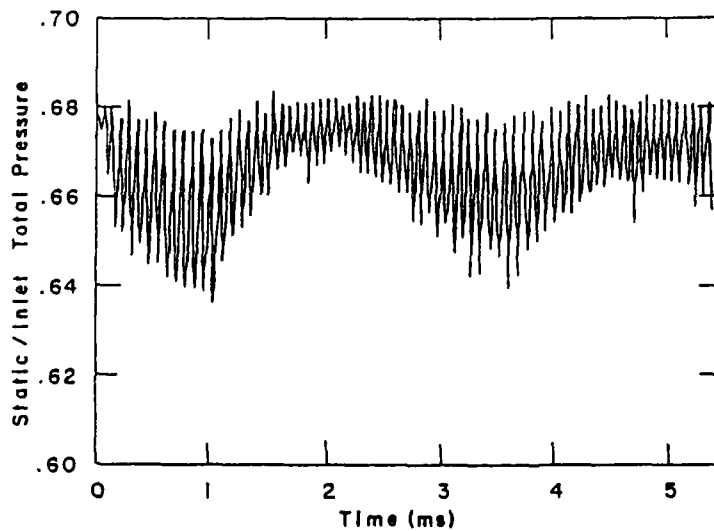FIGURE 7. Variation of T_t along pathline; moving row of vortices [21].

FIGURE 8. Computed static pressure history at trailing edge of transonic compressor airfoil [23].

be roughly $U_V \Gamma/h$, where U_V is the vortex velocity as seen in the blade fixed system, Γ is the circulation of a vortex, and h is the vortex spacing. As is evident from this basic discussion, the variations in temperature and pressure observed will scale approximately as relative Mach number squared.

Wake structure can affect the efficiency that one infers from high response measurements and, as indicated in [23], can give rise to apparent differences of order 1% between machines which actually have the same performance.

5.3 Unsteady Separation

Vortex shedding is a phenomenon with characteristic frequency of order ten kilohertz for a half meter diameter transonic fan. There are also much lower frequency sources of unsteadiness that exist, which may affect not only performance, but may be in a frequency range to excite blade vibrations.

To understand the cause of the low frequency unsteadiness, two-dimensional unsteady viscous calculations have been carried out [23] using the midspan geometry of a transonic rotor. The vortex shedding shows up quite clearly in the calculated trailing edge static pressure, Figure 8, along with a lower frequency which modulates its amplitude and the frequency, similar to the modulation observed experimentally. The lower frequency correlates with the computed motion of the separation point along the suction surface and with axial motion of the passage shock. The numerical solution indicates a considerable fluctuation in blade moment (roughly 30% for the case examined) at this frequency (~300 Hz) which can be of concern structurally. The exact cause of this movement of the separation point is not yet clear but it does appear similar to instabilities observed in high speed diffusers [23].

The large fluctuations in frequency shown in the numerical simulation also tend to explain the difficulty often encountered in extracting a single, unambiguous frequency estimate from experimental measurements. Fluctuations of this magnitude may also blur the bimodal anemometer histograms. The point to be emphasized is that separation is generically an unsteady process and that there can be aerodynamic, as well as perhaps aeroelastic, consequences of this for turbomachines.

5.4 Stator Pressure Field Effects on Compressor Measurements

Another aspect of un teady flow which is important with respect to supposed steady-state quantities is seen in the interpretation of interstage measurements in turbomachines. A well-known example arises in examining stator leading edge measurements, which often disagree with measur ments made at further downstream locations.

The physical reason for this disagreement is also well-known qualitatively. The circumferentially non-uniform pressure field of the stator causes the rotor to see a time varying flow. The circulation round a given rotor blade, and the local enthalpy rise, thus vary with time. In terms of the time mean quantities seen in the stator coordinate system, this implies that there will be a circumferential variation, with a period of a stator pitch, of rotor stagnation enthalpy rise. Reference [24] shows, in a very neat manner, that the time mean spatial variations in stagnation enthalpy, h'_t, are simply related to the temporal variation in rotor blade circulation, Γ, by

$$\overline{h'_t} = \frac{\Gamma}{S}$$

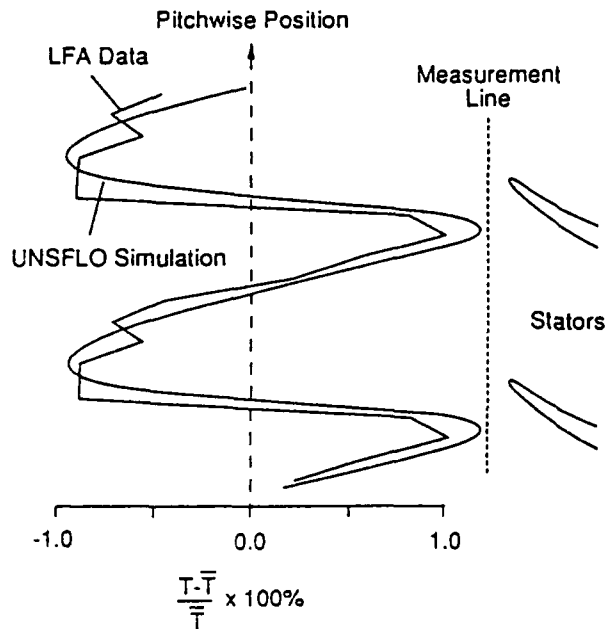where S is the blade pitch; this again illustrates the role of the vortical perturbations discussed in the introduction.

FIGURE 9. Time mean temperature from Euler turbine equation as
a function of pitchwise location. T is local temperature, $\bar{T}$ the area
average tempearture [25].

To show the magnitude of the effect in a representative situation, calculations have been
carried out using a two-dimensional inviscid Euler code for rotor stator interaction [25].
The rotor and stator geometries used were those of the NASA Stage 67 because of the
large amount of data published for the stage. The radial location corresponds to a station
slightly outboard of the sonic radius. The computational procedures, which used a time-
inclined plane approach, are described in [26] and [27].

Figure 9 shows time averaged stagnation temperature computed using the Euler turbine
equation

$$\Delta h_t = U_{blade} \bar{v}_\theta$$

at an axial station between the rotor and stator. Measurements of this quantity using a laser
anemometer are also shown. There are significant variations in the stagnation temperature
across the blade pitch.

It should be evident that the degree to which this effect is important will vary strongly with
the rotor-stator spacing (or, more precisely, primarily with the non-dimensional parameter,
rotor-stator axial spacing/stator pitch), and Ref. [25] presents some parametric studies
showing this variation. Another point is that for efficiency measurements, the relative lo-
cations of the temperature and pressure probes are important. Figure 10, also from [25],
presents contours of error in adiabatic efficiency (local value minus average) as functions
of the pitchwise location of the temperature and pressure probes. The variation for the
worst case, with one probe at mid-passage and the other at the stator leading edge, is 3%,
which is very significant. While probe placement in general would not be expected to be
chosen this crudely, it is clearly important to locate pressure and temperature instrumenta-
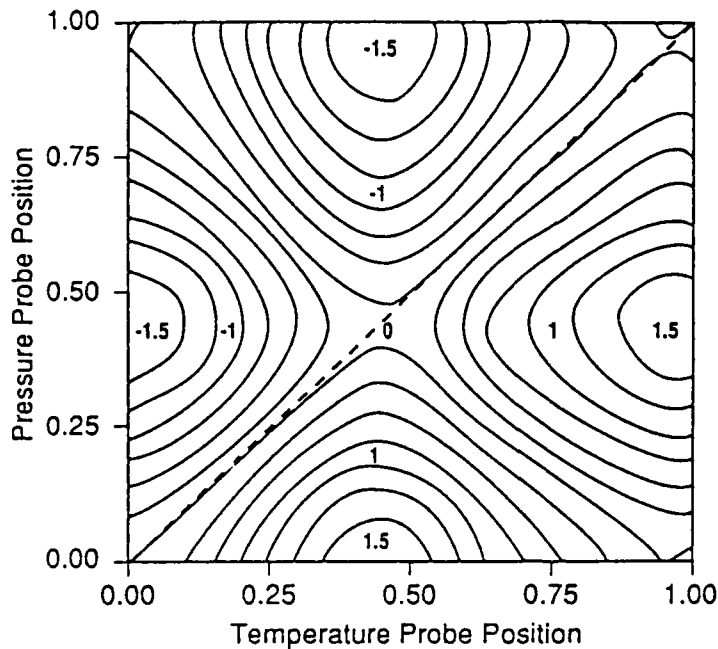tion at close pitchwise locations to avoid sampling errors.

FIGURE 10. Deviation from average efficiency as a function of relative locations of temperature and pressure probes and stators [25].

6. COMPRESSOR PERFORMANCE IN DISTORTED INLET FLOW

6.1 Inlet Distortion Effects on Compressor Flow Instability

One area in which unsteady effects have been addressed because of their importance at even a basic level is engine response to inlet circumferential distortion. Initial attempts to utilize quasi-steady ideas (in the basic parallel compressor theory) were very useful in developing an understanding of asymmetric flow, but they did not capture at all the small effects on stall inception that were encountered with distortions of narrow extent or having several sectors.

These two trends are illustrated graphically in Figures 11a and 11b [28]. The first shows data from a multistage compressor run with circumferential inlet distortions of varying extent. The abscissa is the angle of the distortion generator and the ordinate is the compressor exit pressure at surge, expressed as a percent of the uniform flow value. There is a strong influence of angular extent until an angle of between sixty to ninety degrees, after which there is little change. This behavior has given rise to ideas such as a "critical angle" of distortion to affect the stall point, or a "critical residence time" of the rotor in the low flow region.

Data from another series of tests is shown in Figure 11b. In the figure, the total circumferential extent of the distortion is ninety degrees, but the sector angle is divided so that there are 4 x 22.5° and 2 x 45° sectors as well. The axes are individual sector angle and compressor exit pressure at surge. Although the total extent is the same for all three tests, the smaller sectors, which have stronger unsteady effects, have considerably less adverse influence on stability.
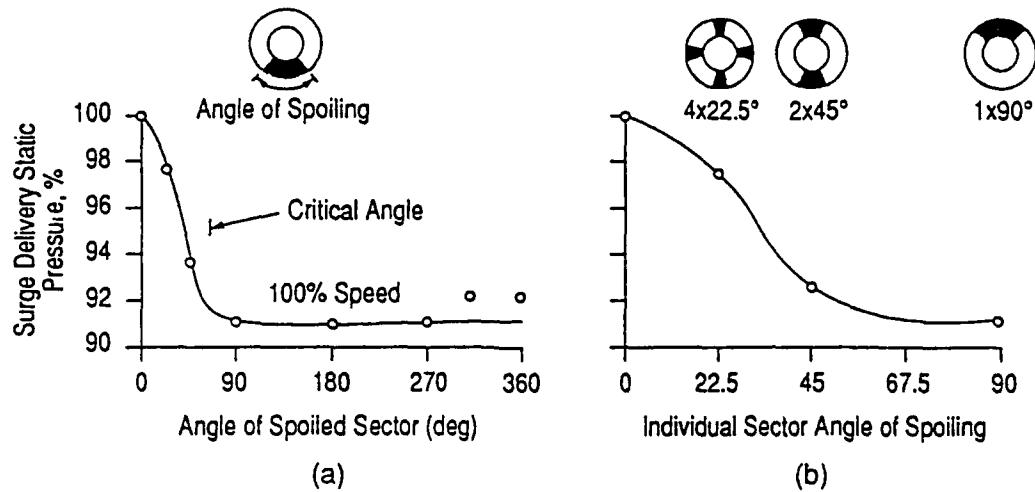
FIGURE 11. Reid's experimental results (taken from [28]): (a) loss in stability margin versus spoiled sector size; (b) loss in stability margin versus number of sectors.
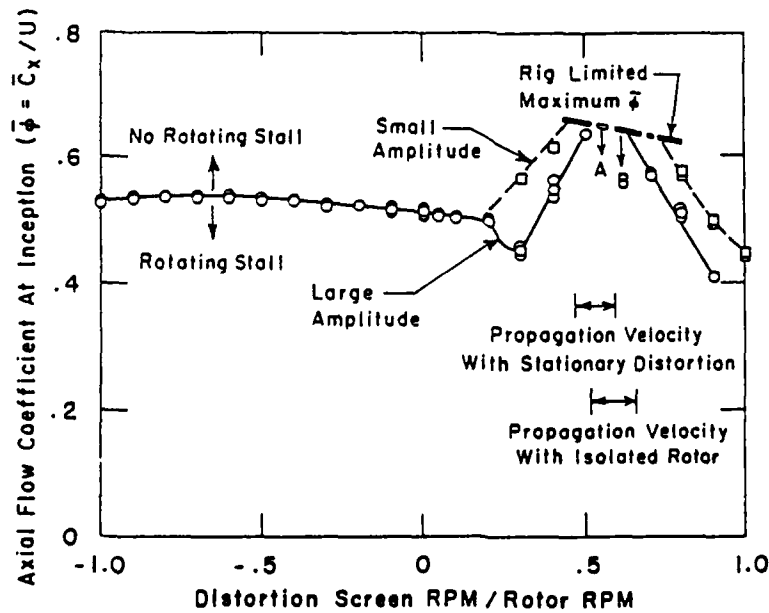

FIGURE 12. Effect of distortion rotation rate on stall point [30].

It was recognized early on that discrepancies between the quasi-steady (parallel compressor) models and this type of data were due to "unsteady response" although precisely what this meant was not clear. The need to include some description of this type of behavior, however, spurred a considerable amount of work. A recent useful review of the present state of the art is given in [29].

To see another example of the effect of unsteadiness, we examine a compressor subjected to a rotating inlet distortion. (This might be caused by rotating stall in a low compressor which was then fed to the high compressor in a two-spool engine.) Experimental results showing flow coefficient at stall versus distortion rotation speed are given in Figure 12 [30]. A marked increase occurs in the value of the flow coefficient when the rotational speed of the distortion is close to the natural speed of stall propagation.

As will be shown below, it is clear that the decrease in stability is not an effect that one can predict from any steady theory. At least in our view, it is associated with the behavior of the disturbance wave structure in the compressor annulus, and its understanding and prediction at even a basic level involves unsteady flow effects.

6.2 Analysis of Compressor Instability With Inlet Distortion

The most important problem associated with inlet distortion is the change in the operating point at which flow instability occurs. One approach currently being pursued as a joint MIT-Cambridge University effort is a rigorous stability analysis of the circumferentially nonuniform flow in a compressor, i.e. the stability (to small amplitude perturbations) of a steady circumferentially non-uniform flow field in an axial compressor [31], [32]. In this, the steady flow non-uniformity must come into the problem in a nonlinear manner, otherwise there is no interaction between distortion and unsteady perturbations. It is also necessary to include not just a description of the compressor, but the compression system as well, because the presence of a travelling wave perturbation in a distorted flow will cause changes in the annulus averaged flow quantities.

A key feature of the calculation procedure is a model for the fluid dynamic interaction between the spoiled and unspoiled sectors of the compressor. This, rather than any critical residence time in the low flow region, appears to be linked most closely to stability. The analysis shows that there is an approximate stability criterion, annulus averaged slope of the compressor pressure rise characteristic equal to zero.

$$\int_0^{2\pi} \frac{d\psi}{d\phi} d\theta = 0$$

where ψ = non-dimensional pressure rise and ϕ = axial flow parameter. This is valid in the many situations when the dynamics of the compressor distorted flow field do not couple strongly to the compression system or when the structure of the imposed distortion is not similar to that of the eigenmodes of the flow in the compressor annulus.

Application of this criterion to different multistage compressors is given in Figure 13 [28]. The figure shows first-of-a-kind computations, based on the theoretical model, of θ_{crit}, which is a parameter used to modify the parallel compressor theory to correlate stall margin loss.

To understand the previously mentioned decrease in stability for rotating distortions, calculations have been carried out [32] for distortions rotating at various fractions of rotor speed, f, from f = -0.6 (against rotor rotation) to f = 0.6. As in the experiments, rotation rate has a marked effect on the overall distorted flow compressor characteristic as well as
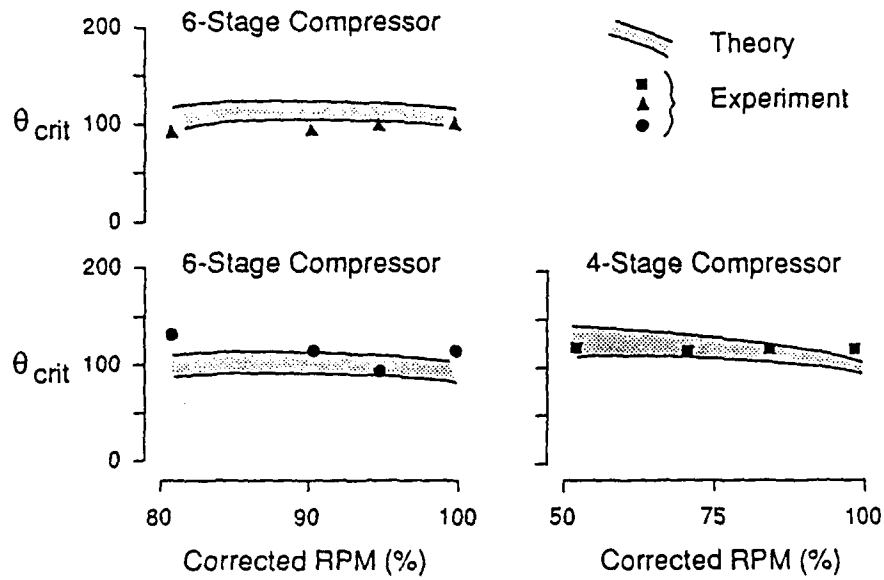
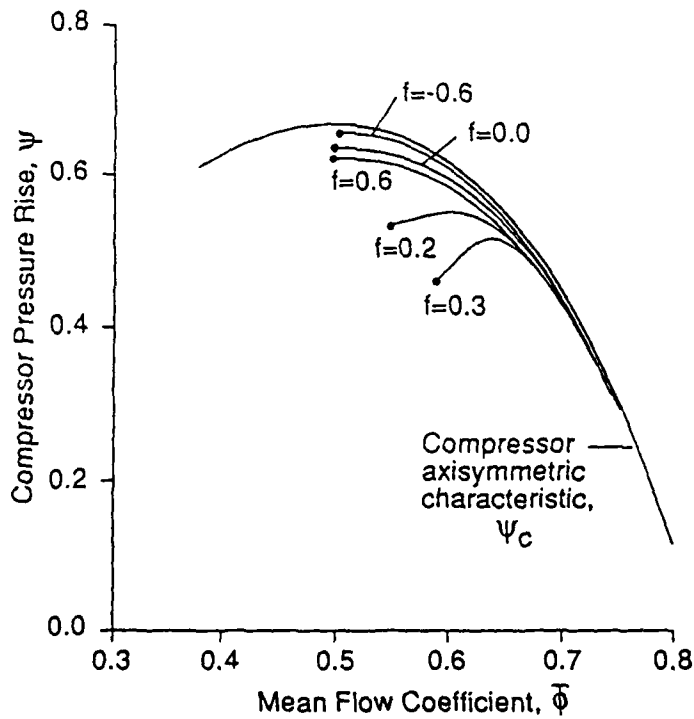FIGURE 13. Predicted and experimental critical sector angles [29].

FIGURE 14. Effect of distortion rotation rate,
f (= $\omega_{distortion}$ r/U) on compressor performance [32].

the stall point. The results are shown in Figure 14, which is based on representative parameters for a three-stage compressor. As the distortion rotation rate is increased from zero to 0.3, there is a drop in the compressor performance and a shift in the stall point, and for $f = 0.3$ there is only a small regime in which the flow is stable. We view this as a (non-linear) resonance between the inlet disturbance and the natural eigenmodes (i.e., the embryo propagating stall modes which have $f \cong 0.33$) of the flow in the compressor annulus.

6.3 Coupled Compressor/Compression System Flow Instability

The analysis in [32] also indicates that with inlet distortion there will be a decrease in stability due to interactions between the compressor and the compression system, when the frequencies of the system (surge-like) and compressor (rotating stall-like) perturbations approach each other. The surge frequency is basically determined by system parameters and independent of rotor and rotation rate, while the rotating stall-like frequencies scale to a good approximation with rotor rotation. As speed is changed, therefore, one can encounter a situation where these two frequencies coincide.

To understand why the stability is adversely affected, it is useful to consider the disturbance wave structure and, for simplicity, represent the eigenmodes by zeroth and first harmonic components only. The former represents the system "part" of the disturbance, the latter the compressor part. A sketch showing the relationships of these two components is given in Figure 15, which portrays different times during a disturbance period. The time-mean flow (the background flow) has a low velocity region from roughly $180° \rightarrow 360°$ and a high velocity region from $0° \rightarrow 180°$, i.e. the local operating points of the compressor lie on a characteristic with positive slope (destabilizing) in the region from $180° \rightarrow 360°$ and with negative slope (stabilizing) in the region from $0° \rightarrow 180°$.
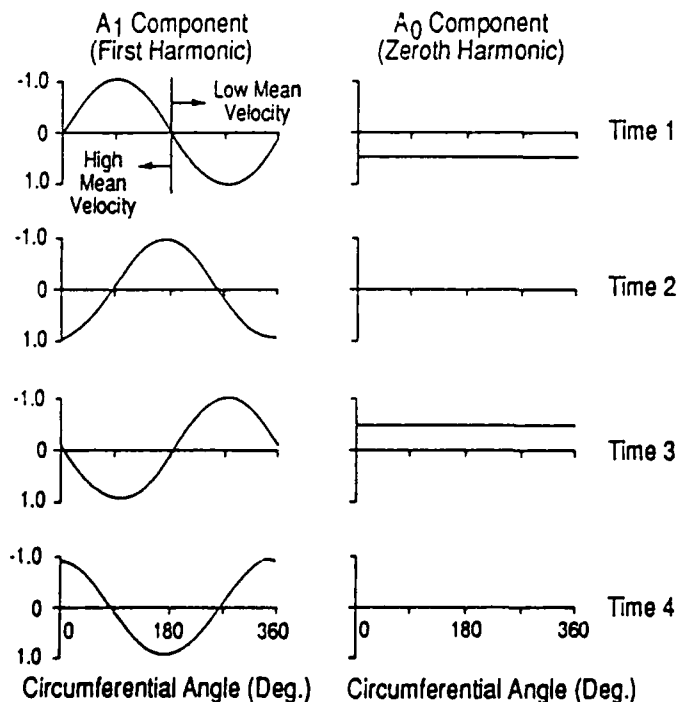

FIGURE 15. Sketch of zeroth and first harmonic component phase relationship near compressor/compression system frequency coincidence [32].
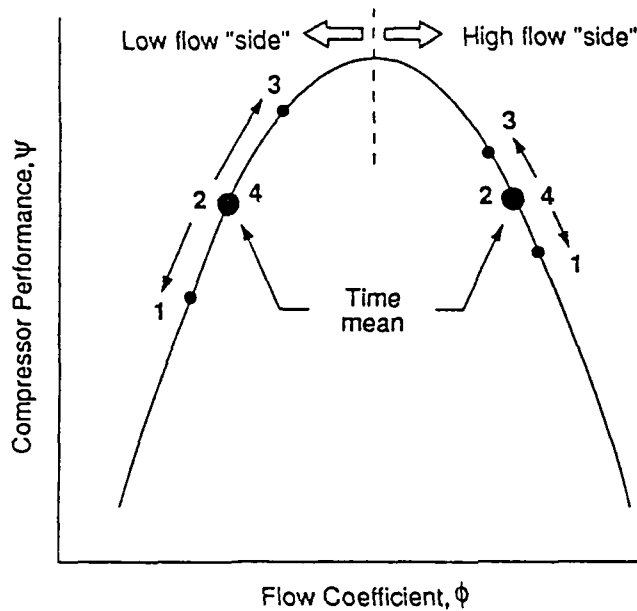
FIGURE 16. Local mass flow and pressure rise excursion near compressor/compression system frequency coincidence [32].

When the travelling wave part of the eigenmode is in phase with the time mean velocity profile, as in the (Time 1) top plot in Figure 15, the system component of the eigenmode has a negative velocity associated with it. When the travelling wave is out of phase with the time mean velocity (Time 3 plot), the system component gives a positive velocity.

The effect of these phase relationships is indicated on a compressor characteristic in Figure 16. Unsteady velocity perturbations are shown for the high flow and low flow regions: the nomenclature 1,2,3,4 refers to the situation at the times in Figure 15. The larger filled symbols refer to a representative time mean operating point in each region, i.e. representative points on the positive and negative sloped regions of the compressor characteristic. The main point is that, at Time 1, the excursion in the low flow (positive slope) region will be larger than that in the high flow region, since both components of the eigenmode contribute a negative velocity in the former. In the high flow region, the travelling wave part of the velocity is positive while the system part is negative so the net excursion is much less.

At Time 2 and Time 4 the perturbation is near zero, but at Time 3 there is again addition of velocities from the different harmonic components in the low flow region and partial cancellation in the high flow region. The kinematics of the phase relationships between compressor perturbations (travelling disturbances) and the system pulsations thus result in velocity fluctuations in the positively sloped region which are much larger than those in the negatively sloped region. This enhances the possibility for mechanical energy addition to the perturbations, and thus to decreased stability, when the two frequencies are close.

7. COMPRESSOR AND COMPRESSION SYSTEM INSTABILITY

Although one cannot now predict the onset of flow field instability in a turbomachine or engine with the desired accuracy from a first-principles basis, there has been significant recent progress in understanding the instabilities that are of practical concern in gas turbine engines.

177

7.1 Rotating Disturbances Prior to Stall

One recent finding has been the demonstration that rotating stall is preceeded by small amplitude waves which travel at roughly the same speed as the fully developed stall cell. Waves of this type can be readily seen by using an array of sensors positioned round the circumference. They have been hypothesized for some time (and in fact lie at the base of all the linearized stability analyses that have been carried out), but the first publication of data showing the phenomenon was in [33], with a single-stage, low speed compressor. Since then, disturbance waves have been found in multistage machines as well [34].

In the experiments that have been carried out, the disturbance waves have been sensed using a circumferential array of six to eight hot wires, approximately 0.4 to 0.5 radii upstream of the compressor. Putting the sensors this far upstream means that the higher harmonic components of the disturbances are filtered (the decay rate is like $e^{nx/R}$, where n is the harmonic number). With eight wires, one can examine the phase and amplitude of the first and second disturbance Fourier components. A plot of the phase of the first harmonic is shown in the lower part of Figure 17, which gives data from a three-stage, low speed research compressor. The actual time trace from a single wire is shown at the top. The time scale is in rotor revolutions, this being the natural unit of time. It is clear from the figure that the disturbance can clearly be detected by its constant phase velocity long before it is evid 't as a velocity disturbance. The low order harmonics are of most interest since it is thes .hat are the most dangerous.

Time traces of the phase and amplitude of the first harmonic show that, when the compressor is operating very near the stall inception point, these small disturbances can be present for several tens or even hundreds of rotor rotations. The disturbance amplitude can also fluctuate with time. The presence of these disturbances appears to be a necessary, but not sufficient, condition for rotating stall onset. Our present view of this is that the compressor is responding as a narrow band system to external disturbances. Near instability where there is very little damping, the "system", i.e. the compressor flow field, response can be a slowly decaying transient which is the natural eigenmode of the compressor annulus. We associate such eigenmodes with the initial (linear) stages of rotating stall cells, so it may not be too surprising that propagating disturbances at near stall cell speed are seen before stall.
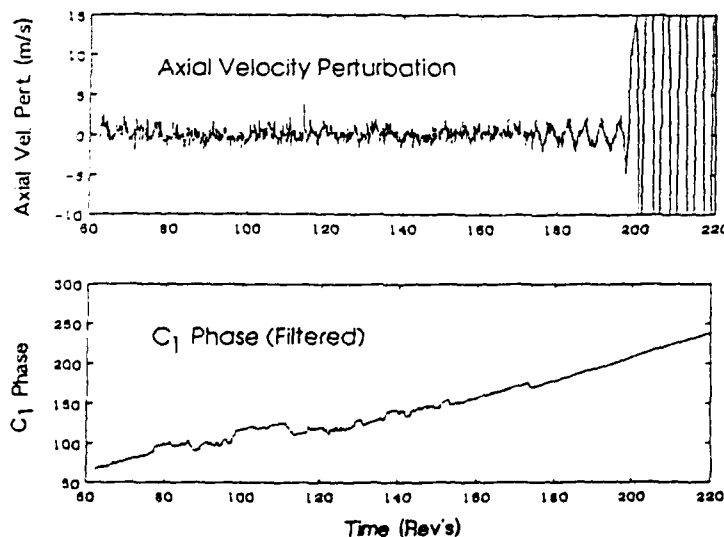

FIGURE 17. Circumferential phase as a rotating stall discriminant [34].

References [34] and [35] were concerned primarily with the detailed passage fluid mechanics near stall, rather than with the wave structure. To this end, detailed unsteady on-rotor measurements were made. These revealed that the endwall blockage fluctuates as the small amplitude velocity disturbance comes round. This is shown in Figure 18 which is based on rotor mounted hot wire measurements. The increase, then decrease, in blockage from a to b to c can be clearly seen. These fluctuations in blockage, which are also not part of any steady state description of compressor stall, again illustrate the importance of recognizing these unsteady effects in formulating a well grounded picture of compressor stall.

Figure 19 shows the nonlinear evolution of such disturbances from small amplitude to fully developed rotating stall [34]. What is plotted in the figure is the amplitude of the first circumferential Fourier component of axial velocity parameter versus time (in rotor revolutions) for a three-stage, low speed compressor. It can be seen that, while the small amplitude disturbances persist for a long time, once the disturbance becomes unstable, the growth (from a level of five percent, say) to a near-asymptotic value is quite rapid, occurring in several rotor revolutions.

An important item is to verify how generic in nature these waves are, as well as what link they have with the stall inception process. Pre-stall waves have so far been found in four different compressors, at MIT and Cambridge University, but they do not appear to be present in at least one other build at Cambridge [36]; the reason is still not clear. This is an area that is largely unexplored at present.
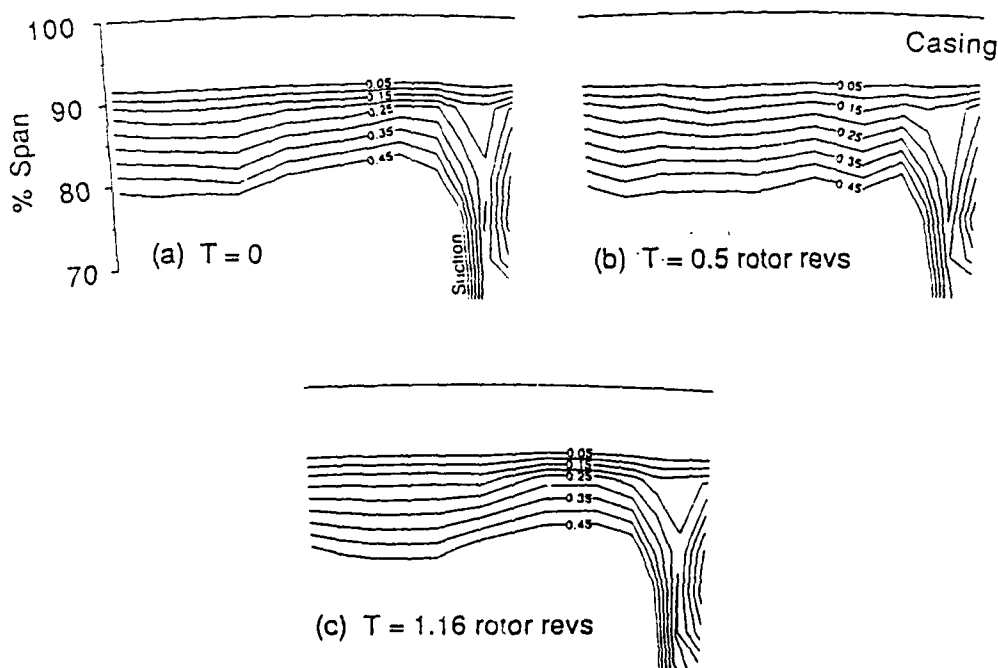

FIGURE 18. Contours of throughflow velocity ratio in casing-suction surface endwall corner showing disturbance passing. Tip clearance/chord ratio is 3%. Contours from 0.05 to 0.45 every 0.05 [35].
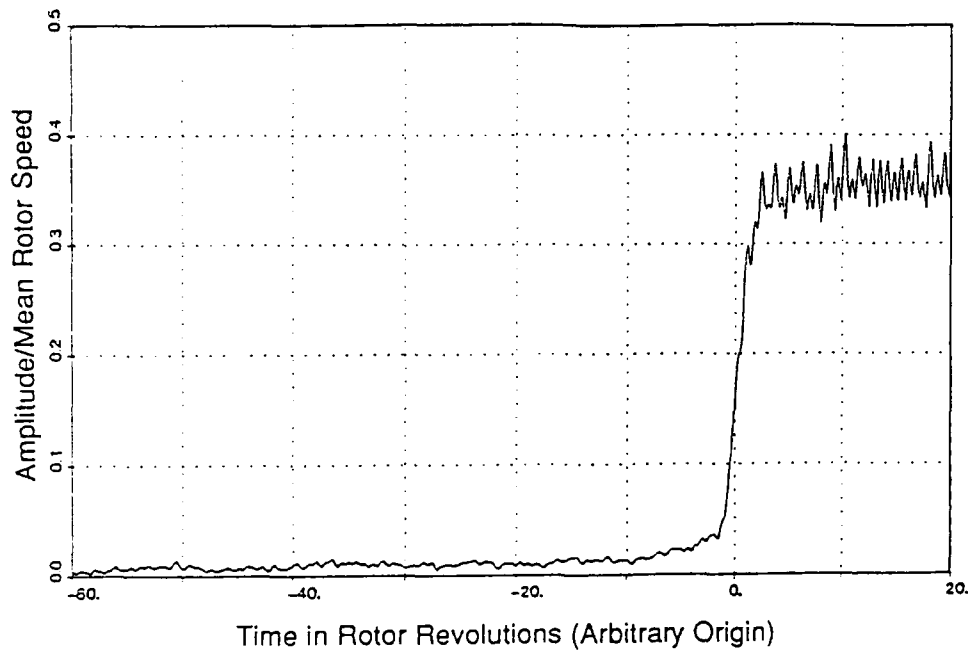
FIGURE 19. Amplitude of first Fourier harmonic axial velocity
disturbance; three-stage compressor, mean Cx/U prior to stall = 0.48.
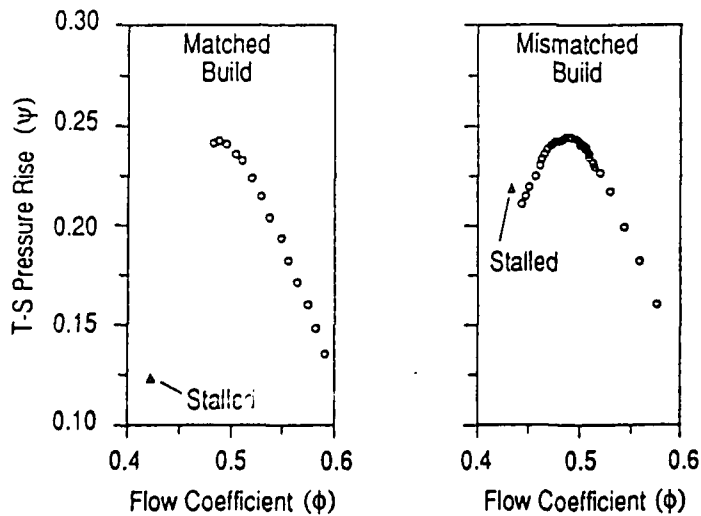Data band-pass filtered between 5% and 120% of rotor frequency [34].

FIGURE 20. Comparison of research stage performance for
different operating environments (downstream components) [37].

7.2 Flow Stabilization by Downstream Stages or Components

Another important finding relating to instability was reported in [37], in which three sets of experiments were carried out with a three-stage compressor. The pressure rise characteristic of the first stage only from these runs is shown in Figure 20. In the first set of experiments, three ideal stages were used. In the second set, stages two and three had stagger angles increased by ten degrees. The result of the increased stagger was that the compressor went into rotating stall at a lower flow coefficient than for the matched build. Of more interest from a basic fluid mechanical viewpoint, however, is the first-stage performance for this mismatched build, which is shown on the right in Figure 20. It can be seen that the stable flow range has been extended appreciably and there is also now a portion of the curve which has a positive slope. Note that, in defining this range, detailed measurements were taken with hot wires to make sure that rotating stall did not exist.

What has occurred is that the downstream stages have suppressed the growth of rotating stall. The mechanism for doing this is most likely through acting on the wavelike disturbances described above The stabilizing effect of downstream components has been noted before (see e.g. [38]) but, to the authors' knowledge, the data in [37] is the first clear demonstration of the existence of an "axisymmetric" compressor characteristic with a reasonably strong positive slope. Figure 21 is a plot of the first-stage performance in all three situations: isolated stage, matched three-stage compressor, and mismatched build. It can be seen that there is very little difference indeed, except for the difference in stall point, between the three experiments.

There are several implications that one can draw from these tests. First is that no computation of the flow in a blade passage only will lead one to encounter rotating stall. Details of the fluid dynamic processes associated with the tip leakage flow, for example, are crucial in setting the stage performance but knowledge of the stage performance is not enough. Rather, one must be able to account for the interaction between the blade passage and the upstream and downstream flow field. Put another way, the stall point and the stalled per-
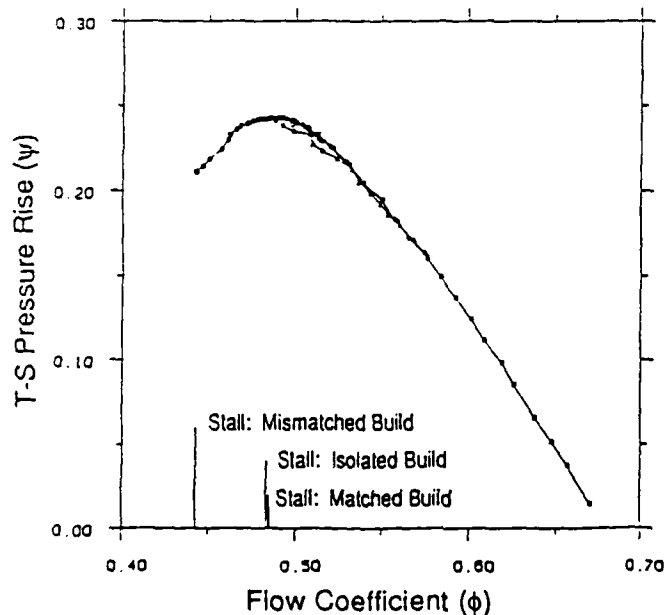

FIGURE 21. Unstalled axisymmetric performance of research stage in the three different environments [37].

formance of a stage, or even of a compressor, are a property of the fluid mechanic environment as well as the local stage behavior.

7.3 Behavior Subsequent to Instability Onset

Another important question related to instability is whether a given compression system will exhibit large amplitude oscillations of mass flow and pressure ratio (surge), or whether the system will operate in rotating stall where the annulus averaged mass flow and pressure ratio are essentially steady, but are greatly reduced from the pre-stall values [39]. Initial analysis of the nonlinear system behavior employed a simple lumped parameter representation. For a given compression system, it was shown that there is an important nondimensional parameter, B, on which the system response depends:

$$B = \frac{U}{2\omega L_c}$$

where ω is the Helmholtz resonator frequency of the system, L_c is an "effective length" of the compressor duct, and U is the rotor speed. For a given compressor, there is a critical value of B which determines whether the mode of instability will be surge or rotating stall [38].

An examination of stall transients in compressors from a more general point of view, encompassing surge and rotating stall as special cases, is given in [40]. Nonlinear coupling exists between the (local) compressor performance and the (global) system behavior for two reasons. First, the rate of growth of the stall cell is dependent on the annulus averaged velocity at the compressor face, which is dependent on the system dynamic behavior. Second, the overall pressure rise depends on the shape (extent, amplitude, etc.) of the rotating stall cell which is a function of the unsteady compressor performance. The general transient can be viewed as the approach to two limit cycles. One, in θ, is rotating stall and is embedded in a more global limit cycle in time, which is surge.

The calculations that have been carried out show a complex axial velocity waveform during surge. It includes disturbances that propagate around the circumference, pulsations that are roughly planar, and an admixture of both, at different times in the cycle. The post-stall transients seen in actual machines, however, appear to have many of the same features. In addition, as in many other nonlinear systems over a range of parameters, the computations for a two-mode representation of the axial velocity exhibit what appears to be chaotic behavior at instability [41]. These features can be of import in attempting to devise control strategies for extending the stable flow range.

7.4 Stability Enhancement Using Endwall Region Flow Management

In connection with the general topic of flow instabilities in turbomachines, one other aspect that deserves mention is the large increases in stability that can be achieved through alterations in the endwall flow region. For example, so-called "casing treatments" (grooves in the shroud over the tip of a rotor) have been known for almost two decades, and can even be seen in some civil aircraft engines as one boards. The precise mechanism of operation of these grooves is still not clear but some general, design-oriented guidelines have emerged from the work done on this topic. One of these is shown in Figure 22, derived from experiments using grooves on a rotating hub underneath a cantilevered stator to simulate (for ease of instrumentation) representative rotor tip flow. The figure shows the increase in peak pressure rise capability (i.e., blade row pressure rise at stall) as a function of normalized streamwise momentum flux from the groove, for three different groove geometries. There is a strong correlation between this streamwise momentum injection and the pressure rise at stall. While several competing mechanisms can be proposed for this in-
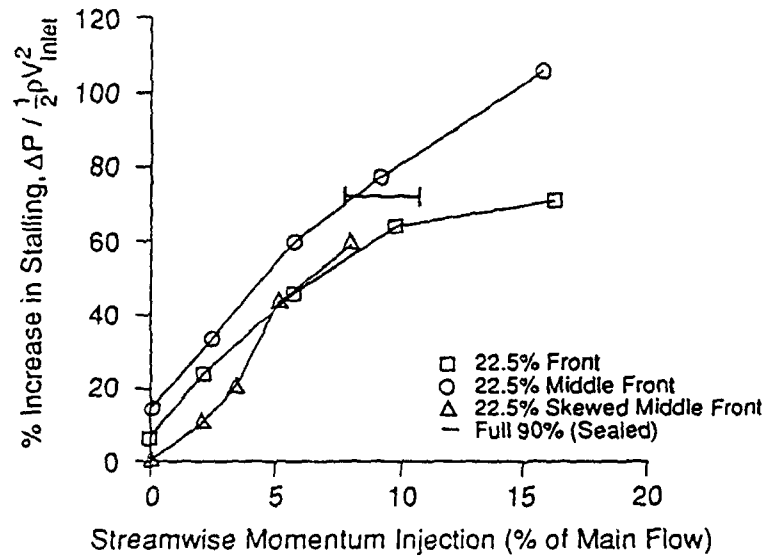
FIGURE 22. Variation in stalling pressure rise increase with stream-
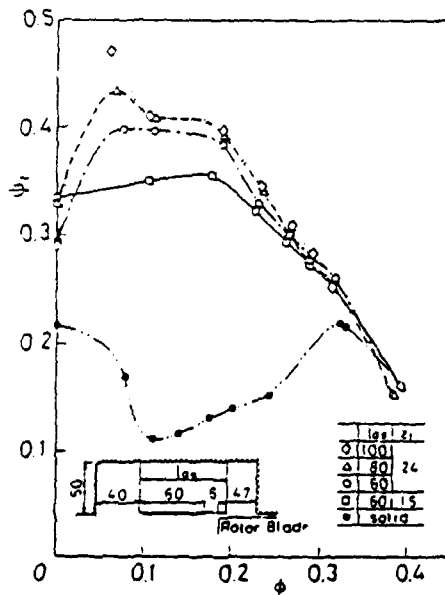wise momentum influx; slots covering 22.5% of axial chord [42].

FIGURE 23. Effect of separator fins on fan pressure rise [43].

crease ([42] gives some discussion of these), the point here is that the observed trend gives a strong message to the groove designer as to what is desired.

Most of the groove geometries examined initially were configured to fit within the casing of an aircraft engine, and thus had only small depth (compared to blade span, say). Recently, however, there have been several tests of shroud geometries with much larger depths, which have yielded very impressive results. Figure 23 shows an example of one of these configurations for an axial fan [43]. The fan solidity is not representative of aircraft engine turbomachines, but other experiments [44] have been carried out with more generic type blading and these also show large increases in peak pressure rise. Investigation of these increased vane treatments for more representative aero-engine geometries seems a fruitful area to pursue.

These shroud (or casing) treatments have been mentioned for two reasons. Although they do not necessarily represent a phenomenon that one must think about in terms of unsteady flow, they certa' 'y do represent a method for controlling or suppressing undesirable unsteady effects connected with rotating stall. Further, they serve to highlight the critical role of the endwall region in setting the overall blade row pressure rise, and the onset of instability. In essence, it is the view of the authors that, in most modern turbomachines, rotating stall is due to phenomena associated with endwall effects, and these devices work directly on the source of the problem.

8. DYNAMIC CONTROL OF UNSTEADY FLOWS IN TURBOMACHINES

An exciting and relatively new topic in unsteady fluid mechanics is the use of integrated control in turbomachines to alter many of the aspects of operation from open loop to closed loop. Topics now being pursued are active stabilization, i.e. using unsteady effects to suppress aerodynamic instabilities, such as surge and rotating stall [45], as well as "passive" stabilization through the use of tailored structures. This work is still very much in its initial stages, but it may have a significant potential for altering stall margin requirements. The approach is fundamentally different from those tried previously and is based on the recognition that the instabilities of interest are dynamic phenomena. If the aerodynamic damping (of these instabilities) were increased using active control, one might operate in a previously unstable, high performance region (as illustrated conceptually on the (deliberately provocative) compressor map in [45]).

8.1 Control of Rotating Stall

We consider first (briefly) the local instability, rotating stall, which we view as the growth of an unsteady propagating flow disturbance. The method of control is to sense this disturbance and generate an additional disturbance, possibly with a transducer system driven from processing data measured inside the turbomachine. The controlled system constitutes a machine of fundamentally different characteristics in which stable operation can be achieved under conditions which previously implied breakdown of the flow.

We have analyzed some initial control strategies, where an upstream velocity non-uniformity was generated of the form

$$\left(\delta C_x\right)_{\text{far upstream}} = Z\left(\delta C_x\right)_{\text{compressor face}}$$

where δC_x denotes a perturbation in axial velocity. A simple proportional controller was used with $Z \rightarrow$ just a complex constant independent of frequency, and the control perturbation was considered to be generated by a row of inlet guide vanes. The results of the calculations, which are discussed in detail in [45], were quite encouraging. They showed a sig-

nificantly increased stable flow range for physically plausible vane motions. This topic is thus currently being examined experimentally.

8.2 Active Control of Compression System Instability (Surge)

Rotating stall is a local instability, but for a multistage axial compressor, one must stabilize both the local (compressor) and the global (compression system) instabilities that can exist. For a centrifugal compressor, however (and perhaps for single-stage axial fans), the local instability that leads to rotating stall is often of less consequence than the system instability. If this is the situation, one can deal with the latter only. This provides an easier entry into the control of instability and has been explored in somewhat more depth. More explicitly, stabilizing surge in a centrifugal compressor may be more accessible than suppressing rotating stall in an axial one because of the spatial uniformity and the low frequency of the oscillations and relatively slow growth rate of the instability.

Experimental and theoretical investigations of centrifugal compressors are reported in [46] and [47], also in complementary MIT-Cambridge University efforts. The experiments were based on the two simple approaches set out in [45]: control using a moveable plenum wall and a downstream throttle motion respectively. Both methods were found to suppress surge and to extend the stable flow regime. Some of the experimental results of [47] are shown in Figures 24, 25, and 26. Figure 24 shows the surge oscillations (limit cycle) in a pressure-mass flow plane for the situation without control; the amplitude of the flow fluctuations is over one hundred percent of the steady state flow. Figure 25 gives the pressure pulsation amplitude versus non-dimensional flow coefficient for the situation with control and without control. The onset of pulsation (surge) can be seen to be moved to a lower flow coefficient, as well as to be decreased in amplitude. In addition, although the controller was designed on the basis of linear theory, it has been found to be able to suppress large amplitude limit cycle oscillations associated with surge, as shown in Figure 26.

To understand the mechanisms by which the controller suppresses the growth of oscillations, it is useful to examine production and dissipation of perturbation energy in the sys-
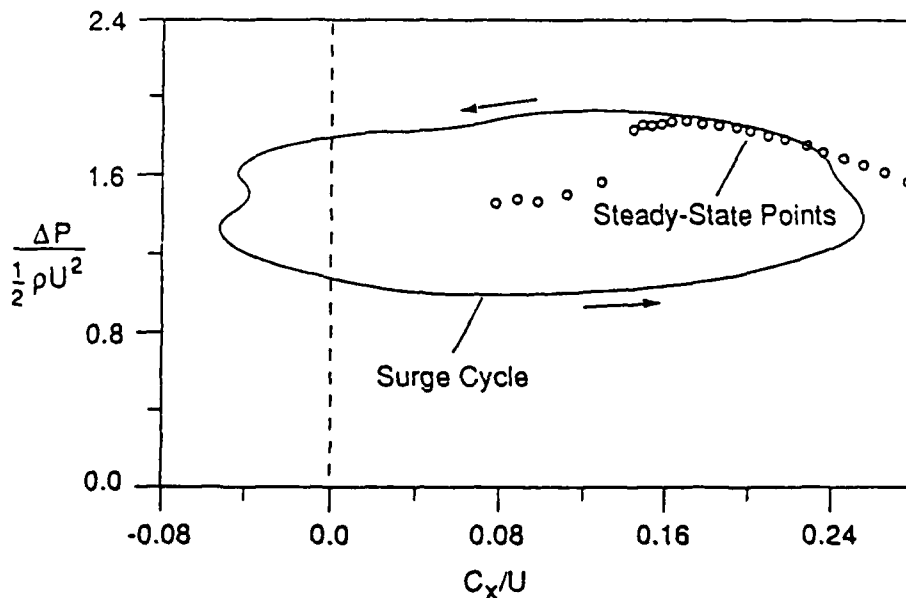

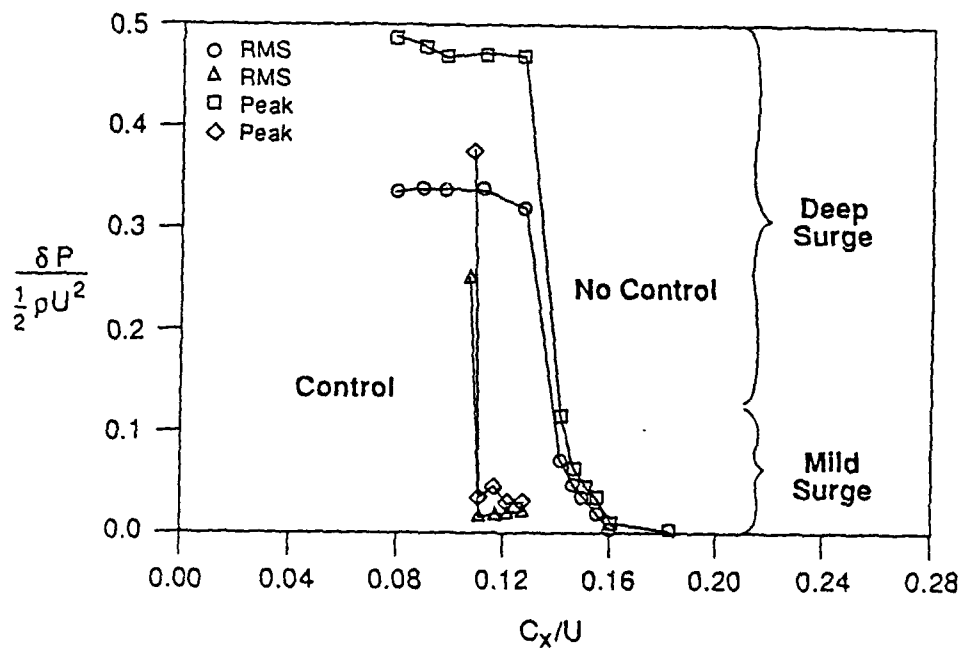FIGURE 24. Centrifugal compressor surge cycle [47].

FIGURE 25. Effect of actively controlled throttle valve on RMS and peak
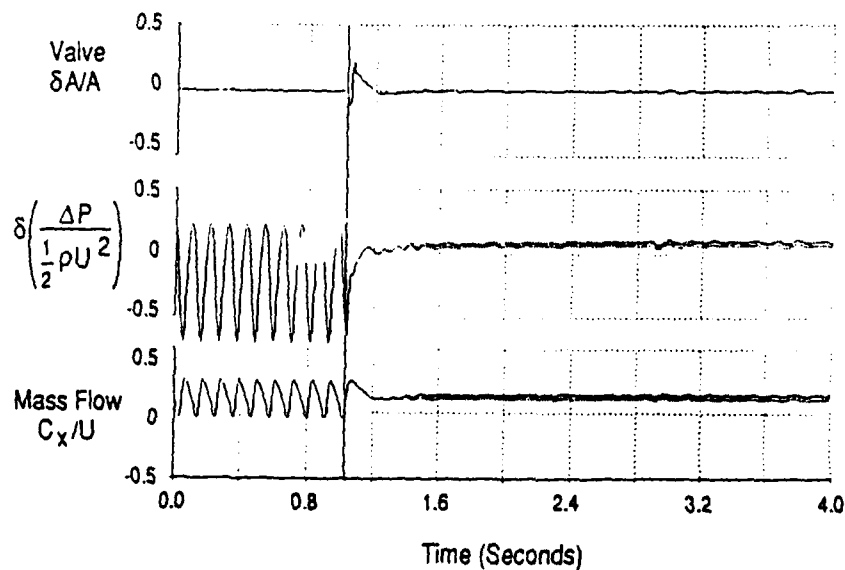fluctuations in plenum pressure [47].

FIGURE 26. Suppression of surge cycle with actively controlled throttle [47].

tem. Detailed discussion is given in [45], but the important point is that it is the unsteady behavior (of the compressor, of the compression system, and of the controller) that must be understood to implement these schemes in an effective manner.

The results presented in [46] and [47] are promising, even though neither of the active control methods is anywhere near optimum, in the sense of having the most authority to affect the system dynamic behavior. Work is now being carried out to define, in fluid dynamic terms, more useful actuation schemes for practical devices. Computations carried out so far indicate that (as perhaps one might expect) the actuation should be closely coupled to the compressor rather than isolated (in some sense) from it by a large volume.

8.3 Instability Control Using Tailored Structures

Another approach to instability control, which also arises out of considerations of unsteady system behavior, is the use of tailored structures in a passive control scheme. A schematic of the general concept can be seen in Figure 27 [48]. One wall of the plenum in the system has been made compliant to be able to respond to pressure perturbations, such as those encountered as a precursor to the surge [49]. The basic concept is that wall motion results in dissipation (due to the dashpot), and this dissipation can counter the mechanical energy input into the oscillations due to the unsteady flow through the compressor, although there is no effect on the steady state performance. Calculations have been carried out to define the mass-spring-damper characteristics of the compliant wall so as to maximize the extent of stabilization. Examination of the flux of perturbation energy reveals that the moving wall can provide an order of magnitude more damping of the amplitude oscillations associated with the instability than that existing (due to the flow in the throttle) in the original system.

Based on the calculations, an experiment has been designed incorporating a plenum with a moving wall. Results for a centrifugal compressor (turbocharger) operated with this system are shown in Figure 28. It can be seen that the compliant wall gives an increase in stable operating regime over the whole speed range. Further results illustrating parametric trends are given in [48].
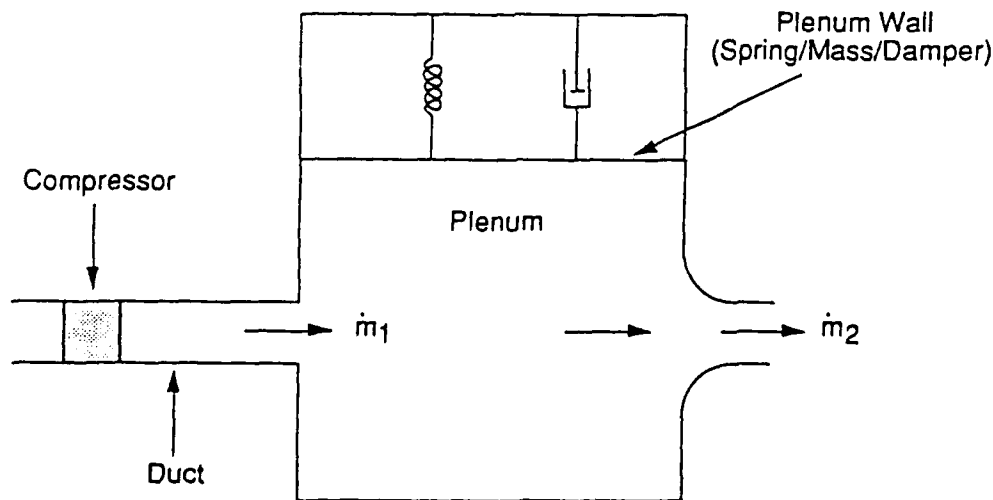

FIGURE 27. Schematic of compression system with tailored structure (plenum wall) [48].
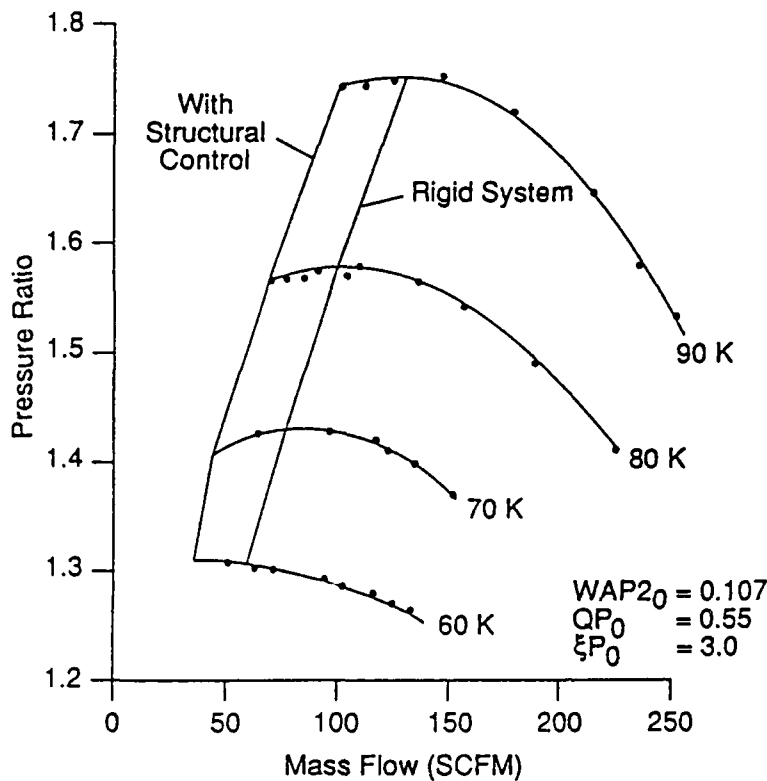
FIGURE 28. Turbocharger range extension using tailored structure [48].

9.0 MIXING PROCESSES IN TURBOMACHINES AND OTHER PROPULSIVE DEVICES

In predicting the performance of a turbomachine, especially a multistage machine, it is important to be able to account for mixing processes that occur, such as radial transport of quantities from the endwall regions to near midspan. Mixing is included in the phenomena covered in this lecture because it is viewed here inherently as an unsteady process.

In this connection, we can briefly note some of the recent results concerning mixing in situations that are much simpler than turbomachines, for example, turbulent plane shear layers [50], where it is recog zed that the "turbulence" has a definite organized unsteady vortical structure to it. Descriptions using this structure appear to provide a more fundamental picture of the flow than approaches which do not. In this instance, at least, it seems that there is an increase in insight if one recognizes the inherent unsteadiness of the phenomena, rather than tries to devise procedures which suppress the unsteadiness through some sort of averaging.

The mixing process in turbomachines is more complex and, in the past five years, two different descriptions have been put forth. One of these attributes is the radial transport to an organized secondary flow [51], the second to "turbulent diffusion" [52]. Although the descriptions are based on totally different mechanistic ideas, they both appear to give good results when applied to multistage machines. (As stated in [9]: "One conclusion one might reach is that the introduction of any spanwise mixing model is better than none at all in attempting to predict multi-stage compressor performance.")

Some resolution of the two viewpoints has been made by Wisler [53], who showed that a combination of both mechanisms occurs. What is not well known is how mixing is influenced by compressor design parameters. If a turbulent-like process is indeed occurring, it would seem useful to examine it using some of the recent concepts concerning coherent turbulence structure, i.e. by again recognizing the unsteadiness and vortical structure and not trying to simply fit the process into an *ad hoc* gradient transport framework. The whole topic of mixing in turbomachines is an area of unsteady flow which needs further exploration on a b sic level.

10. FLOW CONTROL USING EMBEDDED STREAMWISE VORTICITY

A final topic, which is related to the two previously described areas of mixing and flow control, and which has been of considerable recent interest, is flow control using embedded streamwise vorticity. This differs from other phenomena that we have been discussing in that the process involved may not be intrinsically unsteady (at least on the larger scale of the motion involved). Nevertheless, it is appropriate to include it because of the potential offered for decreasing base drag in subsonic flows (through the strong effect on the unsteady vortex shedding which is critical in setting the base pressure), suppressing airfoil separation, altering wake structure in turbomachines, reducing unsteadiness in stall and diffusing passages, and enhancing mixing in a variety of propulsive devices. In connection with the last aspect, one point to be noted when examining mixing results is that the level of mixing needed for different processes in turbomachines and propulsive system components can vary considerably. Combustion requires that the mixing take place on a molecular scale, while ejector or mixer nozzle aerodynamic performance may require that the flow be mixed in a bulk fashion, i.e. larger length scale.

The genesis of the idea arose from work done over a decade ago on forced mixer nozzles for turbofan engine noise reduction. A generic configuration is shown schematically in Figure 29 [53]. The presence of convolutions or lobes, in the surface between two streams, creates trailing vorticity, similar to that from a finite wing. Streamwise vorticity in these flows can be much stronger than that seen in natural mixing layers between two streams.
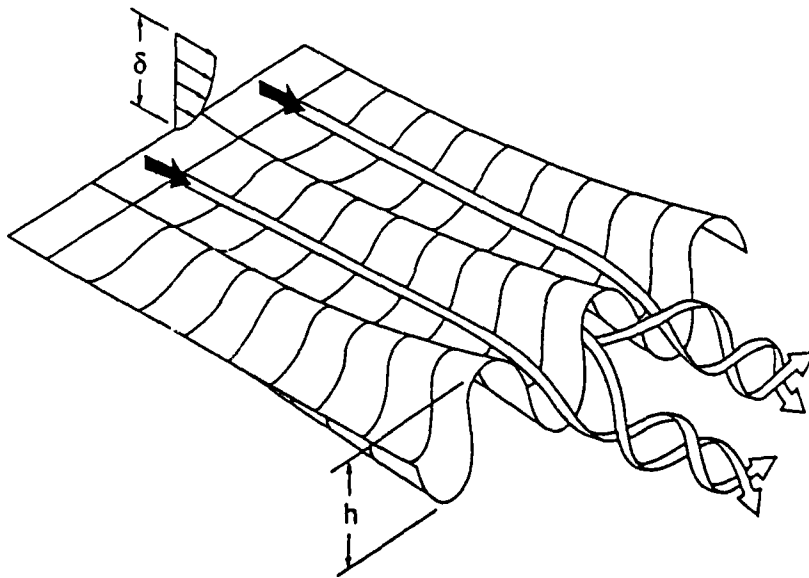
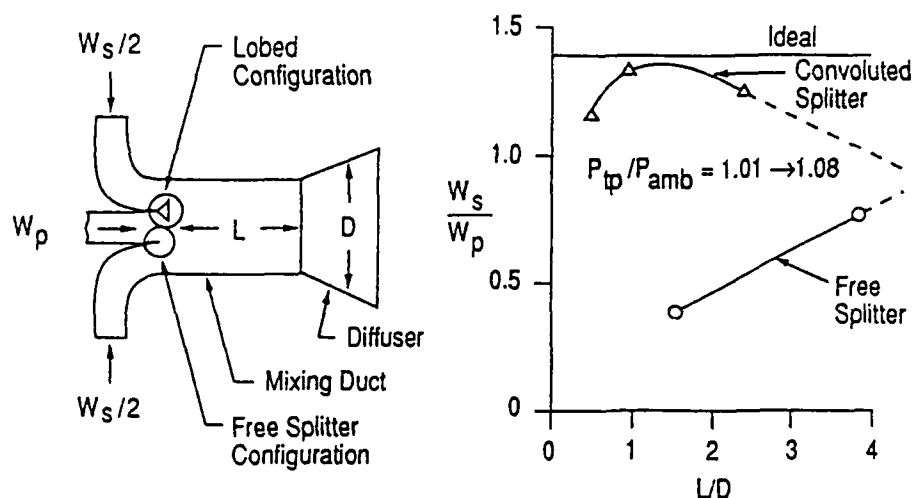FIGURE 29. Sketch of mixer lobe geometry [54].

FIGURE 30. Mixer ejector application [54].

Studies of the behavior of flow downstream of the lobes reveal an abrupt transition (as a function of downstream distance) from well-defined spiraling motion to a highly mixed state. Mixer nozzles, as well as other fluid dynamic devices relying on mixing for their operation, can accomplish this much sooner than with natural mixing, i.e. with a splitter plate between them. One can thus drastically shorten an ejector, for example, and still obtain almost ideal performance. Strong streamwise vorticity can also inhibit coherence of spanwise vortex shedding, altering the flow in the base region of airfoils and decreasing base drag [53].

Figure 30 presents sample results for an ejector tested with free and with convoluted splitters [53]. Secondary to primary flow rates (pumping) versus overall ejector lengths are shown. Calculations based on a simple control volume analysis are also indicated by the "ideal" line. Over the regime tested, the convoluted splitter increased injector pumping by over 100 percent, due to the greatly increased mixing. A major effect of the streamwise vortices was to improve the downstream diffuser performance because the large scale vortices sweep low energy boundary layers away from the outer wall surface [54].

A basic question concerning operation of these mixers is the extent to which the increased mixing is due to the increased area of the interface between the two streams or to the stirring action of the streamwise vortical structure. Exploratory investigations have been carried out using a flat plate, a mixer nozzle having a geometry similar to that reported in [52], and a configuration which had a parallel walled section, approximately one lobe height in length, downstream of the mixer lobes. This last configuration thus had the same cross-section as the mixer nozzles, but (due to the parallel walled extension) less streamwise vorticity at exit. Preliminary results indicate that, although the increased area is a factor, the streamwise vorticity has a very strong effect on the overall mixing level.

The central problem of designing mixing lobes of this type can be posed as questions about: 1) What is the distribution of vorticity in the flow that will lead to the desired flow modification? and 2) How does one create this distribution? While these questions are complex, there appear to be substantial opportunities for improvements in propulsion system performance using embedded streamwise vorticity.

9. Lighthill, M.J., Physical Interpretation of the Mathematical Theory of Wave Generation by Wind, *Journal of Fluid Mechanics*, Vol. 14, pp. 385-398, 1962.

10. Wennerstrom, A.J., Low Aspect Ratio Compressors: Why and What It Means, 1986 SAE Cliff Garrett Lecture, to be published in *ASME J. Turbomachinery*.

11. Scott, J.N., Hankey, W., Navier-Stokes Solution of Unsteady Flow in a Compressor Rotor, *ASME J. Turbomachinery*, Vol. 108, pp. 206-215, 1986.

12. Richardson, S.M., A Numerical Study of Unsteady Flow Effects in a Supersonic Compressor Cascade, in AGARD CP-401, *Flow in Transonic and Supersonic Turbomachines*, 1987.

13. Sharma, O.P., et al., Rotor-Stator Interaction in Multi-Stage Axial-Flow Turbines, AIAA Paper AIAA-88-3013, 1988.

14. Mayle, R.E., Dullenkopf, K., A Theory for Wake Induced Transition, to be presented at ASME Gas Turbine Conference, 1989.

15. Hansen, J.L., Okiishi, T.H., Rotor Wake Influence on Axial Compressor-Stator Boundary Layers, *J. Propulsion and Power*, Vol. 5, pp. 89-93, 1989.

16. Dong, Y., Cumpsty, N.A., Compressor Blade Boundary Layers, Parts I and II, ASME Papers 89-GT-50 and 89-GT-51, 1989.

17. Adamczyk, J.J., Mulac, R.A., Celestina, M.L., A Model for Closing the Inviscid Form of the Average-Passage Equation System, *ASME J. Turbomachinery*, Vol. 108, pp. 180-187, 1986.

18. Adamczyk, J.J., Model Equation for Simulating Flows in Multistage Turbomachinery, ASME Paper 85-GT-226, 1985.

19. Adamczyk, J.J., Private Communication, 1988.

20. Hathaway, M.D., Gertz, J.B., Epstein, A.H., Strazisar, A.J., Rotor Wake Characteristics of a Transonic Axial-Flow Fan, *AIAA Journal*, Vol. 24, pp. 1802-1810, 1986.

21. Kurosaka, M., et al., Energy Separation in a Vortex Street, *J. Fluid Mech.*, Vol. 178, pp. 1-29, 1987.

22. Preston, J.H., The Non-Steady Irrotational Flow of an Inviscid Incompressible Fluid, With Special Reference to Changes in Total Pressure Through Flow Machines, *Aeronautical Quarterly*, pp. 353-360, Nov. 1961.

23. Epstein, A.H., Gertz, J.B., Owen, P.R., Giles, M.B., Vortex Shedding in Compressor Blade Wakes, in AGARD CP-401, *Flow in Transonic and Supersonic Turbomachines*, 1987.

24. Giles, M.B., Private Communication, 1989.

25. Epstein, A.H., Shang, T., Giles, M.B., Sehra, A.K., Blade Row Interaction Effects on Compressor Measurements, to be presented at AGARD Meeting on Unsteady Flows in Compressors, 1989.

26. Giles, M.B., Calculation of Unsteady Wake/Rotor Interaction, *J. Propulsion and Power*, Vol. 4, pp. 356-362, 1988.

9. Lighthill, M.J., Physical Interpretation of the Mathematical Theory of Wave Generation by Wind, *Journal of Fluid Mechanics*, Vol. 14, pp. 385-398, 1962.

10. Wennerstrom, A.J., Low Aspect Ratio Compressors: Why and What It Means, 1986 SAE Cliff Garrett Lecture, to be published in *ASME J. Turbomachinery*.

11. Scott, J.N., Hankey, W., Navier-Stokes Solution of Unsteady Flow in a Compressor Rotor, *ASME J. Turbomachinery*, Vol. 108, pp. 206-215, 1986.

12. Richardson, S.M., A Numerical Study of Unsteady Flow Effects in a Supersonic Compressor Cascade, in AGARD CP-401, *Flow in Transonic and Supersonic Turbomachines*, 1987.

13. Sharma, O.P., et al., Rotor-Stator Interaction in Multi-Stage Axial-Flow Turbines, AIAA Paper AIAA-88-3013, 1988.

14. Mayle, R.E., Dullenkopf, K., A Theory for Wake Induced Transition, to be presented at ASME Gas Turbine Conference, 1989.

15. Hansen, J.L., Okiishi, T.H., Rotor Wake Influence on Axial Compressor-Stator Boundary Layers, *J. Propulsion and Power*, Vol. 5, pp. 89-93, 1989.

16. Dong, Y., Cumpsty, N.A., Compressor Blade Boundary Layers, Parts I and II, ASME Papers 89-GT-50 and 89-GT-51, 1989.

17. Adamczyk, J.J., Mulac, R.A., Celestina, M.L., A Model for Closing the Inviscid Form of the Average-Passage Equation System, *ASME J. Turbomachinery*, Vol. 108, pp. 180-187, 1986.

18. Adamczyk, J.J., Model Equation for Simulating Flows in Multistage Turbomachinery, ASME Paper 85-GT-226, 1985.

19. Adamczyk, J.J., Private Communication, 1988.

20. Hathaway, M.D., Gertz, J.B., Epstein, A.H., Strazisar, A.J., Rotor Wake Characteristics of a Transonic Axial-Flow Fan, *AIAA Journal*, Vol. 24, pp. 1802-1810, 1986.

21. Kurosaka, M., et al., Energy Separation in a Vortex Street, *J. Fluid Mech.*, Vol. 178, pp. 1-29, 1987.

22. Preston, J.H., The Non-Steady Irrotational Flow of an Inviscid Incompressible Fluid, With Special Reference to Changes in Total Pressure Through Flow Machines, *Aeronautical Quarterly*, pp. 353-360, Nov. 1961.

23. Epstein, A.H., Gertz, J.B., Owen, P.R., Giles, M.B., Vortex Shedding in Compressor Blade Wakes, in AGARD CP-401, *Flow in Transonic and Supersonic Turbomachines*, 1987.

24. Giles, M.B., Private Communication, 1989.

25. Epstein, A.H., Shang, T., Giles, M.B., Sehra, A.K., Blade Row Interaction Effects on Compressor Measurements, to be presented at AGARD Meeting on Unsteady Flows in Compressors, 1989.

26. Giles, M.B., Calculation of Unsteady Wake/Rotor Interaction, *J. Propulsion and Power*, Vol. 4, pp. 356-362, 1988.

27. Giles, M.B., Stator/Rotor Interaction in a Transonic Turbine, AIAA Paper AIAA-88-3093, 1988.

28. Bowditch, D.N., Coltrin, R.E., A Survey of Inlet Engine Distortion Capability, NASA TM-83421, 1983.

29. Williams, D.D., Review of Current Knowledge of Engine Response to Distorted Inflow Conditions, in Engine Response to Distorted Inflow Conditions, AGARD CP-400, 1987.

30. Ludwig, G.R., Nenni, J.P., Arendt, R.H., Investigation of Rotating Stall in Axial Flow Compressors and Development of a Prototype Stall Control System, Technical Report USAF-APL-TR-73-45, 1973.

31. Hynes, T.P., Greitzer, E.M., A Method for Assessing Effects of Inlet Flow Distortion on Compressor Stability, to be published in *ASME J. Turbomachinery*.

32. Hynes, T.P., et al., Calculations of Inlet Distortion Induced Compressor Flow Field Instability, to be published in *International Journal of Heat and Fluid Flow*.

33. McDougall, N.M., Cumpsty, N.A., Hynes, T.P., Stall Inception in Axial Compressors, ASME Paper 89-GT-63, 1989.

34. Garnier, V.H., Experimental Investigation of Rotating Waves as a Rotating Stall Inception Indication in Compressors, M.S. Thesis, Department of Aeronautics and Astronautics, MIT, 1989.

35. McDougall, N.M., Stall Inception in Axial Compressors, Ph.D. Thesis, Department of Engineering, Cambridge University, 1988.

36. Day, I.J., Private Communication, 1989.

37. Longley, J.P., Hynes, T.P., Stability of Flow Through Multistage Axial Compressors, ASME Paper 89-GT-311, 1989.

38. Greitzer, E.M., The Stability of Pumping Systems - The 1980 Freeman Scholar Lecture, *ASME J. Fluids Eng.*, Vol. 103, pp. 193-243, 1980.

39. Stetson, H.D., Designing for Stability in Advanced Turbine Engines, in AGARD CP-324, *Engine Handling*, October 1982.

40. Moore, F.K., Greitzer, E.M., A Theory of Post-Stall Transients in Axial Compression Systems, Parts I&II, *ASME J. Gas Turbines and Power*, Vol. 108, pp. 68-76 and pp. 231-240, 1986.

41. McCaughan, F., Application of Bifurcation Theory to Axial Flow Compressor Instability, ASME Paper 88-GT-231, 1988.

42. Lee, N.K.W., Greitzer, E.M., Effects of Endwall Suction and Blowing on Compressor Stability Enhancement, ASME Paper 89-GT-64, 1989.

43. Miyake, Y., Inaba, T., Kato, T., Improvement of Unstable Characteristics of an Axial FLow Fan by Air-Separation Equipment, *ASME J. Fluids Eng.*, Vol. 109, pp. 35-40, 1987.

44. Azimian, A.R., Elder, R.L., McKenzie, A.B., Application of Recessed Vane Casing Treatment to Axial Compressors, ASME Paper 89-GT-68, 1989.

45. Epstein, A.H., Ffowcs Williams, J.E., Greitzer, E.M., Active Suppression of Aerodynamic Instabilities in Turbomachines, *J. Propulsion and Power*, Vol. 5, pp. 204-211, 1989.

46. Huang, X., Active Control of Aerodynamic Instabilities, Ph.D. Thesis, Engineering Department, Cambridge University, 1988.

47. Pinsley, J.E., Active Control of Centrifugal Compressor Surge, M.S. Thesis, Department of Aeronautics and Astronautics, MIT, 1988.

48. Gysling, D., Control of Compressor Aerodynamic Instabilities Using Tailored Structures, M.S. Thesis, Department of Aeronautics and Astronautics, MIT, 1989

49. Fink, D.A., Surge Dynamics and Unsteady Flow Phenomena in Centrifugal Compressors, MIT Gas Turbine Laboratory Report No. 193, 1988.

50. Dimotakis, P.E., Two-Dimensional Shear Layer Entrainment, *AIAA Journal*, Vol. 24, pp. 1791-1796, 1986.

51. Adkins, G.G., Jr., Smith, L.H., Jr., Spanwise Mixing in Axial-Flow Turbomachines, Trans. ASME, *J. of Eng. for Power*, Vol. 104, pp. 97-110, January 1982.

52. Gallimore, S.J., Cumpsty, N.A., Spanwise Mixing in Multistage Axial Flow Compressors: Part I - Experimental Investigation, Trans. ASME, *J. of Turbomachinery*, Vol. 108, pp. 2-9, July 1986.

53. Wisler, D.C., Bauer, R.C., Okiishi, T.H., Secondary Flow, Turbulent Diffusion, and Mixing in Axial Flow Compressors, ASME Paper GT-16, 1987.

54. Werle, M.J., Paterson, R.W., Presz, W.M., Flow Structure in a Periodic Axial Vortex Array, AIAA Paper 87-0610, 1987.

55. Skebe, S.A., McCormick, D.C., Presz, W.M., Parameter Effects on Mixer Ejector Pumping Performance, AIAA Paper AIAA-88-0188, 1988.